

Direct spectrum tomography of the Earth's mantle using normal modes

Elisabeth Anna Alexia Maria Jagt

Utrecht Studies in Earth Sciences
No. 256

Examination committee:

Dr. S. Cottaar
Department of Earth Sciences
University of Cambridge, UK

Prof. dr. G. Laske
Scripps Institution of Oceanography
University of California, San Diego, USA

Prof. dr. J. Ritsema
Department of Earth and Environmental Sciences
University of Michigan, USA

Prof. dr. B. Romanowicz
University of California, Berkeley, USA
Collège de France, Paris, France
Institut de Physique du Globe de Paris, France

Prof. dr. J. A. Trampert
Department of Earth Sciences
Universiteit Utrecht, The Netherlands

ISBN: 978-90-6266-624-9

Copyright © 2022 by E.A.A.M. Jagt, Utrecht, The Netherlands

Cover illustration: S-wave velocity models for the one-step (top) and two-step (bottom) inversions.

Direct spectrum tomography of the Earth's mantle using normal modes

Directe spectra tomografie van de aardmantel met behulp
van normal modes
(met een samenvatting in het Nederlands)

Proefschrift

ter verkrijging van de graad van doctor
aan de Universiteit Utrecht
op gezag van de rector magnificus, prof. dr. H.R.B.M. Kummeling,
ingevolge het besluit van het college voor promoties
in het openbaar te verdedigen op dinsdag 14 juni 2022 des middags te 4.15 uur

door

Elisabeth Anna Alexia Maria Jagt

geboren op 10 juni 1994
te Amersfoort

Promotor:

Prof. dr. A. F. Deuss

This thesis was accomplished with financial support from the European Research Council (ERC) under the European Union's Horizon 2020 research and innovation programme (grant agreement no. 681535: ATUNE) and a Vici award number 016.160.310/526 from the Netherlands organization for scientific research (NWO).

voor mijn ouders

Contents

Summary	xi
Samenvatting	xiii
1 Introduction	1
1.1 Large Low Shear-wave Velocity Provinces	3
1.1.1 Seismic observations	3
1.1.2 Geodynamical/mineralogical interpretations	6
1.2 D" layer	10
1.3 Ultra Low Velocity Zones	11
1.4 Subducting slabs	12
1.5 Motivation	13
1.6 Outline	14
2 Normal mode theory	17
2.1 Introduction to normal modes	18
2.1.1 Terminology	18
2.2 General linearised equations of motion	19
2.2.1 Linearisation	20
2.3 Normal modes in a SNREI Earth	22
2.3.1 Radial scalar equations	23
2.4 Perturbations to SNREI model	24
2.4.1 Spherical perturbation and sensitivity kernels	24
2.4.2 General perturbation and splitting matrix	24
2.4.3 Cross-coupling	26
2.4.4 Synthetic spectra	30
3 Comparing one-step with two-step inversion	33
3.1 Introduction	34
3.2 Theoretical framework	36
3.2.1 Forward problem: synthetic spectra	37
3.2.2 Partial derivatives	40
3.2.3 Inversion method	41
3.2.4 Choices in weighting	42
3.2.5 Misfit definition	43
3.2.6 Theoretical comparison of the two methods	44

3.3	Data	44
3.4	Results	47
3.4.1	L-curves and misfits	47
3.4.2	Model characteristics	51
3.4.3	Odd degrees	56
3.5	Discussion and Conclusion	58
A1	Appendix A	60
4	Constraints on v_s, v_p, their ratio and S-Φ correlation	67
4.1	Introduction	68
4.1.1	Ratio between v_s and v_p heterogeneity	68
4.1.2	Previous observations of S- Φ anti-correlation	69
4.1.3	Mineral physics	70
4.2	Data and methods	71
4.2.1	R-median	74
4.2.2	R-RMS	75
4.3	Results for v_s , v_p and $R_{S/P}$	75
4.3.1	L-curves and misfits	76
4.3.2	Model characteristics	79
4.3.3	1D $R_{S/P}$	83
4.3.4	Distributions of $R_{S/P}$, v_s and v_p anomalies	85
4.4	Results for S- Φ correlation	86
4.4.1	Synthetic tests	86
4.4.2	Real data inversion for v_s and v_ϕ	89
4.4.3	Effect of a v_ϕ starting model	91
4.4.4	Extracting bulk sound from S-wave and P-wave velocity	93
4.5	Discussion	95
4.5.1	$R_{S/P}$ as indicator of chemical heterogeneity	95
4.5.2	(Anti-)correlation between v_s and v_ϕ anomalies	96
4.6	Conclusion	97
B1	Appendix B	99
5	Density	103
5.1	Introduction	104
5.2	Data and methods	107
5.3	Results	108
5.3.1	Misfit	112
5.3.2	Model characteristics	112
5.3.3	Synthetic inversions	115
5.3.4	Effect of a density starting model	115
5.4	Discussion and Conclusion	120
5.5	Outlook	122
C1	Appendix C	124
6	Shear attenuation in the mantle	129
6.1	Introduction	130
6.1.1	1D and 3D models of shear attenuation	131

6.2	Data and methods	134
6.3	Synthetic 3D $v_s + q_\mu$ inversions	136
6.4	Real data inversions	138
6.4.1	Starting model	142
6.5	Synthetic inversions simulating real data	145
6.6	Discussion and conclusion	148
D1	Appendix D.	151
7	Synthesis	153
7.1	General findings	153
7.1.1	On the nature of LLSVPs	155
7.2	Suggestions for future work	155
	Acknowledgements	161
	Bibliography	163
	Curriculum Vitæ	179
	List of Publications	180

Summary

The thermochemical nature of the lower mantle, and the two Large Low Shear-wave Velocity Provinces (LLSVPs) in particular, remains a topic of active debate. Exclusively imaging seismic velocity anomalies only provides limited ability to distinguish between thermal and compositional origins. In this thesis we use whole Earth oscillations, or normal modes, to study 3D variations in mantle shear wave velocity (v_s), compressional wave velocity (v_p), bulk sound velocity (v_ϕ), density (ρ) and shear attenuation (q_μ). These observations provide new constraints on the presence of lower mantle chemical heterogeneity. Normal mode observations are commonly included in seismic tomographic models in the form of splitting functions, a convenient intermediate step from normal mode spectra to a tomographic model. Here, we compare the two-step splitting function inversion method to the less frequently used, computationally more expensive one-step direct spectrum inversion. In theory, the one-step inversion suffers less from non-uniqueness and only requires regularization once. In practice, we find that the average spectral misfits for the one-step inversion are lower for each combination of mantle parameters we invert for.

Dissimilarities in model patterns and amplitudes between the two inversion methods grow larger when adding independent parameters to a v_s -only inversion, resulting in differences in thermochemical interpretations. The ratio between v_s and v_p anomalies obtained from their joint inversion, proposed to be an indicator of chemical heterogeneity when exceeding a threshold predicted by mineral physics, varies significantly between the two inversion methods. The method of computing the ratio is just as important. We obtain ratios exceeding the threshold in the lower mantle only when dividing the root mean square amplitudes of our v_s and v_p models, although lower than some previous studies suggest. However, by taking the median ratio from a grid at each depth, we barely exceed the threshold. Instead of relying on these 1D representatives of the ratio, we infer chemical heterogeneity in certain depth ranges based on a wide spread in distributions of v_s , v_p anomalies and their ratio.

Another constraint on the presence of chemical heterogeneity comes from the anti-correlation of v_s and v_ϕ structure. Whereas many previous studies find an anti-correlation in the lower mantle, we find (de-)correlation in the lower mantle in joint v_s and v_ϕ inversions, with only slightly negative correlation for the two-step inversion. We shift towards more negative correlation values when extracting v_ϕ from our previously obtained v_s and v_p models.

Lower mantle density structure has remained elusive and controversial in recent decades. In joint inversions for v_s , v_p , ρ and discontinuity topography, we show that a basal layer of excess density is located underneath part of the otherwise lighter-than-average LLSVPs, reconciling previous observations. This dense layer is more robust in the one-step inversion and does not result from high-amplitude ghost pat-

terns that are thought to have plagued earlier normal mode studies. Compositional variations such as iron enrichment may explain this dense but seismically slow layer.

Finally, we obtain preliminary results for imaging lower mantle shear attenuation in joint v_s and q_μ one-step inversions. As this is a pioneering study, we first select the best way of inverting for 3D q_μ in synthetic tests, before applying this method to real data. Mode selection appears to be crucial, as modes with limited q_μ sensitivity do not contribute in a constructive manner. We also need to properly account for detailed elastic structure to minimize leakage into anelastic structure. The preliminary 3D q_μ model shows low attenuation in LLSVPs and high attenuation in the surrounding lower mantle, possibly indicating a dominant role for grain size.

Samenvatting

De thermochemische status van de ondermantel, en van de twee Large Low Shear-wave Velocity Provinces (LLSVPs) in het bijzonder, is al lang een onderwerp van discussie. Door alleen te kijken naar variaties in seismische golfsnelheden kunnen we slechts in beperkte mate onderscheid maken tussen thermische en chemische oorzaken van mantelstructuren. In dit proefschrift gebruiken we de eigentrillingen van de aarde, ook wel normal modes genoemd, om 3D variaties in transversale golfsnelheid (v_s), longitudinale golfsnelheid (v_p), bulk geluidssnelheid (v_ϕ), dichtheid (ρ), en attenuatie of damping (q_μ). Deze observaties bieden nieuwe inzichten over de aanwezigheid van chemische heterogeniteit in de ondermantel. Normal mode observaties worden vaak meegenomen in seismische tomografische modellen in de vorm van splitting functies; een handige tussenstap als je van normal mode spectra naar een tomografisch model gaat. Hier vergelijken we deze twee-staps splitting functie inversie met de zelden gebruikte, rekenkundig dure één-staps directe spectra inversie. Theoretisch gezien lijdt de één-stapsinversie minder aan niet-uniekheid en vereist deze slechts eenmaal regularisatie. In de praktijk zien we dat de gemiddelde spectrale misfits lager zijn in de één-stapsinversie voor elke combinatie van mantelvariabelen waarvoor we inverteren.

Verschillen in modelpatronen en -amplitudes tussen de twee inversiemethodes groeien wanneer onafhankelijke parameters worden toegevoegd aan een pure v_s -inversie, wat leidt tot verschillende thermochemische interpretaties. De ratio tussen variaties in v_s en v_p verkregen uit hun gezamenlijke inversie, een indicator van chemische heterogeniteit als de ratio een drempelwaarde uit de mineraalfysica overschrijdt, verschilt aanzienlijk tussen de twee inversiemethodes. Net zo belangrijk is de methode waarmee de ratio berekend wordt. We verkrijgen alleen ratio's die de drempelwaarde in de ondermantel overschrijden als we de kwadratische gemiddeldes van de v_s en v_p modellen door elkaar delen, hoewel onze ratio's lager zijn dan eerder gesuggereerd. Echter, als we op elke diepte de mediaan uit een grid nemen komen we nauwelijks boven de drempelwaarde uit. In plaats van te vertrouwen op deze 1D representaties van de ratio, halen we aanwijzingen voor chemische heterogeniteit op bepaalde dieptes uit de wijde spreiding in de distributies van v_s en v_p variaties en hun ratio.

Een andere indicator van chemische heterogeniteit is de anti-correlatie tussen v_s en v_ϕ structuren. Terwijl veel eerdere onderzoeken een anti-correlatie vinden in de ondermantel, vinden wij (de-)correlatie in de ondermantel in gezamenlijke inversies voor v_s en v_ϕ , met een lichte negatieve correlatie voor de twee-stapsinversie. De correlatie verschuift naar meer negatieve waarden als we v_ϕ extraheren uit onze eerder verkregen v_s en v_p modellen.

De dichtheidsstructuur van de ondermantel is de laatste decennia ongrijpbaar en controversieel gebleken. Gezamenlijke inversies voor v_s , v_p , ρ en topografie van dis-

continuïteiten laten zien dat er een laag met hoge dichtheid op de kern-mantelgrens ligt, deels onder de verder lichte LLSVPs, wat eerdere observaties kan verzoenen. Deze dichte laag is robuuster in de één-stapsinversie en is niet het resultaat van overheersende “ghost” patronen, die in eerdere normal mode onderzoeken een grote rol kunnen hebben gespeeld. Compositionele variaties zoals ijzerverrijking zouden deze dichte maar seismisch langzame laag kunnen verklaren.

Als laatste doen we een inleidend onderzoek naar het in kaart brengen van attenuatie of demping in de ondermantel door middel van één-stapsinversies voor v_s en q_μ gezamenlijk. Aangezien we hiermee pionier zijn, selecteren we eerst de beste manier om voor 3D q_μ te inverteren uit synthetische testen, alvorens deze methode toe te passen op echte data. De selectie van normal modes lijkt cruciaal, omdat modes met beperkte gevoeligheid voor q_μ geen constructieve bijdrage leveren. We moeten ook rekening houden met gedetailleerde elastische structuren om de te zorgen dat ze niet in de anelastische structuur lekken. Het voorlopige 3D q_μ model heeft lage demping in LLSVPs en hoge demping in de omringende ondermantel, wat mogelijk wijst op een dominante rol van korrelgrootte.

1

Introduction

The vast majority of the Earth is physically inaccessible to us, shielded by the crust. We can only directly observe certain features at the surface, such as faults and volcanoes that are expressions of processes happening deeper in the Earth, and sense the earthquakes and volcanic eruptions that are associated with them. Advances in seismic tomography, where we use earthquake waves to image the deep Earth in 3D, have allowed us to indirectly observe the Earth's deep interior with ever increasing resolution; painting a picture of places where only sci-fi scientists can physically travel to.

The main topic of this thesis is using normal modes to image the Earth's mantle, which ranges from just below the crust-mantle boundary (the so-called Moho-discontinuity) to 2891 km depth at the core-mantle boundary (CMB). We aim to improve tomographic models of large-scale mantle structure in terms of its 3D shear-wave velocity (v_s), compressional-wave velocity (v_p), bulk sound velocity (v_ϕ), density (ρ) and shear attenuation (q_μ), by directly extracting information from normal mode spectra. The Earth's mantle plays an important role in the dynamics of the Earth as a whole. The mantle is heated from below by the outer core and from within by radioactive decay, and loses heat to the universe, implying that the Earth is slowly cooling down. This heat transport gives rise to mantle convection, with upwelling plumes (forming hotspot volcanoes) and downwelling subducted slabs as main contributors to vertical displacement. A significant portion of mantle material has been mixed by ongoing convection for millions of years, where some regions are affected more than others. The mantle is therefore not a homogeneous medium. Heterogeneities in the order of tens to thousands of kilometres have been mapped by seismic tomography (see recent review by Ritsema & Lekić (2020)).

Representing the Earth's properties as an average 1D radial profile, e.g. PREM (Dziewonski & Anderson, 1981) or ak135 (Kennett et al., 1995), provides a good first-order fit to a range of seismic observations, including body wave travel times, normal mode eigenfrequencies, and surface waves. The inner core – outer core interface is characterized by a major drop in shear-wave velocity (Fig. 1.1), from

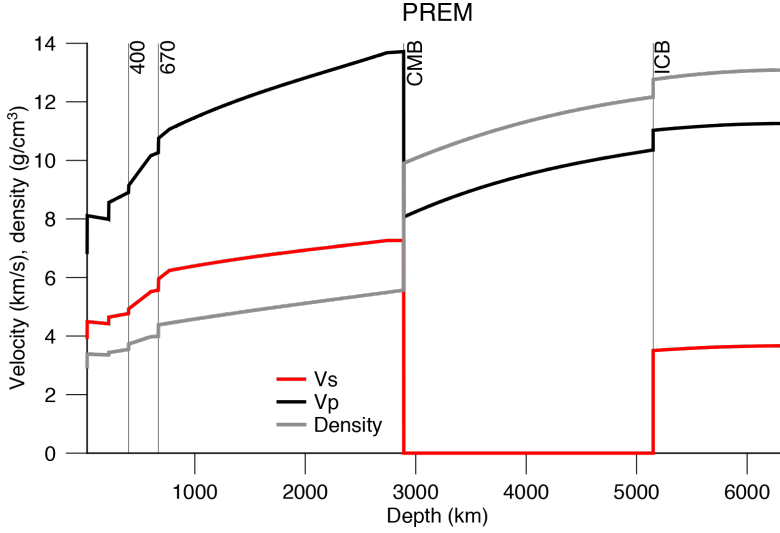


Figure 1.1: 1D Preliminary Reference Earth Model (PREM) (Dziewonski & Anderson, 1981), from the surface to the centre of the Earth, showing (isotropic) v_s (red), v_p (black) and density (grey), and major discontinuities ‘400’ and ‘670’ in the mantle transition zone, the core-mantle boundary (CMB) and the inner core boundary (ICB).

about 3.5-3.7 km/s in the solid iron-nickel alloy inner core to zero in the vigorously convecting fluid outer core, generating the Earth’s magnetic field. Another major interface is the CMB, which is characterized by a large drop in density and jump in seismic velocities from outer core to lower mantle (Fig. 1.1).

Distinct regions in the mantle from top to bottom derived from a 1D profile are (i) the upper mantle, (ii) mantle transition zone from 400 to 670 km depth and (iii) lower mantle. Velocities and density gradually increase with depth throughout the mantle, with discontinuities at the top and bottom of the mantle transition zone (Fig. 1.1). These transition zone interfaces are associated with global phase changes in the main upper mantle mineral olivine. The lower mantle hosts a number of regional and local scattering bodies or reflectors, but is not characterized by any more of these global discontinuities, the only exception potentially being the seismically distinct D” layer in the lowermost couple of hundred kilometres.

Seismic tomography maps spatial variations of a certain parameter (e.g. velocity, density, attenuation) with respect to a 1D average, often PREM. The three main types of seismic waves used in these studies are, in order of increasing period: body waves, surface waves and normal modes (whole Earth oscillations). Each type comes with its own depth sensitivity, lateral resolution, limitations and approximations. Seismic tomographic resolution generally decreases with increasing depth, so 3D upper mantle structures are more well-known than lower mantle structures. Even the nature and origin of the largest heterogeneities found in the Earth’s interior, the Large Low Shear-wave Velocity Provinces that we will introduce shortly, is heavily debated, as they are situated in the lowermost mantle where seismic resolution is

poorest.

I will give an overview here of the most studied lower mantle structures, from the largest (~ 1000 s kms) to the smallest (~ 10 s kms) heterogeneities, and how they are currently explained in terms of composition, temperature and their role in mantle dynamics. Apart from consensus on the existence of these structures, nearly every (thermo)chemical interpretation is debated, although some explanations seem more plausible than others.

1.1. Large Low Shear-wave Velocity Provinces

1.1.1. Seismic observations

The most prominent structures in global seismic tomographic models (Fig. 1.2), including those using normal modes, are two nearly anti-podal low velocity regions, dominated by spherical harmonic degree 2 (e.g. Li & Romanowicz, 1996; Ritsema et al., 1999, 2011; French & Romanowicz, 2015). One is located in the lower mantle beneath Africa, which was dubbed “Tuzo”, and the other is located beneath the Pacific Ocean, and was given the nickname “Jason” (Burke, 2011).

Originally called “superplumes”, these regions are currently referred to as Large Low Shear-wave Velocity Provinces (LLSVPs) (Garnero & McNamara, 2008) to avoid any implications on dynamic behaviour in their name, and simply refer to their low-velocity signature in 3D v_s models instead. Some recent studies started calling them Large Low Velocity Provinces (LLVPs), since their v_p is also lower than average (e.g. Masters et al., 2000a; Houser et al., 2008b; Koelemeijer et al., 2016). Although they are degree-2 dominant structures, their shapes in map view (Fig.

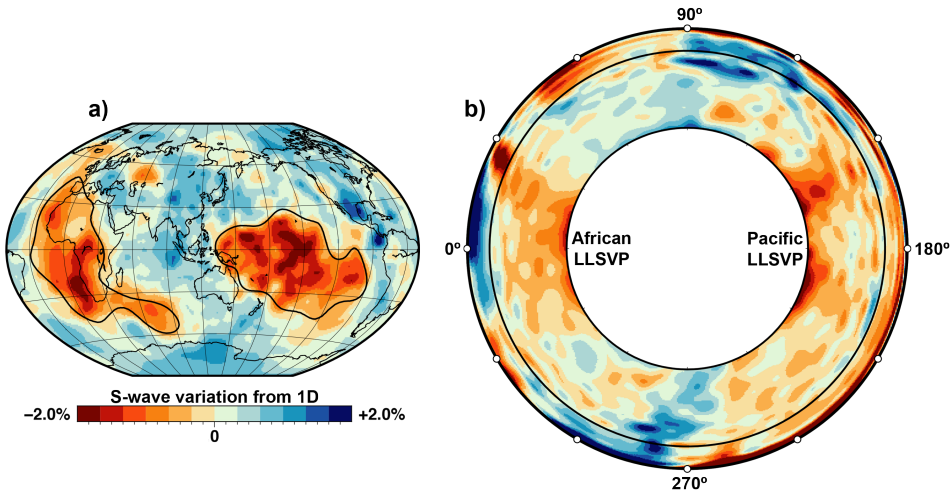


Figure 1.2: Tomographic S-wave velocity model S40RTS (Ritsema et al., 2011) a) in map view at 2800 km depth, with LLSVP outlines by Koelemeijer et al. (2016), b) in cross-section view showing the radial extent of the LLSVPs, where the section intersects at the equator, and the degrees represent degrees east from the meridian.

1.2a) and cross-section view (Fig. 1.2b) are not identical. For example, the African LLSVP is more elongated in a north-west south-east direction, whereas the Pacific LLSVP is more rounded.

Although the exact details of LLSVP geometry vary due to different modelling approaches and data sets, cluster analyses have shown that tomographic studies agree very well on the lateral extent of LLSVPs in S-wave velocity models (Lekic et al., 2012) (Fig. 1.3), and to a lesser degree in P-wave velocity models (Cottaar & Lekic, 2016; Garnero et al., 2016). Global tomographic models agree less well (correlation < 0.4) for spherical harmonic degrees higher than 16, which comes down to structures of about 2,500 km and smaller (Meschede & Romanowicz, 2015) that have been excluded from cluster analyses. LLSVPs, or LLVPs, do not even appear as coherent continent-sized low velocity regions in some P-wave velocity models, but instead as a collection of smaller scattered regions (Houser et al., 2008b; Hosseini et al., 2019). Detailed seismic waveform analysis infer that LLSVPs may be bounded by steep lateral gradients in v_s (e.g. Ni et al., 2002; Wang & Wen, 2004; He et al., 2006). Their sharpness at the top and their vertical extent are less well defined, ranging from approximately 300-400 to 2000 km above the CMB and varying for both LLSVPs (e.g. Garnero & McNamara, 2008; He & Wen, 2009; Tanaka et al., 2009; French & Romanowicz, 2015).

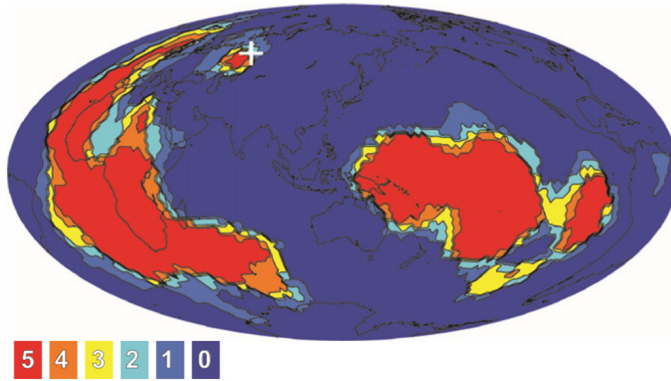


Figure 1.3: Taken from Lekic et al. (2012). Vote map resulting from a cluster analysis of slower-than-average v_s anomalies in 5 global tomographic models (Méglin & Romanowicz, 2000; Houser et al., 2008b; Kustowski et al., 2008; Simmons et al., 2010; Ritsema et al., 2011) in depth range 1000-2800 km. Colours point to the number of models that agree on a slow anomaly in a particular region.

The large uncertainty in their vertical extent translates to large variations in volume estimates of LLSVPs. The volume fraction of both LLSVPs based on the $-1.0\% \delta v_s/v_s$ contour in v_s model SMEAN (Becker & Boschi, 2002), the average of three 3D v_s models, adds up to 1.6% of the mantle. This is a conservative estimate according to Cottaar & Lekic (2016), who argue this number is 8% based on cluster analysis of five tomographic models. The volume fraction of LLSVPs is strongly dependent on the choice of velocity contour or other measures used to define their boundaries, and to a lesser extent on the tomographic models. The volume occupied

by the LLSVPs has implications for their nature and origin, and for the size of a geochemical reservoir potentially residing within them.

There is a high geographic correlation between LLSVP edges at the CMB on the one hand and past and present hotspots at the Earth's surface (Thorne et al., 2004), large igneous provinces (LIPs) (Torsvik et al., 2006), and kimberlites (Torsvik et al., 2010) on the other hand. Moreover, the probability of obtaining the specific degree 2 configuration of LLSVPs is 0.001 by randomly generating the 5 degree 2 spherical harmonic coefficients (Dziewonski et al., 2010), so these structures were hardly formed accidentally. All of these observations suggest that LLSVPs are stable and long-lived features of the lower mantle. The geographic correlations suggest a relation between LLSVP edges and surface expressions in the form of mantle plumes (e.g. Burke et al., 2008; French & Romanowicz, 2015), although correlations between LIPs and the interior of LLSVPs is statistically indistinguishable from the correlation with the edges (Austermann et al., 2014). These plumes would have to be nearly completely vertical conduits, neglecting horizontal convective flow. Furthermore, correlation does not necessarily imply causation and these surface expressions also correlate well with other features such as diverging plate boundaries (Julian et al., 2015).

The prominent degree 2 signal in mantle tomography is also present in gravity anomalies. The geoid is elevated above the LLSVPs, after correcting for the gravity signal of subducting slabs (e.g. Hager et al., 1985). Interpreting the gravity signal in terms of LLSVP density is complicated by the non-unique nature of gravity measurement owing to trade-offs between underlying density and dynamic topography. Hot rising superplumes can create positive geoid anomalies due to the dominant effect of dynamic topography, whereas dense piles can result in positive geoid anomalies if excess density would be the most important contributor to the geoid.

The lower mantle is characterized by a high ratio of S- to P-wave velocity variations, with even higher values for the LLSVPs (e.g. Masters et al., 2000a; Koelemeijer et al., 2016; Moulik & Ekström, 2016), and wide distributions of this ratio laterally (Deschamps & Trampert, 2003). Whereas S-wave velocity (v_s) in LLSVPs is lower than average, bulk sound velocity (v_ϕ) is often found to be higher, leading to an anti-correlation between v_s and v_ϕ anomalies (e.g. Su & Dziewonski, 1997; Ishii & Tromp, 1999, 2001; Masters et al., 2000a; Resovsky & Trampert, 2003; Trampert et al., 2004; Mosca et al., 2012).

In addition to low S- and P-wave velocities, LLSVPs are commonly characterized by a higher-than-average density, at least in a significant part of them. High LLSVP density is primarily constrained by normal mode splitting measurements (e.g. Ishii & Tromp, 1999; Resovsky & Trampert, 2003; Trampert et al., 2004; Mosca et al., 2012; Moulik & Ekström, 2016), and the Earth's tides (Lau et al., 2017), implying an anti-correlation between v_s and density anomalies. However, Stoneley modes, a certain type of normal modes sensitive to depths just above the CMB, prefer lighter than average LLSVPs (Koelemeijer et al., 2017), providing an apparently contradicting observation of LLSVP density. Recent efforts to reconcile these observations come from looking at the different depth sensitivities to density between Stoneley modes

and tides. Both observations can be satisfied by a dense layer at the base of LLSVPs (Lau et al., 2020; Robson et al., 2021; van Tent et al., 2021). Despite concerns on the resolvability of lower mantle density (Resovsky & Ritzwoller, 1999b; Romanowicz, 2001; Kuo & Romanowicz, 2002), especially in earlier studies, we slowly converge to a better understanding of density heterogeneities in the deep mantle.

Besides imaging elastic structures, seismic waves also provide information on anelastic processes in the mantle. Intrinsic seismic attenuation, i.e. energy of seismic waves being transformed into heat, of LLSVPs has been measured using body waves and normal mode splitting functions, yielding apparently contradicting results. Body wave studies infer the LLSVPs to be regions of high attenuation, at least in part of them (Lawrence & Wyssession, 2006b; Hwang & Ritsema, 2011; Liu & Grand, 2018), whereas an inversion of anelastic splitting functions results in low attenuation in LLSVPs (Talavera-Soza et al., 2021b). The biggest challenge of imaging seismic attenuation using body waves is separating the intrinsic attenuation from apparent attenuation due to scattering and focussing of seismic energy. This distinction is more easily made in normal mode research, in part because of the negligible sensitivity of normal modes to small-scale scatterers. Reconciling the above-mentioned observations and improving techniques to image lower mantle attenuation are important steps for the seismological community to take in the near future.

Normal modes are the only seismic waves directly sensitive to anomalies in density, in addition to v_s , v_p , v_ϕ , and seismic attenuation, and are therefore especially well-suited to make robust observations of the large-scale seismic signature of LLSVPs. We will provide novel constraints on these parameters within the LLSVPs by using an extensive normal mode data set and reviving a long overlooked direct spectrum inversion approach.

1.1.2. Geodynamical/mineralogical interpretations

LLSVPs most likely play a very important role in mantle dynamics. In spite of many observations of various parameters, as outlined above, their exact role is not yet clear. Several conceptual models of LLSVPs and the surrounding lower mantle have been put forward (e.g. Kellogg et al., 1999; Courtillot et al., 2003; Dziewonski et al., 2010; Torsvik et al., 2014). Four endmember models encountered in geodynamic modelling efforts have been described by Garnero et al. (2016) (Fig. 1.4), which we will discuss here. The significant variations in morphology between these models reflect the uncertainties regarding the nature and origin of LLSVPs. Normal modes can only resolve large-scale morphological features, and will therefore need to be combined with higher frequency seismic observations to distinguish between piles, superplumes and plume clusters.

One possible nature of LLSVPs is that they are in fact a collection of smaller plumes, originating from the CMB (Fig. 1.4a), which only appear as coherent structures through the blurry lense of seismic tomography (Schubert et al., 2004). Plume conduits have always been notoriously difficult to image in seismic tomography because of an effect called wavefront healing, where seismic waves that have interacted with a small low velocity anomaly, such as a plume conduit, restore their original

wavefront before arriving at the seismic station. Employing dense seismic arrays to measure waves diffracted by a plume-like structure could improve their resolvability (e.g. Stockmann et al., 2019). Recent improvements in resolution of seismically slow and narrow structures suggests that the LLSVPs may indeed not be as continuous as they seem in lower spherical harmonic degree (<18) models (French & Romanowicz, 2015; Lei et al., 2020). Davaille & Romanowicz (2020) argue that the position and morphology of the plume clusters in this case are dictated by the degree 2 pattern of subduction, and have shifted depending on patterns of past subduction throughout the Earth's evolution. This kind of mantle convection is slab-driven, known as a “top-down” convection model. The proposed plumes may entrain dense material and still maintain overall buoyancy (Davaille & Romanowicz, 2020).

Another conceptual model portrays the LLSVPs as buoyant superplumes or domes (Fig. 1.4b), which was first observed by Tackley et al. (1998) in numerical simulations and by Davaille (1999) in laboratory experiments with an initially stratified fluid. Superplumes are long-lived thermochemical structures, stabilized by counteracting forces from positive buoyancy due to high temperatures and negative buoyancy due to chemical composition.

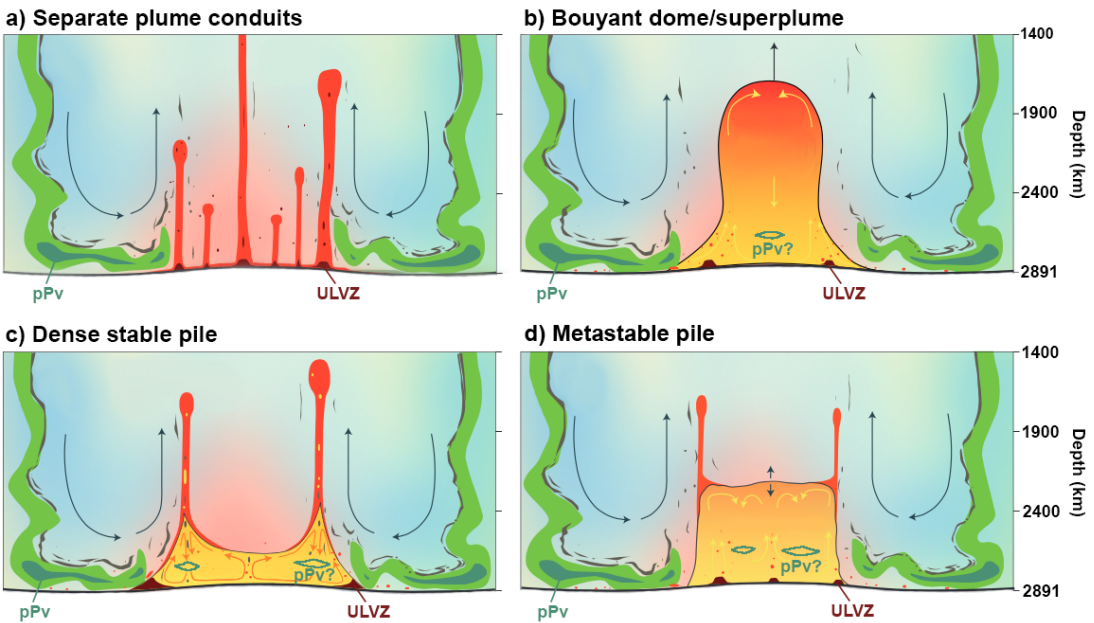


Figure 1.4: Adapted from Garnero et al. (2016). Conceptual models of the lowermost ~1500 km of the mantle. The four proposed morphologies of LLSVPs are surrounded by subducting slabs (light green), possibly containing post-perovskite (pPv; dark green), and carrying oceanic crust (thin slivers of brown). Dark red small-scale structures on top of the CMB are ULVZs (ultra-low velocity zones). The four LLSVP cases consist of a) clusters of separate plume conduits, b) buoyant domes or superplumes, c) dense stable piles, and d) metastable piles. Faded background colours represent the blurry picture of slow (red) and fast (blue) areas from seismic tomographic models.

Finally, LLSVPs may be denser-than-average stable piles (Fig. 1.4c) (e.g. Li et al., 2014; Gülcher et al., 2021) or meta-stable piles with an internal density cross-over (Fig. 1.4d) (e.g. Tan & Gurnis, 2005; Bower et al., 2013), with long-lived plumes generated along their margins, and possibly even short-lived secondary plumes from their roofs (Ballmer et al., 2016). In these two models the LLSVPs are stable and may have anchored mantle convection in its degree 2 configuration. This type of convection is referred to as “bottom-up” convection (Dziewonski et al., 2010), in contrast to the slab-driven top-down convection model mentioned earlier.

Seismic observations of LLSVPs mentioned before generally require some degree of thermochemical heterogeneity to explain them (e.g. Ishii & Tromp, 1999; Trampert et al., 2004; Simmons et al., 2010; Mosca et al., 2012; Moulik & Ekström, 2016). However, some studies argue for a dominant role of thermal heterogeneity. Sharp edges might indicate compositional boundaries, but we cannot exclude sharp edges corresponding to a purely thermal anomaly, according to geodynamical studies (Schuberth et al., 2009; Davies et al., 2012). They also argue from their mantle convection simulations that thermochemical LLSVPs regularly overpredict deep mantle S-wave velocity anomalies, compared to purely thermal buoyant LLSVPs. Furthermore, anti-correlation between v_s and v_ϕ anomalies and the high ratio between 3D v_s and v_p may be explained by post-perovskite (e.g. Murakami et al., 2004; Oganov & Ono, 2004; Tsuchiya et al., 2004), a high-pressure polymorph of the most abundant mantle mineral bridgmanite, not requiring the presence of chemical heterogeneity (Koelemeijer et al., 2018). However, the stability field of post-perovskite is still highly debated, and has even been proposed to be situated at outer core pressures (e.g. Cobden et al., 2012). Recent in-situ high-pressure and -temperature experiments suggest that the phase transition does occur under lower mantle conditions (Kuwayama et al., 2021).

In the thermochemical pile paradigm (Fig. 1.4c,d), proposed compositions of the LLSVPs include recycled oceanic crust (e.g. Christensen & Hofmann, 1994; Hirose et al., 2005; Jones et al., 2020), ancient primordial material (e.g. Labrosse et al., 2007; Deschamps et al., 2012), or a combination of the two (e.g. Tackley, 2012; Ballmer et al., 2016; Gülcher et al., 2021). Deschamps et al. (2012) argue that material enriched in perovskite (bridgmanite) and iron provides a good explanation for the seismic signature of the LLSVPs, and that LLSVPs being composed of recycled oceanic crust seems highly unlikely, as this MORB would have to heat up to unrealistically high temperatures to produce the observed low velocities. On the other hand, geodynamical studies such as Jones et al. (2020) show that long-term recycling of oceanic crust is able to create warm low-velocity piles with a dense base, complying with seismic observations, as long as the density contrast between subducted basaltic material and the ambient mantle is sufficient. The geochemical nature of LLSVPs partly determines the start of modern-day plate tectonics, as dense primordial LLSVPs could have a profound delaying impact on this onset (Kreielkamp et al., 2022).

Geochemical evidence supports the existence of a primordial reservoir in the mantle. The mantle is thought to be composed of various geochemical reservoirs, inferred from the observation of different geochemical compositions of basalts at the

surface (see review by White (2015)). The source material of these basalts originates from a range of depths in the mantle. Hotspot basalts, called Ocean Island Basalts, or OIBs for short, have a different geochemical signature than the basalts found at mid-ocean ridges, called Mid Ocean Ridge Basalts, or MORBs. Within OIBs there are subclasses with different trace element isotope ratios, potentially reflecting different degrees of mixing, whereas MORBs are relatively uniform in chemical signature. Furthermore, OIBs are less degassed and less depleted in incompatible elements than MORBs, which are elements that preferentially go into the melt phase upon partial melting, indicating that their source material has undergone limited recycling and melting in the past. If this primordial geochemical reservoir resides inside LLSVPs, they must have been denser to survive being entrained in mantle convection over geological time scales (Tackley, 2012). If hotspots originate from within LLSVPs or from their margins, as spatial correlations suggest, they might be tapping into the LLSVPs as a geochemical reservoir (e.g. Kellogg et al., 1999), showing signatures of both primordial material and recycled oceanic crust (e.g. Christensen & Hofmann, 1994). Recent geochemical analyses on OIBs of the Galápagos Archipelago revealed that the recycled oceanic crust component might be related to the Pacific LLSVP margin only, not to the enriched interior (Gleeson et al., 2021), which agrees with the slab configuration in the conceptual models of Fig. 1.4.

Alternatively, Ballmer et al. (2017) propose that the LLSVPs are composed of recycled oceanic crust, and the ambient mantle in between as viscous primordial geochemical reservoirs, called bridgmanite-enriched ancient mantle structures (BEAMS) (Fig. 1.5). These BEAMS would have survived mantle convection due to their high viscosity and are being sampled by plumes on their way up, explaining the enriched signature of OIBs.

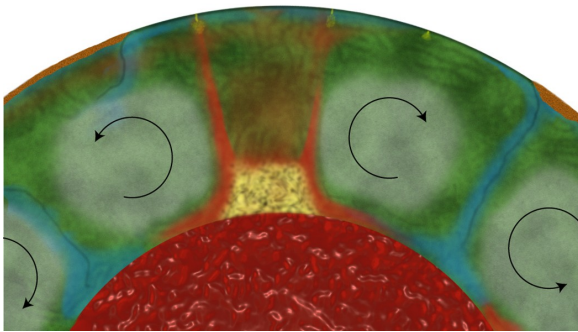


Figure 1.5: Taken from Ballmer et al. (2017). Conceptual mantle model showing the high viscosity BEAMS (grey blobs), one LLSVP (yellow), plumes (red) and slabs (blue).

We will contribute to the thermal versus thermochemical LLSVPs debate by interpreting our normal mode models of various seismic parameters. If LLSVPs are chemically distinct, normal mode observations of 3D velocities, density and attenuation combined with mineral physics may predict their preferred bulk composition.

1.2. D" layer

The D" region at the base of the mantle is also of great interest to mantle dynamics, as it directly overlays the outer core, and therefore any interaction between the mantle and core takes place in this region. It is thought to host the roots of mantle plumes, and possibly accumulated ancient subducted slabs. The D" layer is seismically distinct from the rest of the lower mantle (Bullen, 1949) and marked by a discontinuity at the top. This D" reflector has been found in many regions with a depth averaging around 200-300 km above the CMB, constrained mostly by travel times of seismic waves reflected off the top of this layer (e.g. Lay & Helmberger, 1983). Several explanations have been suggested for this reflector, such as subducted slabs (e.g. Kendall & Silver, 1998), disconnected scattering bodies (e.g. Scherbaum et al., 1997), and the phase change from bridgmanite to post-perovskite (Murakami et al., 2004; Oganov & Ono, 2004; Tsuchiya et al., 2004).

A comparison between polarities of D" reflected waves (PdP, SdS) on one hand and direct waves (P,S) and CMB reflections (PcP, ScS) on the other hand provides information on the velocity change across the D" reflector. Polarity observations vary globally. In some locations, PdP polarities are opposite to P and PcP waves, indicating a decrease in v_p velocity across D" (e.g. Thomas et al., 2011; Pisconti et al., 2019), while SdS polarities agree with S and ScS waves, indicating a positive velocity jump in v_s across D" (e.g. Chaloner et al., 2009; Cobden & Thomas, 2013). These observations discard a purely thermal origin and can be explained by the presence of post-perovskite (Thomas et al., 2022). In regions where both SdS and PdP have opposite polarities to the main phases, post-perovskite may still cause the D" reflector, within a MORB layer, if the P-wave velocity change is positive across the phase transition. This could be the case, as the P-wave velocity change is small and could be slightly positive or negative depending on the exact composition of post-perovskite (e.g. Tsuchiya & Tsuchiya, 2006b).

An alternative explanation for these variations in polarity observations is seismic anisotropy (e.g. Thomas et al., 2011; Pisconti et al., 2019). Contrary to most of the lower mantle, the D" region is characterized by strong seismic anisotropy, especially in the areas surrounding the LLSVPs, where observations of SKS, ScS or S_{diff} splitting were made. Typically, horizontally polarized shear waves (v_{sh}) travel faster than their vertically polarized counterparts (v_{sv}), whereas regions within the LLSVPs have either no significant anisotropy, laterally varying anisotropy or faster v_{sv} (see review by Romanowicz & Wenk (2017)) (Fig. 1.6). The observed anisotropy might reflect the preferred orientations of crystals that are aligned due to horizontal flow outside of the LLSVPs and vertical flow inside the LLSVPs, as part of mantle convection (e.g. McNamara et al., 2002; Wenk et al., 2011). Combined observations of shear wave splitting and polarity observations, over a range of distances and azimuths, are required to uniquely constrain the (anisotropic) nature and composition of this D" layer (Creasy et al., 2019).

Studying 3D variations in D" anisotropy with normal modes is beyond the scope of this thesis, but large-scale radial anisotropy has been modelled through observations of resonance (i.e. cross-coupling) between the two main types of normal modes: spheroidal and toroidal (Schneider & Deuss, 2021b). Their radial anisotropy model

matches the body wave studies that generally find $v_{sh} > v_{sv}$ surrounding LLSVPs and $v_{sv} \geq v_{sh}$ within LLSVPs (Fig. 1.6).

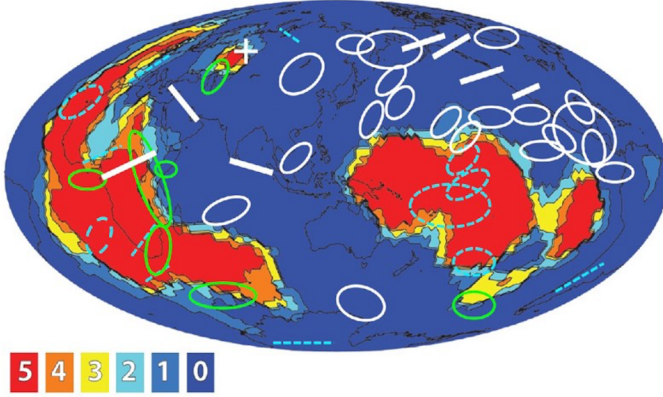


Figure 1.6: Taken from Chandler et al. (2021), adapted from Romanowicz & Wenk (2017). Ellipses and lines superimposed on the map by Lekic et al. (2012) where shear wave splitting observations infer $v_{sv} > v_{sh}$ (cyan dashed), $v_{sh} > v_{sv}$ (white), or the presence of strong lateral anisotropic variations (green).

1.3. Ultra Low Velocity Zones

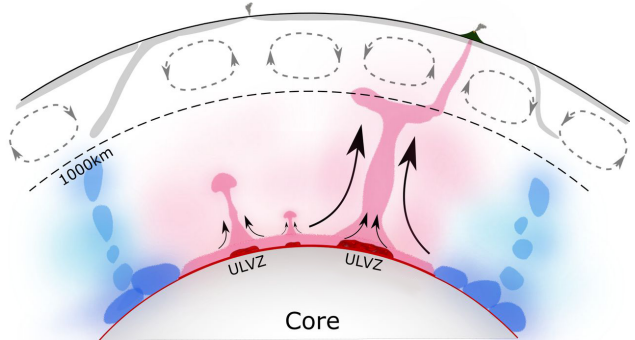
Other important features observed in seismic studies are Ultra Low Velocity Zones (ULVZs), which are 5-40 km thick regions in the D'' layer, directly overlying the CMB, characterized by very low seismic velocities ($> 10\%$ drop in velocity) (Garnero et al., 1998). An increase in density of about 10% has also been inferred for some ULVZs by fitting synthetic to observed seismograms (Rost et al., 2005). They are primarily located within the LLSVPs and near their margins, with only a few ULVZs spotted away from LLSVPs (see review by McNamara (2019)). Although Yu & Garnero (2018) found no clear correlation of ULVZs with hotspots, a couple of hotspot locations at the surface are linked to large ULVZs at the CMB (e.g. Cottar & Romanowicz, 2012; Yuan & Romanowicz, 2017), with seismic tomography suggesting a link between them in the form of a plume (French & Romanowicz, 2015), as depicted in the conceptual models of Fig. 1.4. At the time of conducting their study, Yu & Garnero (2018) found that roughly 17.1% of the CMB area has been probed for ULVZs, with 10.3% corresponding to positively identified ULVZs. There is an uneven and patchy coverage of studies probing the CMB for ULVZs due to the localized sensitivity of body waves and uneven distribution of suitable earthquake-receiver pairs. Normal mode studies provide global tomographic models and do not suffer from this uneven distribution. However, small-scale ULVZs can only be measured by high frequency waves (i.e. body waves), so our normal mode models will not provide novel constraints for these anomalous features.

The exact cause of the very low seismic velocities within ULVZs is unknown. Some studies argue for partial melt as the cause for ULVZs, as they found the drop

in S-wave velocity to be up to 3 times larger than the drop in P-wave velocity (e.g. Williams & Garnero, 1996; Rost et al., 2005). However, ULVZs without this difference in velocity drop between v_s and v_p also exist (e.g. Hutko et al., 2009), which may point to a chemical component to ULVZs, or multiple origins. Contrary to partial melt causing the low velocities, Mao et al. (2006) suggest ULVZs are made up of solid post-perovskite, having higher density due to enrichment in iron, formed by core-mantle reactions. If ULVZs anchor hotspot mantle plumes through time, their high densities would help stabilize them (Garnero et al., 2016).

Some studies propose that these ULVZs are remnants of an ancient basal magma ocean, implying that they have to be denser than average to remain gravitationally stable features at the base of the mantle throughout the Earth’s evolution (Labrosse et al., 2007). Increased iron content in partial melt, caused by a different iron partitioning due to the iron spin transition, could explain the extreme drop in velocities and make the melt denser than the surrounding solid mantle (Nomura et al., 2011).

Figure 1.7: Taken from Yuan & Romanowicz (2017). Conceptual model showing the thin basal partially molten layer (red, 10x vertically exaggerated) with local thickening resulting in ULVZs, from which plumes arise. This model assumes the “bundle” of plumes scenario for LLSVPs (see also Fig. 1.4a). A change in viscosity around 1000 km is also depicted.



ULVZs may also represent detectable thickened features in an otherwise seismically virtually undetectable thin (i.e. with a thickness of several kilometres) partially molten layer (Fig. 1.7) (Garnero & Helmberger, 1996; Yuan & Romanowicz, 2017). This thin basal layer is a candidate for excess density in the lowermost mantle found by normal mode and tidal studies (e.g. Trampert et al., 2004; Moulik & Ekström, 2016; Lau et al., 2017), while at the same time being invisible to Stoneley modes that did not find excess density (Koelemeijer et al., 2017). We will use a large data set of normal modes, including these Stoneley modes, to provide constraints on the exact location of the proposed lower mantle excess density, and find a way to reconcile prior observations. Unfortunately, a layer of several kilometres in thickness lies well below the detection limit of normal modes, so such a basal layer would need to be much thicker to be visible in our density models.

1.4. Subducting slabs

Oceanic plates subducting into the mantle are downwellings that displace mantle material and thereby play a key role in mantle convection. Subducting slabs, both from present subduction and paleosubduction processes, explain the upper mantle

high velocity regions around the Pacific Ocean (i.e. “the ring of fire”), and are a plausible explanation for the high velocity ring around the LLSVPs in the lower mantle interpreted to be a “slab graveyard”. Both of these high-velocity rings are visible in large-scale normal mode models, although individual slabs are hard to image using normal modes only. High-velocity features do not suffer from wave-front healing, making thin slabs easier to image than narrow plumes. However, agreement between 14 tomographic models on current slab locations decreases in the lower mantle, where tomographic resolution drops and thermal diffusion and dissipation could make the slabs look more smeared (Shephard et al., 2017). Although subducted oceanic crust is arguably denser than the ambient mantle at all depths greater than 720 km (Hirose et al., 2005), viscous forces might be too strong to overcome for the subducted slab to penetrate all the way down to the CMB (Wang et al., 2020). Seismic tomography cannot give us a definitive answer (yet) on whether or not slabs reach the CMB as illustrated in Figs. 1.4, 1.5 and 1.7, but it does seem likely. Our normal mode studies will not provide any definitive answers to that question, as individual slabs will appear as smeared high-velocity regions.

Fukao & Obayashi (2013) defined four categories of slabs in their detailed P-wave model resulting from an inversion of more than 10 million P-wave travel times: i) stagnating above the 670-discontinuity, ii) penetrating the 670-discontinuity, iii) trapped in uppermost lower mantle (670-1000 km depth), and iv) descending into the deep lower mantle. They found most slabs to reside in stages i and iii, and stages ii and iv to likely be transient stages.

Slab stagnation in the mid-mantle, combined with ponding of low-velocity plumes in some tomographic models (French & Romanowicz, 2015), could be linked to viscosity changes. Rudolph et al. (2015) inferred a jump in viscosity around 1000 km depth, based on geoid analysis. Studies using teleseismic body waves also find mid-mantle reflectors around this depth (e.g. Jenkins et al., 2017; Waszek et al., 2018). The exact reason behind a possible viscosity jump is still debated, as there are no known phase changes in major mantle constituents related to this depth.

The viscous BEAMS mentioned before (Fig. 1.5) are one of the explanations for an inferred mid-mantle increase in viscosity. Explanations for slab stagnation specifically involve a viscosity change in ferropericlase surrounding subducting slabs due to an increase in strength (Marquardt & Miyagi, 2015), and a density cross-over in a basalt enriched lower mantle rendering some subducting slabs neutrally buoyant, while other slabs still penetrate to the deep mantle (Ballmer et al., 2015). Alternatively, the iron spin transition in ferropericlase, predicted to occur at mid-lower mantle pressures and temperatures (Badro et al., 2003; Tsuchiya et al., 2006), reduces viscosity in regions outside of the proposed BEAMS, resulting in a low viscosity channel where slabs might accelerate (Marquardt & Miyagi, 2015).

1.5. Motivation

As we have seen in this general introduction, there are still a lot of active questions regarding the thermochemical state of the mantle, particularly of the deep mantle. Could post-perovskite be a dominant constituent of the D” layer? Why do upwellings and downwellings seem to pond or stagnate at particular depths in

the mantle? Can we reconcile seemingly contradicting observations of lower mantle density? Regarding LLSVPs, what is their role in mantle convection (stable mantle anchors or buoyant superplumes) and what can we say about their thermochemical nature? Based on the observations mentioned earlier, LLSVPs are most likely thermochemical structures, but the relative importance of temperature and composition is poorly understood. Are LLSVPs geochemical reservoirs for primordial material, and/or recycled MORB? The aim of this thesis is providing novel observations of v_s , v_p , v_ϕ , ρ and q_μ anomalies in the mantle, using the one-step direct spectrum inversion of normal modes. Results of the one-step inversion will be compared to those of the more commonly used two-step splitting function inversion (more details on these methods in Chapter 3), for which we use the same spectral data as starting point. We will compare these two inversion methods throughout the entire thesis, for each combination of mantle parameters, to see whether the one-step inversion improves our models. While normal modes are sensitive to large-scale structures only, and will hence not be able to resolve e.g. mantle plumes or ULVZs, they will be able to provide new perspectives on the thermochemical nature of LLSVPs. We expect that the one-step inversion will contribute towards better constraints on lower mantle density and attenuation especially, two of the least well-known seismic parameters. Motivated by an increase in computational power and recent large earthquakes, we are extending the work done by Li et al. (1991), and more recently Akbarashrafi (2020), in terms of an expanded data set, more detailed tomographic models, and adding more independent parameters to v_s in the inversion.

1.6. Outline

We will start with an introduction to the seismic data that we will be using throughout this thesis in Chapter 2: normal modes, or Earth's free oscillations. In addition to clarifying the terminology used in normal mode research, we give a brief overview of the theory behind normal modes; how we go from conservation of momentum and mass to a description of normal mode displacement. We also demonstrate the main concepts related to normal modes and the Earth's heterogeneity: cross-coupling and singlet splitting. These two phenomena are described by the splitting matrix, which, as we will show, is used to compute synthetic spectra.

In Chapter 3 we compare the one-step direct spectrum inversion to the two-step splitting function inversion, in a continuation of the study by Li et al. (1991) using an expanded normal mode data set. Whereas the two-step inversion involves an intermediate step of inverting for splitting functions, which can be non-unique and not necessarily agree with a single mantle model, the one-step inversion inverts the spectra directly, but is computationally more expensive. A comparison between these inversion methods is drawn in a theoretical sense, by outlining the differences in their equations, and in a practical sense, by inverting the same spectral data for a model of 3D shear-wave velocity (the parameter that normal modes are most sensitive to). Both inversion methods yield very similar v_s models to those reported by other tomographic studies using normal modes, however, there are differences in the more detailed structures of the two models. We find the one-step inversion producing lower spectral misfits than the two-step inversion, for the same number of

effective eigenvalues, but the two-step inversion still performs decently. We finally show that our current data set has insufficient odd-degree sensitivity to make robust claims on odd-degree structures in the mantle. We require more measurements of mode pairs that couple for odd degrees to study, for example, any (dis)similarities between the two LLSVPs.

We then focus our attention in Chapter 4 on relaxing the scaling factor (introduced in Chapter 3) between v_s and v_p heterogeneity in the mantle, and invert for these two parameters jointly. The ratio $R_{S/P}$ between $\delta \ln v_s$ and $\delta \ln v_p$ has been suggested to be indicative of chemical heterogeneity when exceeding a certain threshold from mineral physics calculations. The way that this ratio is computed varies greatly between studies. We compute the 1D depth-dependent ratio for our one-step and two-step v_s and v_p models in the two most common ways: i) by dividing their RMS amplitudes, and ii) by taking the median $R_{S/P}$ at each depth. The ratios, and thereby the thermochemical interpretations, depend both on the inversion method, and on the method of computing this 1D $R_{S/P}$. For completeness, we show the distributions of $R_{S/P}$ and v_s and v_p anomalies with depth for both inversion methods, as this will yield a more representative view of the ratio. A wider distribution points to more than one underlying cause of the spread, i.e. temperature is not the only mechanism. We find depth ranges where the presence of thermochemical heterogeneity is required to explain our observations of $R_{S/P}$, although the exact depths differ between the one-step and two-step models. In addition, we invert jointly for v_s and v_ϕ heterogeneity. The anti-correlation between $\delta \ln v_s$ and $\delta \ln v_\phi$ has also been proposed as indicator of chemical heterogeneity, as a purely thermal mantle cannot generate a S - Φ anti-correlation. We perform synthetic inversions and starting model tests to explore the robustness of inverting for 3D bulk sound velocity. The upper and lowermost mantle are most poorly constrained by the data, especially in the two-step inversion. In the bulk of the mantle we find S - Φ (de-)correlation, contrary to most other studies. We do find anti-correlation in the lower mantle when extracting $\delta \ln v_\phi$ from our v_s and v_p models.

In Chapter 5, we seek to relax another scaling factor employed in the previous chapters, the scaling factor between v_s and density heterogeneity. Independent observations of density contribute to the understanding of the buoyancy and thermochemical nature of LLSVPs. Normal modes are the only seismic data sensitive to lower mantle density, but previous density models based on Stoneley modes and Earth's tides have produced seemingly conflicting results. We present state-of-the-art density models obtained by inverting for v_s , v_p , ρ and topography on the '400', '670' discontinuities and core-mantle boundary (CMB), using the one-step and two-step inversions. Both density models show a dense sliver just above the CMB, partly overlapping with the LLSVPs, which is more robust in the one-step inversion with respect to density starting models. We perform synthetic tests to assess the degree of contamination of velocity structure into density. There is some leakage, but it is smaller in amplitude than the observed density models. We therefore believe that the dense base is robust, which provides a way of reconciling previous contradicting observations. This sliver could be related to iron enrichment.

We have investigated elastic structures in the mantle thus far. In Chapter 6,

we direct our final modelling efforts towards attenuation, which is the anelastic process of wave energy transforming into heat. Attenuation is a key parameter for mapping variations in temperature, partial melt, water content, and composition. Lower mantle attenuation is relatively unknown, so we will perform the first one-step normal mode inversion for mantle attenuation here, and compare our results to new constraints from splitting functions. We start running synthetic tests for four plausible direct spectrum inversion schemes to see whether we can recover various 3D input v_s and q_μ models. The inversion scheme that is most successful in recovering the input models concerns first inverting for v_s anomalies, which then serves as a starting model for a joint inversion for v_s and q_μ . One-step and two-step attenuation models for the same normal mode data set display significant differences, which might be resolved when we invert for detailed elastic structures in the one-step inversion, thereby minimizing leakage of elastic into anelastic structure.

Finally, the main points of this thesis are summarized in the synthesis chapter. We will also try to combine the observations of all explored parameters to make a final interpretation of the thermochemical state of the lower mantle. In the end, we suggest directions for future research.

2

Normal mode theory

In this chapter we describe the background and theory of normal modes; the seismic data that we use in order to get information on the Earth's interior. It is beyond the scope of this thesis to provide a thorough overview of all the theory, and instead we refer to Dahlen & Tromp (1998) for a more comprehensive and complete story. We will first look at the physical basis for normal modes, starting from the momentum equation and Poisson's equation, and ending up with the linearised equations of motion for a general Earth model. We then simplify these equations for a spherical non-rotating elastic isotropic (SNREI) Earth, and introduce the eigenfunctions and eigenvalues that arise as natural solutions for the displacement field. These eigenfunctions and eigenvalues corresponding to normal modes are perturbed when the Earth model deviates from SNREI, removing the degeneracy of the modes' singlet frequencies. We finally introduce the splitting matrix, including various degrees of cross-coupling between modes, and how to use the splitting matrix to compute synthetic seismograms.

2.1. Introduction to normal modes

Seismic tomographic studies employ measurements of three different types of waves sampling the Earth's interior, which are, from the highest to the lowest frequencies, body waves, surface waves and normal modes. The first two wave types are travelling waves or travelling disturbances of the medium, and the latter are standing waves. It is important to note that these different types are, in fact, equivalent. Travelling waves can be obtained by superposition of standing waves, which is often done when computing synthetic seismograms, and vice versa (e.g. Masters & Widmer, 1995). Surface waves in a seismogram can be replicated by fundamental normal modes ($n = 0$), since their energy is concentrated near the Earth's surface. The normal-mode equivalent of body waves such as S, SS, SSS, and P, PP, PPP are modes that have oscillatory energy distribution, followed by a turning point where the energy starts decaying exponentially. Summation of normal modes with the same turning point as the ray turning point of body waves, creates a very similar seismogram to actual body wave arrivals. Finally, we have a normal-mode equivalent of ScS and PcS (core-reflected) body waves: modes whose energy oscillates all the way until the core-mantle boundary. In the remainder of this chapter and thesis, our primary focus is on normal modes, since it is the type of data we use in the inversions for 3D mantle structure. We will outline some of their general characteristics and theoretical and physical background below.

2.1.1. Terminology

Earth's free oscillations, or normal modes, are long-period standing waves along the surface and radius of the Earth. Due to their nature as standing waves, they only exist at discrete frequencies, typically between 0.3 and 10 mHz. Normal modes involve 3D oscillations of the Earth as a whole, similar to the 2D harmonics that arise after plucking a guitar string. The disturbance needed to excite normal modes comes from large earthquakes, typically magnitude M_w 7.4 or higher. Modes can be subdivided into two main categories, based on the nature of their displacement: i) spheroidal modes, which are characterised by P-SV motion similar to Rayleigh waves, and ii) toroidal modes, which are similar to Love waves and hence involve SH motion (Fig. 2.1).

Each normal mode has a unique displacement pattern, governed by radial eigenfunctions marked by integers n , l , and spherical harmonics marked by n , l and m in the lateral direction. The number of zero crossings in the radial direction is given by overtone number n . If $n = 0$ we call the mode a fundamental mode, and if $n > 0$ it is called an overtone. This is similar to the terminology for a guitar string, where overtones are also referred to as harmonics. l is the angular order and m the azimuthal order. The number of nodal surfaces in the longitudinal direction is given by $|m|$ and the number of nodal surfaces in the latitudinal direction is given by $|l - m|$. Azimuthal order m is limited to the interval $-l \leq m \leq l$, whereas n and l can be any non-negative integer. Each mode consists of $2l + 1$ eigenfunctions, or singlets, which is why the ensemble of all $2l + 1$ singlets is called multiplet. In this thesis, when we say "mode" it refers to multiplet. Each singlet is denoted by azimuthal order m . In a spherically symmetric non-rotating Earth, all singlet eigenfrequencies

are the same, or degenerate. The degeneracy of singlet frequencies is removed when the Earth departs slightly from this spherical symmetry, as is the case in the real Earth. This phenomenon is called splitting, as a single symmetric peak for the entire multiplet will split into separate peaks for each singlet in the frequency spectrum. The effects of the Earth's rotation and ellipticity on singlet splitting are well-known, which leaves the effect of Earth's 3D structure as the unknown parameter that we invert for.

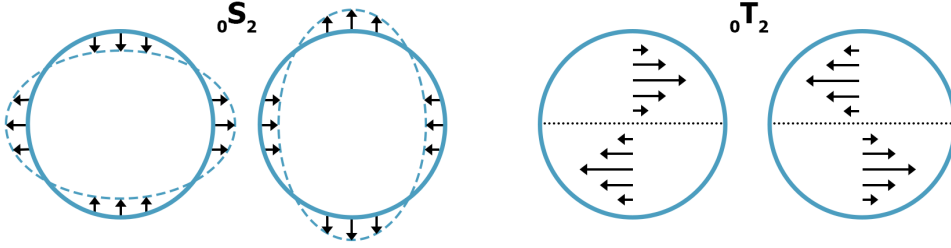


Figure 2.1: Oscillation patterns for a spheroidal mode ${}_0S_2$ (also called “rugby” mode) and a toroidal mode ${}_0T_2$, both for $m = 0$.

2.2. General linearised equations of motion

Before we arrive at the equation describing normal modes, we need to start with the equilibrium equations, and then expand upon them using conservation of momentum and mass. We initially consider an Earth model in mechanical equilibrium, i.e. undisturbed, only acted upon by self-gravitation of the planet. We omit the centrifugal potential here, as our reference Earth is non-rotating. In this case, the equations of mechanical equilibrium and gravitation are:

$$\tau_{ij,j}^0 = \rho^0 \phi_{,i}^0 \quad (2.1)$$

$$\phi_{,ii}^0 = 4\pi G \rho^0 \quad (2.2)$$

where τ_{ij}^0 is the initial static stress field, ϕ^0 the initial gravitational potential, ρ^0 the initial density, which are all functions of position \mathbf{x} . G is the gravitational constant, and $\phi_{,i}$ implies differentiation of ϕ with respect to x_i , i.e. $\partial\phi/\partial x_i$.

When the state of equilibrium is perturbed (i.e. an earthquake occurs), the particle that was at original location \mathbf{x} will move to new location $\mathbf{r} = \mathbf{r}(\mathbf{x}, t)$, therefore the stress tensor and gravitational potential are now depending on space *and* time. If we want to write the momentum equation (eq. 2.1) and Poisson's equation (eq. 2.2) for this new location $\mathbf{r} = \mathbf{r}(\mathbf{x}, t)$, we obtain:

$$\frac{\partial \tau_{ij}}{\partial r_j} = \rho \frac{\partial \phi}{\partial r_i} + \rho D_t^2 r_i \quad (2.3)$$

$$\frac{\partial^2 \phi}{\partial r_i \partial r_i} = 4\pi G \rho \quad (2.4)$$

where the Lagrangian material time derivative $D_t = \partial_t + \mathbf{v} \cdot \nabla_r$ (the time derivative at constant \mathbf{x}) is introduced, in which \mathbf{v} is the Eulerian velocity. Note that the zero superscripts are dropped here for the material properties, since we are not at the equilibrium position any more. Alternatively, we can make the stress tensor and gravitational potential functions of \mathbf{x} again:

$$\frac{\partial x_k}{\partial r_j} \frac{\partial \tau_{ij}}{\partial x_k} = \rho \frac{\partial x_k}{\partial r_i} \frac{\partial \phi}{\partial x_k} + \rho D_t^2 r_i \quad (2.5)$$

$$\frac{\partial x_k}{\partial r_i} \frac{\partial}{\partial x_k} \left(\frac{\partial x_l}{\partial r_i} \frac{\partial \phi}{\partial x_l} \right) = 4\pi G \rho \quad (2.6)$$

The equivalence between eqs. 2.3 and 2.5 on one hand, and eqs. 2.4 and 2.6 on the other hand is clear when eliminating all the double x_k and x_l terms.

Apart from conservation of momentum, we also take conservation of mass into account. If we compare the mass of a small volume element in the equilibrium state, $\rho^0 d^3x$, to the mass of its corresponding element after perturbation, ρd^3r , they must be equal as no mass is lost, hence $\rho^0 d^3x = \rho d^3r$. Conservation of mass is then defined as

$$J\rho = \rho^0 \quad (2.7)$$

where J is the Jacobian determinant:

$$J = J(\mathbf{x}) = \frac{\partial(r_1, r_2, r_3)}{\partial(x_1, x_2, x_3)} = \det(r_{i,j}) \quad (2.8)$$

2.2.1. Linearisation

For linearisation purposes, we now introduce the displacement vector \mathbf{s} , that connects the original position \mathbf{x} to the new position \mathbf{r} (Fig. 2.2):

$$r_i = x_i + s_i \quad (2.9)$$

where s_i is small, which is why we will ignore all higher order terms of s_i in the derivation that follows.

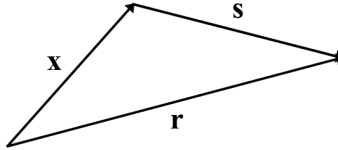


Figure 2.2: Displacement vector \mathbf{s} connecting the old position \mathbf{x} to the new position \mathbf{r} .

We can use this s_i to linearise the density ρ and gravitational potential ϕ in eqs. 2.5, 2.6 and 2.7. The first order changes in density ρ^1 and gravitational potential ϕ^1 are related to the deformation at a fixed point in space, so they follow an Eulerian description:

$$\rho^1 = \rho(\mathbf{r}) - \rho^0(\mathbf{r}) \quad (2.10)$$

$$\phi^1 = \phi(\mathbf{r}) - \phi^0(\mathbf{r}) \quad (2.11)$$

Using eq. 2.9, we linearise these two equations as:

$$\rho = \rho(\mathbf{r}) = \rho^0(\mathbf{x} + \mathbf{s}) + \rho^1 = \rho^0 + s_k \rho_{,k}^0 + \rho^1 \quad (2.12)$$

$$\phi = \phi(\mathbf{r}) = \phi^0(\mathbf{x} + \mathbf{s}) + \phi^1 = \phi^0 + s_k \phi_{,k}^0 + \phi^1 \quad (2.13)$$

We can approximate the determinant of eq. 2.7 using eq. 2.9, neglecting any higher order terms:

$$J = \det(r_{i,j}) = \det((x_i + s_i)_{,j}) = \det(\delta_{ij} + s_{i,j}) = 1 + s_{j,j} \quad (2.14)$$

Substituting eq. 2.12 and eq. 2.14 into 2.7 gives the expression:

$$\rho^0 = (1 + s_{j,j})(\rho^0 + s_k \rho_{,k}^0 \rho^1) \quad (2.15)$$

which, when neglecting any higher order terms and implementing the product rule, becomes:

$$\rho^1 = -s_k \rho_{,k}^0 - \rho^0 s_{k,k} = -(\rho^0 s_k)_{,k} \quad (2.16)$$

To complete the system of equations of motion, we need a constitutive law relating the incremental stress change τ_{ij}^1 at a material particle (Lagrangian description) to the elastic displacement s_i . An in-depth derivation is given by Biot (1965), but we will keep it brief here. The Lagrangian incremental Cauchy stress change is described by:

$$\tau_{ij}^1 = \tau_{ij}(\mathbf{r}) - \tau_{ij}^0(\mathbf{x}) \quad (2.17)$$

Following Dahlen & Tromp (1998), the linearized constitutive relation between τ_{ij}^1 and the displacement s_i can be expressed in terms of a new fourth-order tensor Υ_{ijkl} :

$$\tau_{ij}^1 = \Upsilon_{ijkl} s_{l,k} \quad (2.18)$$

Using the fact that

$$\Upsilon_{ijkl} = \Lambda_{ijkl} + \tau_{jk}^0 \delta_{il} - \tau_{ij}^0 \delta_{kl} \quad (2.19)$$

with $\Lambda_{ijkl} = c_{ijkl} + \tau_{ik}^0 \delta_{jl}$ as the fourth-order tensor relating the incremental first Piola-Kirchhoff stress tensor to the displacement. The first Piola-Kirchhoff stress tensor relates forces on a material surface in the deformed state at position \mathbf{r} to the corresponding undeformed surface at the original position \mathbf{x} . In the end, it can be shown that the perturbation can be written as:

$$\tau_{ij}^1 = \Lambda_{ijkl} s_{l,k} + \tau_{jk}^0 s_{i,k} - \tau_{ij}^0 s_{k,k} \quad (2.20)$$

where the term $\Lambda_{ijkl} s_{l,k}$ represents the incremental first Piola-Kirchhoff stress: \mathbf{T}^{PK1} .

When we substitute the first order approximations of eqs. 2.12, 2.13 and 2.17 into the equations of motion (eqs. 2.5 and 2.6), using the expressions found in eqs. 2.16 and 2.20, and employ the first order approximation:

$$\frac{\partial x_i}{\partial r_j} = \delta_{ij} - \frac{\partial s_i}{\partial x_j} \quad (2.21)$$

we finally obtain the equations of motion:

$$\rho^0(\partial_t^2 s_i + \phi_{,i}^1 + s_j \phi_{,ij}^0) = (\Lambda_{ijkl} s_{l,k})_{,j} \quad (2.22)$$

$$\phi_{,ii}^1 = -4\pi G(\rho^0 s_i)_{,i} \quad (2.23)$$

in which $s_i(\mathbf{x}, t)$ and $\phi^1(\mathbf{x}, t)$ are the unknowns that govern Earth's free oscillations. The other quantities, ρ^0 , ϕ^0 , τ_{ij}^0 and Λ_{ijkl} are assumed to be known parameters of the Earth model. All of the parameters are subject to boundary conditions, such as continuity of traction and displacement across welded (solid-solid) boundaries, continuity of displacement perpendicular to free-slip (fluid-solid) boundaries, and that the gravitational potential vanishes at infinity.

In order to excite the Earth's free oscillations, we need a force distribution $\mathbf{F}(\mathbf{x}, t)$ representing an earthquake, which we introduce in eq. 2.22 to get

$$\rho^0(\partial_t^2 s_i + \phi_{,i}^1 + s_j \phi_{,ij}^0) - (\Lambda_{ijkl} s_{l,k})_{,j} = F_i \quad (2.24)$$

or, in vector notation:

$$\rho^0(\partial_t^2 + \nabla \phi^1 + \mathbf{s} \cdot \nabla \nabla \phi^0) - \nabla \cdot \mathbf{T}^{\text{PK1}} = \mathbf{F} \quad (2.25)$$

A symbolic way to write down this general equation that determines the seismic displacement \mathbf{s} is:

$$(\mathcal{H}^0 + \rho^0 \partial_t^2) \mathbf{s} = \mathbf{F} \quad (2.26)$$

where \mathcal{H}^0 represents the integro-differential operator corresponding to the left-hand-side of eq. 2.24.

2.3. Normal modes in a SNREI Earth

It is convenient to compute normal modes for a spherical non-rotating elastic isotropic (SNREI) Earth first, and treat the asphericity, rotation, anelasticity and anisotropy with perturbation theory. The general equations given in the previous section are hence simplified. This reference Earth model also has a initial hydrostatic stress field:

$$\tau_{ij}^0 = -\delta_{ij} p^0(r) \quad (2.27)$$

where $p^0(r)$ is the initial pressure distribution depending only on the radius r . When we use this expression of hydrostatic stress in eqs. 2.18 and 2.19 for the stress perturbation, we obtain:

$$\tau_{ij}^1 = \Upsilon_{ijkl} s_{l,k} \quad (2.28)$$

with

$$\Upsilon_{ijkl} = c_{ijkl} - p^0(\delta_{jl} \delta_{ik} + \delta_{il} \delta_{jk} - \delta_{ij} \delta_{kl}) \quad (2.29)$$

$$\Lambda_{ijkl} = \Upsilon_{ijkl} + p^0(\delta_{il} \delta_{jk} - \delta_{ij} \delta_{kl}) \quad (2.30)$$

Substituting eq. 2.30 into the equation of motion (eq. 2.22), we end up with

$$\rho^0(\partial_t^2 s_i + \phi_{,i}^1 + s_j \phi_{,ij}^0) - (\Upsilon_{ijkl} s_{l,k})_{,j} - (p^0 s_{i,j})_{,j} + (p^0 s_{k,k})_{,j} = F_i \quad (2.31)$$

In the case of isotropy, which is assumed throughout this thesis, we get a simple expression for Υ_{ijkl} depending on only the bulk $\kappa(r)$ and shear modulus $\mu(r)$:

$$\Upsilon_{ijkl} = \mu(\delta_{ik}\delta_{jl} + \delta_{il}\delta_{jk}) + (\kappa - \frac{2}{3}\mu)\delta_{ij}\delta_{kl} \quad (2.32)$$

As in the general case (eq. 3.6), we may write down the problem that involves determining the seismic displacement \mathbf{s} in a symbolic way:

$$(\mathcal{H}^0 + \rho^0 \partial_t^2) \mathbf{s} = \mathbf{F} \quad (2.33)$$

After taking the Fourier transform in time, effectively replacing ∂_t by $i\omega$, we get:

$$(\mathcal{H}^0 - \rho^0 \omega^2) \mathbf{s} = \mathbf{F} \quad (2.34)$$

For the homogeneous solution ($\mathbf{F} = 0$), we can rewrite the problem in terms of its eigenfunctions \mathbf{s}_k and eigenvalues ω_k :

$$\mathcal{H}^0 \mathbf{s}_k = \rho^0 \omega_k^2 \mathbf{s}_k \quad (2.35)$$

The solution to eq. 2.34 (with $\mathbf{F} = 0$) then becomes a harmonic function of time:

$$\mathbf{s}(\mathbf{x}, t) = \mathbf{s}_k(\mathbf{x}) e^{i\omega_k t} \quad (2.36)$$

in which $\mathbf{s}_k(\mathbf{x})$ represents the spatial shape of a free oscillation that resonates in the Earth long after the earthquake rupture has ceased.

2.3.1. Radial scalar equations

Following e.g. Woodhouse (1980), we seek solutions for the eigenfunctions employing spherical harmonics and spherical polar coordinates (r, θ, ϕ) , in the form:

$${}_n \mathbf{s}_l^m = {}_n U_l(r) Y_{lm}(\theta, \phi) \hat{\mathbf{r}} + {}_n V_l(r) \nabla_1 Y_{lm}(\theta, \phi) + {}_n W_l(r) \hat{\mathbf{r}} \times \nabla_1 Y_{lm}(\theta, \phi) \quad (2.37)$$

in which operator ∇_1 means $\hat{\boldsymbol{\theta}} \partial_\theta + \text{cosec} \theta \hat{\boldsymbol{\phi}} \partial_\phi$, $\hat{\mathbf{r}}$, $\hat{\boldsymbol{\theta}}$ and $\hat{\boldsymbol{\phi}}$ are unit vectors pointing in the coordinate directions, and ${}_n U_l(r)$, ${}_n V_l(r)$, ${}_n W_l(r)$ are the radial scalar eigenfunctions. $Y_{lm}(\theta, \phi)$ are the scalar spherical harmonics as defined by Edmonds (1960). The subscript k in \mathbf{s}_k has been replaced by the three integer numbers mentioned at the beginning of this chapter that describe a mode singlet: n, l, m . We can formulate solutions for the gravitational potential in a similar way, with radial scalar eigenfunctions $P(r)$:

$$\phi^1 = {}_n P_l(r) Y_{lm}(\theta, \phi) \quad (2.38)$$

They can be solved for the appropriate boundary conditions.

It can be shown that $U(r)$, $V(r)$, and $P(r)$ are completely decoupled from $W(r)$ (e.g. Dahlen & Tromp, 1998; Woodhouse & Deuss, 2007), from which the natural distinction between spheroidal and toroidal modes originates. For toroidal modes, $U = V = P = 0$, and displacement is purely horizontal in a SNREI Earth, implying that these modes do not affect the Earth's density distribution nor its gravitational

potential. On the other hand, $W(r) = 0$ for spheroidal modes, with displacement composed of both vertical and horizontal components.

We also note here that radial eigenfunctions $U(r)$, $V(r)$, $W(r)$ and $P(r)$ do not depend on azimuthal order m in a SNREI Earth, which is where the degeneracy of the eigenfrequencies ω_k comes from. All $2l + 1$ singlets within a mode/multiplet have different spherical harmonic horizontal motions depending on azimuthal order m , but the same eigenfrequency and radial displacement patterns.

2

2.4. Perturbations to SNREI model

As mentioned before, it is convenient to have a SNREI model as reference, and treat the deviations from the reference state with perturbation theory. We distinguish here between a spherical perturbation and a general aspherical perturbation (parameterised in spherical harmonics).

2.4.1. Spherical perturbation and sensitivity kernels

Let us consider a model parameterised in terms of shear wave velocity v_s , compressional wave velocity v_p and density ρ , containing internal discontinuities. The frequency of a mode is affected by changes in the spherical structure of the Earth: $\omega \rightarrow \omega + \delta\omega$. This first order perturbation in angular frequency $\delta\omega$ due to perturbations $\delta v_s(r)$, $\delta v_p(r)$, $\delta\rho(r)$ in the elastic parameters and δh_d in the discontinuities can be described by:

$$\delta\omega = \int_0^a \left(K_{v_s}(r) \frac{\delta v_s(r)}{v_s^0(r)} + K_{v_p}(r) \frac{\delta v_p(r)}{v_p^0(r)} + K_\rho(r) \frac{\delta\rho(r)}{\rho^0(r)} \right) dr + \sum_d K_d \frac{\delta h_d}{h_d^0} \quad (2.39)$$

in which a is the Earth's radius and K_{v_s} , K_{v_p} , K_ρ and K_d are the sensitivity kernels to variations in v_s , v_p , ρ and topography on internal discontinuities, respectively. Expressions for such sensitivity kernels are given by Woodhouse (1980).

We show some example sensitivity kernels for v_s , v_p and ρ for a few representative modes (Fig. 2.3): a fundamental mode (${}_0S_6$), a CMB Stoneley mode (${}_2S_{16}$) and a mode with a high overtone number (${}_{13}S_{19}$). The v_s and v_p sensitivity kernels of a fundamental mode are not oscillatory with depth (Fig. 2.3a), and the higher the l , the more they act like surface waves, with their sensitivity kernels peaking in the uppermost part of the mantle. On the other hand, density kernels often oscillate around zero, even for fundamental modes, which could explain the difficulty in making robust density models. The sensitivity of a CMB Stoneley mode peaks at the core-mantle boundary (Fig. 2.3b), especially for v_p . The other two kernels, v_s and ρ , peak above the CMB. For higher n , the eigenfunctions of a mode become more oscillatory with depth, and their sensitivity kernels as well, as demonstrated for mode ${}_{13}S_{19}$ (Fig. 2.3c).

2.4.2. General perturbation and splitting matrix

Woodhouse & Dahlen (1978) and later Woodhouse (1980) have proposed formulations for a general perturbation to SNREI and its effects on the eigenvalue problem

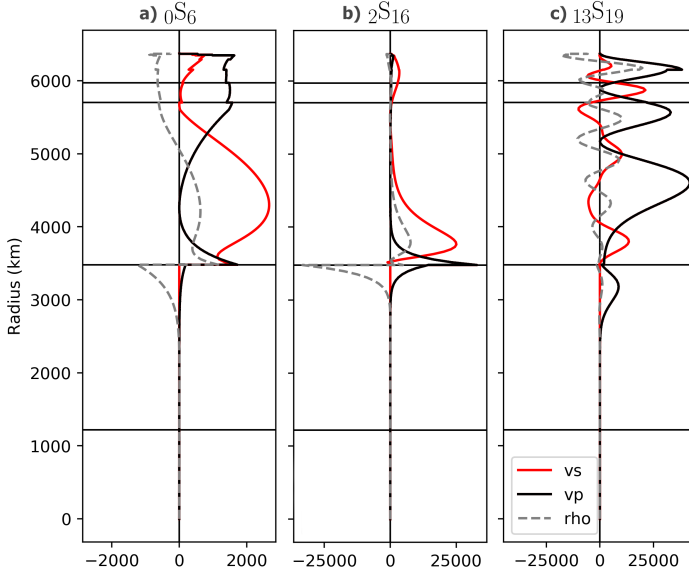


Figure 2.3: Sensitivity kernels for v_s , v_p , ρ for modes $0S_6$, $2S_{16}$ and $13S_{19}$. The 400- and 670-km discontinuity, core-mantle boundary and inner-outer core boundary are plotted.

of eq. 3.9. Under the influence of rotation, ellipticity and 3D structure, the perturbed eigenvalue equation becomes:

$$[\mathcal{H}^0 + \mathcal{H}^1 - (\rho^0 + \rho^1)\sigma^2] \mathbf{u} = 0 \quad (2.40)$$

where σ and \mathbf{u} are the eigenfrequencies and eigenfunctions of the perturbed system, and ρ^1 and \mathcal{H}^1 are the perturbations in density and the integro-differential operator. Rewriting \mathbf{u} in a different way:

$$\mathbf{u} = \sum_{km} |km\rangle \langle km | \rho^0 | u \rangle \quad (2.41)$$

where eigenfunctions of the unperturbed system are written as $|km\rangle = \mathbf{s}_k^m$, and their complex conjugates as $\langle km| = \mathbf{s}_k^{m*}$, where $k = (n, l, q)$ is the collection of overtone number, angular order and mode type (i.e. S(pheroidal) or T(oroidal)). As the degeneracy of mode singlets is removed when perturbations are introduced, we have separated the azimuthal order m from the other integers. Using the unperturbed eigenvalue equation (eq. 3.9) to rewrite \mathcal{H}^0 and substituting the expression for \mathbf{u} , we arrive at:

$$\sum_{km} \langle k'm' | [(\mathcal{H}^1 - \rho^1 \sigma^2) - (\sigma^2 - \omega_k^2) \rho^0] | km \rangle \langle km | \rho^0 | u \rangle = 0 \quad (2.42)$$

Using the requirement that $\sigma^2 = \omega_0^2 + \delta\omega$, where ω_0 is a reference frequency close to the unperturbed frequencies ω_k , here defined as $\omega_0 = 0.5(\omega_k + \omega_{k'})$, and $\delta\omega$ be a

small perturbation, we end up with:

$$\sum_{km} [(k'm'|(\mathcal{H}^1 - \rho^1 \omega_0^2)|km) - (\omega_0^2 - \omega_k^2 + \delta\omega) \delta_{kk'} \delta_{mm'}] (km|\rho^0|u) = 0 \quad (2.43)$$

where $\delta_{kk'}$ is the Kröneckers delta. It becomes apparent that the perturbations in unperturbed eigenfrequencies $\delta\omega$ are the eigenvalues of the matrix:

$$\mathbf{M}_{(k'm')(km)} = (k'm'|(\mathcal{H}^1 - \rho^1 \omega_0^2)|km) - (\omega_0^2 - \omega_k^2) \delta_{kk'} \delta_{mm'} \quad (2.44)$$

which we call the splitting matrix. The splitting matrix describes singlet splitting and cross-coupling between modes due to asphericities. It consists of blocks with size $(2l+1) \times (2l'+1)$ on the off-diagonal corresponding to the intersection of two different modes, and blocks with size $(2l+1) \times (2l+1)$ on the main diagonal corresponding to a single mode. Elements of the splitting matrix are described explicitly in Woodhouse (1980) and Dahlen & Tromp (1998), including the *Woodhouse kernels*. We will describe the splitting matrix constituents in Chapter 3. In the following section, we will look at the splitting matrix as a whole.

2.4.3. Cross-coupling

The splitting matrix records whether or not modes are coupled through rotation, ellipticity and/or 3D structure. Cross-coupling of modes involves energy exchange, or resonance, between modes, further removing the degeneracy of singlet frequencies. This effect is especially strong between modes that have similar unperturbed eigenfrequencies. Some spheroidal-toroidal mode pairs may even form “crossover” pairs that become almost indistinguishable in terms of their singlet eigenfrequencies and eigenfunctions (e.g. ${}_0S_{19} - {}_0T_{20}$; Dahlen & Tromp, 1998).

A potential benefit of cross-coupling is that inner core confined toroidal modes (e.g. Woodhouse, 1980), which we cannot observe directly, could in theory be observed when they couple to spheroidal modes we can measure on the surface. Another potential benefit of cross-coupling is sensitivity to odd-degree structure. Modes treated as isolated are only sensitive to symmetric even-degree structure (up to maximum spherical harmonic degree $2l$), whereas cross-coupling can give a mode sensitivity to odd-degree structure (e.g. Deuss et al., 2010).

Normal mode cross-coupling follows certain selection rules, meaning that a certain set of modes can only couple through structure of certain spherical harmonic degrees. This set of rules is (e.g. Laske & Widmer-Schmidrig, 2007):

- i) The Coriolis force and the Earth’s ellipticity cause spheroidal-toroidal mode coupling when their angular degrees differ by 1: ${}_nS_l - {}_{n'}T_{l\pm 1}$.
- ii) Earth’s ellipticity also causes spheroidal-spheroidal or toroidal-toroidal coupling between modes that differ in angular order by 0 or 2: ${}_nS_l - {}_{n'}T_l$ or ${}_nS_l - {}_{n'}T_{l\pm 2}$.
- iii) The Earth’s rotation causes spheroidal-spheroidal mode coupling for modes with the same angular order: ${}_nS_l - {}_{n'}T_l$.

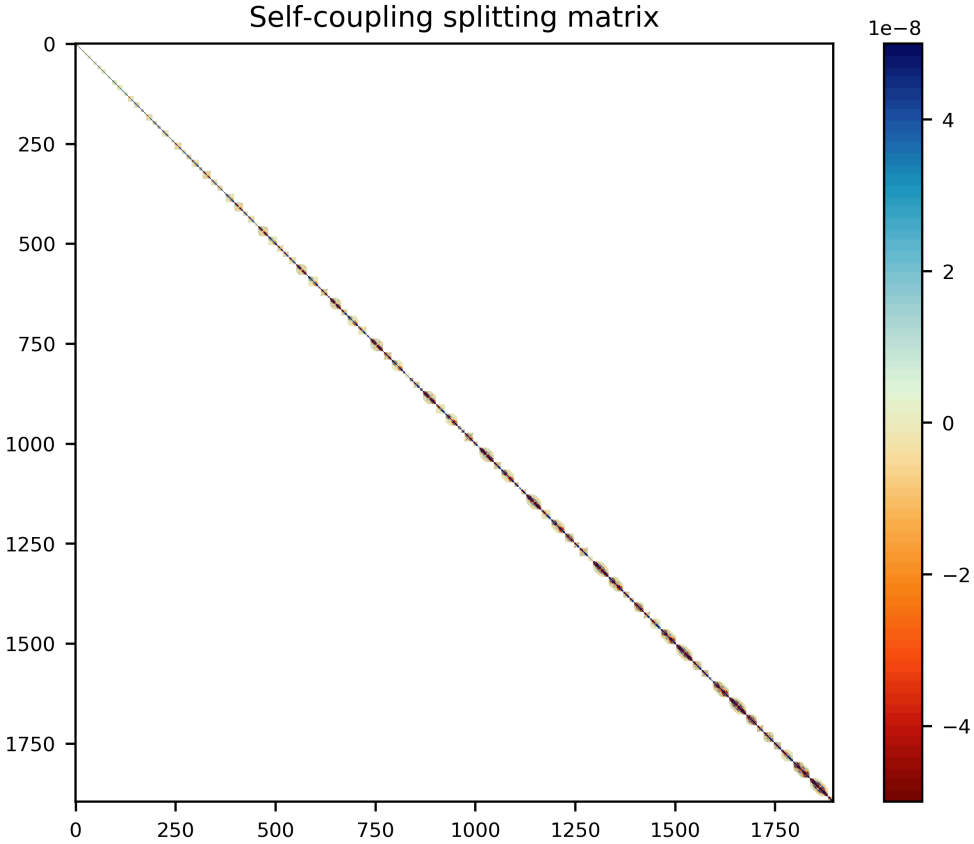


Figure 2.4: Real part of the splitting matrix for self-coupled modes in frequency band 0-3 mHz with coupling for rotation, ellipticity, and for mantle v_s model S20RTS, with v_p and ρ variations scaled to v_s variations with factors 0.5 and 0.3, respectively.

- iv) Lateral heterogeneity of spherical harmonic degree s causes spheroidal-toroidal mode coupling if $|l - l'| + 1 \leq s \leq l + l' - 1$ and $l + l' + s$ is odd.
- v) Lateral heterogeneity of degree s causes spheroidal-spheroidal or toroidal-toroidal mode coupling if (1) $m + t - m' = 0$, (2) $l + l' + s$ is even, and (3) $|l - l'| \leq s \leq l + l'$.

We can take three approaches in computing the splitting matrix (e.g. Deuss & Woodhouse, 2001), from least to most amount of cross-coupling: (i) self-coupling (SC) approximation, (ii) group-coupling (GC) approximation (also known as quasi-degenerate perturbation theory), (ii) full-coupling (FC). For full-coupling, the first-order approximation theory becomes exact when coupling an infinite number of modes for all possible spherical harmonic degrees. However, since this is computationally intractable, full-coupling is applied to modes in a finite frequency range. We will illustrate the three cross-coupling approaches using the splitting matrix.

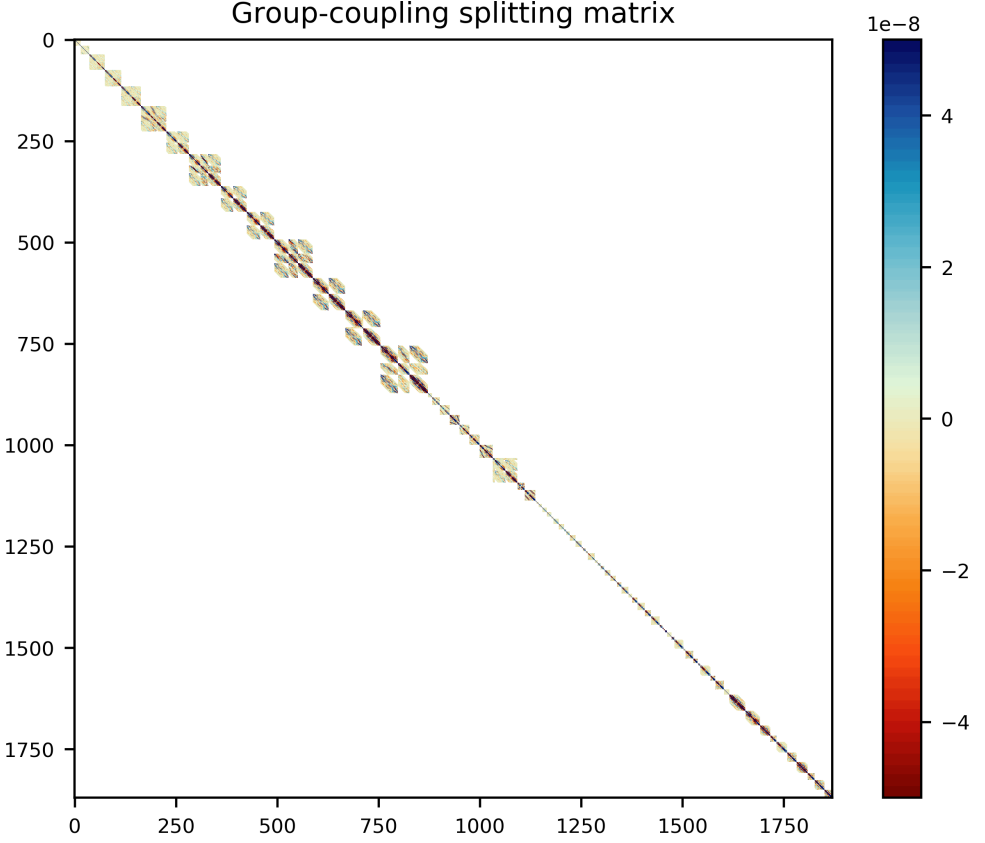


Figure 2.5: Real part of the splitting matrix for group-coupled (and a tail of self-coupled) modes in frequency band 0-3 mHz with coupling for rotation, ellipticity, and for mantle v_s model S20RTS, with v_p and ρ variations scaled to v_s variations with factors 0.5 and 0.3, respectively. The GC-matrix is a bit bigger than the SC- and FC-matrices, since a couple of modes appear twice in two different mode groups.

Matrix elements on the main diagonal are $10^3 - 10^4$ times bigger than the off-diagonal elements. In order to make the off-diagonal elements more visible, all three matrices are cut off at $5 \cdot 10^{-8}$ maximum and $-5 \cdot 10^{-8}$ minimum. If we did not do that, we would only see the main diagonal surrounded by beige. The self-coupling matrix (Fig. 2.4) is very clearly diagonally dominant, which makes this matrix the easiest to diagonalize. It consists exclusively of $(2l+1) \times (2l+1)$ self-coupled blocks on the main diagonal.

The group-coupling splitting matrix (Fig. 2.5) is also diagonally dominant, but contains bigger non-zero squares on the diagonal representing the 2-3 modes in a group that couple with each other through rotation, ellipticity and 3D structure. This GC-matrix would still be relatively easy to diagonalise, requiring only 1.05 times the computation time of the SC-matrix. In practice, we do not need to diagonalize the entire SC- or GC-matrix as a whole, since these matrices can be

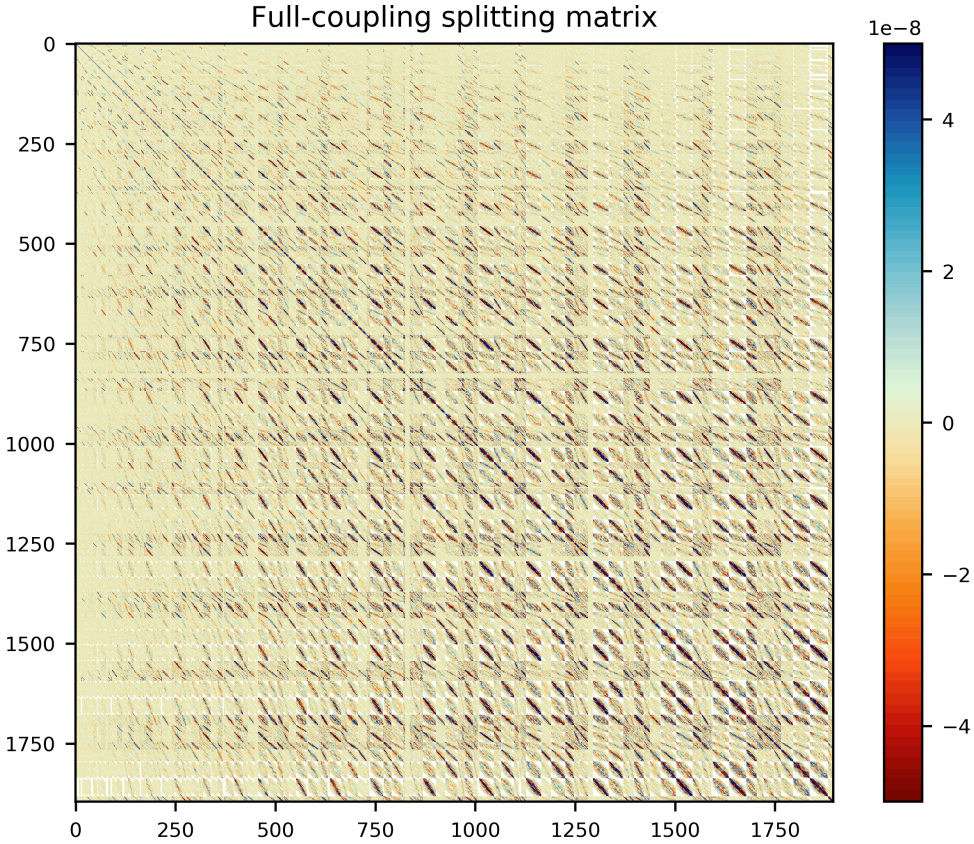


Figure 2.6: Real part of the splitting matrix for fully-coupled modes in frequency band 0-3 mHz with coupling for rotation, ellipticity, and for mantle v_s model S20RTS, with v_p and ρ variations scaled to v_s variations with factors 0.5 and 0.3, respectively.

decoupled into all the individual modes or, in the group-coupling case, into the small mode groups. We can then diagonalize each section separately.

The full-coupling splitting matrix (Fig. 2.6) up to 3 mHz is almost completely populated. It is not fully populated as we only introduce 3D structure up to degree 20, setting parts of the matrix that couple for degrees higher than 20 to zero. We can still see the main diagonal clearly, but it is now surrounded by non-zero elements across the entire matrix. Diagonalising the full-coupling matrix takes a lot more computational power: 3.4 times more than the SC-matrix in the case of frequency band 0-3 mHz. Computational power will grow even more for bigger splitting matrices, which is one of the reasons this coupling scheme has never been used before in an inversion of normal mode spectra for Earth's 3D structure. In this thesis, we will use the group-coupling approximation, with self-coupling where modes are sufficiently isolated in the spectrum.

2.4.4. Synthetic spectra

From the splitting matrix, we can compute synthetic spectra. Following e.g. Woodhouse & Girnius (1982); Deuss & Woodhouse (2001), the time series for synthetic normal mode spectra is given by

$$u(t) = (\mathbf{R} \cdot \mathbf{U}) e^{i\sqrt{\Lambda}t} (\mathbf{U}^{-1} \cdot \mathbf{S}) \quad (2.45)$$

where the real part is understood, and where the splitting matrix has been rewritten using eigenvalue decomposition: $\mathbf{M} = \mathbf{U}\mathbf{\Lambda}\mathbf{U}^{-1}$, with $\mathbf{\Lambda}$ containing the eigenvalues, and \mathbf{U} the corresponding eigenvectors. The receiver vector \mathbf{R} incorporates the instrument response and orientation of the seismic station, and the source vector \mathbf{S} depends upon the earthquake moment tensor. In the next chapter, we will explain two different ways to use the synthetic normal mode spectra in the inversion for mantle heterogeneity.

Here, we inspect the synthetic spectra computed for the SC, GC and FC splitting matrices depicted previously. We include all modes within the 0-4mHz frequency band for full-coupling here, since cross-coupling all modes up to 1 mHz higher than the cut-off frequency provides a more accurate synthetic spectrum (Akbarashrafi et al., 2018). In comparing the three synthetic spectra to observed spectra (Fig. 2.7), we see that the SC approximation does not closely resemble the observed spectra. By excluding the cross-coupling between neighbouring modes, we are not able to match, for example, the two peaks of ${}_0S_{11} - {}_2S_7$. SC does a much better job in the lower frequency range (up to 1.5 mHz (Yang & Tromp, 2015)), except for toroidal modes, as they do not show up on the vertical component of a SC spectrum. The GC approximation already does a much better job at fitting the observed spectra, by matching the position of nearly all peaks in the amplitude spectrum. For the full-coupling case, i.e. including cross-coupling between all modes in the entire 0-4mHz frequency band, the synthetic spectra do not deviate much from the GC approximation. Hence, it seems that we can confidently treat full-coupling as a second-order effect. However, this minor difference in the spectra could be significant when trying to observe structures with a small signal (Deuss & Woodhouse, 2001).

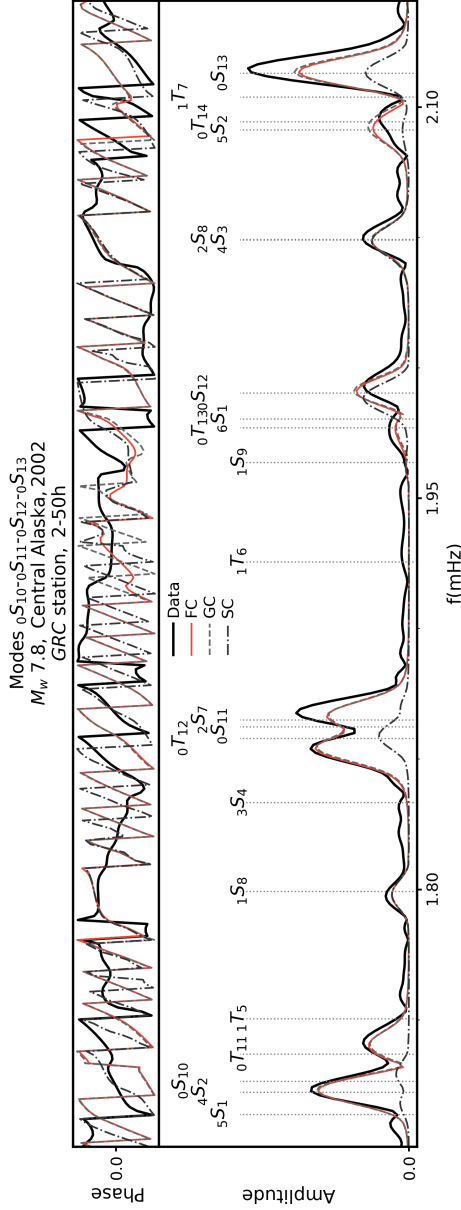


Figure 2.7: Observed spectra (thick black line) and three synthetic spectra for the three splitting matrices of all modes in range 0-3mHz with various degrees of cross-coupling: full-coupling (FC; red), group-coupling (GC; grey dashed), and self-coupling (SC; grey dash-dotted), computed for mantle model S20RTS (Ritsema et al., 1999). Top plot shows phase and bottom plot shows amplitude. The PREM frequencies of the modes in this frequency band are shown with vertical lines.

3

Comparing one-step with two-step inversion in normal mode tomography

Normal modes provide important constraints on Earth's large-scale 3D structure. In addition to constraining shear and compressional wave velocities, they are the only seismic data directly sensitive to lower mantle density perturbations. Previous studies have found contradicting results for lower mantle 3D density, hence the method chosen to invert normal mode data for 3D structure becomes important. In the problem of inverting measured frequency spectra for an Earth model, we can take two approaches: (i) a one-step full-spectrum inversion, where normal mode spectra are directly inverted for a mantle model; (ii) a two-step splitting function inversion, where first the spectra are inverted for splitting functions, which are then inverted for a mantle model. Most previous studies have incorporated normal modes by including splitting function coefficients. However, this method may suffer from possible non-uniqueness or inconsistencies of the splitting functions. Alternatively, normal mode spectra can also be inverted directly in a one-step inversion, but this method has not been used extensively in normal mode studies because of its high computational cost. Here we compare the methodology and results of both approaches, continuing the work done by Li et al. (1991) and Durek & Romanowicz (1999), and extending it to higher spherical harmonic degrees. Employing exactly the same normal mode data set, we use both inversion approaches to make 3D shear wave velocity mantle models. Both approaches give models consistent with previous tomographic studies, although spectral misfits are consistently lower for the one-step full-spectrum inversion. We also show that we cannot draw any conclusions on odd-degree structure in the lower mantle with the currently available normal mode data sets.

The content of this chapter was published as: Jagt, L., & Deuss, A. (2021). Comparing one-step full-spectrum inversion with two-step splitting function inversion in normal mode tomography. *Geophysical Journal International*, 227(1), 559-575.

3.1. Introduction

Normal modes, or free oscillations, are whole Earth oscillations excited by large earthquakes (typically $M_w > 7.5$). These standing waves along the Earth's surface and radius make the Earth 'ring like a bell'. Seismic normal modes are long-period waves, typically studied in the frequency domain between 0.3 and 10 mHz. They constrain large-scale Earth structures, and have been used to make global tomographic models from crust to inner core (e.g. Li et al., 1991; Durek & Romanowicz, 1999; Ishii & Tromp, 1999, 2004; Resovsky & Ritzwoller, 1999; Resovsky & Trampert, 2003; Beghein & Trampert, 2003), often in combination with body wave and surface wave data (e.g. Ritsema et al., 1999, 2011; Koelemeijer et al., 2016; Durand et al., 2016). In addition to providing information on shear wave velocity ($\delta \ln v_s$) and compressional wave velocity ($\delta \ln v_p$) anomalies, modes are sensitive to variations in density ($\delta \ln \rho$) (Ishii & Tromp, 1999; Resovsky & Trampert, 2003). It has proven difficult to determine 3D variations in density due to trade-offs with other parameters such as core-mantle boundary (CMB) topography and v_s , and their strong dependence on a priori constraints (Resovsky & Ritzwoller, 1999; Romanowicz, 2001; Kuo & Romanowicz, 2002). Yet information on density carries important implications for mantle dynamics, since density perturbations drive mantle flow (e.g. Davies & Gurnis, 1986; Kellogg et al., 1999).

Of special interest are the two Large Low Shear-wave Velocity Provinces (LLSVPs) in the lower mantle beneath the Pacific Ocean and Africa. Ever since their first appearance in mantle tomographic models as anomalously low v_s regions with a prominent degree 2 signature (Dziewonski et al., 1977; Giardini et al., 1987), their nature has been controversial. If they have a low density, then they are likely to have a thermal origin. Alternatively, if they are found to have a higher density, they need to have a compositional origin. To answer this question, relative amplitudes of density with respect to seismic velocities as well as the sign of density anomalies have been studied extensively, but nevertheless are still heavily debated (Romanowicz, 2001; Resovsky & Trampert, 2003). Although most normal mode studies argue for a higher than average density (Ishii & Tromp, 1999, 2004; Trampert et al., 2004; Resovsky & Trampert, 2003; Lau et al., 2017), observations of light LLSVPs exist (Koelemeijer et al., 2017). The question of 3D density variations in the mantle thus remains unanswered.

Modes appear as distinct peaks in frequency spectra by Fourier transforming several days to week-long seismograms from the time to the frequency domain. The shape and position of normal mode peaks change due to departures of Earth from a spherical, non-rotating, elastic, isotropic (SNREI) Earth. Measurements of spectral peaks are data input for inversion procedures aiming to image the Earth's interior. In principle, two different inversion approaches can be used for obtaining an Earth model from normal mode data, either (1) in one step, by directly inverting the spectra, or (2) in two steps, via the splitting function method (see Fig. 3.1).

The one-step full-spectrum inversion involves a direct inversion of normal mode spectra for an Earth model in terms of velocity and/or density perturbations. This approach was first used by Li et al. (1991) and has only been used a few times in the last decades (Li et al., 1991; Durek & Romanowicz, 1999; Kuo & Romanowicz,

2002; Akbarashrafi, 2020). The problem is that it is a non-linear method involving diagonalisation of large matrices and requires large computer power.

The two-step splitting function inversion was introduced by Giardini et al. (1987) to separate the inversion into two smaller steps which require less computer power. As the name suggests, it involves first inverting the normal mode spectra for splitting function coefficients, also called structure coefficients (e.g. Resovsky & Ritzwoller, 1998; Deuss et al., 2013), as an intermediate step. Splitting functions describe the weighted depth average of lateral heterogeneities that a mode ‘sees’, and are similar to phase velocity maps for surface waves. Splitting functions are linearly dependent on 3D variations in Earth structure. They can be visualised as splitting function maps showing where locally the frequency of a given mode is slightly lower or higher than its average frequency. The splitting function coefficients are then inverted in the second step for variations in velocity and density. Splitting functions are most commonly used when normal mode constraints are included in global tomographic models, often in combination with other data such as body waves and surface waves, for example in constructing mantle models S40RTS (Ritsema et al., 2011), SP12RTS (Koelemeijer et al., 2016) and SEISGLOB1 (Durand et al., 2016). Generally, measuring splitting functions and performing the two-step splitting function inversion are more common in normal mode studies (e.g. Giardini et al., 1987; He & Tromp, 1996; Resovsky & Ritzwoller, 1998, 1999; Masters et al., 2000b; Deuss et al., 2013; Pachhai et al., 2016; Koelemeijer et al., 2017), than the one-step direct spectrum inversion.

So far, only Li et al. (1991), Kuo & Romanowicz (2002), Durek & Romanowicz (1999) and Akbarashrafi (2020) have attempted to directly invert the spectra for a model. A splitting function inversion may have multiple local, or sometimes global, minima (Megnin & Romanowicz, 1995). The problem may be especially relevant for core-sensitive modes and therefore Durek & Romanowicz (1999) performed a one-step full-spectrum inversion to make an anisotropic model of the inner core to circumvent the problem of non-uniqueness in measuring splitting functions. We will discuss the theoretical differences between the two inversion methods in more detail in section 2.4. Splitting functions predicted for their preferred model matched the measured splitting functions retrieved from spectral data well. The one exception ($_{13}\text{S}_1$) was attributed to non-uniqueness of its measured splitting function. Here, we will investigate the difference between the two methods for mantle sensitive modes. Kuo & Romanowicz (2002) inverted synthetic spectra directly for v_s , v_p and ρ simultaneously and looked at whether 3D variations in mantle density could be resolved with then available normal mode data set. They found that density structure obtained from their normal mode data set was not reliable, due to contamination of seismic velocity structure into density.

Li et al. (1991) compared the one-step full-spectrum inversion and two-step splitting function inversion methods by making tomographic models based on the same normal mode data set. Their models included v_s mantle structure, CMB topography and inner core anisotropy. Resulting mantle models from the two approaches were in good agreement, which prompted the authors to conclude that splitting functions can serve as a convenient intermediate step in obtaining Earth models from normal

mode splitting. Indeed, the two-step splitting function inversion method has been the preferred choice in the last decades to include normal modes in tomographic models.

Recently, Akbarashrafi (2020) performed synthetic and real data one-step inversions for 3D variations in v_s , v_p and ρ for self- and group-coupled modes up to 3 mHz. The models were parameterized up to spherical harmonic degree 4, containing 21 splines in the radial direction. The synthetic tests showed that all parameters are relatively well constrained, except upper mantle density variations. However, in real data inversions, v_p and ρ models strongly depended on starting model and regularization.

It is important to revisit the one-step versus two-step approach again in light of recent theoretical developments, the expansion of data and increase in computer power. For example, Li et al. (1991) used the self-coupling approximation, meaning that they treated each mode in isolation. It has recently been suggested that self-coupling may be a reasonable approximation for modes below 1.5 mHz that are isolated in the frequency spectrum (Yang & Tromp, 2015), but all modes exchange varying amounts of energy with other modes, especially when their frequencies are close. Deuss & Woodhouse (2001) showed that this so-called cross-coupling (i.e. resonance) in large groups of modes needs to be taken into account to accurately calculate synthetic spectra, even below 1.5 mHz (Akbarashrafi et al., 2018). So, the question is what happens when we take this cross-coupling between modes into account in the one-step full-spectrum inversion and two-step splitting function inversion. Here, we will extend the work done by Li et al. (1991), using the large normal mode data set initially compiled by Deuss et al. (2013) to make a new catalogue of splitting function measurements. Owing to greater computational power, we will also be able to go to higher spherical harmonic degrees, significantly increase the amount of data, and test the influence of cross-coupling.

We will make a shear wave velocity model using both the one-step full-spectrum inversion and the two-step splitting function inversion methods and investigate the effect of the two methods on the misfits and resulting models.

3.2. Theoretical framework

We will use normal modes to make tomographic models of Earth's mantle. There are two types of normal modes: spheroidal modes, which involve P-SV motion and are similar to Rayleigh waves, and toroidal modes, which involve SH-motion and are similar to Love waves. Normal modes are characterized by their overtone number n and angular order l : ${}_nS_l$ for spheroidals and ${}_nT_l$ for toroidals. A mode with a given l consists of $2l + 1$ singlets, or eigenfunctions, which are labelled with azimuthal order m . In a SNREI Earth, all $2l + 1$ singlets of a mode will be degenerate, i.e. they all have the same eigenfrequency ω_0 . Rotation, ellipticity and 3D structure of the Earth remove the degeneracy and lead to spectral splitting of singlets, giving each singlet a different frequency. Contributions of rotation and ellipticity are known exactly and only depend on the 1D Earth model (Woodhouse & Dahlen, 1978), so we can invert the observed remaining spectral splitting of normal modes for the contribution due to 3D heterogeneity in v_s , v_p and ρ . We will use both the one-step

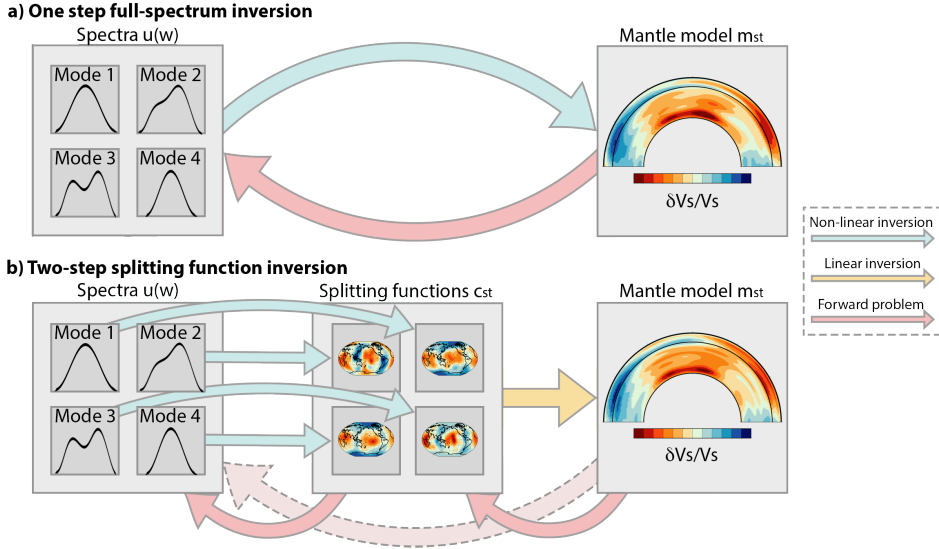


Figure 3.1: Inversion procedure for a) one-step full-spectrum inversion with only one non-linear inversion (blue arrow) inverting all spectra for all modes simultaneously for a mantle model; b) two-step splitting function inversion with non-linear inversions (blue arrows) to obtain splitting functions from spectra for all modes separately; and then inverting all those splitting functions simultaneously for a mantle model in a linear inversion (yellow arrow). All of the forward (synthetic) calculations are represented by red arrows.

full-spectrum inversion approach and the two-step approach with the intermediate splitting functions estimation. A detailed explanation for both approaches is given in the sections below.

An overview of the main steps and the major differences between the two inversion schemes is outlined in Fig. 3.1. The one-step full-spectrum inversion (Fig. 3.1a) has only one inversion step (blue arrow), in which we invert the normal mode spectra non-linearly for a mantle model. The fit to the original spectra is determined by computing synthetic spectra for the resulting mantle model (red arrow). The two-step splitting function inversion (Fig. 3.1b) first involves inverting the normal mode spectra for splitting functions for each mode separately (blue arrows), which is a non-linear process. Secondly, the splitting functions are linearly inverted simultaneously for a mantle model (yellow arrow). Different data fits are determined for the resulting mantle model, both to the measured splitting functions (red arrow) but also to the original spectra by computing synthetic spectra (light red arrow).

3.2.1. Forward problem: synthetic spectra

In both inversion approaches we need to calculate synthetic spectra for given mantle model coefficients m_{st} or splitting function coefficients c_{st} (see red arrows in Fig. 3.1), in order to minimize the spectral misfit between data and synthetics. We use

the ‘Coriolis and kinetic energy approximation’ explained in Deuss & Woodhouse (2001) to compute synthetics. As we have seen in the previous chapter, synthetic normal mode seismograms in the time domain for a given Earth structure are harmonic functions of time t given by:

$$u(t) = \text{Re} \left[\mathbf{R} \cdot e^{i\sqrt{\mathbf{M}}t} \cdot \mathbf{S} \right] \quad (3.1)$$

where $u(t)$ is the synthetic seismogram, \mathbf{S} is the source vector depending on the moment tensor, \mathbf{R} is the receiver vector depending on the instrument location and orientation, and \mathbf{M} is the splitting matrix which includes contributions due to 3D variations in Earth structure, ellipticity and rotation (Woodhouse, 1980), either in terms of the model coefficients m_{st} or splitting function coefficients c_{st} . We obtain the moment tensors from the Global CMT catalog (Ekström et al., 2012) and treat the source equally in both inversion methods. Hence we will not discuss the effects of uncertainties and errors in the source parameters on the $\delta \ln v_s$ models. In the presence of ellipticity, rotation and asphericities, \mathbf{M} is not diagonal, so we need to diagonalize this matrix to compute the exponential. This is done by eigenvalue decomposition: $\mathbf{M}\mathbf{U} = \mathbf{U}\mathbf{\Lambda}$, where \mathbf{U} contains the eigenvectors and $\mathbf{\Lambda}$ contains the eigenvalues on the diagonal. The synthetic seismogram (Eq. 3.1) then becomes:

$$u(t) = \text{Re} \left[(\mathbf{R} \cdot \mathbf{U}) e^{i\sqrt{\mathbf{\Lambda}}t} (\mathbf{U}^{-1} \cdot \mathbf{S}) \right] \quad (3.2)$$

The splitting matrix \mathbf{M} contains the degenerate frequencies ω_0^2 on the diagonal and additional diagonal and non-diagonal contributions from ellipticity, rotation, 3D heterogeneity in v_s , v_p , ρ and anisotropy. For a mode pair k, k' with degenerate frequencies $\omega_k, \omega_{k'}$ in the reference model, we can write \mathbf{M} as:

$$\mathbf{M}_{mm'}^{(kk')} = \omega_0^2 \delta_{kk'} + \omega_0 \mathbf{W}_{mm'}^{(kk')} + \mathbf{H}_{mm'}^{(kk')} \quad (3.3)$$

where s is the angular order or structural degree, t is azimuthal order, $\omega_0 = (\omega_k + \omega_{k'})/2$, matrix \mathbf{W} describes the Coriolis force due to rotation, and matrix \mathbf{H} describes ellipticity, 3D heterogeneity in v_s , v_p and ρ and anisotropy. Please note that the dimension of the splitting matrix is ω^2 (Woodhouse, 1980), hence the square root in Eq. 3.1. In the self coupling case, \mathbf{M} is a square matrix of size $(2l+1)(2l+1)$ and $k = k'$ so $\delta_{kk'} = 1$, and, in the absence of 3D structure, the splitting matrix is diagonal. The cross coupling is described by matrix contributions of size $(2l+1)(2l'+1)$ and $k \neq k'$ so $\delta_{kk'} = 0$.

For modes that are sufficiently isolated in the spectrum, we use the self-coupling approximation, meaning that only singlets belonging to the same mode exchange energy. We use the group-coupling approximation for small groups of 2–3 modes that interact strongly. The modes that we allowed to couple varies for each method. It is an advantage of the one-step inversion that we can easily include coupling between all modes in a particular spectral segment. In the two-step inversion, this is more complicated, since we cannot always include all cross-coupling, since that would result in too many unknown model parameters compared to the limited data availability per mode. It has been shown that full-coupling would probably be a

more accurate approach (Deuss & Woodhouse, 2001; Al-Attar et al., 2012; Yang & Tromp, 2015), but the aim of the present paper is to compare v_s models obtained using either direct spectrum inversion or splitting functions, and therefore we need to use the same theoretical approximations in both. In addition, full-coupling is computationally very expensive and will be the subject of a further paper.

One-step full-spectrum inversion

The two inversion methods differ in the calculation of \mathbf{H} . In the one-step full-spectrum method the matrix \mathbf{H} depends on the model coefficients m_{st} . The splitting matrix elements are then computed using the ‘Woodhouse kernels’ in equation A.17 of Woodhouse (1980), which can also be found in Appendix D of Dahlen & Tromp (1998). Matrix \mathbf{H} is in this case a function of m_{st} , which include 3D perturbations in v_s , v_p , ρ , anisotropy and discontinuity topography:

$$\mathbf{H}_{mm'}^{(kk')} = \sum_{s=l-l'}^{l+l'} \sum_{t=-s}^s \gamma_{ll's}^{mm't} \left[\int_0^a \delta m_{st}(r) K_{s(kk')}(r) dr + \sum_d \delta h_{st} H_{s(kk')}^d \right] \quad (3.4)$$

where the coefficients $\gamma_{ll's}^{mm't}$ are given by:

$$\gamma_{ll's}^{mm't} = \int_0^{2\pi} \int_0^\pi Y_l^{m*}(\theta, \phi) Y_s^t(\theta, \phi) Y_l^{m'}(\theta, \phi) \sin\theta d\theta d\phi \quad (3.5)$$

with Y_l^m as the fully normalized spherical harmonics according to Edmonds (1960). Woodhouse (1980) and Dahlen & Tromp (1998) describe how to evaluate this integral. δm_{st} and δh_{st} describe Earth’s elastic heterogeneity ($\delta \ln v_s$, $\delta \ln v_p$, $\delta \ln \rho$) and discontinuity topography, respectively, parameterized in spherical harmonics with angular order s and azimuthal order t . $K_s(r)$ and H_s^d are known kernels (Woodhouse, 1980).

Two-step splitting function inversion

In the two-step splitting function inversion, the matrix \mathbf{H} depends on the splitting function coefficients c_{st} instead. The heterogeneity matrix in \mathbf{H} can then be readily described using splitting function coefficients c_{st} as:

$$\mathbf{H}_{mm'}^{(kk')} = \sum_{s=l-l'}^{l+l'} \sum_{t=-s}^s \gamma_{ll's}^{mm't} c_{st(kk')} \quad (3.6)$$

It is interesting to note that the splitting matrix now only depends on c_{st} values and these can be estimated without any knowledge of the underlying 3D heterogeneity. This is what is being used in the first step of the splitting function inversion. Only in the second step we use the fact that the splitting function coefficients c_{st} do linearly depend on 3D heterogeneity and are given by:

$$c_{st(kk')} = \int_0^a \delta m_{st}(r) K_{s(kk')}(r) dr + \sum_d \delta h_{st} H_{s(kk')}^d \quad (3.7)$$

3.2.2. Partial derivatives

Synthetic seismograms $u(t)$ and the corresponding spectra are non-linearly dependent on either (1) the model parameters m_{st} in the one-step inversion, or (2) the splitting function coefficients c_{st} in the two-step inversion. Therefore we need to linearize these two problems using partial derivatives.

One-step full-spectrum inversion

In the one-step inversion we need to calculate derivatives of the synthetic spectra with respect to the model parameters m_{st} (see blue arrow in Fig. 3.1a). The partial derivatives of seismogram $u(t)$ (see eq. 3.2) with respect to model parameters m_{st} are given by:

$$\frac{\partial u(t)}{\partial m_{st}} = \text{Re} \left[e^{i\omega t} \left(\mathbf{r} \cdot \frac{\partial \mathbf{U}}{\partial m_{st}} \right) (\mathbf{U}^{-1} \cdot \mathbf{s}) + (\mathbf{r} \cdot \mathbf{U}) \left(\frac{\partial \mathbf{U}^{-1}}{\partial m_{st}} \cdot \mathbf{s} \right) + (\mathbf{r} \cdot \mathbf{U}) i t \frac{\partial \omega}{\partial m_{st}} (\mathbf{U}^{-1} \cdot \mathbf{s}) \right] \quad (3.8)$$

where ω is diagonal matrix $\sqrt{\Lambda}$. We use Rayleigh's principle to find perturbations in the eigenvectors \mathbf{U} and eigenvalues Λ of splitting matrix \mathbf{M} resulting from a perturbation δm_{st} in the model coefficients. The eigenvalue correction is given by:

$$\delta \omega_n^2 = \delta \Lambda = \mathbf{u}_n^{-1} \delta \mathbf{M} \mathbf{u}_n \quad (3.9)$$

where \mathbf{u}_n is a column vector of \mathbf{U} and \mathbf{u}_n^{-1} is a row vector of \mathbf{U}^{-1} . The eigenvector corrections are given by:

$$\delta \mathbf{u}_n = \sum_{l \neq n} \frac{\mathbf{u}_l^{-1} \delta \mathbf{M} \mathbf{u}_n}{\omega_n^2 - \omega_l^2} \mathbf{u}_l \quad (3.10)$$

$$\delta \mathbf{u}_n^{-1} = \sum_{l \neq n} \frac{\mathbf{u}_n^{-1} \delta \mathbf{M} \mathbf{u}_l}{\omega_n^2 - \omega_l^2} \mathbf{u}_l^{-1} \quad (3.11)$$

where ω_n are the diagonal elements of $\omega = \sqrt{\Lambda}$. These eigenvalue and eigenvector corrections are substituted in eq. 3.8 for $\frac{\partial \omega}{\partial m_{st}}$, $\frac{\partial \mathbf{U}}{\partial m_{st}}$ and $\frac{\partial \mathbf{U}^{-1}}{\partial m_{st}}$ to evaluate the derivatives. Here, we will only calculate derivatives with respect to v_s , so m_{st} only contains $\delta \ln v_s$. If we extend this to v_p and ρ then m_{st} contains three sets of independent parameters for which derivatives need to be calculated.

Two-step splitting function inversion

First step - splitting function measurement In the first step of the splitting function inversion method, we need to calculate derivatives of the synthetic spectra with respect to the splitting function coefficients c_{st} (see blue arrows in Fig. 3.1b). We can easily obtain the equation for the partial derivatives by replacing every instance of m_{st} in equation 3.8 by c_{st} . These derivatives are then used in the first step of estimating the splitting function coefficients in the two-step inversion method. This equation is also given in Deuss et al. (2013) as equation 12. These are then the derivatives needed to measure the splitting function coefficients from the normal mode spectra in the first step of the splitting function inversion. We will not do this first step in this paper, because it was already done by Deuss et al. (2013) and we

will use their measured c_{st} 's for the second step.

Second step - splitting function inversion We then need to calculate the derivatives of the splitting function coefficients c_{st} with respect to the model parameters m_{st} (see yellow arrow in Fig. 3.1b). Because it is a linear problem, the partial derivatives are the same as what we use to do the forward calculation (eq. 3.7):

$$\frac{\partial c_{st}}{\partial m_{st}} = K_s(r) \quad (3.12)$$

where $K_s(r)$ appear once again as known kernels (Woodhouse, 1980). This is the step we will perform in this paper, represented by the yellow arrow in Fig. 3.1b.

3.2.3. Inversion method

We use the iterative least squares approach of Tarantola & Valette (1982) to estimate the model (m_{st}) or splitting function coefficients (c_{st}) from the normal mode spectra (see blue arrows in Fig. 3.1). In both approaches we minimize the same objective function, but the model parameters are m_{st} ($\delta \ln v_s$) in the one-step inversion (section 2.3.1). The model parameters are splitting function coefficients c_{st} in the first step (blue arrow in Fig. 3.1b) and m_{st} ($\delta \ln v_s$) in the second step of the two-step inversion (section 2.3.2) (yellow arrow in Fig. 3.1b). We will compare the two inversion approaches based on their fit to the original spectral data, shape of their L-curves, robustness to choices in weighting, and similarity of the resulting models.

One-step full-spectrum inversion

The total objective function Φ that we try to minimize in both methods is:

$$\Phi(\mathbf{m}) = \frac{1}{2}[\mathbf{d} - \mathbf{u}(\mathbf{m})]^T \mathbf{C}_d^{-1}[\mathbf{d} - \mathbf{u}(\mathbf{m})] + \frac{1}{2}[\mathbf{m} - \mathbf{m}_0]^T \mathbf{C}_m^{-1}[\mathbf{m} - \mathbf{m}_0] \quad (3.13)$$

in which \mathbf{d} is observed data, $\mathbf{u}(\mathbf{m})$ is synthetic data given a model \mathbf{m} , \mathbf{m}_0 is the starting model, and \mathbf{C}_d^{-1} and \mathbf{C}_m^{-1} are the a priori data and model covariance matrices, respectively. Since we are not applying any smoothing to the model, \mathbf{C}_m^{-1} purely contains norm damping on the main diagonal. In the one-step method the model \mathbf{m} contains the m_{st} model parameters for $\delta \ln v_s$. Function Φ minimizes both misfit to the data and size of the model parameters in a least squares sense (Tarantola, 2005).

The spectra $\mathbf{u}(\mathbf{m})$ depend non-linearly on the model parameters \mathbf{m} , so we need to iterate the inversion. The model that minimizes this objective function is obtained through the Gauss-Newton (or quasi-Newton) method, a gradient-based approach (Tarantola & Valette, 1982; Pratt et al., 1998). The final expression for the iterative damped least squares inversion is given by:

$$\mathbf{m}^{i+1} = \mathbf{m}^i + (\mathbf{A}_i^T \mathbf{C}_d^{-1} \mathbf{A}_i + \mathbf{C}_m^{-1})^{-1} \times [\mathbf{A}_i^T \mathbf{C}_d^{-1} (\mathbf{d} - \mathbf{u}(\mathbf{m}^i)) - \mathbf{C}_m^{-1}(\mathbf{m}^i - \mathbf{m}^0)] \quad (3.14)$$

where $\mathbf{A} = \left[\frac{\partial \mathbf{u}}{\partial \mathbf{m}} \right]$ is the matrix of partial derivatives (equation 3.8), \mathbf{m}^0 is the starting model, \mathbf{m}^i the vector containing the model coefficients m_{st} for $\delta \ln v_s$ for the previous iteration and \mathbf{m}^{i+1} the updated model coefficients for the current iteration, \mathbf{d} the measured spectra, and $\mathbf{u}(\mathbf{m}^i)$ the synthetic spectra (equation 3.2).

Two-step splitting function inversion

First step The first step of the splitting function method is very similar to the one-step method, but instead of inverting for m_{st} we now invert for splitting function coefficients c_{st} . The main difference is that we estimate the c_{st} 's for each mode separately, so we run a non-linear iterative inversion for every mode. Because the same inverse theory applies, we obtain the non-linear splitting function inversion from the spectra by replacing \mathbf{m} by \mathbf{c} in equations 3.13 and 3.14 to obtain splitting function coefficients in the iterative inversion of this first step.

Second step Once the c_{st} 's have been measured for all the different modes, we then linearly invert the c_{st} 's for model parameters m_{st} in the second inversion step. The c_{st} are linearly related to the m_{st} through known kernels (eq. 3.7). A collection of splitting function coefficients for a large number of modes is inverted jointly for a model of 3D elastic structure, using the fact that each mode has a different depth sensitivity. This is now a linear inversion. We solve for the model coefficients in a damped least squares inversion:

$$\mathbf{m} = \mathbf{m}^0 + (\mathbf{A}^T \mathbf{C}_d^{-1} \mathbf{A} + \mathbf{C}_m^{-1})^{-1} \mathbf{A}^T \mathbf{C}_d^{-1} (\mathbf{c} - \mathbf{c}(\mathbf{m}^0)) \quad (3.15)$$

where $\mathbf{A} = [\frac{\partial \mathbf{c}}{\partial \mathbf{m}}]$ is the matrix of partial derivatives, and \mathbf{C}_m^{-1} again contains norm damping on the main diagonal. Comparing equation 3.15 for the second step of the splitting function inversion with equation 3.14, we see the advantage of eq. 3.15: it does not have to be iterated because it is a linear inversion.

3.2.4. Choices in weighting

The choice of weighting the data is very important in any inversion scheme and is included by assigning varying values to the a priori data covariance matrix \mathbf{C}_d^{-1} . We found that weighting in the one-step direct spectrum inversion is done automatically, since modes with more data have a larger weight by virtue of contributing more data. Hence those modes are more dominant in determining the updated model. Weighting in the one-step inversion is therefore implicit (i.e. $\mathbf{C}_d^{-1} = \mathbf{I}$; no explicit variations required for the different modes). The first step in the two-step splitting function inversion does not require variations in \mathbf{C}_d^{-1} either, because only one mode (or a pair) is measured at a time (see Deuss et al. (2013)). However, the second step in the two-step splitting function inversion depends much more strongly on weighting of the different splitting function coefficients. We will apply weighting by using the errors assigned to the coefficients in the first step of the splitting function inversion. Other weighting schemes have also been used. Li et al. (1991), for example, included all splitting function coefficients with equal weight. They found that their splitting function coefficient errors for modes with little splitting were unrealistically small, and decided to assume the same standard error for all splitting function coefficients. We require non-uniform weighting of the splitting function coefficients to get reasonable models. We decided to use the errors σ_d estimated by Deuss et al. (2013) on the diagonal of the data covariance matrix \mathbf{C}_d^{-1} as $1/\sigma^2$ with $\sigma = \sqrt{\sigma_d}$, leading to a weighting range from 0.15 to 51. Using $\sigma = \sigma_d$ instead would give a much larger range of weighting coefficients: 0.02–2,646, making modes with the smallest errors too dominant.

A spectral segment is defined by a time and frequency window in the spectrum corresponding to a single seismogram. Modes with more segments generally have lower error estimates of their splitting function coefficients, so the error-based weighting of the two-step splitting function inversion is comparable to the implicit weighting by data amount in the one-step direct spectrum inversion. Contrary to the procedure outlined so far, we could choose to weigh each mode in the one-step inversion equally. The expected outcome is that modes with less segments will get a lower spectral misfit in the equal weights procedure. This is indeed what we see. The resulting models are still highly similar, with a correlation coefficient of 0.96. This indicates that the one-step inversion is robust to changes in the weighting scheme. The two-step inversion is more dependent on the weighting scheme, since treating all modes as equally important in the second inversion of the two-step inversion does not give a v_s model that looks similar to models in previous studies. Applying equal weights worked for Li et al. (1991), but in our case it resulted in very large c_{st} misfits. Furthermore, the models did not look like $\delta \ln v_s$ obtained in previous studies, possibly due to the higher maximum degree of the model and/or including more data.

3.2.5. Misfit definition

For the two-step inversion we can compute two kinds of misfit for a model: c_{st} misfit and spectral misfit (red arrows in Fig. 3.1b). For the one-step inversion we only compute the spectral misfit (red arrow in Fig. 3.1a).

One-step direct spectrum inversion

The spectral misfit per mode segment is defined as:

$$\text{spectral misfit} = \frac{1}{N} \sum \frac{\sum_{i=1}^n (\mathbf{d}_i - \mathbf{u}_i(m_{st}))^2}{\sum_{i=1}^n (\mathbf{d}_i)^2} \quad (3.16)$$

which is the squared difference between n spectral data points in observed spectra \mathbf{d}_i and synthetic spectra $\mathbf{u}_i(m_{st})$, divided by the norm of the data, averaged over the number of spectral segments N . The total average spectral misfit of all modes combined is calculated by weighing each spectral segment misfit by the number of segments per mode.

Two-step splitting function inversion

The first step in the two-step method was already performed by Deuss et al. (2013), using the same spectral misfit definition as in equation 3.16, with m_{st} replaced by c_{st} . Here we performed the second inversion step of fitting the splitting functions measured by Deuss et al. (2013). The c_{st} misfit of splitting function coefficients (i.e. the misfit that is minimized in the second step of the splitting function inversion) is defined as:

$$c_{st} \text{ misfit} = \frac{1}{n_{tot}} \sum n \cdot \frac{\sum_{s,t} |c_{st}^{obs} - c_{st}^{mod}|}{\sum_{s,t} |c_{st}^{obs}|} \quad (3.17)$$

where c_{st}^{obs} are the measured splitting function coefficients, c_{st}^{mod} are the predicted coefficients for the new model, n is the number of c_{st} 's per mode, N the total number

of modes and n_{tot} the total number of c_{st} 's. This begs the question of whether our final model still fits the original spectral data from which those splitting functions were derived in the first step (dashed red arrow in Fig. 3.1b)? We have a unique opportunity to compare the two inversion methods, since we use the same initial spectral data set and can therefore calculate the spectral data fit of all resulting models. Another important question for the two-step inversion is: would the model that we choose based on the splitting function misfits be the same model that we choose based on spectral misfits? Hence, we also use equation 3.16 to calculate the spectral misfit for the model obtained in the two-step splitting function inversion.

3

3.2.6. Theoretical comparison of the two methods

Based on the overview of the two inversion schemes in previous sections, we now list the advantages and disadvantages of both methods. The advantage of the one-step method is that all data is fitted with the best model. The disadvantage is that it is computationally intensive, amounting to approximately 4-5 days on a High-Performance Computing cluster to reach convergence. The advantage of the two-step inversion is its lower computational cost, since the problem is decoupled into a number of smaller problems. The first step of the two-step inversion takes up to a few hours until reaching convergence, and the second step only a few minutes. The decoupling also leads to splitting functions in the first inversion step being obtained for each mode or mode group separately. These splitting functions are therefore not required to be consistent with a single Earth model (e.g. Kuo & Romanowicz, 2002). If a measured splitting function does not represent the unique solution corresponding to true properties of the Earth, the error will propagate into the final model (Li et al., 1991). Weighting in the second inversion step is necessary to make measurements with large uncertainties less important, otherwise erroneous splitting function measurements will dominate the model. Furthermore, regularization is applied twice in the two-step inversion, hence information is lost twice.

What are the practical implications of these theoretical differences? That is what we will explore in the rest of this paper.

3.3. Data

We use normal mode spectra as starting point of our inversions. These spectra are obtained by taking vertical component seismic data of tens of hours length, removing the first few hours since the earthquake onset, and then transforming them to the frequency domain. For the one-step inversion (blue arrow in Fig. 3.1a) we use the spectral segments of Deuss et al. (2013), consisting of vertical component data for 91 large events since 1976 with $M_w \geq 7.4$. For the two-step approach we use the spheroidal mode splitting functions obtained by Deuss et al. (2013), and only execute the second inversion step in this paper (yellow arrow in Fig. 3.1b). So, both inversion schemes use exactly the same spectral data. We exclude spheroidal modes that are sensitive to the inner core or couple strongly to an inner core mode, since our focus is on the mantle. This makes the total number of spectral segments 84,248, for 76 modes and mode groups in the one-step inversion and 104 self-coupled and 8

Table 3.1: Spectral segments containing the mode groups that were used in the one-step full-spectrum inversion, with the number of events as N_{ev} .

Spectral segment	N_{ev}	Spectral segment	N_{ev}
$0S_2$	8	$5S_7$	78
$0S_3 - 0T_2 - 2S_1$	37	$5S_8$	87
$0S_4 - 0T_3 - 1S_2$	56	$5S_{11} - 7S_8$	73
$0S_5$	65	$5S_{12}$	63
$0S_6$	82	$5S_{14} - 9S_8$	79
$0S_7$	87	$5S_{16} - 8S_{10}$	80
$0S_8 - 4S_1 - 0T_9$	89	$5S_{17}$	65
$0S_9 - 0T_{10}$	91	$6S_9 - 7S_6$	87
$0S_{11} - 2S_7 - 0T_{12}$	86	$6S_{10}$	84
$0S_{13} - 0T_{14}$	91	$6S_{15} - 9S_{10}$	62
$0S_{14} - 2S_9 - 0T_{15}$	91	$6S_{18}$	78
$0S_{15} - 0T_{16}$	91	$7S_5$	89
$0S_{16} - 0T_{17}$	91	$7S_7$	77
$0S_{17} - 2S_{11} - 0T_{18}$	91	$7S_9 - 9S_6$	57
$0S_{19} - 0T_{20}$	90	$8S_6$	56
$0S_{21} - 1S_{14} - 0T_{22}$	91	$8S_7$	59
$1S_2 - 0S_4 - 0T_3$	9	$9S_{11}$	72
$1S_4$	77	$9S_{12} - 10S_{10}$	66
$1S_5 - 2S_4$	84	$9S_{13} - 5S_{22}$	58
$1S_6 - 2S_5$	82	$9S_{14} - 14S_7$	49
$1S_7$	74	$9S_{15} - 14S_8$	39
$1S_8$	75	$10S_{20} - 15S_{12} - 16S_{10}$	57
$1S_9$	74	$11S_9$	40
$1S_{10}$	70	$11S_{10} - 4S_{28}$	42
$2S_1 - 0S_3 - 0T_2$	3	$11S_{23} - 13S_{18} - 19S_{10}$	50
$2S_6$	84	$11S_{24} - 15S_{15}$	42
$2S_8 - 4S_3$	91	$11S_{25}$	35
$2S_{10} - 4S_5$	89	$12S_6$	36
$2S_{12}$	90	$12S_7$	56
$2S_{13}$	90	$12S_{13}$	49
$3S_6$	87	$12S_{14}$	42
$3S_7 - 5S_5$	86	$12S_{15}$	41
$3S_9$	90	$13S_{16} - 14S_{13} - 16S_{11}$	50
$4S_2 - 0S_{10} - 0T_{11}$	90	$13S_{19} - 19S_{11}$	43
$4S_4 - 1T_8$	86	$13S_{20}$	39
$5S_3$	86	$14S_{14}$	26
$5S_4 - 2T_4$	89	$15S_{16} - 17S_{15}$	49
$5S_6 - 0S_{21} - 0T_{22}$	86	$17S_{14}$	29

Table 3.2: Modes and mode pairs for which their measured splitting functions were used in the two-step inversion, with the number of events as N_{ev} . Modes between brackets were included in the forward computations, but not inverted for.

Splitting function	N_{ev}	Splitting function	N_{ev}	Splitting function	N_{ev}
$0S_2$	8	$3S_6$	87	$9S_6(-7S_9)$	57
$0S_3(-0T_2 - 2S_1)$	37	$3S_7(-5S_5)$	86	$9S_8(-5S_{14})$	79
$0S_4(-0T_3 - 1S_2)$	56	$3S_7 - 5S_5$	86	$9S_{10}(-6S_{15})$	62
$0S_5$	65	$3S_9$	90	$9S_{11}$	72
$0S_6$	82	$4S_1(-0S_8 - 0T_9)$	89	$9S_{12}(-10S_{10})$	66
$0S_7$	87	$4S_2(-0S_{10} - 0T_{11})$	90	$9S_{12} - 10S_{10}$	66
$0S_8(-4S_1 - 0T_9)$	89	$4S_3(-2S_8)$	91	$9S_{13}(-5S_{22})$	58
$0S_9(-0T_{10})$	91	$4S_4(-1T_8)$	86	$9S_{14}(-14S_7)$	49
$0S_{11}(-2S_7 - 0T_{12})$	86	$4S_5(-2S_{10})$	89	$9S_{15}(-14S_8)$	39
$0S_{11} - 2S_7(-0T_{12})$	86	$5S_3$	86	$10S_{10}(-9S_{12})$	66
$0S_{13}(-0T_{14})$	91	$5S_4(-2T_4)$	89	$10S_{20}(-15S_{12} - 16S_{10})$	57
$0S_{14}(-2S_9 - 0T_{15})$	91	$5S_5(-3S_7)$	86	$11S_9$	40
$0S_{15}(-0T_{16})$	91	$5S_6(-0S_{21} - 0T_{22})$	86	$11S_{10}(-4S_{28})$	42
$0S_{16}(-0T_{17})$	91	$5S_7$	78	$11S_{23}(-13S_{18} - 19S_{10})$	50
$0S_{17}(-2S_{11} - 0T_{18})$	91	$5S_8$	87	$11S_{24}(-15S_{15})$	42
$0S_{17} - 2S_{11}(-0T_{18})$	91	$5S_{11}(-7S_8)$	73	$11S_{25}$	35
$0S_{19}(-0T_{20})$	90	$5S_{12}$	63	$12S_6$	36
$0S_{21}(-1S_{14} - 0T_{22})$	91	$5S_{14}(-9S_8)$	79	$12S_7$	56
$1S_2(-0S_4 - 0T_3)$	9	$5S_{14} - 9S_8$	79	$12S_{13}$	49
$1S_4$	77	$5S_{16}(-8S_{10})$	80	$12S_{14}$	42
$1S_5(-2S_4)$	84	$5S_{16} - 8S_{10}$	80	$12S_{15}$	41
$1S_6(-2S_5)$	82	$5S_{17}$	65	$13S_{16}(-14S_{13} - 16S_{11})$	50
$1S_7$	74	$6S_9(-7S_6)$	87	$13S_{18}(-11S_{23} - 19S_{10})$	50
$1S_8$	75	$6S_{10}$	84	$13S_{19}(-19S_{11})$	43
$1S_9$	74	$6S_{15}(-9S_{10})$	62	$13S_{20}$	39
$1S_{10}$	70	$6S_{18}$	78	$14S_7(-9S_{14})$	49
$1S_{14}(-0S_{21} - 0T_{22})$	91	$7S_5$	89	$14S_8(-9S_{15})$	39
$2S_1$	3	$7S_6(-6S_9)$	87	$14S_{13}(-16S_{11} - 13S_{16})$	50
$2S_4(-1S_5)$	84	$7S_7$	77	$14S_{13} - 16S_{11}(-13S_{16})$	50
$2S_5(-1S_6)$	82	$7S_8(-5S_{11})$	73	$14S_{14}$	26
$2S_6$	84	$7S_9(-9S_6)$	57	$15S_{12}(-16S_{10} - 10S_{20})$	57
$2S_7(-0S_{11} - 0T_{12})$	86	$8S_6$	56	$15S_{12} - 16S_{10}(-10S_{20})$	57
$2S_8(-4S_3)$	91	$8S_7$	59	$15S_{15}(-11S_{24})$	42
$2S_9(-0S_{14} - 0T_{15})$	91	$8S_{10}(-5S_{16})$	80	$15S_{16}(-17S_{15})$	49
$2S_{10}(-4S_5)$	89			$16S_{10}(-15S_{12} - 10S_{20})$	57
$2S_{11}(-0S_{17} - 0T_{18})$	91			$16S_{11}(-14S_{13} - 13S_{16})$	50
$2S_{12}$	90			$17S_{14}$	29
$2S_{13}$	90			$17S_{15}(-15S_{16})$	49
				$19S_{10}(-13S_{18} - 11S_{23})$	50
				$19S_{11}(-13S_{19})$	43

cross-coupled splitting functions for the two-step inversion (Tables ?? and 3.2). Our data set displays a significant increase with respect to only 10 events, 33 self-coupled spheroidal mode splitting functions and approximately 1,000 spectral segments of Li et al. (1991). We invert for v_s , which is the observable that modes are most sensitive to. To reduce the number of independent parameters, we assume that the aspherical perturbations in compressional velocity, $\delta \ln v_p$, and density, $\delta \ln \rho$, are proportional to $\delta \ln v_s$ with factors 0.5 (Li et al., 1991) and 0.3 (Karato, 1993), respectively. We will remove these scaling factors in Chapters 4 and 5. Crustal contributions are included using model CRUST 5.1 (Mooney et al., 1998). In the one-step inversion, crustal effects are included in the splitting matrix for computing synthetic spectra. Splitting function predictions for the crust are subtracted from the measured c_{st} 's, effectively removing the crust.

We use the same parameterization as global mantle shear wave velocity models S20RTS (Ritsema et al., 1999) and S40RTS (Ritsema et al., 2011), using 21 splines for depth, and spherical harmonics laterally. Models S20RTS and S40RTS go up to spherical harmonic degree 20 and 40, respectively, but here we will use maximum degree 8. We will initially invert for even degrees only, but explore the odd degrees as well. We use 1D model PREM (Dziewonski & Anderson, 1981) as starting model for the one-step inversion and for the second step of the two-step inversion.

3.4. Results

We invert normal mode data for a shear velocity mantle model using the one-step direct spectrum inversion and the two-step splitting function inversion. We will compare the resulting models and misfits in detail below.

3.4.1. L-curves and misfits

We investigate and compare the L-curves and corresponding misfits of the models resulting from the one-step and two-step inversions (Fig. 3.2). All L-curves show the characteristic shape of decreasing misfit as a function of model size (Fig. 3.2a) and also as a function of number of effective unknowns or independent model parameters (Fig. 3.2b). Model size is defined as

$$\text{msize} = \sum_{s=0}^{s_{max}} \sum_{t=-s}^s m_{st}^2 \quad (3.18)$$

and the number of effective unknowns as the trace of the resolution matrix. The most optimum model is usually defined at the "kink" in the L-curve, at which the misfit does not significantly decrease anymore but model size and the number of effective unknowns still increase, filling the null space. As mentioned in section 2.4.2, we can compute two kinds of misfit for the two-step inversion: misfit to the measured splitting function coefficients and misfit to the spectra. We find that the shapes of the L-curves for the two-step inversion are similar for both the c_{st} misfit (dotted line in Fig. 3.2a) and the spectral misfit (dashed line in Fig. 3.2a) and that the kink in the curve is found in the same place for both misfits (black dots in Fig. 3.2a). So, the chosen best model based on spectral misfit is the same model we would choose

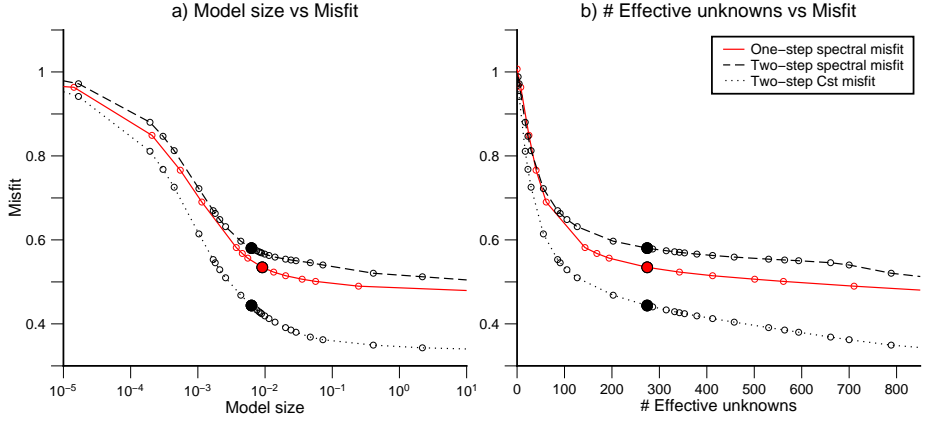


Figure 3.2: L-curve for the one-step inversion spectral misfits (red), and L-curves for the c_{st} misfits (dotted) and spectral misfits (dashed) for the models resulting from the two-step inversion, as a function of a) model size and b) number of effective unknowns. Red dot: best model for one-step inversion. Black dots: best model for the two-step inversion.

based on c_{st} misfit. The c_{st} misfit is lower than the spectral misfits, but it cannot be directly compared to the spectral misfits, since it is a different kind of misfit for a different kind of data (i.e. c_{st} 's instead of spectra). The two chosen $\delta \ln v_s$ models have approximately the same number of effective unknowns (Fig. 3.2b), which allows for direct comparison between the models. It is interesting to note that for the same number of effective unknowns, the one-step model has a slightly larger model size than the two-step model, which is probably a direct consequence of the inversion method. The same feature is also often seen in full-waveform model inversions, which usually have stronger anomalies than simple arrival time inversions.

The most important observation we make from the L-curves is that the total average spectral misfit for the one-step inversion is consistently lower than for the two-step inversion, for all model sizes and numbers of effective unknowns (compare solid curve to dashed curve in Fig. 3.2). Thus, the one-step inversion results in a better fit to the original data making the one-step model the preferred choice. Also, it shows that the worries initially voiced by Li et al. (1991) and Durek & Romanowicz (1999) that information might be lost in the two-step inversion resulting in a worse fit to the original data, are valid. It is possible that by applying a different splitting function weighting procedure we might succeed to shift the two-step spectral misfit L-curve to lower misfits, but we think weighting by error is the most logical procedure and most similar to implicit weighting by data amount in the one-step inversion.

All our inversions are started from PREM, only taking rotation and ellipticity into account. If we examine the average spectral misfit per mode or small group of modes (Fig. 3.3), we see that both our models improve the spectral data fit with respect to PREM plus rotation and ellipticity across almost the entire mode range. For some low angular order modes the misfit neither decreases nor increases

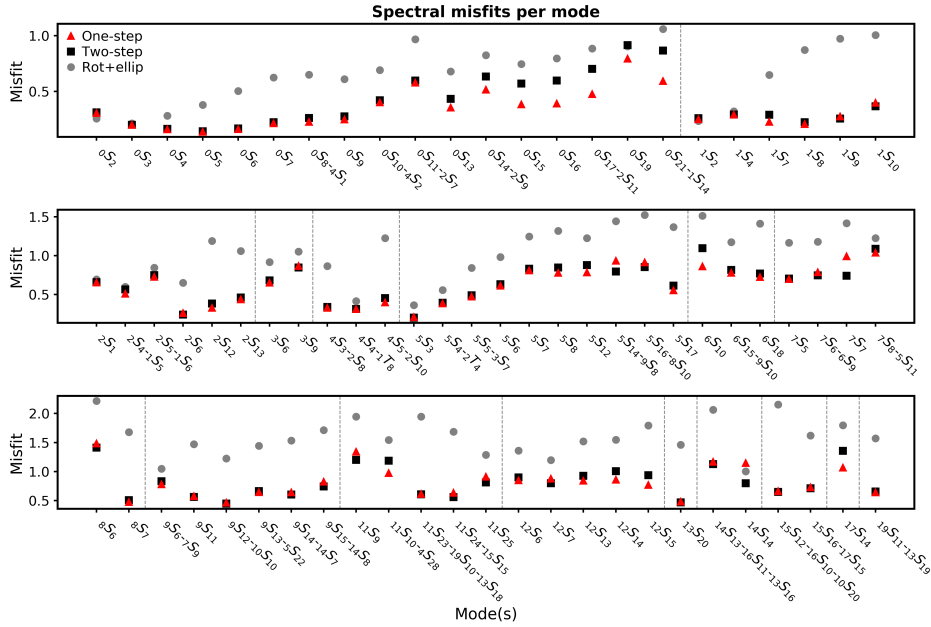


Figure 3.3: Average spectral misfit per mode or mode group for the best models from the one-step (red triangles) and two-step (black squares) inversion, compared to predicted misfits for PREM plus rotation and ellipticity (grey dots).

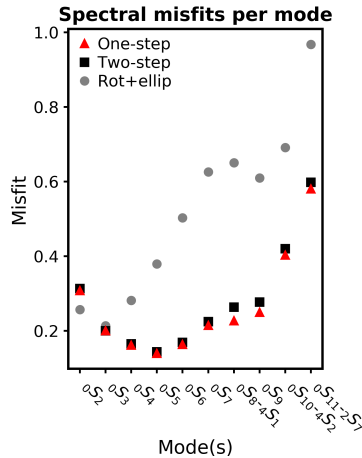


Figure 3.4: Zooming in on the lower angular order fundamentals of Fig. 3.3.

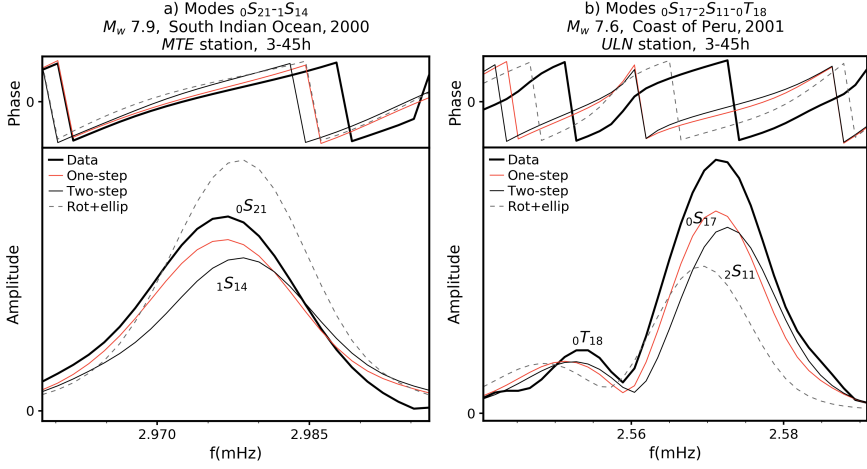


Figure 3.5: Synthetic spectra for 1D structure plus coupling for rotation and ellipticity (grey dashes), and for the best models from the one-step inversion (red), and from the two-step inversion (thin black). Thick black spectra represent real data of events a) in the South Indian Ocean and b) off the coast of Peru.

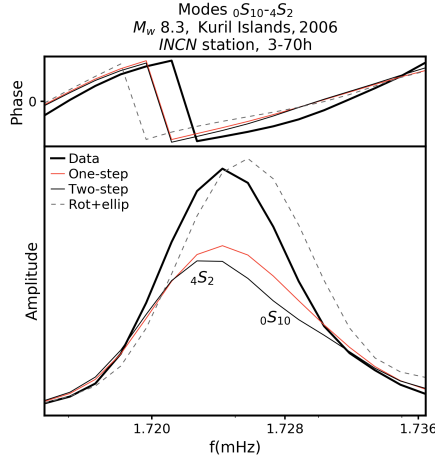


Figure 3.6: Synthetic spectra for 1D structure plus coupling for rotation and ellipticity (grey dashes), and for the best models from the one-step inversion (red), and from the two-step inversion (thin black). Thick black spectrum represents real data of an event near the Kuril Islands.

significantly. The lower average spectral misfit of the one-step model is mostly due to lower misfits for the higher angular order fundamental modes (${}_0S_{13} - {}_0S_{21}$), however, the average spectral misfit without these modes of the one-step inversion is still lower (0.55) than for the two-step inversion (0.56). The one-step model fits the spectra better than or equally well as the two-step model for the majority of modes. Even if it seems that there is no difference between the one-step and two-step spectral misfit, such as for the lower angular order fundamentals, for some modes the one-step spectral misfit is lower (Fig. 3.4). The few exceptions are mainly v_p sensitive modes.

The difference in misfit between the two inversion methods is also clearly visible in synthetic spectra based on the two best models (Fig. 3.5). Although both our models fit the spectra better than PREM + rotation and ellipticity, the model resulting from the one-step inversion fits the position and amplitude of the peaks better, especially for modes with lower overtone numbers such as the fundamentals shown in Fig. 3.5. Not all individual spectra can be fitted better when including 3D v_s variations, with scaled v_p and density (Fig. 3.6). In these cases, adding independent constraints on v_p and density might improve the fit.

3.4.2. Model characteristics

We first look at the general features of the two models. Model slices at several depths in the mantle show the similarities in pattern and amplitude of $\delta \ln v_s$ (Fig. 3.7a-b) of the models made using the two different approaches. At first glance, the two models look very similar. Both show the fast slab anomalies in the upper mantle around 500 km depth, and the Large Low Shear Velocity Provinces (LLSVPs) in the lowermost mantle. If you look in more detail, small differences become visible, for example in the low velocity anomalies in the LLSVPs around 2000 and 2800 km depth which show stronger negative velocity anomalies in the one-step than in the two-step model. We also compare our models to SP12RTS- v_s (Koelemeijer et al., 2016) and S40RTS (Ritsema et al., 2011). Both of these models include measurements of body wave travel times, and Rayleigh surface wave phase velocities, in addition to normal mode splitting function coefficients, providing more data sensitive to the uppermost and lowermost parts of the mantle. From a depth of 500 km onward, our models start to look similar to SP12RTS and S40RTS. The differences around 200 km depth are due to the lack of surface waves in our models which are based only on normal mode data.

The differences between our two models become more apparent in cross-sections through the mantle (Fig. 3.8). We see in the top panel of Fig. 3.8 that the Pacific LLSVP in the one-step model is more stretched in a Northwest-Southeast orientation, compared to the two-step model. The slab subducting beneath Japan seems more continuous in the two-step model. In the bottom panel of Fig. 3.8, the African LLSVP in the two-step model seems to be more connected to the East African Rift anomaly in the upper mantle than in the one-step model.

The one-step and two-step models are similar in their power spectrum per structural degree (Figs 3.9a,b), though the power distribution as a function of depth appears to be smoother in the one-step than in the two-step inversion. Any dif-

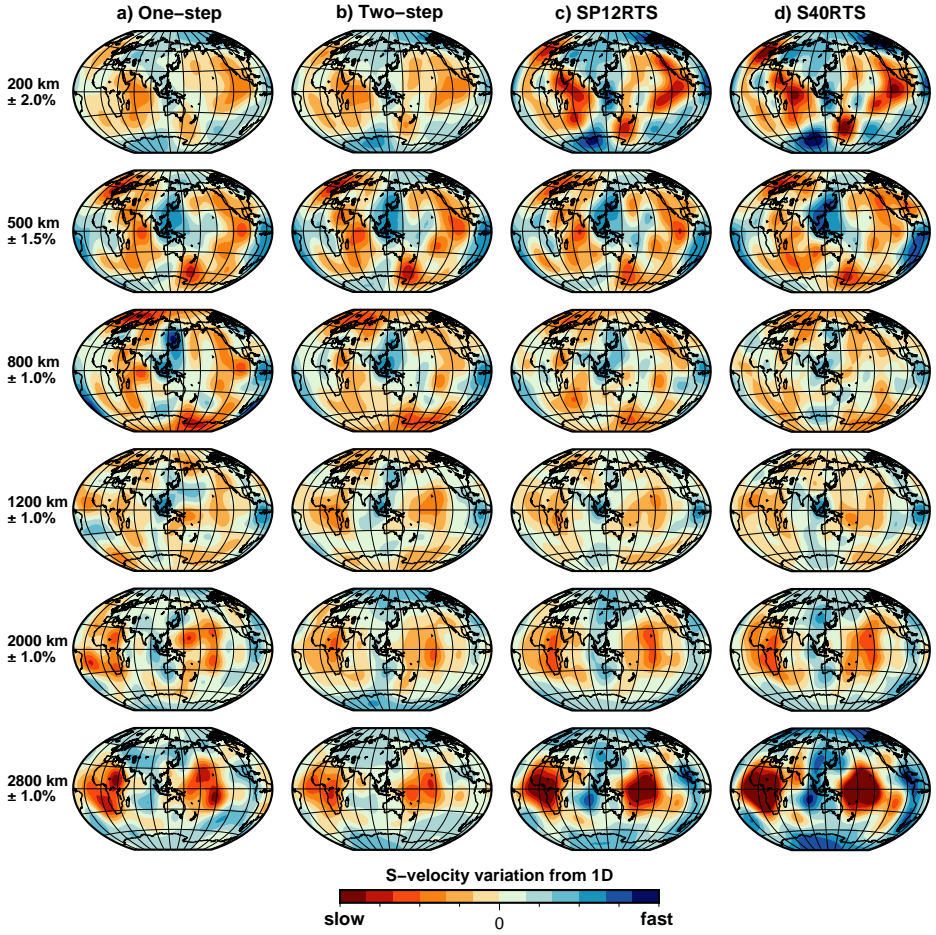


Figure 3.7: Model slices showing even degrees 2, 4, 6, 8 for a) the one-step inversion; b) two-step inversion; c) SP12RTS (Koelemeijer et al., 2016); d) S40RTS (Ritsema et al., 2011).

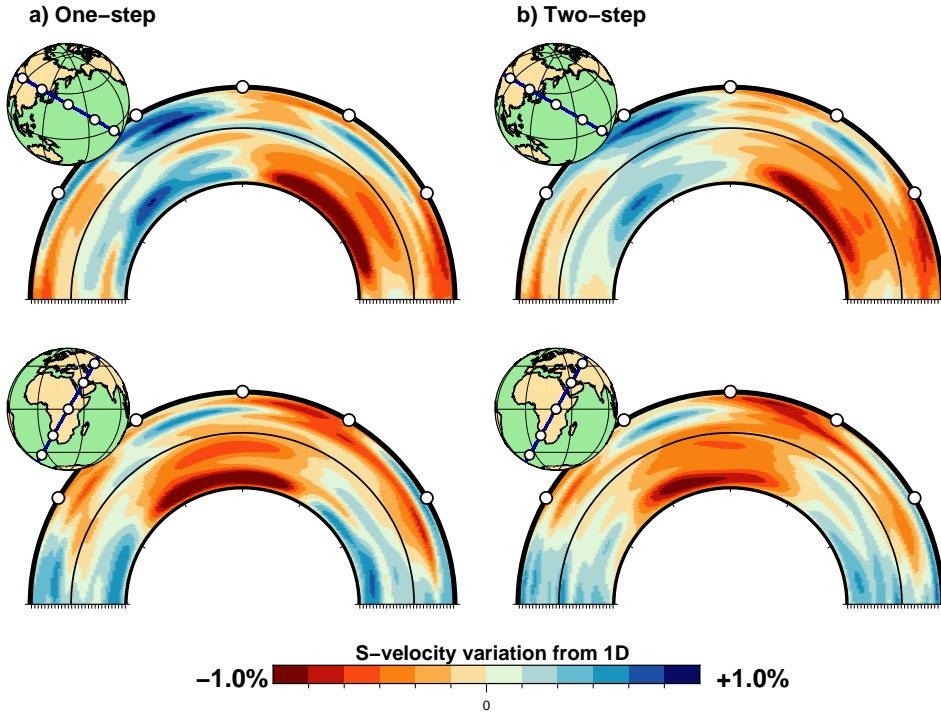


Figure 3.8: Cross-sections through the models from the a) one-step inversion; b) two-step inversion. Top panel shows the subducted plate near Japan and part of the Pacific LLSVP; bottom panel shows the African LLSVP.

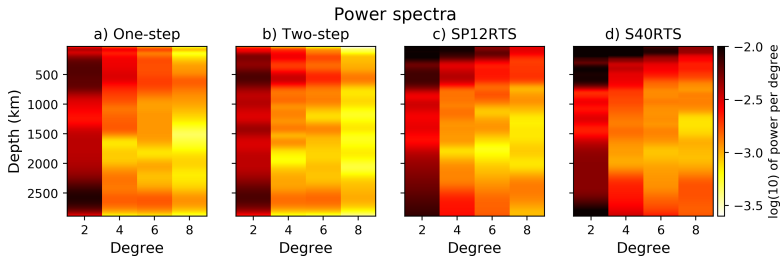


Figure 3.9: Power spectra per spherical harmonic degree for the four $\delta \ln v_s$ models shown in Fig. 3.7.

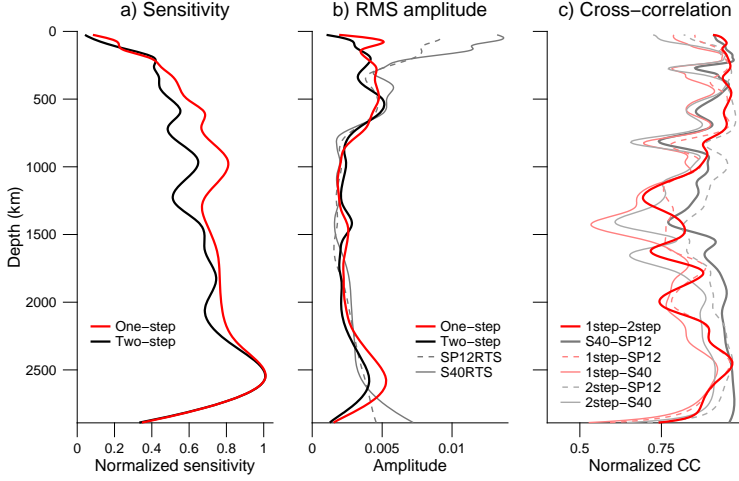


Figure 3.10: a) Normalized sensitivity for one-step and two-step models; b) Root mean square amplitude of the four models in Fig. 3.7; c) Normalized cross-correlation coefficients of all combinations of the same four models (SP12 = SP12RTS, S40 = S40RTS).

ferences in power spectra per degree could arise from the inversion method, or the difference in the amount of mode coupling between the two methods. Our models share the characteristic of SP12RTS and S40RTS (Figs 3.9c,d) of a dominant degree two structure, especially in the upper and lower parts of the mantle. Degree two structure in the uppermost mantle is the consequence of tectonic processes, where subducting slabs form the ‘ring around the Pacific’. LLSVPs result in a large degree two signature in the lowermost mantle. As we already saw in the depth slices (Figs 3.7a,b), the power in the uppermost 200 km of the mantle is weaker in our models compared to SP12RTS and S40RTS, probably due to a lack of surface waves in our inversions. Lower power in the CMB region could be the result of omitting Stoneley modes and core-diffracted body waves from our inversions.

By visualizing data sensitivity of our normal mode data set, we get a better understanding of our resulting models. Data sensitivity to each depth spline is related to the diagonal elements of the $\mathbf{A}^T \mathbf{A}$ matrix. Following Gu et al. (2001) and Koelemeijer et al. (2016), data sensitivity for the k th spline is defined by a horizontal average:

$$(\widetilde{\mathbf{A}^T \mathbf{A}})_k = \tilde{a}_k = \sqrt{\frac{1}{4\pi} \sum_{st} a_{st,k}} \quad (3.19)$$

where $a_{st,k}$ are diagonal elements of $(\mathbf{A}^T \mathbf{A})_k$. Both the one-step and two-step models have peak sensitivity at the second to deepest spline (2600 km depth) and least sensitivity in the most shallow part of the mantle (Fig. 3.10a). Note that the sensitivity in Fig. 3.10a is normalized. We cannot draw any conclusions from the absolute sensitivities in the two inversion approaches, because it is not possible to compare the $\mathbf{A}^T \mathbf{A}$ of the linear two-step inversion to that of the non-linear one-step

inversion.

The root mean square (RMS) amplitudes of the four models paint the same picture as the power spectra: higher amplitudes are seen in the uppermost mantle and CMB region for SP12RTS and S40RTS than for our two models (Fig. 3.10b). In the depth range of 700-2500 km all v_s models have similar RMS amplitudes. It is the depth range dominated by the normal mode data in SP12RTS and S40RTS, which explains the similarity in RMS amplitudes across all four models. Comparing our own models, we again see that the RMS amplitude of the one-step model varies more smoothly as a function of depth than the RMS amplitude of the two-step model.

The cross-correlations between the four models as a function of depth are shown in Fig. 3.10c. The correlation between our two models is close to 1.0 in the upper 1000 km of the mantle and drops to values of less than 0.9 around 1250 km depth and the CMB. The drop around 1250 km depth can be explained by looking at the 1200 km slice in Fig. 3.7 and the power spectra in Fig. 3.9. Here, the one-step model has a higher power for degree 6, resulting in more dominant small-scale structures than in the two-step model. The drop around the CMB is caused by differently shaped LLSVPs, especially the Pacific LLSVP. In the one-step model both LLSVPs consist of two elongated slow regions in a North-South configuration, whereas in the two-step model both LLSVPs are more stretched in an East-West direction. These drops in correlation between the one-step and two-step models are probably the consequence of the inversion method and might be due to errors propagating from the intermediate splitting function measurement into the final model in the two-step inversion method, since we used the same spectral data in both methods.

Our two models correlate better with SP12RTS than with S40RTS. Correlation of all other three models with S40RTS is especially poor at 800 and 1400 km depth, although their RMS amplitudes are similar. The poor correlation could be caused by S40RTS not including modes with overtone number > 5 , in contrast to our models and SP12RTS which do include higher overtones.

We have started the one-step inversion and the second step of the two-step inversion from PREM. To check whether or not we converge to a local minimum, we also experimented with starting our inversions from S20RTS (Ritsema et al., 1999) and a random model (Figs S1-S4). If we apply sufficiently low damping, we end up with models that look very similar to the ones obtained starting from PREM, for both inversion methods and all starting models, converging to comparable misfits and model sizes (Fig. S5). The only difference in observed patterns is in the uppermost 200 km of the mantle, implying that this part of the mantle is most poorly constrained by the normal mode data. The data sensitivity distribution in our models (Fig. 3.10a) agrees with this observation. Including spheroidal fundamentals with higher angular order, which are similar to Rayleigh surface waves, might improve the data coverage of this part of the Earth. An important observation for this study is that the spectral misfit for the one-step inversion is always lower than for the two-step inversion, independent of the starting model (Fig. S5).

3.4.3. Odd degrees

We have so far only considered even degree structure, but we are wondering if odd-degree structure can also be resolved and if there is also a difference between the two inversion methods for odd-degree structure. Sensitivity of normal modes in self-coupling is limited to even degrees, since waves travelling in opposite directions destructively interfere for odd-degree structure. This can also be understood from the coupling rules, which state that two spheroidal modes nS_l and $n'S_{l'}$ only couple for structure $|l - l'| \leq s \leq |l + l'|$. In the case of cross-coupling, we will get sensitivity to odd-degree structure if $l - l'$ is an odd number. Therefore we are bound to mode pairs that couple for odd-degree structure according to the coupling rules and are close enough in frequency to form a group or ‘hybrid’ mode pair. Unfortunately, we will show below that only a very small number of spheroidal modes pairs differ in their angular order l by an odd-number and are close enough in frequency, limiting the number of cross-coupled splitting functions and spectral data available to constrain odd-degree structure.

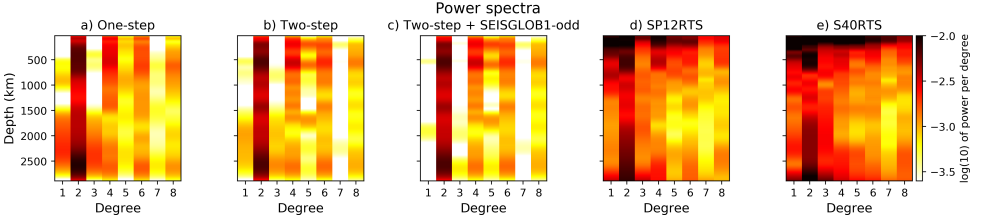


Figure 3.11: Power spectra per spherical harmonic degree, including odd degrees, showing in a, b, d, e the four $\delta \ln v_s$ models shown in Fig. 3.7, and c) two-step model including odd degree couples from Durand et al. (2016).

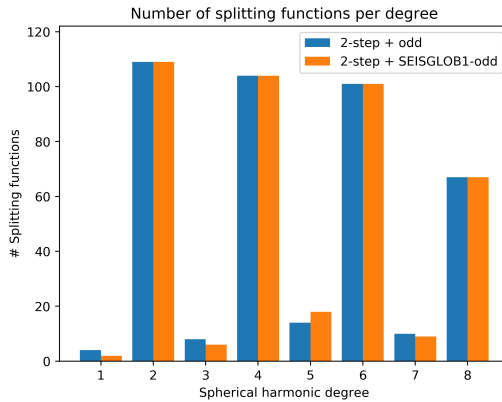


Figure 3.12: Number of splitting functions (self- and cross-coupled) that constrain the spherical harmonic degrees for a two-step inversion including the odd-degree c_{st} coefficients of Deuss et al. (2013) (in blue) and Durand et al. (2016) (in orange).

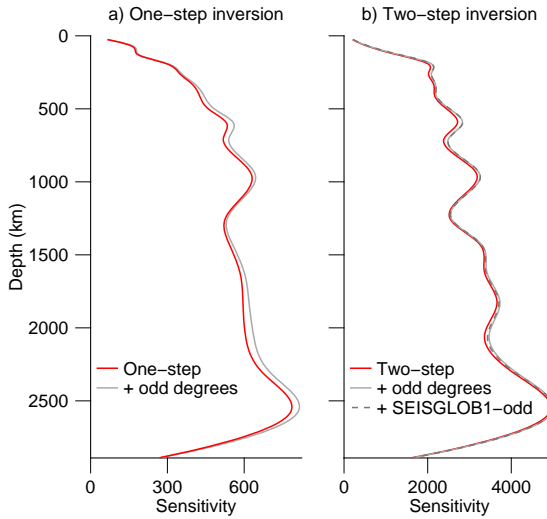


Figure 3.13: Data sensitivity kernels (not normalized) for a) one-step model (red), plus odd degrees by Deuss et al. (2013) (grey); b) two-step model (red), plus odd degrees by Deuss et al. (2013) (grey), plus odd degrees in SEISGLOB1 (Durand et al., 2016) (dashed).

We extend the one-step and two-step inversion to include odd degrees. Allowing modes in the small mode groups of Deuss et al. (2013) to couple for odd degrees yields a one-step model with a power spectrum containing significantly less power in odd degrees than in even degrees (Fig. 3.11a). Adding odd-degree splitting functions to the even-degree two-step inversion gives the same observation in the power spectrum (Fig. 3.11b), with less power for degree 1, 3 and 7. This is because measurements of odd-degree cross-coupled splitting functions by Deuss et al. (2013) are limited, especially compared to the large number of even-degree splitting functions available (blue bars in Fig. 3.12). Odd and even degrees were given the same norm damping to illustrate the lack of normal mode data sensitive to odd degrees compared to even degrees. The extra data added in this manner does not contribute greatly to the data sensitivity kernels (Fig. 3.13), though the relative increase in sensitivity is larger in the one-step inversion than in the two-step inversion. Thus there is only little information contained in the small amount of cross-coupled splitting functions for odd-degree structure. Group coupling in the one-step inversion, which includes a small number of mode pairs sensitive to odd degrees, does not add much information either.

Nonetheless, a recent study by Durand et al. (2016) argues that adding odd-degree splitting function coefficients results in odd-degree structure in the lowermost mantle becoming stronger than previously believed. Their mantle model SEISGLOB1 contains a higher spectral amplitude for degree 3 than degree 2 at 2800 km depth. Their cross-coupled normal mode data comprises measurements of Resovsky & Ritzwoller (1998) and Deuss et al. (2013). The odd-degree cross-coupled splitting

functions of Deuss et al. (2013) and Resovsky & Ritzwoller (1998) comprises 16 and 3 spheroidal-spheroidal measurements, respectively, with some overlap. We also run our two-step inversion using their odd-degree mode pairs with equal damping for all degrees, which results in the power spectrum of Fig. 3.11c. Because they actually included a few modes less than we did, there is still some power around 2800 km for degree 3, but in fact less than in our two-step inversion (Fig. 3.11b) and in all cases the degree 3 structure stays smaller than the degree 2 structure. Again, the data sensitivity kernels (Fig. 3.13b) also show that there is negligible data sensitivity to odd degrees in the model made using the same cross-coupled splitting functions as Durand et al. (2016).

Similar to Durand et al. (2016), who increased the weights of odd-degree splitting functions to fit these data, the only way in which we are able to obtain strong odd-degree lowermost mantle patterns as in SEISGLOB1 is by applying degree-dependent damping, even though the L-curves of these odd degrees do not show any indication to do so. The non-characteristic shape of the L-curves per degree illustrates that the amount of splitting function coefficients used by Durand et al. (2016) is not enough to constrain whole-mantle odd-degree structure. To support this statement, we would like to add that the six mode pairs in the SEISGLOB1 data set sensitive to degree 3 (i.e. $6 \times 7 = 42$ splitting function ‘data’ coefficients) are not sufficient to constrain all model parameters at degree 3 for 21 depth splines (i.e. $21 \times 7 = 147$ ‘unknown’ model coefficients). Overall, we find that the two-step inversion would need more cross-coupled splitting functions that are sensitive to odd-degree structure to make robust v_s models of odd-degree structure. Although there is stronger odd-degree sensitivity in the one-step inversion, even there we also need to include more mode couples sensitive to odd degrees to make robust models of odd-degree structure.

3.5. Discussion and Conclusion

We have explored two different inversion methods that have been used in normal mode tomography: (i) the computationally intensive one-step full-spectrum inversion and (ii) the commonly used two-step splitting function inversion, using the same spectral data set of Deuss et al. (2013) as a starting point. Theoretically, the two-step inversion is more sensitive to data weighting, and information might be lost in the intermediate step of measuring splitting functions. We find that we need to weigh the splitting function coefficients by their error or uncertainties, otherwise the resulting mantle models will not be similar to v_s models obtained in previous studies, which were made with other data types including body waves and/or surface waves. The one-step inversion is more robust, both from a theoretical and a practical point of view, since all spectral data are inverted at once. Neither of the two inversion methods depends on the starting model in our inversion for v_s only, except in the uppermost mantle, where normal mode sensitivity is lacking in our data set.

The average spectral misfit for the one-step inversion is lower for all model sizes and numbers of effective unknowns, as displayed in the inversion L-curves. The model resulting from the one-step inversion is smoother than the model resulting

from the two-step inversion, even when the model size and number of unknown parameters are the same between the two models. Moreover, the anomalies in v_s are stronger in the one-step model for the same number of effective unknowns, similar to stronger anomalies being observed in a full waveform inversion compared to conventional travel time tomography (Rickers et al., 2013). Whether this statement still holds when we invert for other parameters that modes are less sensitive to, such as v_p and ρ , will be addressed in upcoming chapters. The two-step splitting function inversion for v_s does a decent job, especially when combined with other data types (i.e. surface waves and body waves), and could be suitable for Monte Carlo model space search techniques (e.g. Fichtner et al., 2019; van Tent et al., 2020).

We cannot draw any conclusions yet on odd-degree structure in the mantle based on the currently available small number of cross-coupled odd-degree normal mode splitting functions. It will be essential to expand the data set of odd-degree cross-coupled splitting functions in order to be able to robustly constrain odd-degree structure, especially in the lower mantle, where the odd degrees are currently poorly constrained by normal modes. To conclude, the one-step inversion results in lower misfits to the spectral data. Furthermore, the resulting model is more smooth and has stronger anomalies for the same number of effective unknowns. This makes the one-step inversion, even though more computational intensive, the preferred choice, when possible.

Data availability

The c_{st} measurements underlying this article are available in the supplementary materials of Deuss et al. (2013), and through the GitHub of FrosPy at <https://github.com/s-schneider/frosPy>.

A1. Appendix A

Here we show the models (Figs. A1-A4) and L-curves (Fig. A5) for the one-step and two-step inversions for starting models PREM, S20RTS (up to degree 8, only even degrees) and a random model. It is well known that the success of a full-waveform inversion heavily depends on the quality of the starting model, since it is hard to reach convergence (e.g. Biondi & Almomin, 2014). Thus the resulting models depend on the starting model, and it is important to check that the inversion did not converge towards a local minimum (e.g. Virieux & Operto, 2009). In our full-spectrum normal mode inversion (i.e. the one-step inversion), we find that our resulting models do not depend so strongly on the starting model as in a full-waveform inversion. We arrive at the same models for sufficiently low damping (Fig. A5), hence it seems to be less likely to end up in a local minimum using our full-spectrum method.

The starting model does dictate how the model size varies as a function of damping. For the same value of strong damping, the PREM starting model will have a small model size, while the S20RTS and random starting models will have a model size very close to said starting models which will be much larger. In the same way, for little damping, the starting model will also dictate at which damping we start filling the model null space. Therefore we do not choose the same damping for the inversions starting from PREM as for the inversions starting from S20RTS and the random model. The final best models we picked for the different starting models therefore do not look exactly the same. The most important point is that our conclusions stay the same for all three starting models: the spectral misfit of the one-step inversion is always smaller than the spectral misfit of the two-step inversion (see Fig. A5).

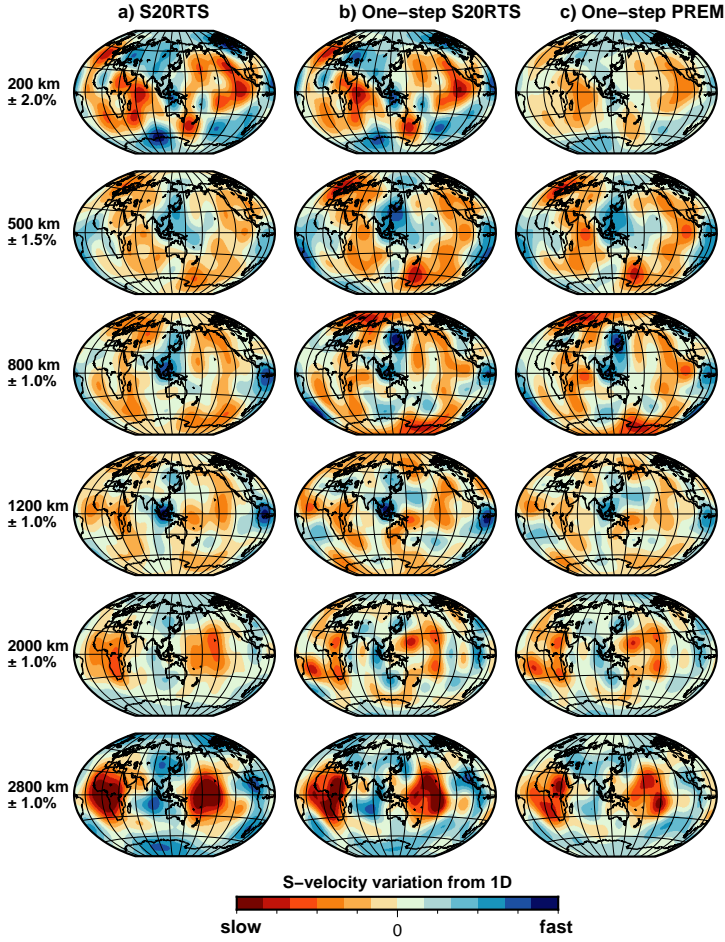


Figure A1: Model slices showing even degrees 2, 4, 6, 8 for a) starting model S20RTS; b) resulting model for the one-step inversion; c) one-step inversion result starting from PREM (as shown in the main paper)

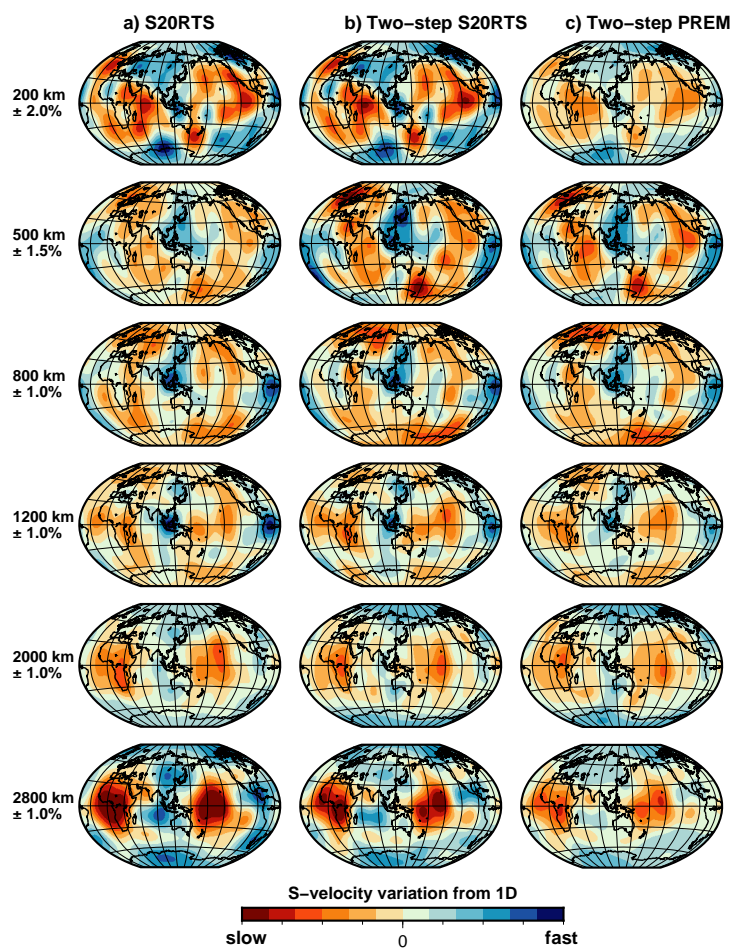


Figure A2: Model slices showing even degrees 2, 4, 6, 8 for a) starting model S20RTS; b) resulting model for the two-step inversion; c) two-step inversion result starting from PREM (as shown in the main paper)

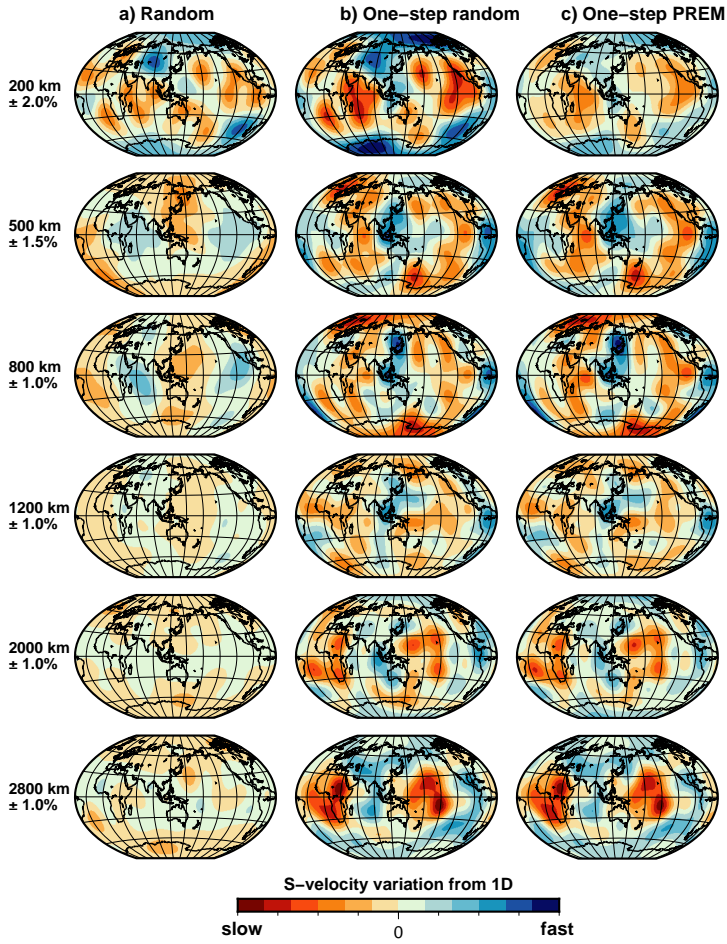


Figure A3: Model slices showing even degrees 2, 4, 6, 8 for a) random starting model; b) resulting model for the one-step inversion; c) one-step inversion result starting from PREM (as shown in the main paper)

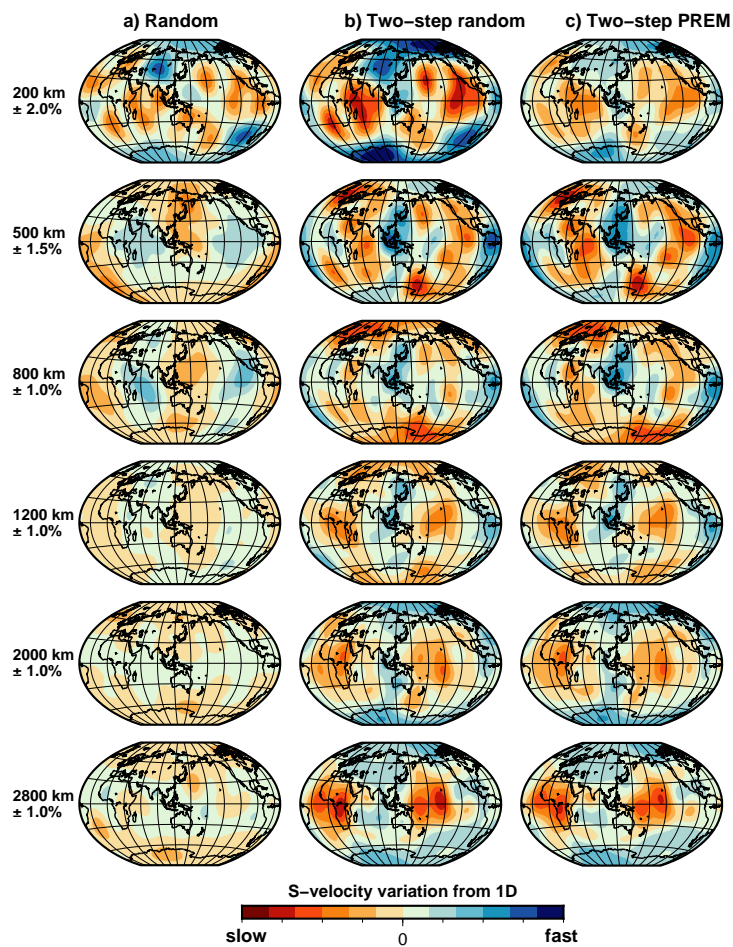


Figure A4: Model slices showing even degrees 2, 4, 6, 8 for a) random starting model; b) resulting model for the two-step inversion; c) two-step inversion result starting from PREM (as shown in the main paper).

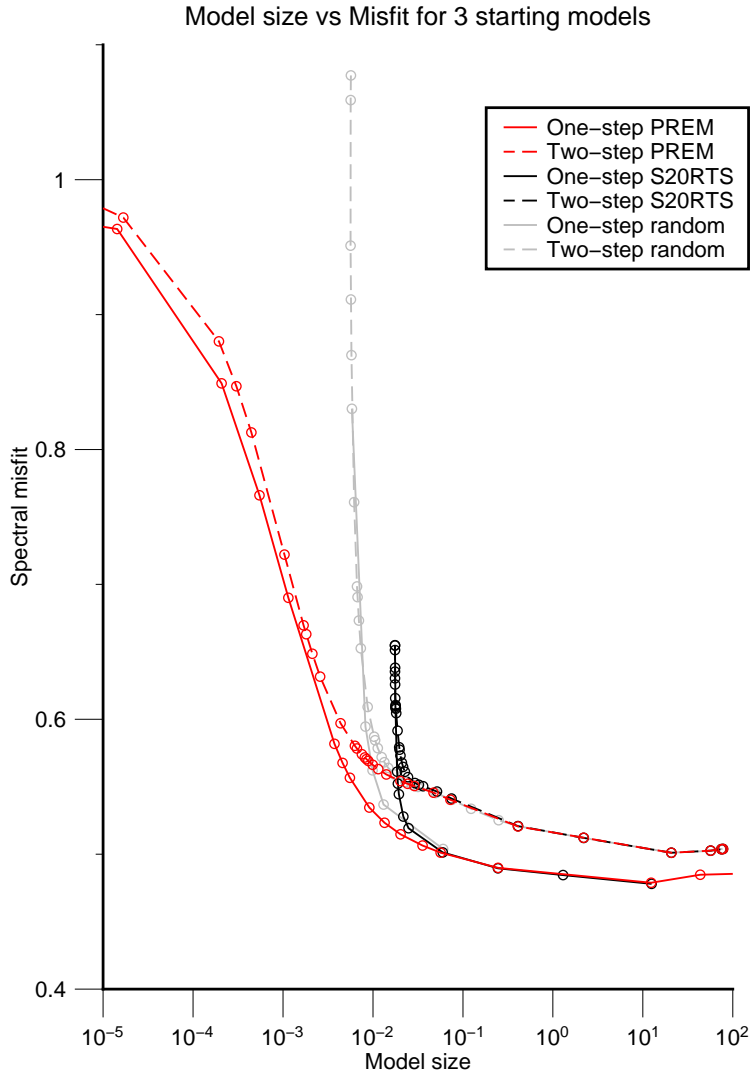


Figure A5: L-curves of starting models PREM (red), S20RTS (black) and random model (grey) and both inversion methods for model size versus average spectral misfit.

4

Normal mode constraints on v_s , v_p , their ratio $R_{S/P}$, and v_s - v_ϕ (anti-)correlation

Spheroidal normal modes are sensitive to both shear (v_s) and compressional (v_p) wave velocity and have the advantage that they do not suffer from different S-wave and P-wave data coverage as is the case for body waves. Thus, modes are ideal for constraining the ratio $R_{S/P} = \delta \ln v_s / \delta \ln v_p$, which may contain information on the presence of thermal or chemical heterogeneity in the mantle and is crucial in the debate on the origin and nature of the two Large Low Shear wave Velocity Provinces (LLSVPs) in the lower mantle. According to mineral physics experiments, $R_{S/P}$ is lower than 2–2.5 in an isochemical lower mantle in the absence of phase transitions. Most of the previously estimated $R_{S/P}$ values in seismological studies increase to about 3 in the bottom ~ 1000 km of the mantle, generally interpreted to be due to the presence of chemical heterogeneity. This observation is usually paired with anti-correlation between v_s and bulk sound velocity (v_ϕ) anomalies. We use normal mode data to make tomographic models of 3D variations in v_s and v_p and constrain $R_{S/P}$ in the Earth's mantle. In addition, we invert for v_s and v_ϕ anomalies in order to determine the S- Φ correlation. We investigate how $R_{S/P}$ and S- Φ correlation depend on the inversion approach (i.e. one-step or two-step inversion), and how different ways of computing this ratio and correlation may lead to different interpretations on the state of the mantle. Looking at distributions of $R_{S/P}$, $\delta \ln v_s$ and $\delta \ln v_p$ combined with 1D representations of the corresponding distributions gives a better overview than the 1D profiles exclusively. We present a new state-of-the-art one-step model of $R_{S/P}$ for the mantle, based on normal mode data including CMB Stoneley modes (sensitive to the lowermost mantle) and higher order fundamental modes (sensitive to the uppermost mantle). We also explore the robustness of inverting for 3D v_ϕ and present novel constraints from the one-step inversion.

4.1. Introduction

For decades, studies have modelled the S- and P-wave velocity of the mantle (e.g. Dziewonski et al., 1977; Woodhouse & Dziewonski, 1984; Masters et al., 2000a; Simmons et al., 2010; Koelemeijer et al., 2016). All lower mantle studies show two low-velocity zones in the lower mantle underneath Africa and the Pacific Ocean. The thermochemical nature of these two Large Low Shear-wave Velocity Provinces (LLSVPs), or sometimes simply called Large Low Velocity Provinces (LLVPs) as they are also visible in P-wave models, is still heavily debated. They could either be thermal only, in which case they would be buoyant superplumes, or compositional, making them potentially more stable (and dense).

Heterogeneity ratios between 3D variations in velocity and density, such as $R_{S/P}$, $R_{\Phi/S}$, $R_{\rho/S}$, have been proposed to discriminate between thermal and compositional heterogeneity (e.g. Masters et al., 2000a; Karato & Karki, 2001; Deschamps & Trampert, 2003). Observations of high $R_{S/P}$ (e.g. Romanowicz, 2001; Ritsema & van Heijst, 2002; Koelemeijer et al., 2016; Moulik & Ekström, 2016), a wider spread in the distributions of $R_{S/P}$ (e.g. Deschamps & Trampert, 2003) and anti-correlated shear and bulk sound velocity variations (e.g. Su & Dziewonski, 1997; Ishii & Tromp, 2001; Trampert et al., 2004) are generally interpreted to be indicators of chemical heterogeneity in the lower mantle. By converting global mantle circulation models to seismic structure, Davies et al. (2012) argue that chemical piles might be present, but are not required to explain the observed lower mantle velocities. Schuberth et al. (2009) on the other hand, propose an isochemical thermal plume model, that can be reconciled with tomographic images because of the limited resolving power of seismic tomography. Thus, better constraints on heterogeneity ratios from seismology are required.

4.1.1. Ratio between v_s and v_p heterogeneity

In this chapter, we will focus on heterogeneity ratio $R_{S/P}$ and we will present results for $R_{\Phi/S}$. We will examine $R_{\rho/S}$ in Chapter 5. Mineral physics calculations predict that in a lower mantle dominated by thermal effects (excluding phase transitions, but including anelasticity), the maximum $R_{S/P}$ is about 2.5 (Karato & Karki, 2001). However, according to Brodholt et al. (2007) the importance of anelasticity was exaggerated and they lowered the probable upper bound of $R_{S/P}$ in the lower mantle to 2.1. Many studies observed $R_{S/P}$ values increasing to about 3 in the lowermost mantle (Fig. 4.1; (Su & Dziewonski, 1997; Romanowicz, 2001; Houser et al., 2008b; Della Mora et al., 2011; Koelemeijer et al., 2016)), which is higher than both 2.1 and 2.5, and therefore have originally been interpreted to be indicative of chemical heterogeneity.

In addition to $R_{S/P}$, we are going to look at another interesting parameter: the correlation between shear-wave velocity and bulk sound velocity. When $R_{S/P}$ at a specific point in the Earth becomes high enough, variations in bulk sound $\delta \ln v_\phi$ start to become anti-correlated to variations in shear-wave velocity $\delta \ln v_s$.

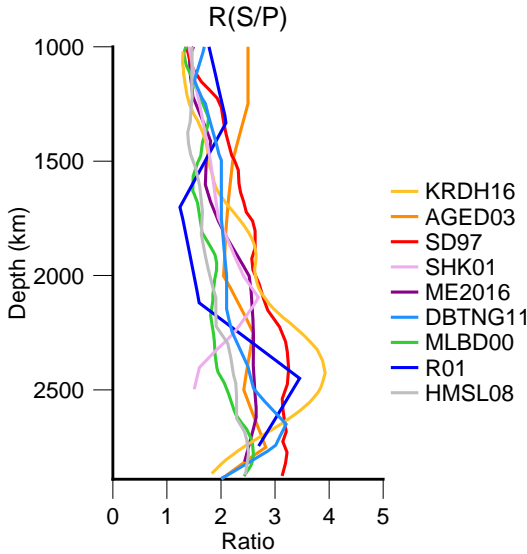


Figure 4.1: Previously measured $R_{S/P}$ profiles for seismic tomographic models from: KR DH16: Koelemeijer et al. (2016), AGED03: Antolik et al. (2003), SD97: Su & Dziewonski (1997), SHK01: Saltzer et al. (2001), ME2016: Moulik & Ekström (2016), DBTNG11: Della Mora et al. (2011), MLD00: Masters et al. (2000a), R01: Romanowicz (2001), HMSL08: Houser et al. (2008b).

4.1.2. Previous observations of S - Φ anti-correlation

The anti-correlation between $\delta \ln v_s$ and $\delta \ln v_\phi$ in the lowermost mantle is observed by many studies (Fig. 4.2) using various seismic data, such as body wave arrival times or splitting function measurements. In some cases, the anti-correlation was observed indirectly from shear- and compressional wave velocity models (e.g Simmons et al., 2010; Koelemeijer et al., 2016; Moulik & Ekström, 2016), using the following relation between v_s , v_p and v_ϕ :

$$\delta \ln v_p = \gamma \delta \ln v_s + (1 - \gamma) \delta \ln v_\phi \quad (4.1)$$

with:

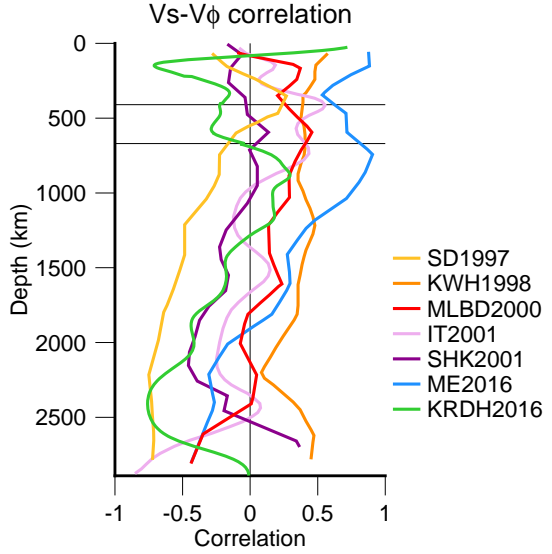
$$\gamma = \frac{4 v_s^2}{3 v_p^2} \quad (4.2)$$

In other cases, the anti-correlation is observed directly from a joint inversion for shear-wave and bulk sound velocity (e.g Su & Dziewonski, 1997; Ishii & Tromp, 1999, 2001; Masters et al., 2000a), and finally, through probabilistic tomography using splitting functions, surface waves (Resovsky & Trampert, 2003) and gravity constraints (Trampert et al., 2004) or body waves (Mosca et al., 2012).

Only two studies have found a slightly positive S - Φ correlation in part of the lowermost mantle: Saltzer et al. (2001) and Kennett et al. (1998). By extracting v_ϕ from v_s and v_p in a body wave study, Saltzer et al. (2001) found a negative S - Φ correlation in the depth range 1700-2100 km, which turns into a moderately positive correlation in the lowermost 200-300 kms of the non-slab regions (Fig. 4.2). Kennett et al. (1998) inverted S and P travel times for shear and bulk sound velocity and did not find any negative correlations throughout the mantle, but only slightly positive correlations to decorrelations (Fig. 4.2). An important note here is that

most of the lower mantle contained very little bulk sound variation, which makes the correlation less significant. Koelemeijer et al. (2018) partly reconcile the differences between body waves and long period (normal mode) S- Φ correlation profiles by more vertical smearing that occurs in body wave dominated studies, when the ray theory approximation is used. Finite frequency effects could also partly explain the large spread in $R_{S/P}$ (Tesoniero et al., 2016; Koelemeijer et al., 2018).

Figure 4.2: Previously observed cross-correlation between $\delta \ln v_s$ and $\delta \ln v_\phi$ by SD1997: Su & Dziewonski (1997), KWH1998: Kennett et al. (1998), MLBD2000: Masters et al. (2000a), IT2001: Ishii & Tromp (2001), SHK2001: Saltzer et al. (2001) in the non-slab regions, ME2016: Moulik & Ekström (2016), KRDH2016: Koelemeijer et al. (2016).



4.1.3. Mineral physics

Bulk sound velocity depends on the bulk modulus κ and density ρ as:

$$v_\phi = \sqrt{\frac{\kappa}{\rho}} \quad (4.3)$$

Contrary to shear- and compressional-wave velocity, bulk sound velocity is independent of the shear modulus μ , and hence not affected much by attenuation (since bulk attenuation is assumed to be negligible). Furthermore, many high pressure laboratory experiments produce results that can be directly linked to bulk sound speed, making observations of bulk sound in the mantle very suitable for mineralogical interpretations.

If we consider elastic effects alone, the correlation between v_s and v_ϕ anomalies cannot be negative (e.g. Karato & Karki, 2001; Matas & Bukowinski, 2007). The magnitude of anelastic effects on both $R_{S/P}$ and the S- Φ correlation has been debated, with some claiming that anelastic effects alone might account for the observed high $R_{S/P}$ values (Karato, 1993; Karato & Karki, 2001), while others reduce the importance of anelastic effects in favour of chemical heterogeneity (Trampert

et al., 2001; Matas & Bukowinski, 2007). Most likely, anelasticity cannot alter the sign of the S - Φ correlation, only its magnitude (Brodholt et al., 2007).

These considerations mean that S - Φ anti-correlation cannot be explained by a purely thermal mantle, not even when anelasticity is taken into account, and is hence thought of as a robust indicator of the presence of chemical heterogeneity. The anti-correlation between $\delta \ln v_s$ and $\delta \ln v_\phi$ is a stronger indicator of chemical heterogeneity than $R_{S/P}$, as chemical heterogeneity can also lower the value of $R_{S/P}$ (Trampert & Van Der Hilst, 2005). In any case, the argument against or in favour of chemical heterogeneity will become stronger when observations of high $R_{S/P}$ values are combined with S - Φ anti-correlation.

Alternatively, the lowermost mantle phase transition from bridgmanite to post-perovskite (pPv) might explain a rise in $R_{S/P}$ combined with S - Φ anti-correlation, which would not require chemical heterogeneity. This phase transition is accompanied by an increase in v_s and little to no change in v_p (e.g. Murakami et al., 2004; Oganov & Ono, 2004; Tsuchiya et al., 2004), resulting in a higher $R_{S/P}$ and S - Φ anti-correlation. Recently, Koelemeijer et al. (2018) have studied the effects of pPv on the S - Φ correlation, and found that lateral variations in the presence of pPv have a dominant effect on the S - Φ correlation. Their finding implies that S - Φ correlation might not be a robust measure to constrain the presence of chemical heterogeneity after all. There is still much unknown about the stability field of pPv (see review by Cobden et al. (2015)), but several seismic studies have found that seismic data prefer or hint towards a pPv-bearing CMB region, including core-diffracted body waves (Cobden et al., 2012), normal modes (Koelemeijer et al., 2017), body waves, surface waves and normal modes (Mosca et al., 2012), and also thermochemical modelling (Koelemeijer et al., 2018). Recent in-situ high-pressure and -temperature experiments also suggest that the phase transition occurs under lower mantle conditions (Kuwayama et al., 2021).

As we have seen in the previous chapter, the one-step and two-step inversions give very similar results when modelling S -wave velocity perturbations, although the one-step model produces slightly lower spectral misfits. Hence splitting functions serve as a convenient intermediate step when modelling 3D shear velocity (Li et al., 1991), but will they still be accurate enough when we also include 3D P -wave velocity or bulk sound velocity in the inversions? The other important question we address here is how the methods of computing $R_{S/P}$ or S - Φ correlation affect the thermochemical interpretations we draw from them.

4.2. Data and methods

We use the same normal mode spectra as starting point of both our inversions. Similar to the procedure in Chapter 3, we invert the normal mode spectra for a mantle model in two ways: i) in a one-step direct spectrum inversion, and ii) in a two-step splitting function inversion. Details on these two methods are outlined in Chapter 3, so we will not discuss them any further here.

In addition to, or sometimes in replacement of, the spectral segments of Deuss et al. (2013), we use the segments of Koelemeijer et al. (2013) and Koelemeijer (2014). The noteworthy additions to the previous data set are high angular order

fundamental modes (${}_0S_{22} - {}_0S_{30}$) and a few core-mantle boundary Stoneley modes (${}_1S_{11-14}$, ${}_2S_{15-17,25}$, ${}_3S_{26}$). All segments consist of vertical component data for 93 large events ($M_w \geq 7.4$) since 1976. For the two-step approach we use the spheroidal mode splitting functions obtained by the same three studies, and only execute the second inversion step in this paper. We exclude spheroidal modes that are sensitive to the inner core or couple strongly to an inner core mode, since our focus is on the mantle. The total number of spectral segments is 118,034, for 88 modes and mode groups in the one-step inversion and 125 self-coupled and 10 cross-coupled splitting functions for the two-step inversion. We use more modes and segments than in the previous chapter (Tables 4.1 and 4.2).

We assign weights to the data in the two inversions in the same way as in Chapter 3. For the one-step inversion the normal mode spectra are weighed implicitly by the number of segments each mode or mode group contributes to the inversion. For the second step of the two-step inversion, the splitting functions are weighed by their maximum error determined by cross-validation. We have already explained that these choices in weighting are comparable.

We invert for aspherical perturbations in shear wave velocity ($\delta \ln v_s$) and compressional wave velocity ($\delta \ln v_p$), which are the two observables that normal modes are most sensitive to. Hereby we remove the scaling factor between $\delta \ln v_s$ and $\delta \ln v_p$ of 0.5 that was present in the inversions of Chapter 3. The constraint of $\delta \ln \rho$ being proportional to $\delta \ln v_s$ by a factor of 0.3 is still present here. In Chapter 5, we will remove this final proportionality constraint. Crustal contributions are included using model CRUST 5.1 (Mooney et al., 1998). In the one-step inversion, crustal effects are included in the splitting matrix for computing synthetic spectra. In the two-step inversion, splitting function predictions for the crust are subtracted from the measured c_{st} 's, effectively removing the crust. We use 1D model PREM (Dziewonski & Anderson, 1981) as starting model for the one-step inversion and for the second step of the two-step inversion.

For the joint $v_s + v_p$ inversion we use the same model parameterization as S20RTS (Ritsema et al., 1999), S40RTS (Ritsema et al., 2011) and SP12RTS (Koele-

Table 4.1: Spectral segments in the one-step inversion containing the mode groups that were added or modified (in *italics*) with respect to the modes in Chapter 3, with the number of events as N_{ev} .

Spectral segment	N_{ev}	Spectral segment	N_{ev}
${}_0S_{15}$	92	${}_0S_{28}$	93
${}_0S_{16}$	93	${}_0S_{29}$	93
${}_0S_{19} - {}_1S_{13}$	91	${}_0S_{30}$	92
${}_0S_{21} - {}_1S_{14}$	93	${}_1S_{11} - {}_0S_{15}$	93
${}_0S_{22} - {}_2S_{14}$	93	${}_1S_{12} - {}_0S_{17}$	91
${}_0S_{23} - {}_1S_{15}$	93	${}_2S_{13}$	92
${}_0S_{24} - {}_2S_{15}$	92	${}_2S_{17} - {}_7S_5$	90
${}_0S_{25} - {}_1S_{16}$	92	${}_2S_{25} - {}_3S_{25}$	76
${}_0S_{26} - {}_2S_{16}$	93	${}_6S_{15} - {}_9S_{10} - {}_3S_{26}$	81
${}_0S_{27}$	93		

Table 4.2: Splitting functions in the two-step inversion that were added or modified (in italics) with respect to the modes in Chapter 3, with the number of events as N_{ev} .

Spectral segment	N_{ev}	Spectral segment	N_{ev}
${}_0S_{15}$	92	${}_1S_{13}$	91
${}_0S_{16}$	93	${}_1S_{14}$	93
${}_0S_{19}$	91	${}_1S_{15}$	93
${}_0S_{21}$	93	${}_1S_{16}$	92
${}_0S_{22}$	93	${}_2S_{13}$	92
${}_0S_{23}$	93	${}_2S_{14}$	93
${}_0S_{23} - {}_1S_{15}$	93	${}_2S_{15}$	92
${}_0S_{24}$	92	${}_2S_{16}$	93
${}_0S_{25}$	92	${}_2S_{17}$	90
${}_0S_{26}$	93	${}_2S_{25}$	76
${}_0S_{27}$	93	${}_3S_{25}$	76
${}_0S_{28}$	93	${}_2S_{25} - {}_3S_{25}$	76
${}_0S_{29}$	93	${}_3S_{26}$	81
${}_0S_{30}$	92	${}_6S_{15}$	81
${}_1S_{10}$	70	${}_7S_5$	90
${}_1S_{11}$	93	${}_9S_{10}$	81
${}_1S_{12}$	91		

meijer et al., 2016), using 21 splines in the radial direction (Fig. 4.3a), and spherical harmonics laterally. We go up to maximum spherical harmonic degree 12, as in SP12RTS, but only invert for the even degrees, since our normal mode data set does not allow for much odd-degree sensitivity (as previously discussed in Chapter 3), especially in the splitting function inversion.

We choose a radial parameterization of 7 equally spaced B-splines (Fig. 4.3b) and a maximum spherical harmonic degree 6 for $v_s + v_\phi$ inversions, as normal mode sensitivity to bulk modulus κ is low. Performing these inversions with 21 splines resulted in models which were highly dependent on damping, with many dissimilarities between the one-step and two-step models. We will start inversions for 3D bulk sound velocity by trying to recover various input models in synthetic inversions. Furthermore, real data inversions will be performed for various v_ϕ starting models, containing zero and non-zero 3D variations, to assess dependence on the starting model. As we have seen before, S- Φ correlation can be obtained either i) through a direct inversion for v_s and v_ϕ heterogeneity, or ii) by extracting v_ϕ from an inversion for v_s and v_p heterogeneity, using the relation of eq. 4.1. We will attempt both ways and compare the resulting correlations.

After we obtain the $\delta \ln v_s$ and $\delta \ln v_p$ models, we compute the ratio $R_{S/P} = \delta \ln v_s / \delta \ln v_p$. $R_{S/P}$ has been estimated previously in a number of different ways: (i) dividing the RMS amplitude of the shear velocity anomalies by the RMS amplitude of the compressional velocity anomalies (e.g. Su & Dziewonski, 1997; Antolik et al., 2003; Koelemeijer et al., 2016); (ii) taking the median value (e.g. Masters et al., 2000a; Davies et al., 2012; Koelemeijer et al., 2016; Moulik & Ekström, 2016;

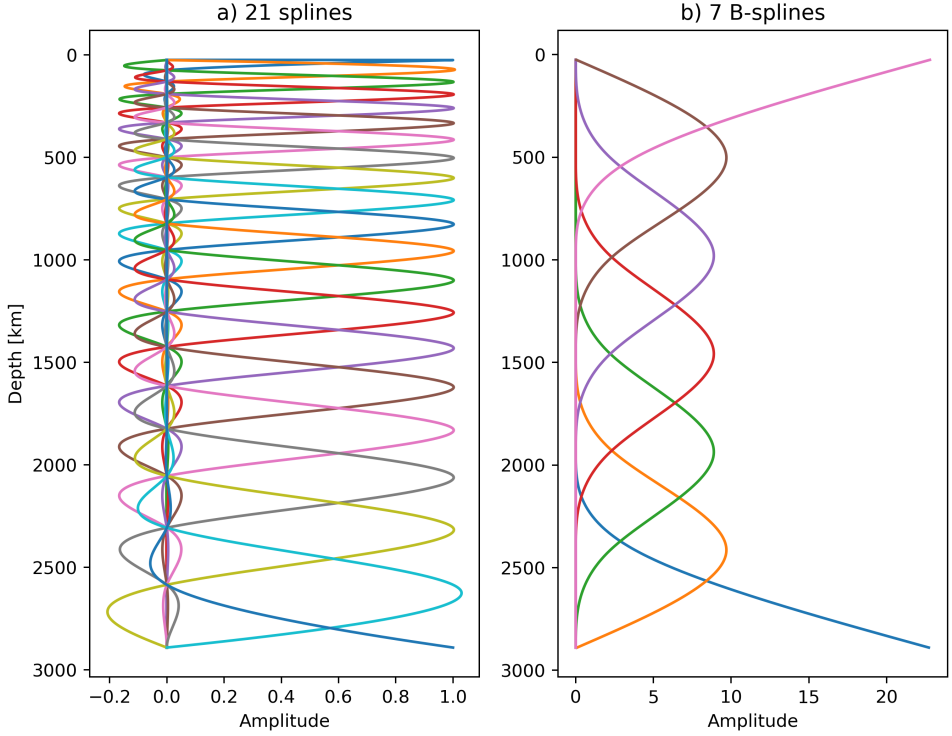


Figure 4.3: Mantle radial parameterizations used in this study: a) 21 splines as used in e.g. S20RTS (Ritsema et al., 1999), S40RTS (Ritsema et al., 2011) and SP12RTS (Koelemeijer et al., 2016), b) 7 equally spaced B-splines.

Tesoniero et al., 2016) or (iii) taking the mean value (e.g. Della Mora et al., 2011) of the ratio at grid points at a certain depth; (iv) computing the slope of the best linear fit through a cloud of $\delta \ln v_s$ against $\delta \ln v_p$ (e.g. Saltzer et al., 2001; Koelemeijer et al., 2016); (v) taking the ratio of the spherically averaged values of $\delta \ln v_s$ and $\delta \ln v_p$ (e.g. Robertson & Woodhouse, 1996). All of these methods result in a 1D depth profile representative of 3D variations in $R_{S/P}$, but, as we will show below, may result in different $R_{S/P}$ values. We will compute $R_{S/P}$ in the two most common strategies, outlined below.

4.2.1. R-median

R-median is defined as the median value of a range of R-values computed by point-by-point division of $\delta \ln v_s$ by $\delta \ln v_p$ on a equidistant grid at a particular depth. We only include grid points for which both $\delta \ln v_s$ and $\delta \ln v_p$ exceed a certain threshold, to discard spurious estimates of $R_{S/P}$ when $\delta \ln v_s$ or $\delta \ln v_p$ are too close to zero. We will try 0.1 and 0.01 as threshold for the absolute $\delta \ln v_s$ and $\delta \ln v_p$ values that needs to be exceeded for inclusion in the distribution. The grid points are positioned on a $5 \times 5^\circ$ grid, with less sampling at the poles to avoid overrepresentation of those areas

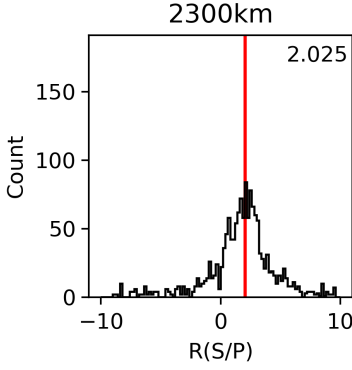


Figure 4.4: Example of a histogram of $R_{S/P}$ at a particular depth, in this case 2300 km. The red line represents the median of this distribution at 2.025, and is the 1D representative that we will use as R-median. The chosen threshold in this example is 0.01 and $R_{S/P}$ is derived from the one-step inversion models.

4

in the histograms. An example of a histogram of $R_{S/P}$ and its median is given in Fig. 4.4. Since it is also useful to look at the spread of $R_{S/P}$ and not just a 1D representative, we will examine the depth-dependence of the distribution of $R_{S/P}$ and of the velocity anomalies themselves. A wider spread in $R_{S/P}$ values is an indication of the presence of chemical heterogeneity, since temperature affects the two velocities in a similar way (Deschamps & Trampert, 2003).

4.2.2. R-RMS

R-RMS is obtained by dividing the RMS amplitudes of $\delta \ln v_s$ by $\delta \ln v_p$. More specifically, the spectral power p_s at a spherical harmonic degree s is defined as:

$$p_s = \sqrt{\frac{1}{2s+1} \left[m_{s0}^2 + \sum_{t=1}^s ((\text{Re}(m_{st}))^2 + (\text{Im}(m_{st}))^2) \right]} \quad (4.4)$$

in which m_{st} are the model coefficients of v_s or v_p corresponding to the spherical harmonics. The total RMS power of degrees 2 to 12 is then given by:

$$p_{\text{rms}} = \sqrt{\frac{1}{\sqrt{4\pi}} \sum_{s=2}^{12} (2s+1) p_s^2} \quad (4.5)$$

In computing R-RMS, we divide the total RMS power of the S-wave model by that of the P-wave model. Since computing RMS values involves squaring model coefficients (eq. 4.4), all negative ratios that could exist are not included, whereas they are included in the R-median approach. This is the reason why R-median will generally give lower estimates of $R_{S/P}$ than R-RMS, as we will see later.

4.3. Results for v_s , v_p and $R_{S/P}$

We invert normal mode data jointly for a shear and compressional wave velocity mantle model using the one-step direct spectrum inversion and the two-step splitting function inversion. We will compare the resulting models, misfits and $R_{S/P}$ in detail below.

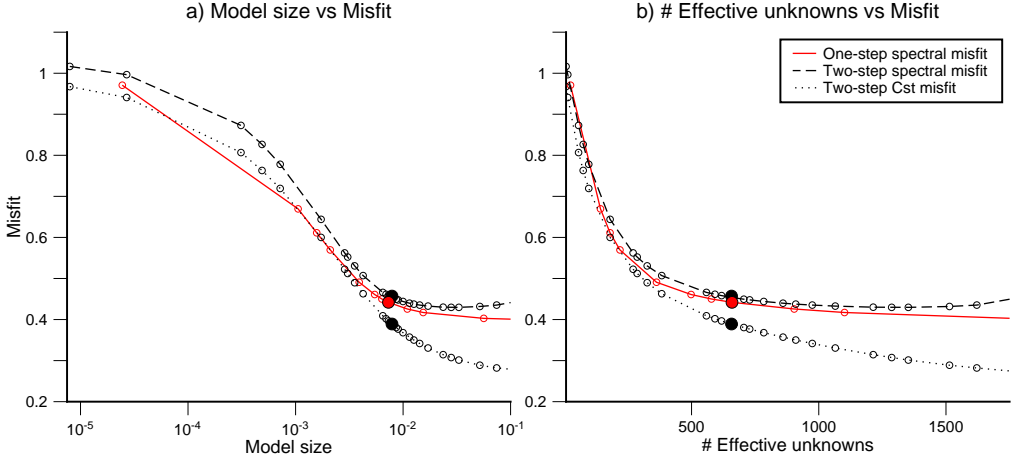


Figure 4.5: L-curve for the one-step inversion spectral misfits (red), and L-curves for the c_{st} misfits (dotted) and spectral misfits (dashed) for the models resulting from the two-step inversion, as a function of a) model size and b) number of effective unknowns. Solid red dot: best model for one-step inversion. Solid black dots: best model for the two-step inversion.

	One-step	Two-step	SP12RTS
\mathbf{v}_s only	0.53	0.58	
$\mathbf{v}_s + \mathbf{v}_p$	0.44	0.45	0.45
$\mathbf{v}_s + \mathbf{v}_p$ with \mathbf{v}_s -only modes	0.47	0.48	

Table 4.3: Spectral misfits for the one-step and two-step inversions, for different cases: a v_s only inversion (performed in Chapter 3), a v_s plus v_p inversion (performed in this chapter), and the same v_s plus v_p inversion with only taking the modes from Chapter 3 into account for computing the misfit. The spectral misfit for SP12RTS using our data is also shown.

4.3.1. L-curves and misfits

We compute two different kinds of misfit for our models: spectral misfit and c_{st} misfit. Spectral misfit is the difference between observed and synthetic spectra, c_{st} misfit is the difference between the measured c_{st} coefficients and the predicted c_{st} 's for the mantle model, as explained more in detail in Chapter 3. For the two-step inversion, we can not only compute the c_{st} misfit, but also the spectral misfit, since we have the original spectral data from which the splitting functions were derived. We choose to compare the one-step and two-step models based on the same number of effective eigenvalues, as we did previously. For the same number of effective eigenvalues, the average spectral misfit and model size of the one-step inversion are slightly lower than for the two-step inversion (Fig. 4.5; Table 4.3).

The spectral misfits per mode or mode group (Fig. 4.6) clearly show that both the one-step (red triangles) and two-step (black squares) models fit the spectra better than PREM plus rotation and ellipticity (grey circles). Compared to the

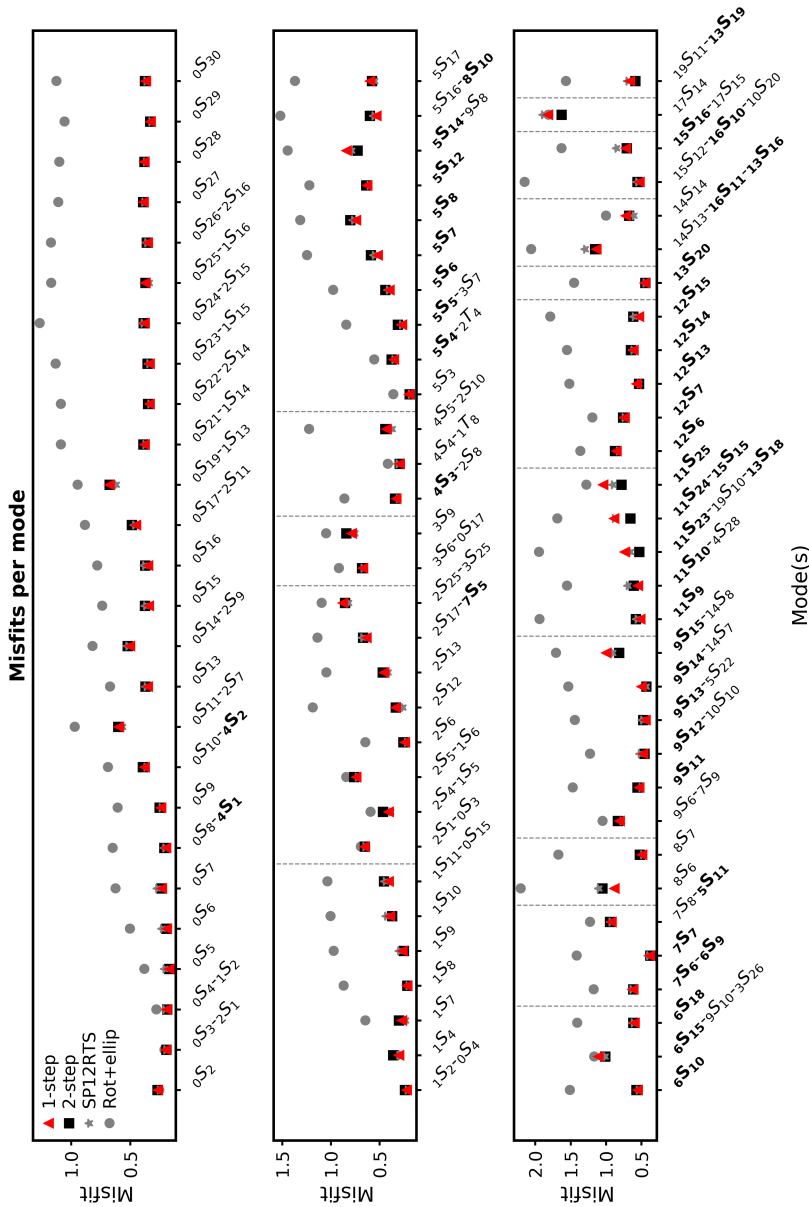


Figure 4.6: Average spectral misfit per mode or mode group for the best models from the one-step (red triangles) and two-step (black squares) $v_s + v_p$ inversion, compared to predicted misfits for SP12RTS (grey asterisks) and PREM plus rotation and ellipticity (grey circles). Bold modes are v_p sensitive.

v_s -only inversion of Chapter 3, the joint v_s and v_p inversion performed here fits the spectral data better on average, both for the one-step inversion and the two-step inversion (Table 4.3). This improvement in data fit is mainly caused by the lower misfits of the added high angular order fundamentals ($0S_{22} - 0S_{30}$). The average

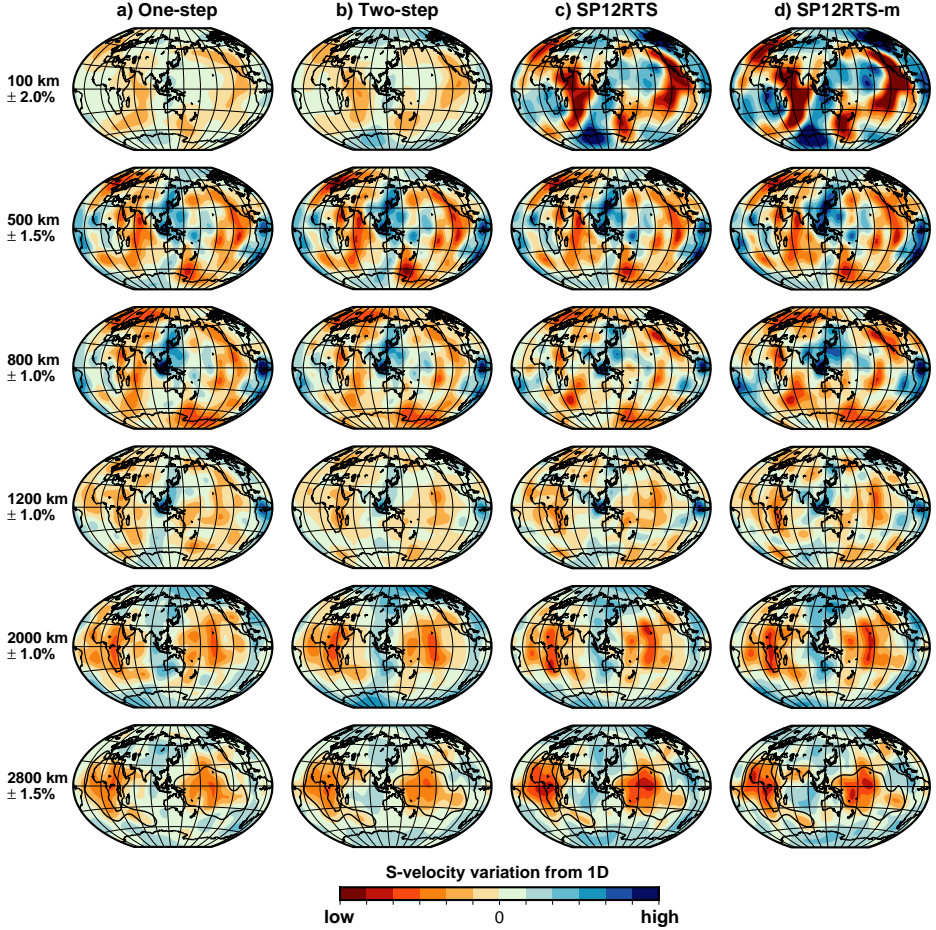


Figure 4.7: Model slices of shear wave velocity (v_s) showing even-degree structure up to degree 12 for a) the one-step inversion; b) two-step inversion; c) SP12RTS (Koelemeijer et al., 2016); and d) SP12RTS dominated by normal modes.

spectral misfits of our models are comparable to the misfit for SP12RTS (grey stars in Fig. 4.6; Table 4.3). Without the modes added with respect to the previous chapter, the spectral misfits for the one-step inversion and the two-step inversion are still lower than the v_s -only inversion (Table 4.3). The improvement in data fit shows that it is probably not representative of the true mantle to scale perturbations in v_s to perturbations in v_p with a single scaling factor throughout the entire mantle (although another contributing factor to the lower misfit could be the increase in maximum degree from 8 to 12). This statement is backed up by almost all of the v_p sensitive modes having improved spectral misfits in the joint v_s - v_p inversion, compared to the inversion where perturbations in v_p were scaled to v_s . The average spectral one-step (two-step) misfit for the v_p sensitive modes has dropped from 0.70

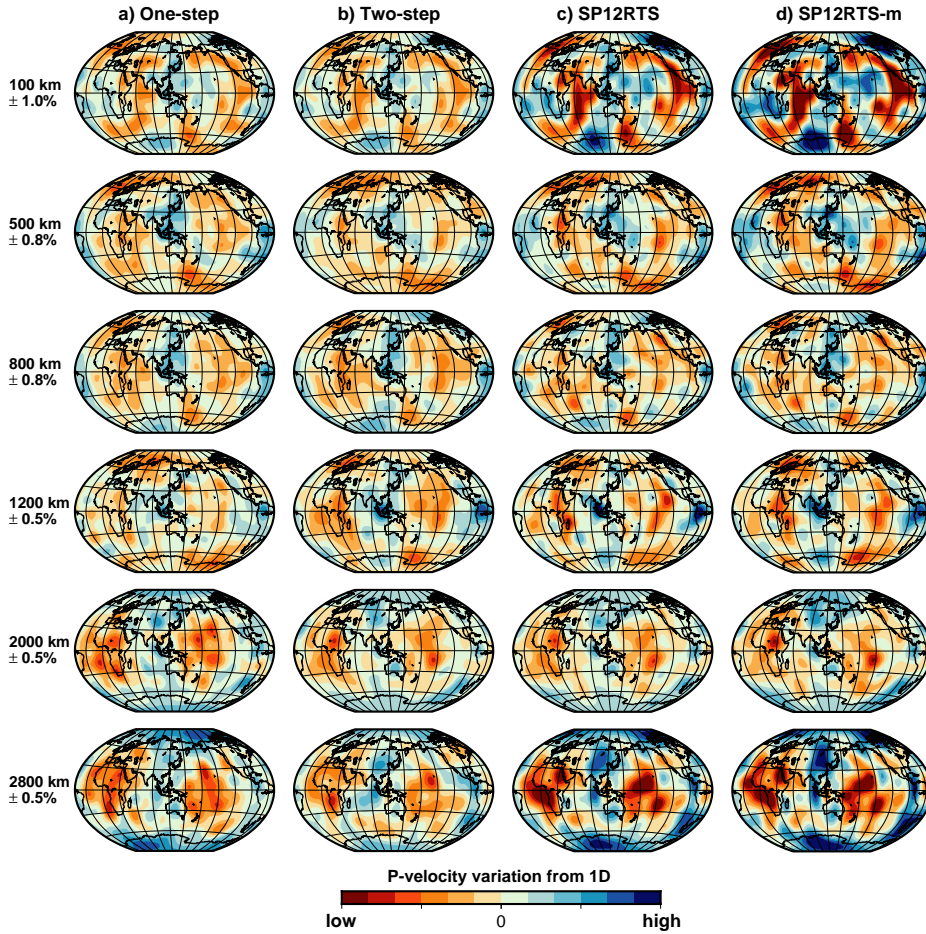


Figure 4.8: Model slices of compressional wave velocity (v_p) showing even-degree structure up to degree 12 for a) the one-step inversion; b) two-step inversion; c) SP12RTS (Koelemeijer et al., 2016); and d) SP12RTS dominated by normal modes.

(0.71) in the v_s -only inversion to 0.55 (0.55) in the current v_s - v_p inversion.

4.3.2. Model characteristics

We compare the v_s and v_p models of the one-step and two-step inversion to SP12RTS (Koelemeijer et al., 2016) and SP12RTS dominated by normal mode splitting functions ('SP12RTS-modes'). The two SP12RTS models do not differ much, since the chosen SP12RTS model already has strong weights assigned to the splitting functions, compared to the surface wave dispersion and body wave travel time data. The large-scale features of our one-step and two-step v_s (Fig. 4.7a,b) and v_p (Fig. 4.8a,b) models agree well with the those found in SP12RTS and SP12RTS-modes (Figs. 4.7c,d and 4.8c,d). When we look in more detail, the two-step models are

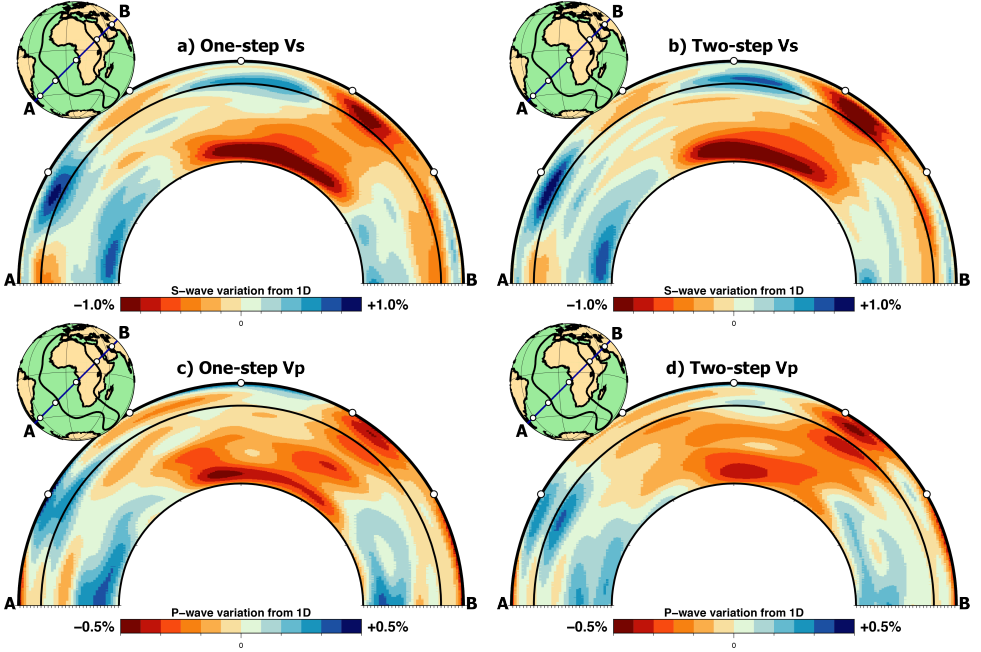


Figure 4.9: Cross-sections through a) one-step v_s and b) two-step v_s models, and c) one-step v_p and d) two-step v_p models, showing the African LLSVP.

more similar to the SP12RTS and SP12RTS-modes models, which is not surprising as they share a large part of their splitting function data set.

In cross-sections through the one- and two-step v_s and v_p models we see the LLSVP (or LLVP) very clearly (Figs. 4.9, 4.10). Both v_s models show a connection between the lower mantle LLSVP and the root of the East African Rift System in the upper mantle in the shape of a broad low velocity conduit (Fig. 4.9a,b). This connection is also present in both v_p models, where it is even wider (Fig. 4.9c,d). The lowest v_s anomaly of the LLSVP is concentrated in the lowermost couple of hundred kilometres, whereas the lowest v_p anomalies are less concentrated in one location. Low velocity material appears to be horizontally deflected at various depths in the mid-mantle, including the 670-discontinuity.

The difference between the one-step model and the other three is more apparent in v_p than in v_s , both in the depth slices (Figs. 4.7-4.8) and the power spectra per degree (Fig. 4.11). Higher spherical harmonic degrees contain more spectral power in the one-step models than in the two-step models, which is likely due to the different amount of coupling we are able to include in the inversion methods. We can include all the mode coupling within a spectral segment up to their theoretical maximum degree in the one-step inversion, whereas splitting function measurements may have to be cut off at a lower degree due to robustness issues for higher degrees. Our models share the characteristic of SP12RTS of a dominant degree two structure, both in v_s and v_p , representing cold and fast subducting slabs in the upper mantle

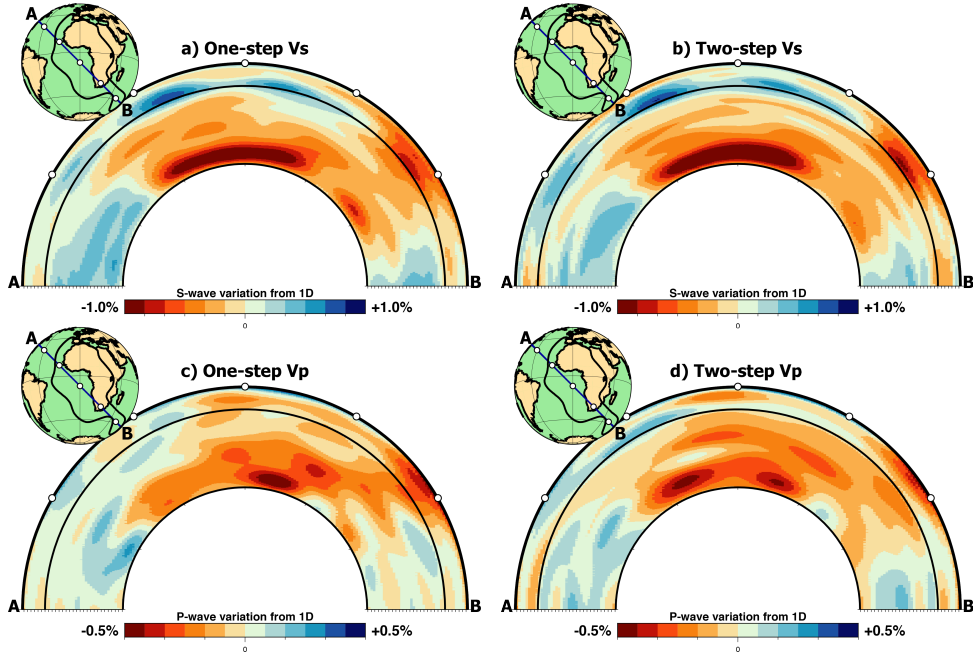


Figure 4.10: Same as Fig. 4.9, showing a different cross-section through the African LLSVP.

and representing LLSVPs (or LLVPs) in the lowermost mantle. The lack of power in the uppermost and lowermost mantle in our models compared to SP12RTS is due to the lack of surface waves and core-diffracted body waves.

These prominent differences in model amplitude between the one- and two-step models on one hand, and the SP12RTS models on the other hand, are also expressed in the root-mean square (RMS) amplitudes of all the models (Fig. 4.12a). The RMS amplitudes of all v_s models and all v_p models are similar in the depth range 400-2200km, and deviate in the uppermost and lowermost mantle. The one-step and two-step models peak in RMS amplitude around 2600km and then decrease again towards the CMB, while the RMS amplitudes of SP12RTS steadily increase until the CMB.

As we have seen in the depth slices through the models, there is less agreement among the v_p models than the v_s models, also shown in the cross-correlation profiles (Fig. 4.12b,c). An interesting observation is the drop in cross-correlation around 1250km between the one-step v_p model and the other v_p models which are all made with a two-step splitting function inversion (Fig. 4.12c). It coincides with a drop in cross-correlation between the one-step v_s and v_p models (Fig. 4.12d) and a decrease in degree-2 spectral power in the one-step v_p model (Fig. 4.11). The decrease in v_s - v_p cross-correlation for the normal mode dominated inversions (one-step, two-step, SP12RTS-modes) near the CMB is another noteworthy feature (Fig. 4.12d). We need to be careful when interpreting $R_{S/P}$ at these depths, since R-RMS loses its meaning when v_s and v_p are poorly correlated. However, a drop in correlation

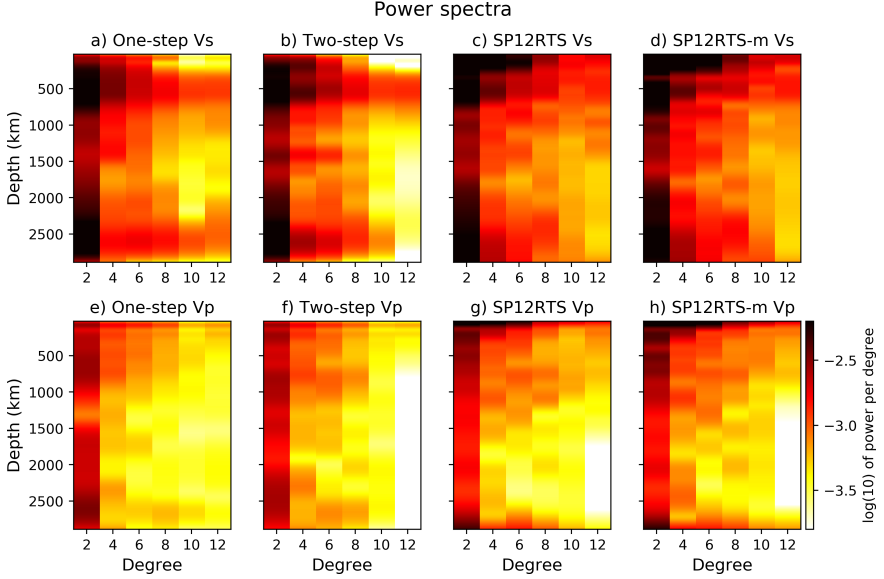


Figure 4.11: Power spectra per spherical harmonic degree for a-d) the four $\delta \ln v_s$ and e-h) four $\delta \ln v_p$ models shown in Figs. 4.7-4.8.

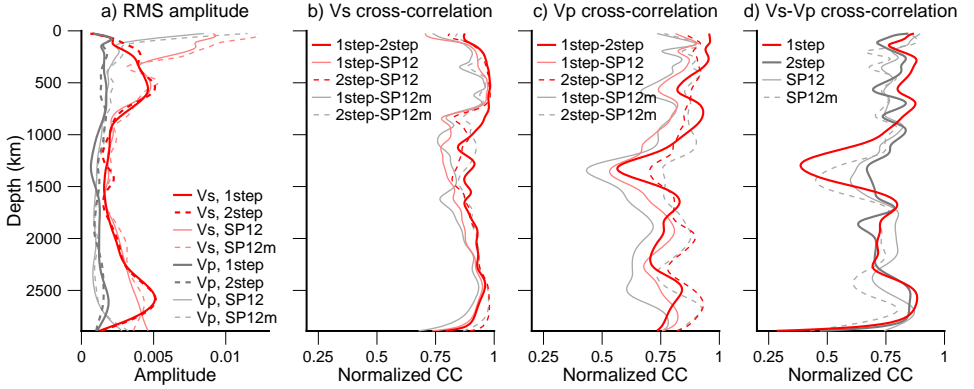


Figure 4.12: a) Root mean square (RMS) amplitudes of the models shown in Figs. 4.7-4.8; b) Normalized cross-correlation coefficients of all combinations of all the v_s models; c) and of all the v_p models; d) and between the v_s and v_p models of all inversions. (SP12 = SP12RTS, SP12m = SP12RTS dominated by modes).

between v_s and v_p in itself could hint towards chemical heterogeneity, since they should be well-correlated in a thermally dominated mantle.

4.3.3. 1D $R_{S/P}$

We have computed R-median and R-RMS as described in section 4.2 for the one-step models, two-step models and both SP12RTS models (Fig. 4.13). For comparison, the mineral physics prediction for a thermally dominated (isochemical) lower mantle, computed by Karato & Karki (2001), is also shown to serve as an upper limit for the isochemical case (blue line in Fig. 4.13). The general trends for the R-median profiles with thresholds 0.01 (Fig. 4.13a) and 0.1 (Fig. 4.13b) are similar in the upper mantle and transition zone, but start to deviate in the lower mantle. In either case, R-median only exceeds the mineral physics upper bound for a thermally dominated mantle in the lower mantle, which is more significant in the two-step inversion. We will use threshold 0.01 in the remainder of our analysis, since it matches the choice made in Koelemeijer et al. (2016) and it includes more information.

The R-RMS values for the one-step and two-step models are lower than the SP12RTS curves, and thereby closer to the mineral physics prediction (Fig. 4.13c). The high R-RMS in the one-step model around 1250 km should not be compared to the mineral physics prediction for a thermally dominated mantle, as the correlation between $\delta \ln v_s$ and $\delta \ln v_p$ is low (Robertson & Woodhouse (1996); Fig. 4.12d), as mentioned before. The decrease in $R_{S/P}$ near the CMB is a striking feature in both the one-step and two-step models. It was believed that the decrease in $R_{S/P}$ was caused by the lowest spline being effectively only half a spline, but we still observe the decrease in boxcar models with a thin lowermost layer (100 km). Furthermore, Koelemeijer et al. (2016) had already proven it to be a robust feature of their model, due to the incorporation of CMB Stoneley modes.

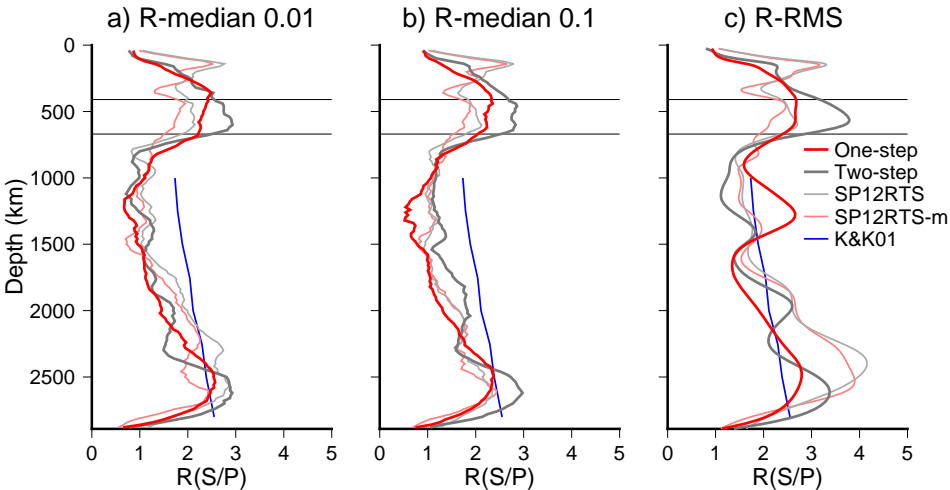


Figure 4.13: a) $R_{S/P}$ based on taking the median value per depth, only including points where $|\delta \ln v_s| > 0.01$ and $|\delta \ln v_p| > 0.01$, and b) only including points where $|\delta \ln v_s| > 0.1$ and $|\delta \ln v_p| > 0.1$; c) $R_{S/P}$ based on the RMS amplitudes of the v_s and v_p models. The blue line represents mineral physics predictions for a thermally dominated (isochemical) lower mantle, including anelasticity (Karato & Karki, 2001).

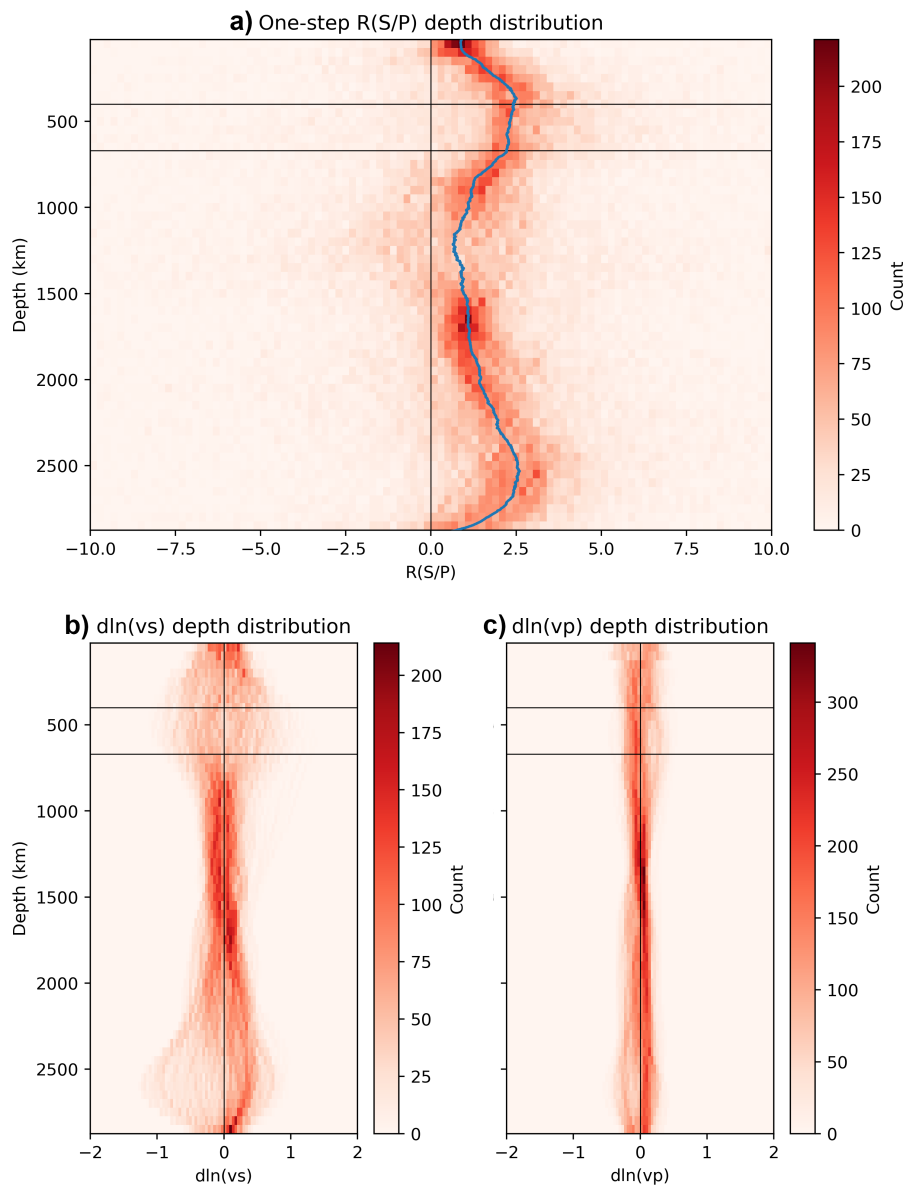


Figure 4.14: Distribution of $R_{S/P}$ versus depth, obtained by point-by-point division of one-step $\delta\ln v_s$ by $\delta\ln v_p$ on a $5 \times 5^\circ$ grid at 57 depths in the mantle. The median with threshold 0.01 is represented by the blue curve. Distributions of b) $\delta\ln v_s$ and c) $\delta\ln v_p$.

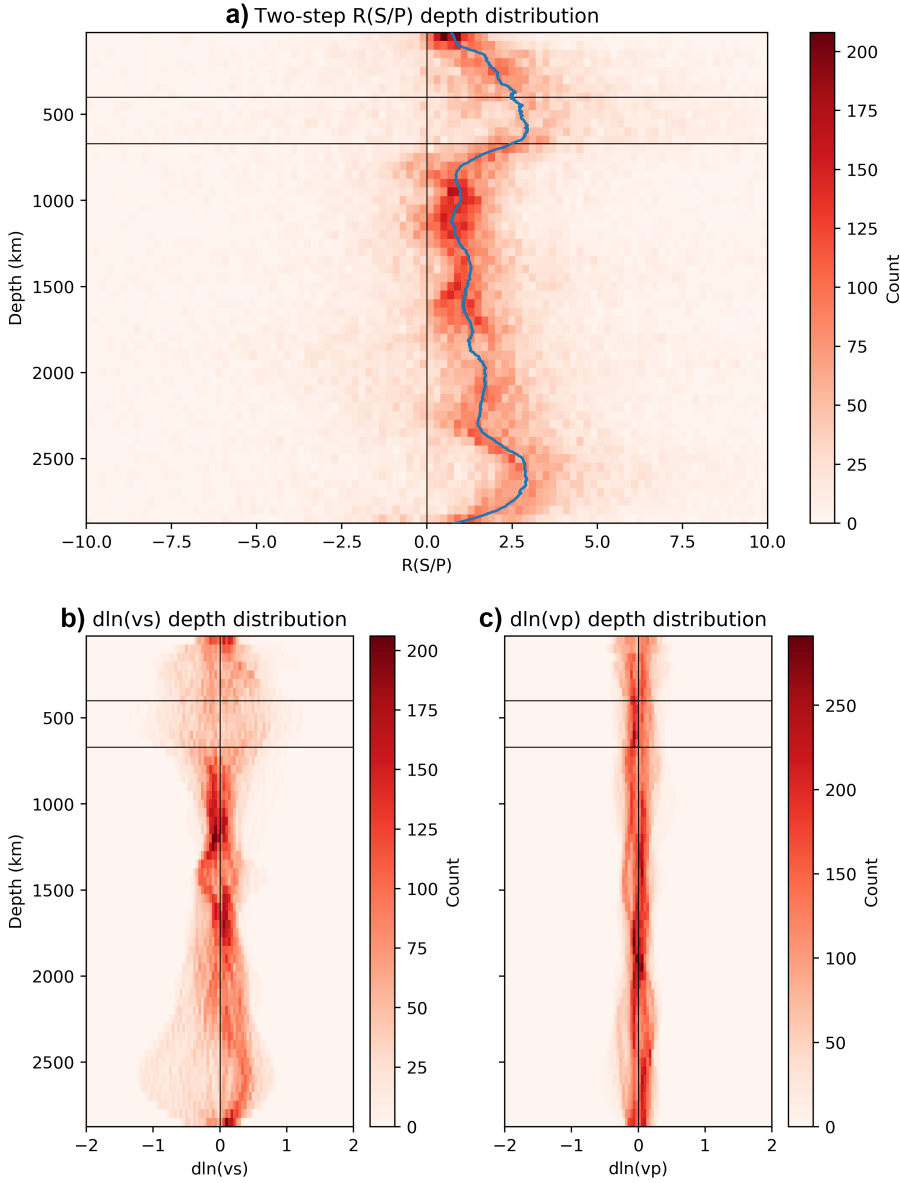


Figure 4.15: Distribution of $R_{S/P}$ versus depth, obtained by point-by-point division of two-step $\delta\ln v_s$ by $\delta\ln v_p$ on a $5 \times 5^\circ$ grid at 57 depths in the mantle. The median with threshold 0.01 is represented by the blue curve. Distributions of b) $\delta\ln v_s$ and c) $\delta\ln v_p$.

4.3.4. Distributions of $R_{S/P}$, v_s and v_p anomalies

We will now look at the distributions of $R_{S/P}$ and the anomalies of v_s and v_p with depth, from points on a $5 \times 5^\circ$ equidistant grid. It gives a more complete view of the

model characteristics than a 1D representative, and helps explaining the features that we see in R-RMS and R-median.

We observe a wide spread in the one-step $R_{S/P}$ values around 1100-1400 km depth with low median values, caused by the relatively large amount of negative ratios compared to other depths (Fig. 4.14a). At this depth we already encountered a drop in S-P cross-correlation (Fig. 4.12d) and a peak in R-RMS (Fig. 4.13c). The v_p distribution is concentrated around zero in this depth range (Fig. 4.14c), reflected by a dip in RMS amplitude for the one-step v_p model (Fig. 4.12a) primarily due to degree 2 (Fig. 4.11e), whereas the v_s distribution is more wide-spread (Fig. 4.14b). This difference results in a relatively higher RMS amplitude for v_s than v_p , causing a peak in R-RMS (Fig. 4.13c), resulting in larger amplitudes in v_s relative to v_p . The drop in S-P correlation is probably related to the large amount of negative $R_{S/P}$ values in the distribution, implying that $\delta \ln v_s$ is often positive where $\delta \ln v_p$ is negative, and vice versa. These features are absent in the two-step histograms (Fig. 4.14).

In the two-step distribution of $R_{S/P}$ we see a wide spread around 200-670 km depth in the upper mantle and transition zone (Fig. 4.15a), with a high R-median (Fig. 4.13a) and an exceptionally high R-RMS (Fig. 4.13c). This feature is caused by the large spread in $\delta \ln v_s$ compared to the spread in $\delta \ln v_p$ (Fig. 4.15b). We see similar features in the one-step model, but less extreme.

Around 2600 km both the one-step and two-step distributions are characterized by a large spread in $\delta \ln v_s$, resulting in high RMS amplitudes of the v_s model compared to v_p , hence a high R-RMS. The combination of a wide-spread $\delta \ln v_s$ distribution and high correlation between the v_s and v_p models at these depths (Fig. 4.12d) results in a high R-median, as grid points with negative $\delta \ln v_s$ and $\delta \ln v_p$ would give a positive contribution to the distribution of $R_{S/P}$. The same holds for two positive velocity anomalies.

Both the one- and two-step velocity distributions converge towards zero near the CMB, which is also where the R-RMS and R-median drop to about 1, reflecting the similar amplitude range of the two velocities (Figs. 4.14b,c and 4.15b,c). However, as the S-P correlation drops to zero at this depth (Fig. 4.12d), we should not use R-RMS to make interpretations.

4.4. Results for S- Φ correlation

4.4.1. Synthetic tests

First, we perform the one-step inversion with synthetic spectra and the two-step inversion with synthetic splitting function coefficients to get an idea of the sensitivity of our normal mode data set to bulk sound velocity. The three scenarios for the input bulk sound velocity of the synthetic data calculations are:

- i) $\delta \ln v_\phi$ correlated to $\delta \ln v_s$ with factor 0.3;
- ii) $\delta \ln v_\phi$ anti-correlated to $\delta \ln v_s$ with factor -0.3;
- iii) no 3D variations, i.e. $\delta \ln v_\phi = 0$

The $\delta \ln v_s$ models are the same in all three scenarios, and density perturbations are

scaled to $\delta \ln v_s$ with factor 0.3. The radial parameterization is set to 7 B-splines. If bulk-sound velocity is well-resolved, output models resulting from the inversions will look very similar to the input models. Scenario iii) is especially enlightening, since any non-zero output 3D v_ϕ is not constrained by the data, and hence an artefact of the inversion method. We will call it the “ghost pattern”, as it was not present in the original input synthetic models.

The synthetic inversion results for the one-step inversion (Fig. 4.16) show that it seems to be easier to retrieve a positive S- Φ correlation, since all the depth slices of the scenario (i) input model (Fig. 4.16a) correspond very well with the output model (Fig. 4.16c). The recovered bulk sound model for the S- Φ anti-correlation input (Fig. 4.16d) shows less resemblance to the scenario (ii) input bulk sound model (Fig.

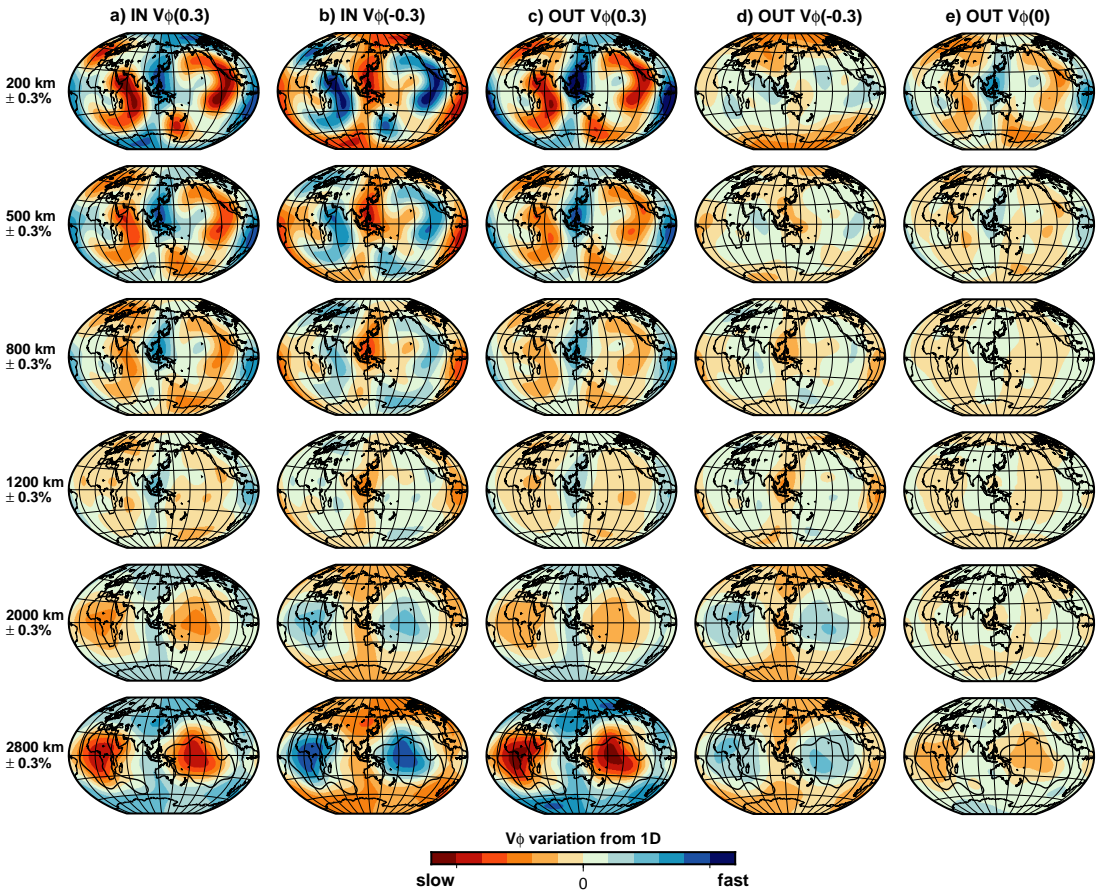


Figure 4.16: One-step synthetic inversion results, showing input v_ϕ models for synthetic spectra (to serve as observed data for the synthetic inversion) for a) positive correlation between $\delta \ln v_s$ and $\delta \ln v_\phi$; b) negative correlation between $\delta \ln v_s$ and $\delta \ln v_\phi$. Output v_ϕ models after one-step inversion for c) input model a); d) input model b); e) input model of zero 3D v_ϕ , which makes this the ghost pattern.

4.16b). The differences between the input and output bulk sound models seem to be captured by the ghost pattern model (Fig. 4.16e) of scenario (iii) which looks like $\delta \ln v_\phi$ correlated to $\delta \ln v_s$. When interpreting the $S\text{-}\Phi$ correlations of real data inversions, we need to keep the ghost pattern in mind.

The synthetic two-step inversion results (Fig. 4.17) show a very dominant ghost pattern in the upper mantle, very similar in pattern to v_s structure, and slightly less dominant ghost pattern in the lowermost mantle, also very similar to v_s structure. These dominant ghost v_ϕ structures result in the output model for the $S\text{-}\Phi$ anti-correlation input models not being able to recover the input model. The one-step inversion is able to recover the high bulk sound velocity in the LLSVPs in the lowermost mantle, since the ghost pattern is smaller in amplitude (Fig. 4.16e).

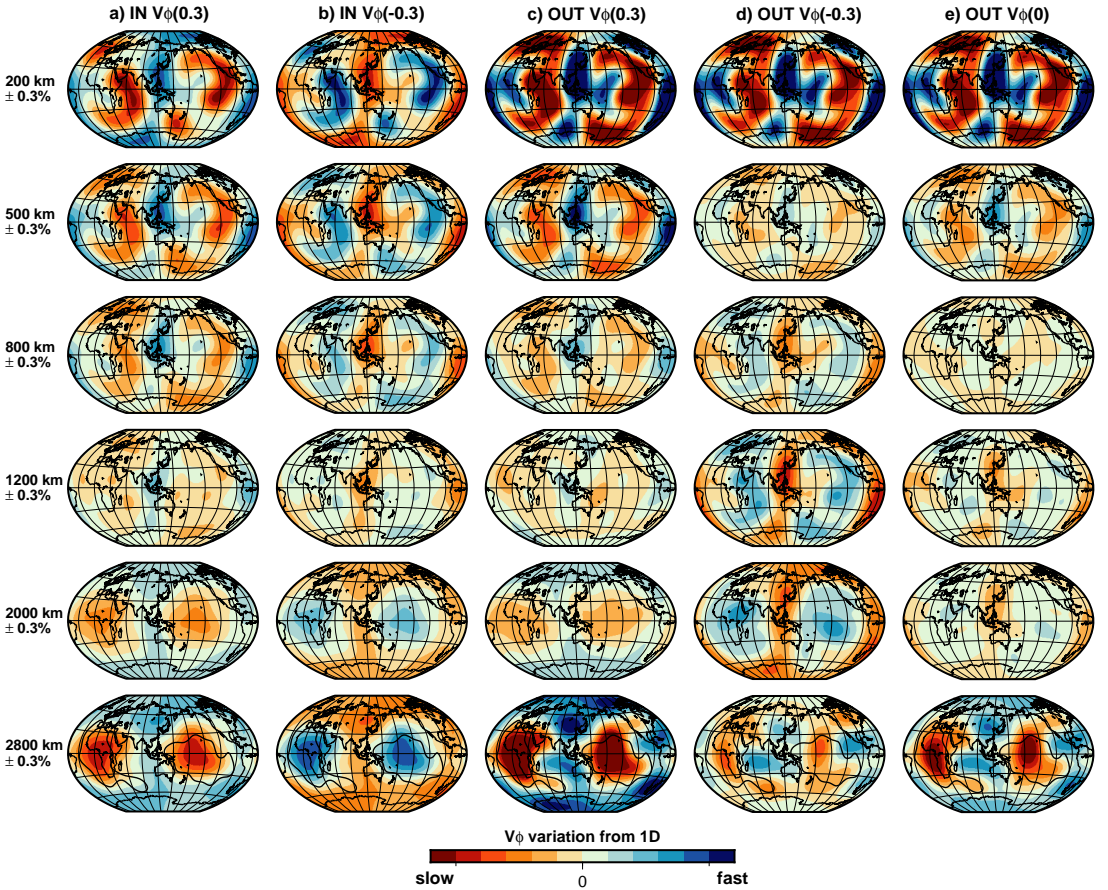


Figure 4.17: Two-step synthetic inversion results, showing input v_ϕ models for synthetic spectra (to serve as observed data for the synthetic inversion) for a) positive correlation between $\delta \ln v_s$ and $\delta \ln v_\phi$; b) negative correlation between $\delta \ln v_s$ and $\delta \ln v_\phi$. Output v_ϕ models after two-step inversion for c) input model a); d) input model b); e) input model of zero 3D v_ϕ , which makes this the ghost pattern.

The two-step ghost pattern (Fig. 4.17e) is anti-correlated to v_s in the mid-mantle, in contrast to the one-step inversion ghost pattern which is correlated to v_s . The recovered bulk sound velocity model for an input S- Φ anti-correlation (Fig. 4.17d) therefore fits the input model better in the mid-mantle, and the recovered model for input S- Φ correlation (Fig. 4.17c) fits the input model better for the upper and lowermost mantle.

4.4.2. Real data inversion for v_s and v_ϕ

Next, we perform joint $v_s + v_\phi$ one-step and two-step real data inversions using the same modes as for the joint $v_s + v_p$ inversions. Similar to the 21-splines one- and two-step v_s models, the one- and two-step 7 B-splines v_s models display mi-

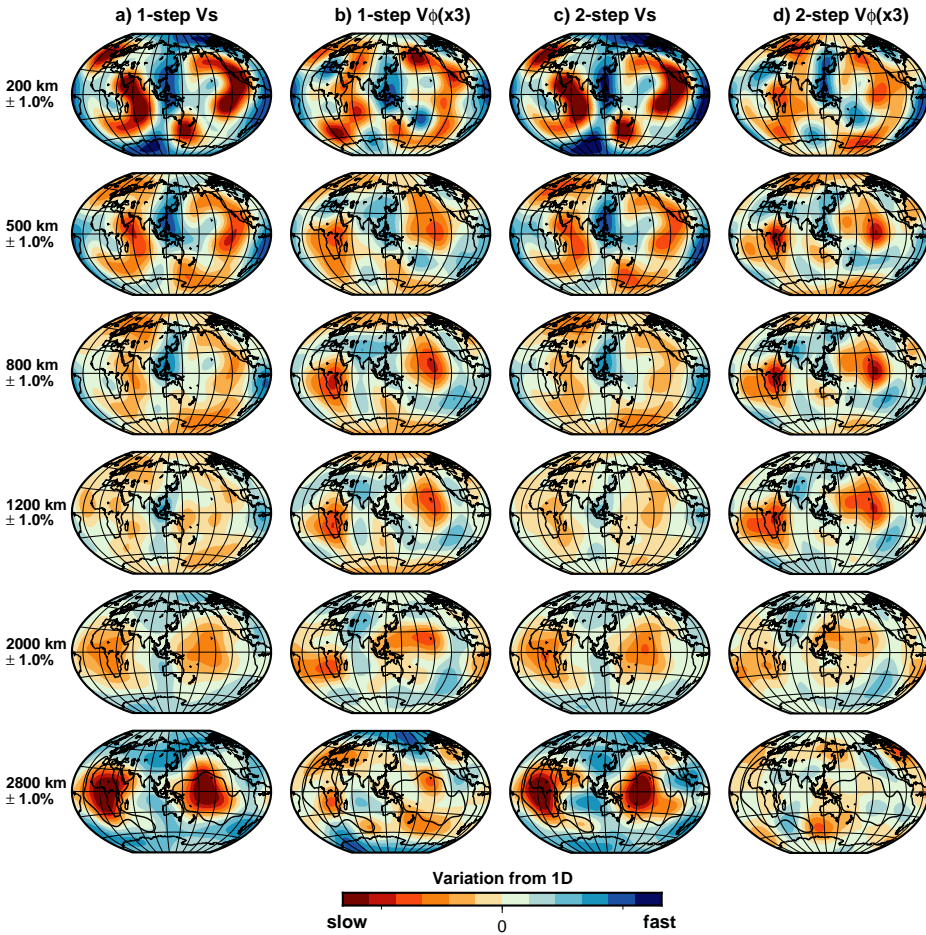


Figure 4.18: S-wave velocity and bulk sound velocity models for real data inversions. a) v_s and b) v_ϕ models for the one-step inversion, and c) v_s and d) v_ϕ models for the two-step inversion.

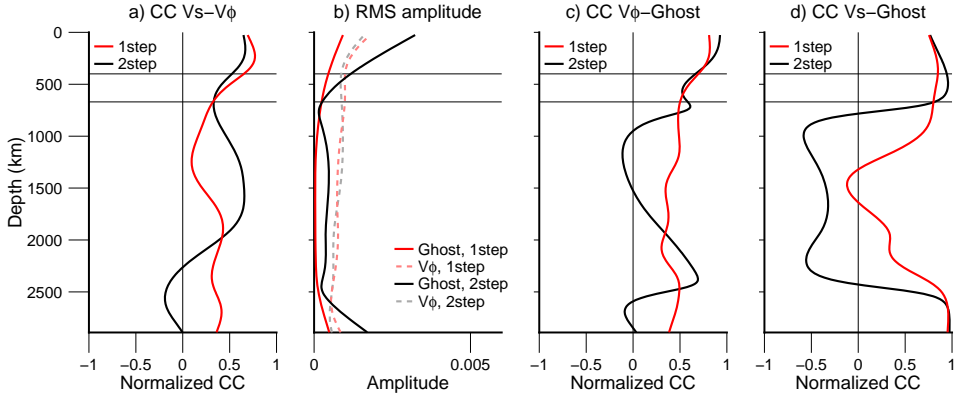


Figure 4.19: a) S- Φ correlations for the one-step (red) and two-step (black) models; b) RMS amplitudes of ghost v_ϕ for the one- (red) and two-step (black) synthetic inversions compared to the RMS amplitudes of v_ϕ of the one- (red dashed) and two-step (grey dashed) real data inversions; c) cross-correlation between ghost v_ϕ and observed v_ϕ for the one- (red) and two-step (black) inversions; d) cross-correlation between observed $\delta \ln v_s$ models and the ghost v_ϕ (1step=one-step inversion, 2step=two-step inversion).

nor differences in their patterns, most noticeably in the mid-lower mantle (Fig. 4.18a,c). The v_ϕ anomalies are characterized by two low bulk sound velocity regions throughout most of the mantle, one underneath Africa and one in the Pacific Ocean, roughly corresponding with the LLSVP locations (Fig. 4.18b,d). The uppermost and lowermost depth slices are the exceptions. In the uppermost mantle we find bulk sound velocity patterns partly coinciding with shear-wave velocity patterns at those depths, and more pronounced differences between one- and two-step v_ϕ . At first glance, the lowermost mantle does not show clear S- Φ correlations and again, significant differences between the one- and two-step v_ϕ models. Amplitudes of v_ϕ anomalies are at least three times smaller than v_s anomalies, which could reflect true mantle properties, or the limited bulk sound sensitivity of normal modes. The spectral misfit of the one-step models (0.51) is lower than for the two-step models (0.53) for the same number of effective eigenvalues.

The S- Φ correlations for the one-step and two-step models reproduce the general trend of more positive correlation in the upper mantle, moving towards more negative correlation in the lower mantle (Fig. 4.19a). The two-step correlation enters negative correlation values, up to -0.2, in the lowermost mantle, whereas the one-step correlation always stays positive, with a drop in the mid-mantle towards de-correlation. Our cross-correlations are thereby on the more positive side of the spectrum of cross-correlations found by other studies (Fig. 4.2). The differences between the one-step and two-step S- Φ correlations are not due to the v_s models, as their cross-correlation exceeds 0.91 throughout the mantle.

How do the observed bulk sound velocity models relate to the ghost bulk sound pattern found in the previous section? In terms of RMS amplitude, the two-step ghost pattern exceeds the one-step ghost pattern while also exceeding the RMS

amplitudes of the observed real data two-step v_ϕ model in the upper mantle and lowermost mantle (Fig. 4.19b). The dominance of the ghost pattern in the two-step inversion may explain the observed significant differences in v_ϕ patterns between the two inversion methods at these depths. The one-step ghost RMS amplitudes also increase in the upper mantle and lowermost mantle, but not to the point of exceeding the observed v_ϕ amplitudes from our real data inversion.

Correlations between observed v_ϕ and ghost v_ϕ (Fig. 4.19c) and between observed v_s and ghost v_ϕ anomalies (Fig. 4.19d) are high in the upper mantle for both inversion methods. This could mean that the ghost pattern, caused by leakage of v_s structure, dominates the observed bulk sound velocity model, which is more likely in the two-step inversion because of the high RMS amplitudes of the ghost pattern. Another likely scenario is that the true 3D bulk sound velocity happens to be highly correlated to 3D v_s structure. Correlation between observed v_s and ghost v_ϕ anomalies is also high in the lowermost mantle, but corresponds to de-correlation between observed v_ϕ and ghost v_ϕ in the two-step model and slightly positive correlation in the one-step model.

4.4.3. Effect of a v_ϕ starting model

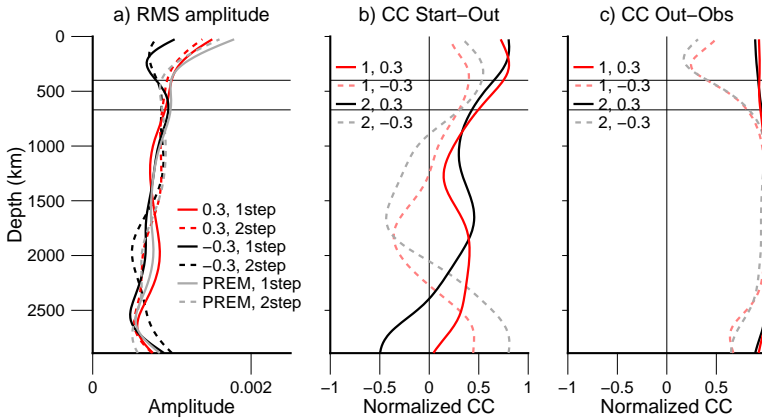


Figure 4.20: a) RMS amplitudes of the v_ϕ models started from correlation ($0.3\delta\ln v_s$), anti-correlation ($-0.3\delta\ln v_s$) and PREM, for the one- and two-step inversions; b) cross-correlations between the v_ϕ starting model (scaled to $\delta\ln v_s$ by 0.3 and -0.3) and resulting model for the one- and two-step inversion; c) cross-correlations between the v_ϕ output model for (anti-)correlated starting model and the v_ϕ observed when starting from PREM.

We examine the effect of a non-zero starting model for bulk sound velocity by starting our real data inversions from a v_ϕ model positively correlated to $\delta\ln v_s$ by factor 0.3 and negatively correlated to $\delta\ln v_s$ by factor -0.3. The effect of the starting model is minimal in the mid-mantle, reflected by high correlation coefficients between models started from (anti-)correlation and from PREM (Fig. 4.20c). Both the one-step and two-step inversions have very similar bulk sound patterns in the mid-mantle regardless of their starting model (Figs. 4.21, 4.22). The v_ϕ model

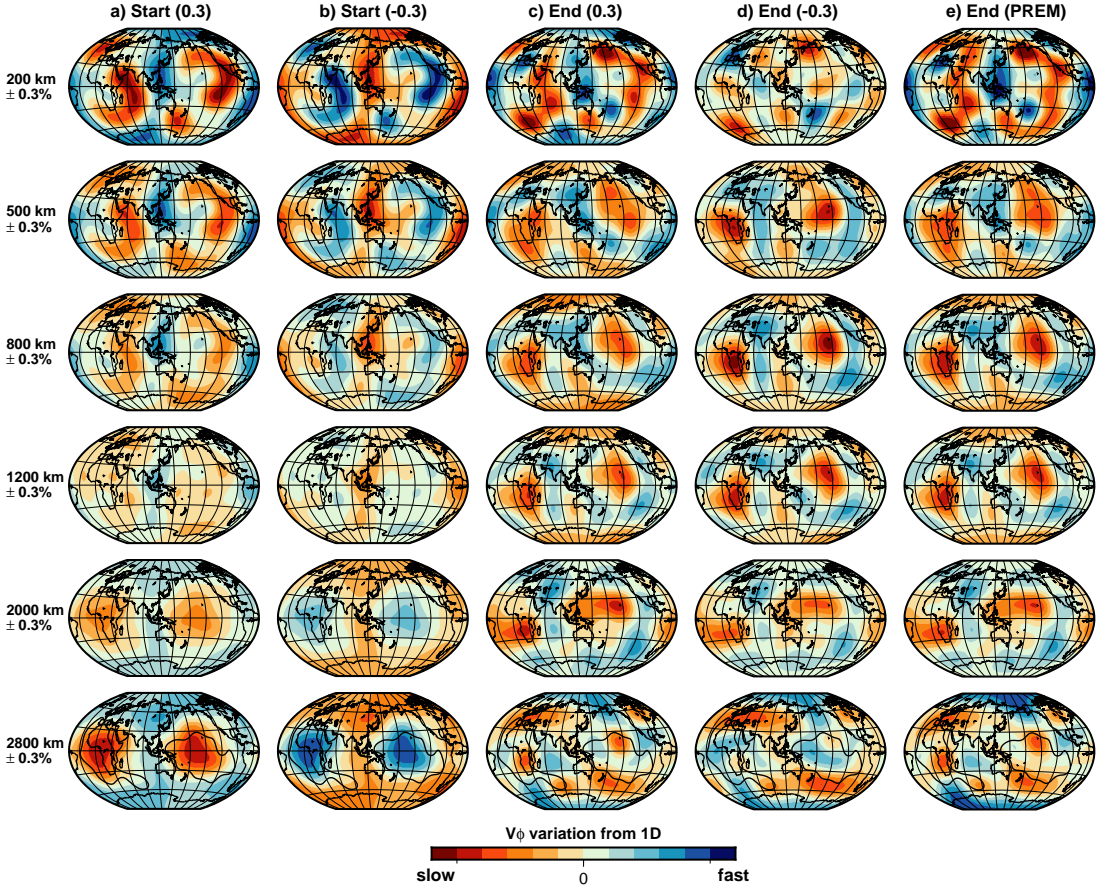


Figure 4.21: Bulk sound velocity models for different starting models in the one-step inversion. a) Starting model scaled to $\delta \ln v_s$ by factor 0.3, b) starting model scaled to $\delta \ln v_s$ by factor -0.3, c) resulting v_ϕ model for correlated starting model, d) resulting v_ϕ model for anti-correlated starting model. The resulting v_ϕ models can be compared to e) the observed v_ϕ started from PREM.

started from positive correlation does a better job at matching the model started from PREM at all depths, but the model started from anti-correlation has a harder time moving away from its starting point in the lowermost mantle and primarily in the uppermost mantle. This is reflected in their RMS amplitudes being lower than for models started from PREM and positive correlation (Fig. 4.20a), and by the low correlation coefficients between these models started from anti-correlation and from PREM (Fig. 4.20c). In terms of spectral misfit, all one-step models end up with the same misfit (0.51) and all the two-step models as well (0.53), implying that the differences in the upper mantle and lowermost mantle do not significantly affect the spectra. So again, we see that v_ϕ in the upper mantle and lowermost mantle is the least well-constrained by normal mode data, and thereby might constitute the model null space.

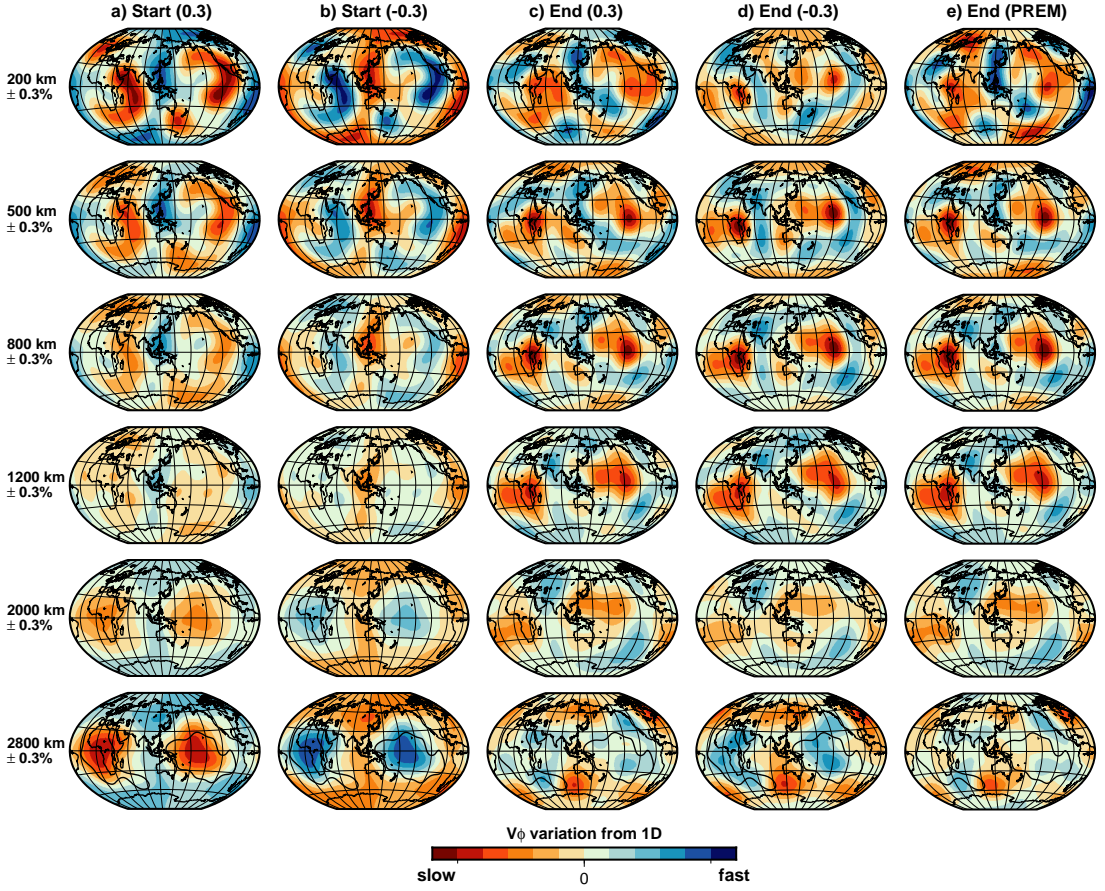


Figure 4.22: Bulk sound velocity models for different starting models in the two-step inversion. a) Starting model scaled to $\delta \ln v_s$ by factor 0.3, b) starting model scaled to $\delta \ln v_s$ by factor -0.3, c) resulting v_ϕ model for correlated starting model, d) resulting v_ϕ model for anti-correlated starting model. The resulting v_ϕ models can be compared to e) the observed v_ϕ started from PREM.

4.4.4. Extracting bulk sound from S-wave and P-wave velocity

Instead of inverting for v_s and v_ϕ heterogeneity directly, some previous studies have extracted v_ϕ from inversions for v_s and v_p heterogeneity. Hence we also tried to construct models of bulk sound velocity from our shear- and compressional wave velocity models, using eq. 4.1. We use the $\delta \ln v_s$ and $\delta \ln v_p$ models obtained previously in this chapter for the one- and two-step inversions to create bulk sound models and compare them to bulk sound extracted from model SP12RTS (Koelemeijer et al., 2016). We should be careful in interpreting any small-scale anomalies that are artefacts of subtracting two distinct 3D fields, i.e. $\delta \ln v_s$ and $\delta \ln v_p$, so instead of interpreting models including all degrees up to 12 (Fig. B3), we henceforth ignore all degrees higher than 6 (Fig. 4.23).

The extracted bulk sound velocity models look very similar for the one- and two-

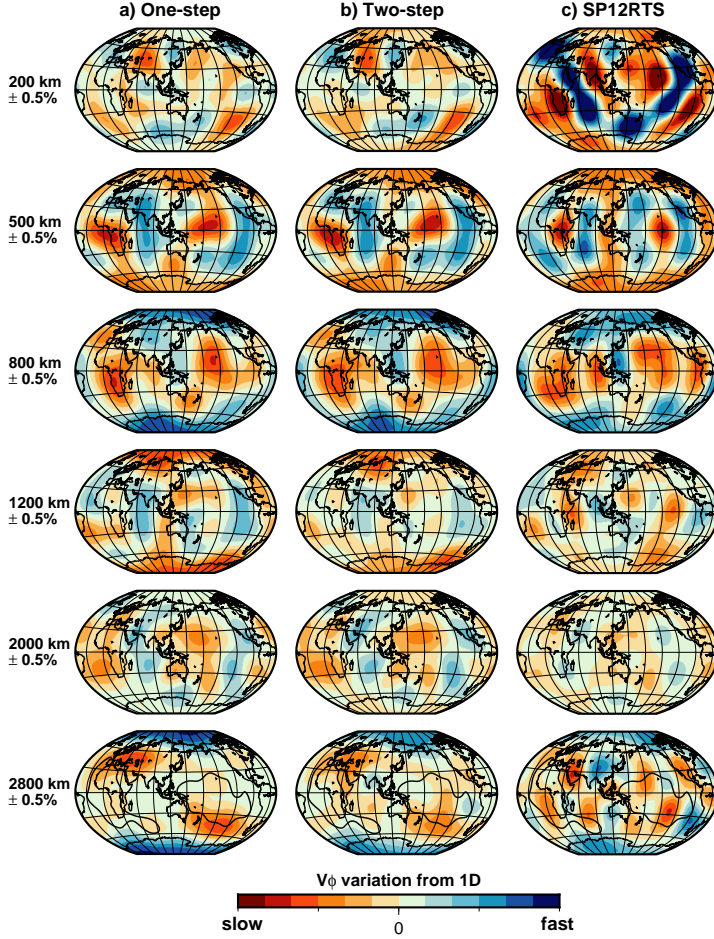


Figure 4.23: Models of $\delta \ln v_\phi$ obtained from $\delta \ln v_s$ and $\delta \ln v_p$ models using eq. 4.1 for a) the one-step inversion, b) two-step inversion, c) even degrees of SP12RTS (Koelemeijer et al., 2016), all cut off at maximum degree 6.

step $v_s + v_p$ inversions (Fig. 4.23a,b), but do not agree well with 3D bulk sound velocity extracted from SP12RTS, especially in the uppermost and lowermost depth slice (Fig. 4.23c). The S- Φ correlations extracted from the joint $v_s + v_p$ inversions (Fig. 4.24b) behave markedly different to those determined from the joint $v_s + v_\phi$ inversions (Fig. 4.24a). The S- Φ correlation for which $\delta \ln v_\phi$ was extracted from $\delta \ln v_s$ and $\delta \ln v_p$ now shows clear anti-correlation in the lower mantle and upper mantle, and in the one-step case also in the mid-mantle, agreeing more with the general trend in the correlation derived from SP12RTS (Fig. 4.24b). To see how much of the differences between these two ways of computing correlation can be explained by the extraction of v_ϕ anomalies and how much comes from the more detailed parameterization, we show the S- Φ correlation for $\delta \ln v_\phi$ extracted from a

joint $v_s + v_p$ 7 B-splines inversion (Fig. 4.24c). In this case the S- Φ correlation is oscillating around zero for both the one-step and two-step profiles, similar to the 21-splines case, but with less extreme maxima and minima, especially for the one-step correlation function. The more oscillatory nature of the 21-splines case can therefore be attributed to the more detailed radial parameterization of 21 splines, instead to the use of 7 B-splines. Thus, the shift in general trend towards more negative values with respect to the correlations directly inferred from $v_s + v_\phi$ inversions may be explained by the different way of obtaining the correlation.

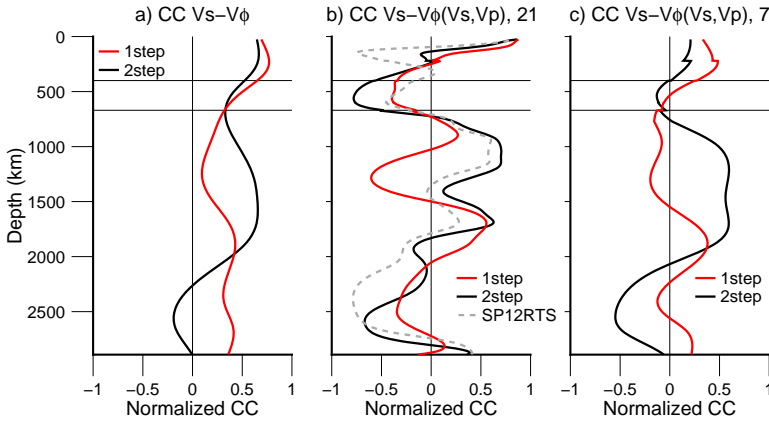


Figure 4.24: a) S- Φ correlations for the one-step (red) and two-step (black) models from the joint $v_s + v_\phi$ inversions; b) S- Φ correlations for observed v_s from the joint $v_s + v_p$ 21 splines inversion and v_ϕ extracted from these v_s and v_p models, for the one-step (red) and two-step (black) inversions, compared the S- Φ correlation extracted from the even degrees of SP12RTS, all cut off at maximum degree 6; c) same as b) but for a joint $v_s + v_p$ inversion for 7 B-splines.

4.5. Discussion

4.5.1. $R_{S/P}$ as indicator of chemical heterogeneity

Cross-sections through our one-step and two-step v_s and v_p models show that low velocity anomalies are horizontally deflected at several depths in the mid-mantle, such as around 670 and 1000 kilometres depth. If LLSVPs are structures from which mantle plumes originate, plumes appear to be ponding at various depths in the mid-mantle. We lack resolution to image separate mantle plumes, so they would appear more smeared here. In a high resolution tomographic model, French & Romanowicz (2015) did seem to image individual mantle plume conduits, which were also horizontally deflected, interpreted as ponding due to viscosity contrasts, inferred by geoid analysis (Rudolph et al., 2015).

We have seen that both the choices in inversion method and in representation of $R_{S/P}$ could result in different thermochemical or mineralogical interpretations. Based on R-RMS, we confirm high $R_{S/P}$ values in the lower mantle (~ 2600 km) exceeding the purely thermal mineral physics prediction, found by many others,

although we find less extreme values than for example SP12RTS. The main difference between the two inversion methods is the 1100-1400 km depth range, where S-P correlation drops in the one-step inversion, but not in the two-step inversion. This drop is associated with low degree-2 spectral power in v_p , high R-RMS and low R-median in the one-step model.

If we would base our interpretations on the 1D R-median only, chemical heterogeneity would not be required in the lower mantle, as we do not exceed or barely exceed the mineral physics prediction for a thermally dominated mantle. When inferring the state of the lower mantle from R-RMS only, we conclude that there could be a degree of chemical heterogeneity, but less than predicted by Koelemeijer et al. (2016), with the exception of 1100-1400 km for the one-step inversion. However, when looking at the distributions of $R_{S/P}$ and the velocities, we arrive at different interpretations.

By using a 1D representative of 3D $R_{S/P}$, we lose information on its spatial distribution. However, when we want to compare our observations to mineral physics predictions, such as the 1D curve by Karato & Karki (2001), we need to use a 1D $R_{S/P}$. In that case, R-median is a better 1D representation of the full range of $R_{S/P}$ values at a certain depth, since negative ratios are also included. The question remains which method is best to compare 1D $R_{S/P}$ from mineral physics predictions to 1D $R_{S/P}$ extracted from seismic tomographic models?

The approach of using a 1D representative of $R_{S/P}$, as most studies have done before, gives at best a qualitative indication of the presence of chemical heterogeneity. 3D distributions of $R_{S/P}$ lead to non-unique interpretations for the source of the heterogeneity, as any linear combination of sources could fit the observed distributions (Deschamps & Trampert, 2003). So for quantitative constraints, we need to look at histograms of $R_{S/P}$ and S- and P-wave velocities in conjunction (Deschamps & Trampert, 2003; Cobden et al., 2012). This statement has been debated by Tesoniero et al. (2016), who claim that even if we look at the 3D distributions of $R_{S/P}$, $\delta \ln v_s$ and $\delta \ln v_p$, the width of histograms and the high values of 1D $R_{S/P}$ in the lower mantle can be replicated in synthetic tests with random noise. They warn against overinterpretation of seismic S- and P-wave velocity models, since model features that are not strictly required by the data should not be interpreted.

Studies by Tesoniero et al. (2016) and Koelemeijer et al. (2018) argue that observations of $R_{S/P}$ based on body-wave ray theory (e.g. Su & Dziewonski, 1997; Della Mora et al., 2011) cannot be used to distinguish between thermal and chemical variations, due to finite-frequency effects. Other studies attribute the high $R_{S/P}$ to wavefront healing in traveling waves, instead of compositional heterogeneity (e.g. Davies et al., 2012). Body waves suffer the most from these effects. Surface waves are affected less, and we do not have to worry about these effects in this normal mode study.

4.5.2. (Anti-)correlation between v_s and v_ϕ anomalies

According to our synthetic inversions and starting model tests, we cannot confidently constrain upper mantle bulk sound velocity with our current normal mode data set in both the one-step and two-step inversions. The lowermost mantle is also

plagued by starting model dependency and high-amplitude ghost patterns, but less severely in the one-step inversion. The one-step inversion provides novel constraints on bulk sound velocity anomalies and their (anti-)correlation with shear wave velocity anomalies, since these parameters have never been studied before using this inversion technique. Interestingly, we do not observe a clear anti-correlation in the lower mantle, especially in the one-step inversion where the correlation is positive in the entire mantle. This observation may be related to the relatively low R-RMS values, for the one-step $v_s + v_p$ inversion especially, compared to e.g. SP12RTS, not requiring a $S\text{-}\Phi$ anti-correlation.

As bulk sound velocities appear to be smaller in amplitude than the other velocities in the mantle (e.g. Kennett et al., 1998), determining correlations becomes tricky, possibly contributing to the large range of $S\text{-}\Phi$ correlations from previous studies (Fig. 4.2). Furthermore, we show that $S\text{-}\Phi$ correlations depend first and foremost on the way of computing the correlation, either i) through a direct inversion for v_s and v_ϕ heterogeneity, or ii) by extracting v_ϕ from an inversion for v_s and v_p heterogeneity, using the relation of eq. 4.1. The latter results here in more negative correlation values overall. This observation alone cannot explain the large spread in $S\text{-}\Phi$ correlations from previous studies (Fig. 4.2), as there is no clear distinction between correlations based on a joint $v_s + v_\phi$ inversion and those based on a joint $v_s + v_p$ inversion. Secondly, the radial parameterization may have a large impact on the amplitudes of extrema in cross-correlation profiles, affecting the thermochemical interpretations attached to it.

We find more positive $S\text{-}\Phi$ correlations and less extreme R-RMS values than SP12RTS (Koelemeijer et al., 2016). These characteristics of SP12RTS were interpreted in a follow-up geodynamics study to indicate the wide-spread presence of post-perovskite in the lowermost mantle, even within the LLSVPs (Koelemeijer et al., 2018). Our observations do not require such an abundance of post-perovskite to explain them, but we cannot entirely rule out the presence of post-perovskite in the lowermost mantle either.

4.6. Conclusion

We confirm what previous studies inferred on the thermochemical state of the lower mantle, solely based on R-RMS values that exceed mineral physics predictions for a thermally dominated lower mantle, except for a decrease towards the CMB. We observe lower R-RMS values than for example SP12RTS, which coincides with slightly positive (one-step) or slightly negative (two-step) $S\text{-}\Phi$ correlation. Based on the spread of v_s , v_p and $R_{S/P}$ and on the 1D R-RMS, we arrive at the conclusion that our results cannot be explained by purely thermal variations only, and that the role of post-perovskite is not dominant. However, when looking at the 1D R-median only, we could also say that we do not require chemical heterogeneity, since R-median barely exceeds the mineral physics prediction for a thermally dominated mantle, except maybe around 2600 km. The 1D representation of the ratio between v_s and v_p has been criticized in the past (Deschamps & Trampert, 2003; Tesoniero et al., 2016; Koelemeijer et al., 2018), so we focus on the distributions of v_s and v_p anomalies and $R_{S/P}$.

Both the one-step and two-step models show a large spread in v_s anomalies in the lower mantle, coinciding with the depth range of high R-RMS values. The wide spread of $R_{S/P}$ and a de-correlation between v_s and v_p structure in the depth range 1100-1400 km in the one-step models are also a sign of the presence of chemical heterogeneity, whereas we infer chemical heterogeneity around 200-670 km depth in the two-step inversion, based on the wide spread of v_s anomalies and $R_{S/P}$. We therefore arrive at different thermochemical interpretations between the one- and two-step inversions for 200-670 km and 1100-1400 km based on these distributions and correlation between $\delta \ln v_s$ and $\delta \ln v_p$, so the inversion method matters for the interpretation. The inversion method matters more than for a v_s -only inversion performed in the previous chapter, but the one-step models still fit the spectra better than the two-step models.

Patterns in 3D v_ϕ agree well between the one- and two-step $v_s + v_\phi$ inversions throughout most of the mantle, showing regions of low bulk sound velocity underneath the Pacific Ocean and Africa. The upper mantle and lowermost mantle v_ϕ structure suffers from starting model dependency and large ghost patterns highly correlated with v_s structure in $v_s + v_\phi$ inversions. The one-step inversion is less affected and more robust, but we still cannot draw any definitive conclusions on the sign of the S- Φ correlations in these depth ranges. We do not find anti-correlation in the rest of the mantle for $v_s + v_\phi$ inversions, except slightly negative correlations for the two-step models around 2500 km. The correlation shifts towards more negative values when $\delta \ln v_\phi$ is extracted from $\delta \ln v_s$ and $\delta \ln v_p$, and the extrema become more pronounced when the radial parameterization becomes more detailed, i.e. 7 B-splines to 21 splines.

We have seen that the robustness of using $R_{S/P}$ and S- Φ correlation for qualitative estimates of chemical heterogeneity has been debated. We will therefore direct our modelling efforts towards density variations (e.g. Deschamps & Trampert, 2003) in Chapter 5.

B1. Appendix B

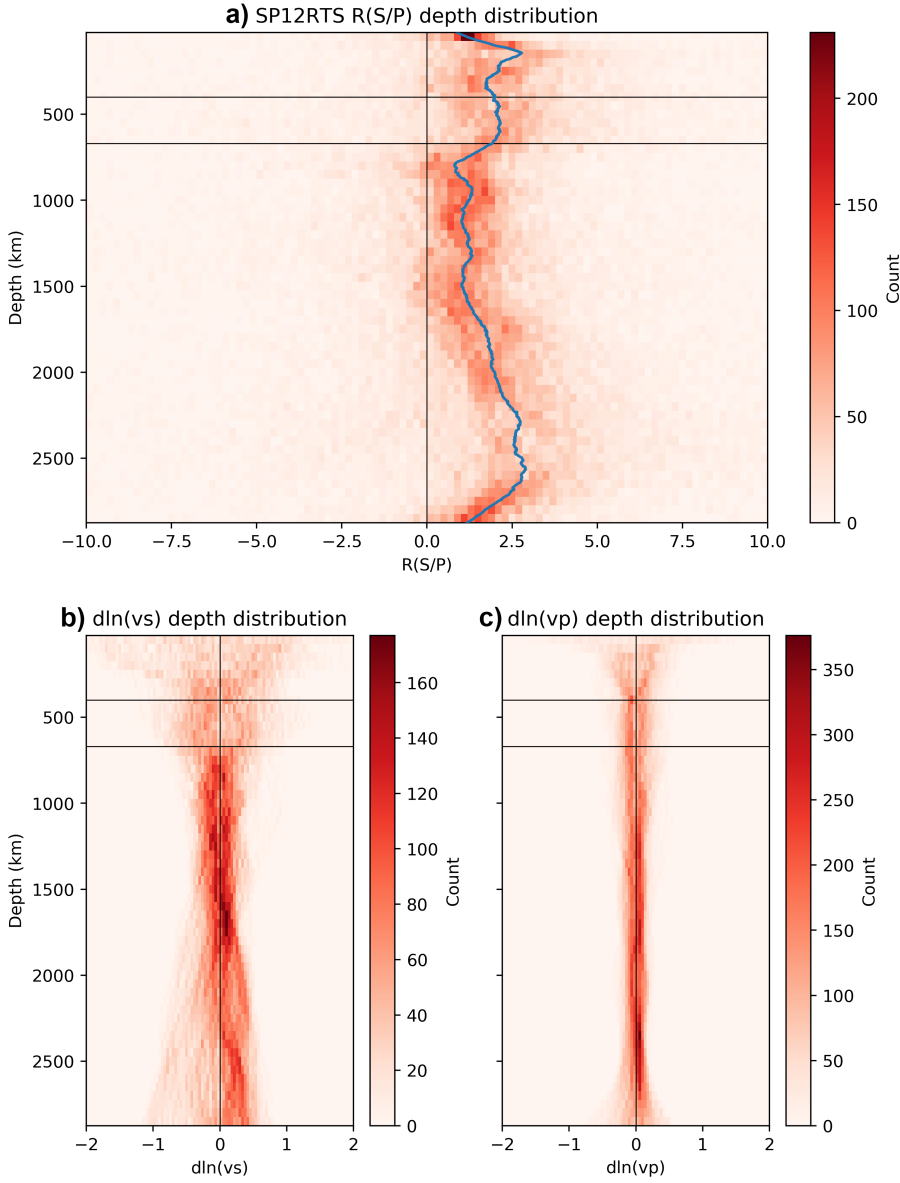


Figure B1: Distribution of $R_{S/P}$ versus depth, obtained by point-by-point division of SP12RTS' $\delta \ln v_s$ by $\delta \ln v_p$ on a $5 \times 5^\circ$ grid at 57 depths in the mantle. The median with threshold 0.01 is represented by the blue curve. Distributions of b) $\delta \ln v_s$ and c) $\delta \ln v_p$.

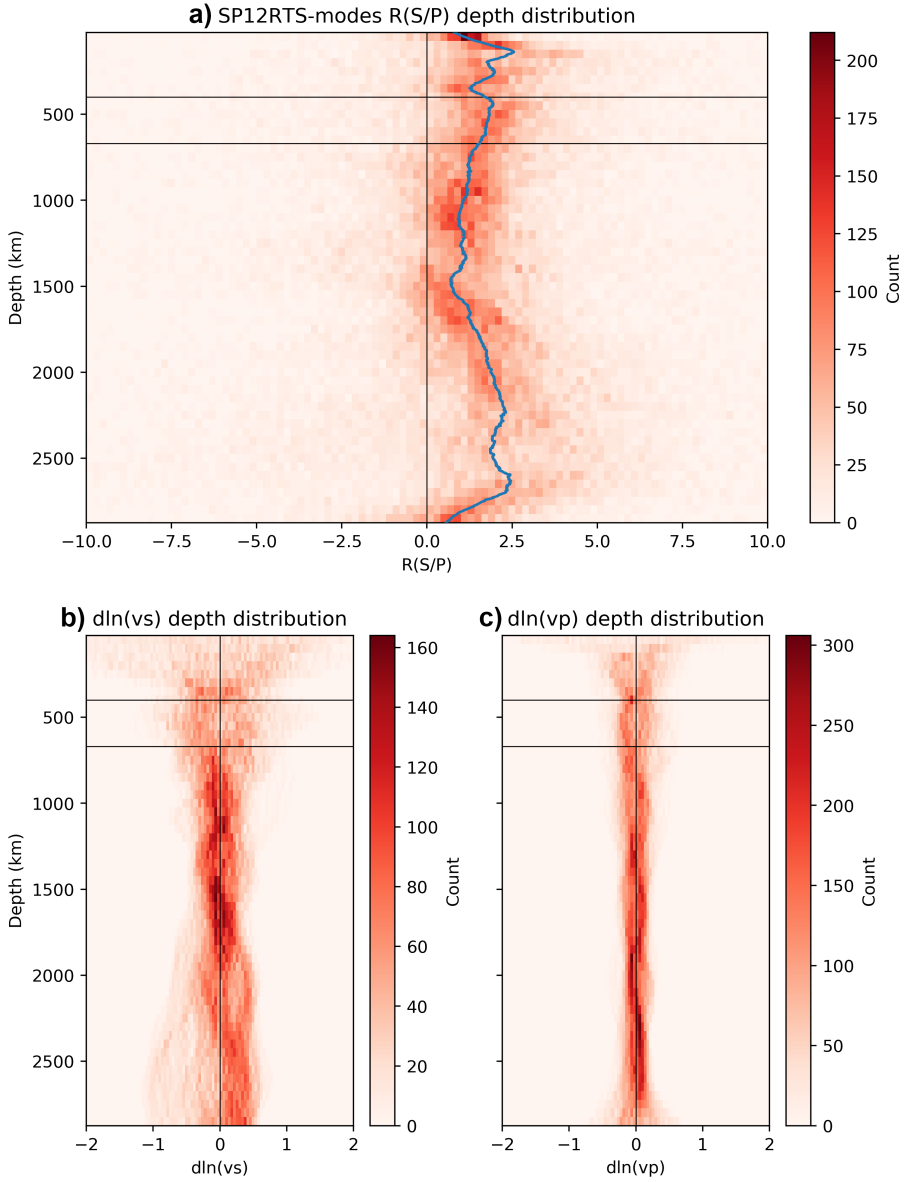


Figure B2: Distribution of $R_{S/P}$ versus depth, obtained by point-by-point division of SP12RTS-modes' $\delta\ln v_s$ by $\delta\ln v_p$ on a $5 \times 5^\circ$ grid at 57 depths in the mantle. The median with threshold 0.01 is represented by the blue curve. Distributions of b) $\delta\ln v_s$ and c) $\delta\ln v_p$.

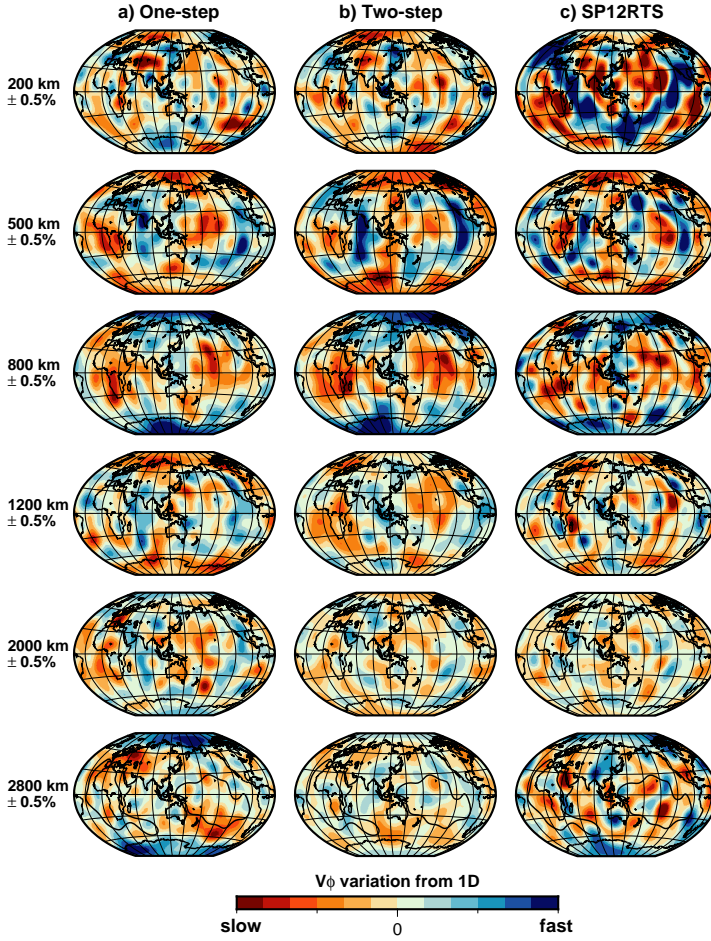


Figure B3: Models of $\delta \ln v_\phi$ obtained from $\delta \ln v_s$ and $\delta \ln v_p$ models using eq. 4.1 for a) the one-step inversion, b) two-step inversion, c) even degrees of SP12RTS (Koelemeijer et al., 2016).

5

New normal mode observations of 3D lower mantle density

Density differences drive mantle convection. Thus, knowledge of 3D variations in density is crucial in distinguishing between a thermal or thermochemical nature of the lower mantle LLSVPs, as this parameter differentiates between buoyant thermal structures and dense stable thermochemical piles. However, there are contradicting direct and indirect observations of lower mantle density variations, with some studies suggesting light LLSVPs and others finding them to be dense. We study mantle density using normal modes, the only seismic data sensitive to lower mantle density, performing both the one-step direct spectrum inversion and two-step splitting function inversion. We invert for 3D v_s , v_p , ρ and topography on the 400- 670- and CMB-discontinuities jointly. The LLSVPs appear as light structures, with a partly dense base, which is more pronounced in the one-step inversion. This observation may reconcile seemingly conflicting past observations. By performing synthetic tests, we show that density does not suffer from velocity structure contamination to the same extent as in Kuo & Romanowicz (2002), and is thus robust. The presence of excess density at the base of LLSVPs depends on the choice of starting model for the two-step inversion, whereas it only affects the extent of this sliver in the one-step inversion. Regions where the 400-discontinuity is shallow match well with dense structures, and vice versa, which is expected for the olivine to wadsleyite phase transition occurring there. The 670-discontinuity topography does not match as well to the density structure, indicating its complex nature. Light parts of the LLSVPs cover shallow parts of the CMB and vice versa, which appears to be due to isostatic compensation.

5.1. Introduction

Whereas tomographic models of lower mantle S-wave velocity structures, and to a lesser extent of P-wave velocity structures, are relatively similar (Cottaar & Lekic, 2016; Shephard et al., 2017), the lower mantle density distribution has been a topic of debate for decades. Density contrasts create positive buoyancy for light structures that evolve into upwellings and negative buoyancy for dense structures, making them sink into the mantle. In other words, density drives viscous mantle flow. The density field, combined with a viscosity profile, therefore needs to be known in order for geodynamicists to make mantle flow calculations. This dependence of mantle flow on density makes density a very important link between seismology and geodynamics.

Density heterogeneity plays an especially important role in determining the nature of Large Low Shear-wave Velocity Provinces (LLSVPs) in the lower mantle. If their density is predominantly low, they will be thermal structures, because density is correlated to velocity in a purely thermal mantle. However, if their density is predominantly high, thereby not correlated or even anti-correlated to velocity, they must be thermochemical structures that have remained stable throughout most of the Earth's history and possibly contain primordial material.

Tomographic models of density have mostly been constructed using normal modes, since body waves do not carry direct information on density, and surface waves are only sensitive to the top couple of hundred kilometres of the mantle. Therefore, normal modes are the only seismic data sensitive to the lower mantle density distribution, because of the important role of the gravitational restoring force for these long-period waves.

Gravity data has also been used in measuring density, often in combination with seismic data (e.g. Ishii & Tromp, 1999, 2001) and other geodynamic constraints (e.g. Forte & Mitrovica, 2001; Simmons et al., 2010; Lu et al., 2020), such as plate motions and (dynamic) topography. Studies that invert seismic and geodynamic data in a joint manner, need a viscosity profile and have employed a scaled relation between v_s and density to linearize the inversion. In this way, 3D density is assumed to be scaled to 3D v_s with a depth-dependent (e.g. Forte & Mitrovica, 2001) or constant scaling factor (Hager et al., 1985), and geodynamic constraints can be successfully explained by a thermally dominated mantle and light LLSVPs. On the other hand, studies that did not have these prior assumptions, or expanded upon the purely thermal case by allowing the v_s - ρ scaling to vary laterally, infer the presence of significant chemical heterogeneity in the lower mantle (e.g. Simmons et al., 2010; Mosca et al., 2012; Lu et al., 2020). A complicating factor when fitting geodynamic data is the need for a radial viscosity model, which is not well-constrained at all (e.g. Rudolph et al., 2020). A viscosity profile can be chosen in such a way that it would fit the geodynamic data for a given velocity and density model.

Most lower mantle density models that were derived from seismic data agree with (partly) dense LLSVPs (Fig. 5.1). By performing a two-step splitting function inversion using the then available normal mode data set of 58 spheroidal and 31 toroidal modes (including some cross-coupled modes), and the free-air gravity anomaly, Ishii & Tromp (1999) determined the LLSVPs to be denser than average (Fig. 5.1a). Their density starting model was correlated to a S-wave velocity model, with factor

0.2, and Ishii & Tromp (1999) claim that their inversion is only weakly dependent on the density starting model. A probabilistic normal mode approach by Mosca et al. (2012) found partly light, partly dense LLSVPs (Fig. 5.1b), possibly due to chemical variations in iron content. Resovsky & Trampert (2003) and Trampert et al. (2004) also inferred chemically distinct dense LLSVPs, in earlier probabilistic tomographic studies using normal mode data. In the seismic tomographic model of Moulik & Ekström (2016), in which surface waves, body waves and normal modes are inverted for v_s , v_p and ρ , we once again encounter denser-than-average anomalies, partially coinciding with the LLSVPs (Fig. 5.1c).

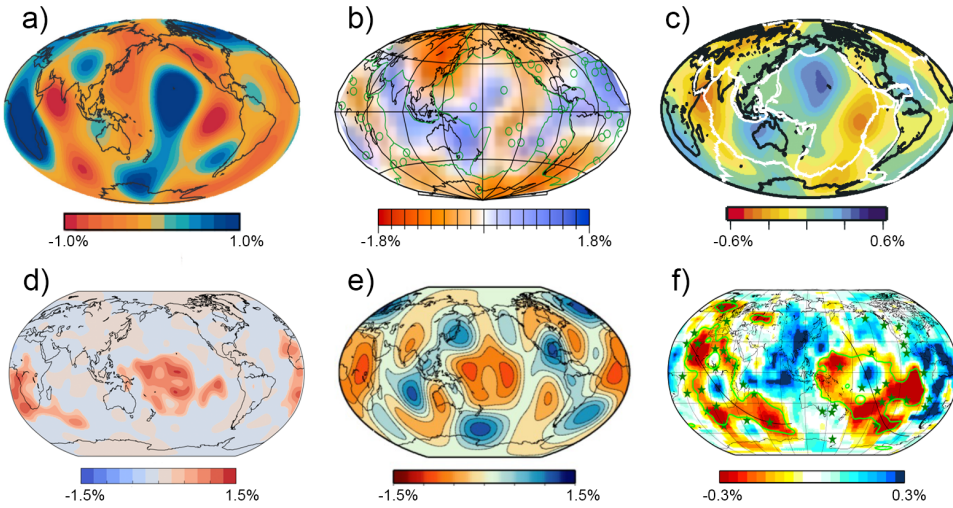


Figure 5.1: Density models by a) Ishii & Tromp (1999) at 2850 km depth, b) Mosca et al. (2012) at 2891 km depth, c) Moulik & Ekström (2016) at 2800 km depth, d) Lau et al. (2017) in a layer from 2541 to 2891 km depth, e) Koelemeijer et al. (2017) in the lowermost mantle, and f) Lu et al. (2020), representing the average density for five different viscosity models in a layer from 2650 to 2891 km depth. Note the flipped colourscale in d) where red means excess density, instead of blue.

More recently, two seemingly contradicting observations of LLSVP density were published in the same year. Lau et al. (2017) demonstrated in a probabilistic study that the Earth's tides prefer the lowermost two-thirds of the LLSVPs to be denser than average (Fig. 5.1d), although the excess density could also be concentrated in the very base of the LLSVPs. On the other hand, a model space search by Koelemeijer et al. (2017) showed that core-mantle boundary (CMB) Stoneley modes prefer overall lighter LLSVPs (Fig. 5.1e), although, again, a dense 100 km basal layer could not be ruled out. A dense basal layer in the center of both LLSVPs was subsequently found by Lu et al. (2020) (Fig. 5.1f), who performed a joint inversion of seismic shear-wave velocity measurements and geodynamic data (free-air gravity anomaly, plate motions, dynamic surface topography and excess CMB ellipticity). This dense base was interpreted to be of non-thermal origin. A first glimpse of a dense basal part of the African LLSVP had been observed earlier by Simmons et al. (2009) (by only including seismic constraints) and Simmons et al. (2010), following

a very similar inversion procedure.

Most studies discussed above have used normal modes to image density. The resolvability of density by normal modes has been questioned by a number of studies. Resovsky & Ritzwoller (1999b) claimed that density was not robust with respect to prior constraints and damping, noting that density models which de-correlate from v_s at different depths fit the splitting functions of Resovsky & Ritzwoller (1998) equally well. In test inversions using degree 2 splitting function coefficients, Romanowicz (2001) showed that the correlation between density and S-wave velocity anomalies was poorly constrained by the data. Kuo & Romanowicz (2002) found significant leakage of v_s and v_p structures into density by looking at the resolution matrix of a synthetic one-step inversion for these three parameters in the mantle. They also performed a direct spectrum (i.e. one-step) inversion of synthetic data with non-zero 3D v_s and v_p variations and zero 3D density variations. The output density model would ideally not have 3D density variations, but unfortunately it did. For one of the synthetic inversions they even found an output density model that resembled the one from Ishii & Tromp (1999). A few years later Ishii & Tromp (2004) performed a synthetic two-step splitting function inversion with a five times larger data set, and found the opposite, with almost no contamination of velocity into density. We currently have even more normal mode data, and we will perform a similar synthetic test as Kuo & Romanowicz (2002) to see who we agree with.

Having more data does not solve the potential problem of the density signal possibly being of similar magnitude as commonly made mode coupling approximations in computing synthetic spectra, and as errors in splitting functions (Akbarashrafi et al., 2018). However, Moulik & Ekström (2016) note that their density model (with partially dense LLSVPs; Fig. 5.1c) significantly improved the fit of mode ${}_0S_2$ in particular, a low-frequency mode which is less affected by coupling approximations. Furthermore, our aim is to actually not use splitting functions, but instead direct spectrum inversion, where cross-coupling is more easily included.

Taking the topography of Earth's internal boundaries into account becomes important when inverting for density heterogeneity. Lowermost mantle density trades off with CMB topography in normal mode studies (e.g. Romanowicz, 2001; Koelemeijer et al., 2017), hence it is not surprising that there is quite some disagreement between global CMB topography models (Fig. 5.2), ranging from elevated topography to partly elevated to depressed topography below the LLSVPs. It is beyond the scope of this thesis to obtain robust discontinuity topography models, but we are hoping to minimize the density-topography trade-off by including many different normal modes with many different sensitivities. In addition to CMB topography, we will also invert for mantle transition zone (MTZ) discontinuity topography at 400 and 670 km depth. The 400-discontinuity is characterized by the phase transition from olivine to wadsleyite, which has a positive Clapeyron slope. At the 670-discontinuity ringwoodite breaks down to form perovskite and magnesio-wüstite, which has a negative Clapeyron slope (e.g. Ringwood, 1991). This simplified view would mean that the MTZ is expected to be thin in warm regions and thick in cold regions. In reality, the nature of the '670' is more complex due to additional phase transitions in garnet and pyroxene, which may have the opposite effect on its

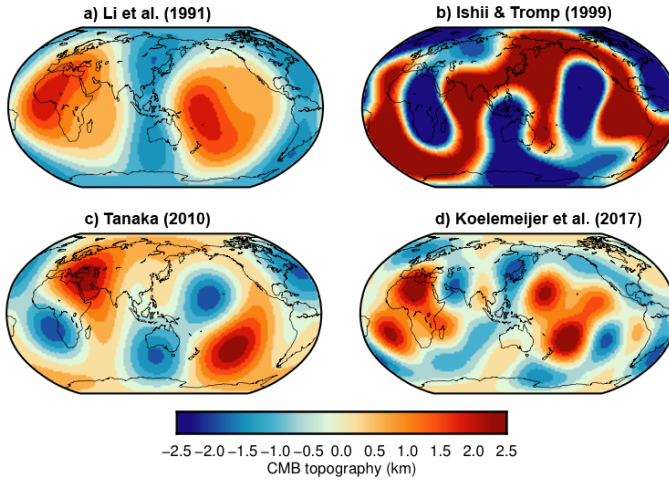


Figure 5.2: CMB topography models from three normal mode studies (a,b,d) and one body wave study (c). Negative values represent depressed areas, and positive values elevated areas. Figure adapted from Koelemeijer (2021).

5

topography (Hirose, 2002).

In this chapter, we will invert normal mode spectra for 3D v_s , v_p , ρ and topography on the 400-, 670- and CMB-discontinuities using an extensive normal mode data set. We will use both the one-step direct spectrum and two-step splitting function inversion schemes (see Chapter 3) and see whether using the one-step method improves the robustness and resolvability of 3D variations in upper and lower mantle density.

5.2. Data and methods

Following the procedure in previous chapters, we invert the normal mode spectra for a 3D mantle tomography model in two ways: i) in a one-step direct spectrum inversion, and ii) in a two-step splitting function inversion. Details on these two methods are outlined in Chapter 3, so we will not discuss them any further here. We use the same normal mode spectra as starting point of both our inversions. In addition to, or sometimes in replacement of, the spectral segments of Deuss et al. (2013), we once again use the segments of Koelemeijer et al. (2013) and Koelemeijer (2014). We incorporate the same nine core-mantle boundary Stoneley modes (${}_1S_{11-14}$, ${}_2S_{15-17,25}$, ${}_3S_{26}$) as the model space search by Koelemeijer et al. (2017) that found preferably lighter LLSVPs. All segments consist of vertical component data for 93 large events ($M_w \geq 7.4$) since 1976. For the two-step approach we use the spheroidal mode splitting functions obtained by the same three studies, and only execute the second inversion step in this paper. We exclude spheroidal modes that are sensitive to the inner core or couple strongly to an inner core mode, since our focus is on the mantle. However, taking inner core modes into account and

inverting for inner core anisotropy and density simultaneously could affect lower mantle density amplitudes (Ishii & Tromp, 2004). The total number of spectral segments is 118,034, for 88 modes and mode groups in the one-step inversion and 125 self-coupled and 10 cross-coupled splitting functions for the two-step inversion.

We invert for 3D v_s , v_p , ρ , and topography on the 400-, 670- and CMB discontinuities simultaneously. In addition to inverting real data, we also perform a synthetic test similar to Kuo & Romanowicz (2002), to assess the leakage of v_s and v_p structure into density. We created synthetic spectra (for the one-step inversion) and synthetic splitting functions (for the two-step inversion) using 3D v_s , v_p and discontinuity topography models that resulted from the real data inversions. The input density is the 1D PREM model (Dziewonski & Anderson, 1981), so not including any 3D variations. We then invert the synthetic data in the same way as with real data, and try to recover the input models. Ideally, the recovered density model should not have any 3D anomalies, but as Kuo & Romanowicz (2002) observed, this output density will probably have a non-zero ‘ghost’ pattern. If the ghost pattern resembles the pattern and strength of density anomalies found in a real data inversion, we need to be very cautious when interpreting those structures. We will also explore the influence of a density starting model correlated or anti-correlated to v_s structure, with uniform scaling factors 0.3 and -0.3 respectively. In the ideal case, the resulting density models will move towards the density model started from PREM.

The models are parameterized up to spherical harmonic degree 6, only even degrees, laterally, and 7 B-splines radially. We have tried to build density models using 21 splines as in Chapters 3 and 4, but those inversions did not give robust results. The size and polarity of the ghost patterns was comparable to density measured from real data, which had light LLSVPs, contrary to Kuo & Romanowicz (2002). Furthermore, starting the real data inversions from density anti-correlated or correlated to v_s did not move the density model towards density from the PREM inversion. These inversions were probably radially overparameterized, so instead of 21 splines, we choose 7 B-splines.

5.3. Results

We invert normal mode data jointly for an S-wave velocity, P-wave velocity and density mantle model, including discontinuity topography, using the one-step direct spectrum inversion and the two-step splitting function inversion. We will compare the resulting models, misfits and other characteristics in detail below. To compare the results from the one-step inversion (Fig. 5.3) to results from the two-step inversion (Fig. 5.4), we compare models with the same number of effective eigenvalues. The one-step model has a 1.26 times larger model size than the two-step model for the same number of effective eigenvalues, which is mainly attributed to the larger one-step density model.

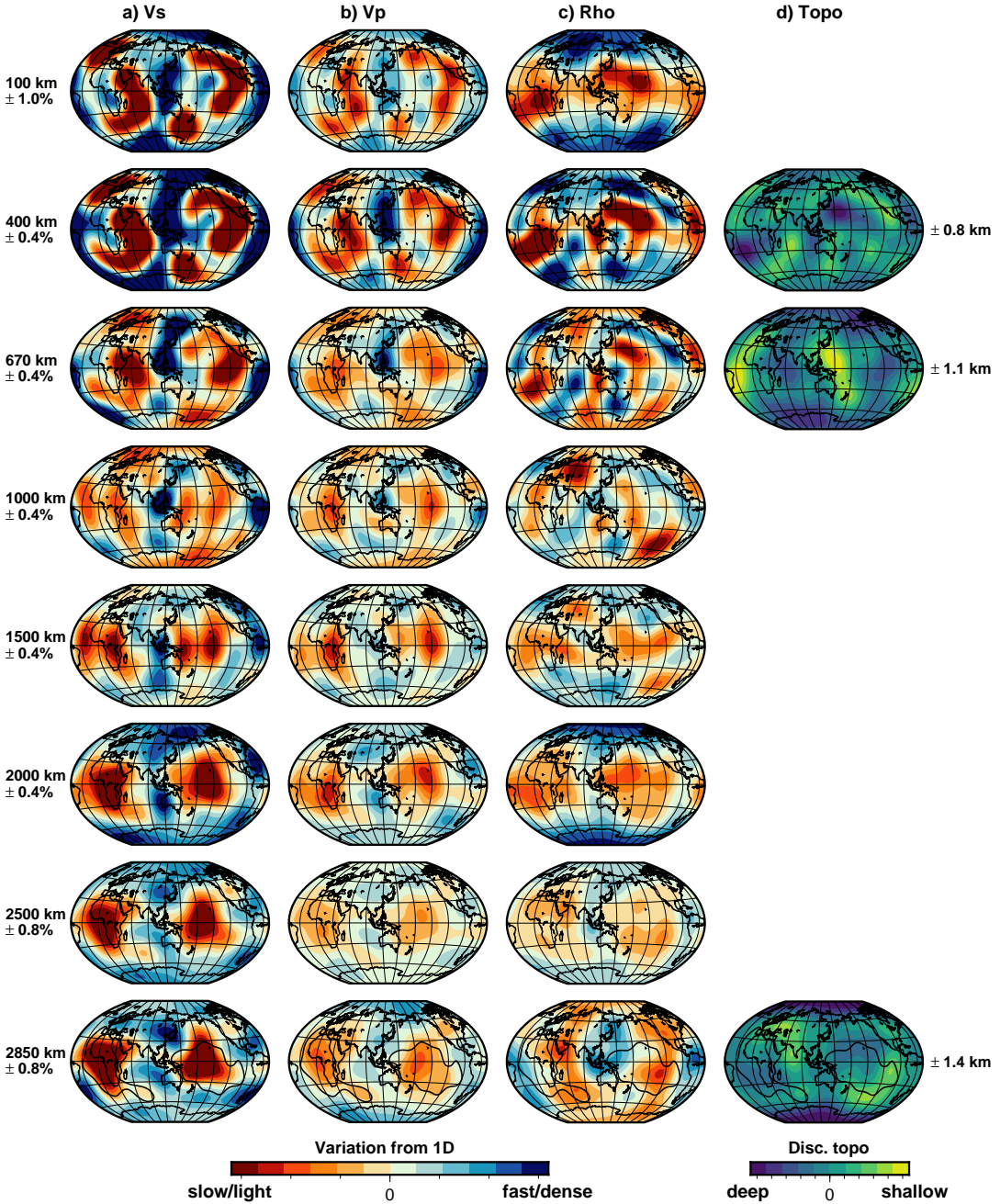


Figure 5.3: Depth slices through one-step models of anomalies in a) shear-wave velocity v_s , b) compressional-wave velocity v_p , and c) density ρ , with d) discontinuity topography for the 400, 670 and CMB.

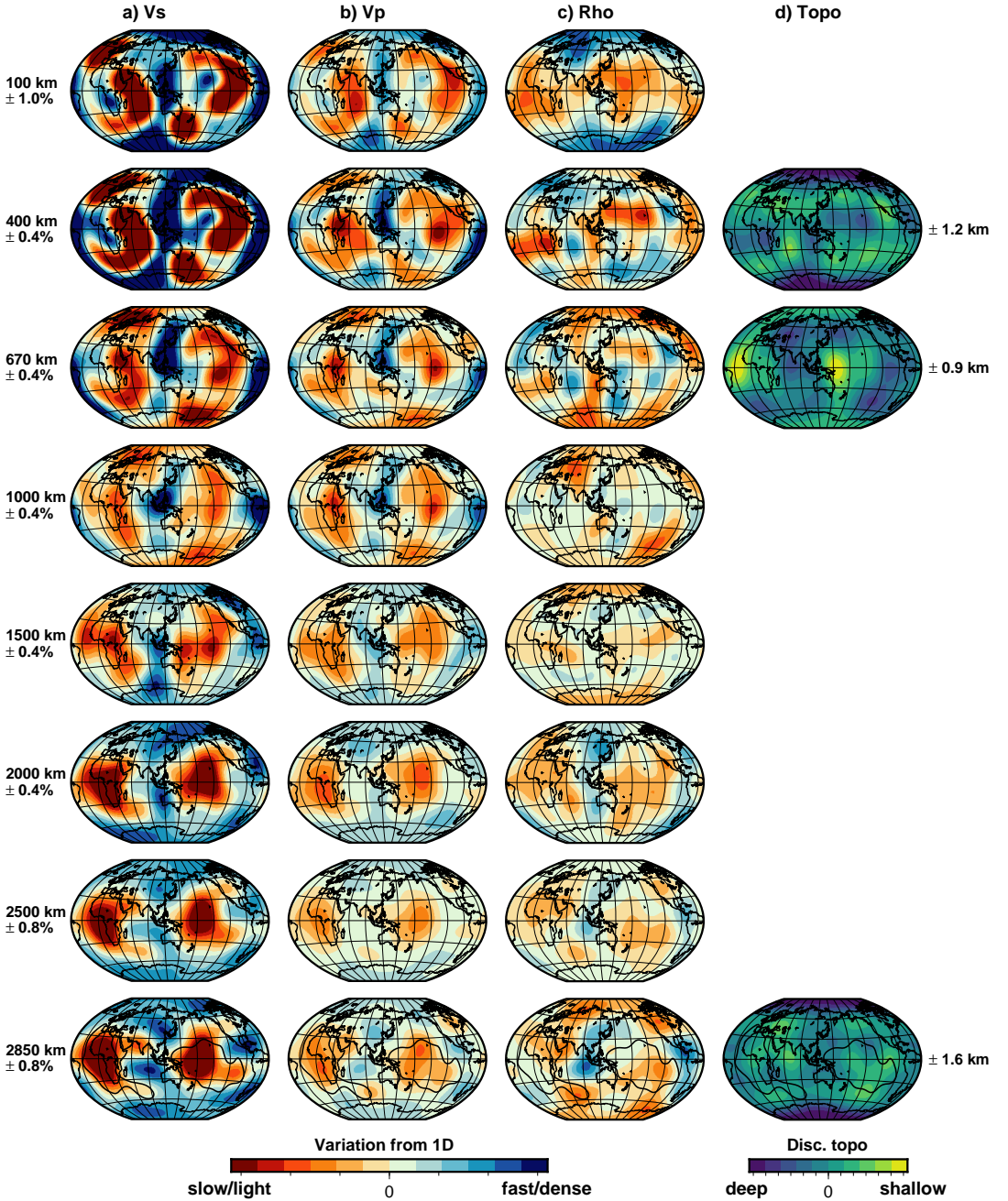


Figure 5.4: Depth slices through two-step models of anomalies in a) shear-wave velocity v_s , b) compressional-wave velocity v_p , and c) density ρ , with d) discontinuity topography for the 400, 670 and CMB.

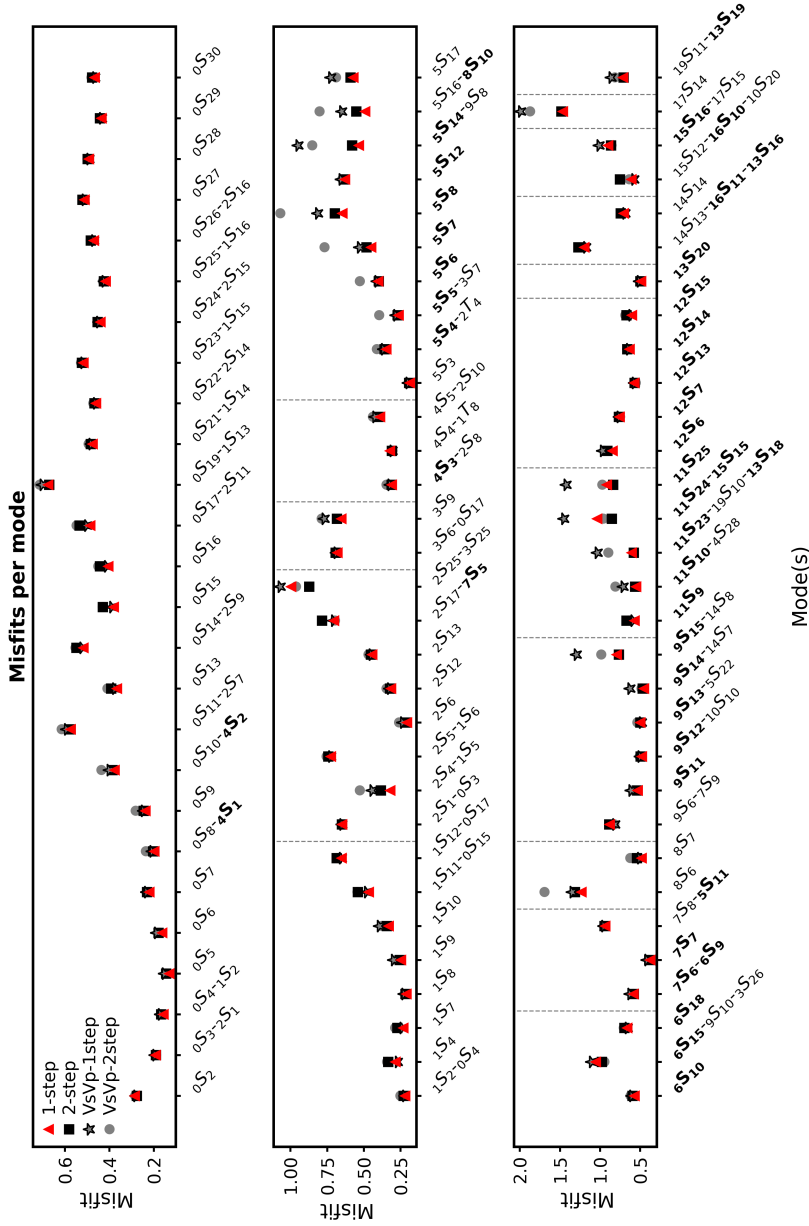


Figure 5.5: Average spectral misfit per mode or mode group for the best models from the one-step (red triangles) and two-step (black squares) $v_s + v_p + \rho$ + topography inversion, compared to spectral misfits for v_s and v_p , with ρ scaled to v_s with factor 0.3 for the one-step (grey asterisks) and two-step (grey circles) inversions. Bold modes are v_p sensitive.

5.3.1. Misfit

The spectral misfits per mode (Fig. 5.5) show that the one-step inversion performs slightly better than the two-step inversion in terms of fitting the normal mode spectra, with a few exceptions. This minor difference is reflected in the average spectral misfit of the one-step model being 0.47, compared to 0.49 for the two-step model. We computed spectral misfits for an inversion for v_s and v_p , with density scaled to v_s by a factor of 0.3, for the same model parameterization (so up to degree 6 and for 7 B-splines), to observe the effect on the misfits of density not being scaled to v_s . We conclude that density generally fits the spectra better if it is not uniformly scaled to v_s with factor 0.3 throughout the mantle, with average spectral misfits dropping from 0.50 (0.53) to 0.47 (0.49) for the one-step (two-step) inversion. Discontinuity topography also contributes to the drop in misfit, but only marginally compared to the density contribution. From the spectral misfit per individual mode or mode group (Fig. 5.5) we see that misfits for the $n = 5$ overtones and some $n = 11$ overtones are especially improved for a non-scaled density model. On the other hand, the high angular order fundamentals ${}_0S_{21-30}$ (of which some are coupled to CMB Stoneley modes) do not seem to improve at all.

5.3.2. Model characteristics

We show slices through our one-step (Fig. 5.3) and two-step (Fig. 5.4) models at representative depths, including the upper and lower bounds of the MTZ, at which we also show their discontinuity topography. In the S-wave and P-wave velocity anomaly models we see the slow ridges and fast subduction zones around the Pacific ocean in the upper mantle of both inversion methods. The density anomalies clearly do not correlate with the velocity anomalies in the upper mantle and transition zone. We would expect the subducting slabs to be dense, so correlated to the fast velocity zones, but the density anomalies only show part of a dense ring around the Pacific. Similarly, low density anomalies do not follow the rift zones entirely, where density might be expected to be low due to upwellings. An example of an anti-correlated region is the Congo craton. In the cross-sections through Africa (Fig. 5.6), we see that the Congo craton has a fast velocity and light density signature. An example of a correlated region is the Andes subducted slab at the left-hand edge of the cross-section profile, which is both dense and fast (Fig. 5.6).

Velocity anomalies become more correlated to density anomalies in the lower mantle (Fig. 5.7b for one-step and 5.7c for two-step). The bulk of LLSVPs is both slow and light, which becomes clear in the cross-sections through the velocity and density models (Fig. 5.6). The large low velocity blobs in the lower mantle seem to be connected to slow structures in the upper mantle, according to the cross-section view, both in v_s and v_p . Only one of these two seemingly plume-like structures (in the Atlantic ocean) has a light and buoyant signature. The other is interrupted by a dense structure.

The correlation between velocity and density decreases near the CMB (Fig. 5.7b,c), where the western part of the LLSVPs is denser than average, but still seismically slow. No matter what velocity contour you choose for defining the edges of the LLSVPs, there is a sliver of dense material at the western base of the LLSVPs.

The slowest part of the LLSVPs is centered in the large low velocity blobs, but the lightest part of the LLSVPs is offset to the East.

Topography on the 400-discontinuity correlates very well to the density anomalies at that depth, for both inversion methods (Figs. 5.3d, 5.4d). Deep parts of the discontinuity correspond to light regions, and shallow parts to dense regions, which might imply that the dense regions are cold and light regions hot. The same level of correlation between the 670-topography and density is not present, although there is a hint of dense-deep and light-shallow correlation, opposite to the ‘400’. The

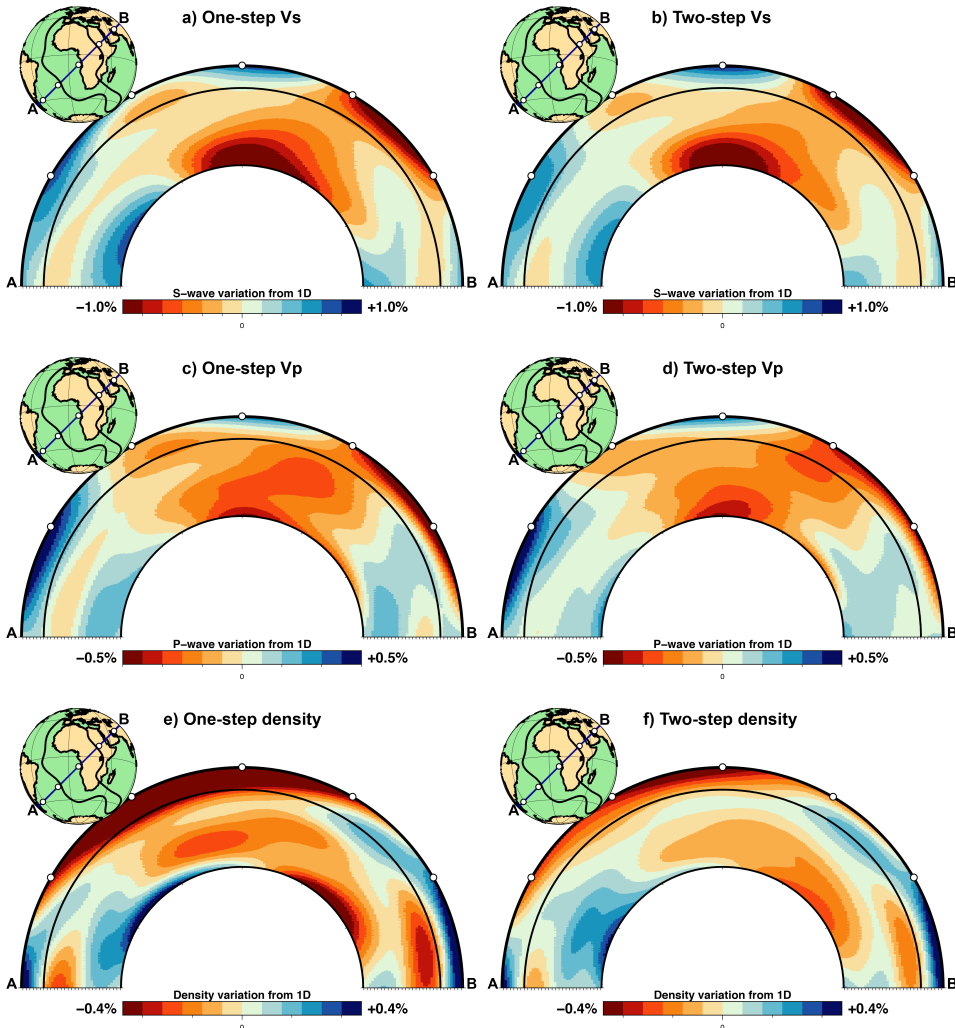


Figure 5.6: Cross-sections through the African LLSVP for the a) one-step v_s , b) two-step v_s , c) one-step v_p , d) two-step v_p , e) one-step ρ , and f) two-step ρ models.

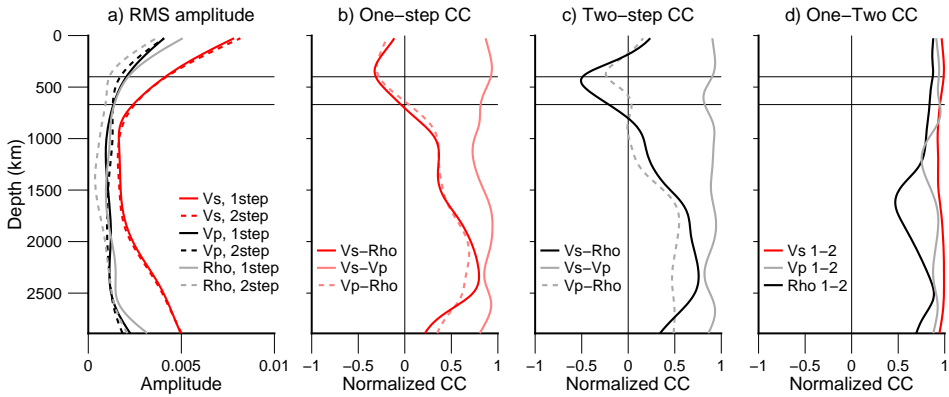


Figure 5.7: a) Root mean square (RMS) amplitudes of the models shown in Figs. 5.3 and 5.4; b) Normalized cross-correlation coefficients of all three one-step models; c) and of all three two-step models; d) and between the one- and two-step v_s , v_p and ρ models.

pronounced shallow regions of the ‘670’ correspond roughly to high velocity regions. Topography on the core-mantle boundary is roughly correlated to density structure at that depth, where uplifted parts correspond to light regions and depressed parts to dense regions, with the exception of polar areas.

The RMS amplitudes of the v_s models are clearly the biggest, but those of v_p and ρ are comparable (Fig. 5.7a). The one-step density model is stronger in amplitude than the two-step density model and two v_p models, reflecting its strong dense and light basal parts of the LLSVPs. Structure in v_s is well-correlated to v_p structure in both inversions (Fig. 5.7b,c), without the drop in correlation at 1500 km that we saw in Chapter 4. The disappearance of the drop in correlation is due to the new depth parameterization of 7 B-splines instead of 21 splines, not due to the inclusion of density and discontinuity topography.

Cross-correlation between velocity and density is not as close to 1.0 as the two velocities, as we have seen qualitatively in the depth slices and cross-sections. It goes from nearly no correlation at the top of the mantle, to negative in the transition zone, towards positive values in the lower mantle, finishing with a drop towards very little correlation near the CMB. This cross-correlation curve is far removed from the often made assumption of 3D v_s being proportional to 3D density throughout the mantle.

Preconceived notions of normal mode sensitivity to v_s , v_p and ρ heterogeneity are confirmed in the cross-correlations between the one- and two-step models of the same parameter (Fig. 5.7d), which reflect dependence on the inversion method. Normal mode sensitivity to S-wave velocity heterogeneity is the biggest of the three parameters, and the difference between the one-step and two-step models the smallest. The next biggest sensitivity is to P-wave velocity structure, for which the similarity between the two models is the second-highest. Density is least well-constrained by normal modes, which shows in the one-step vs two-step density cross-correlation

being the lowest on average. However, apart from the drop in the mid-lower mantle, the cross-correlation of density is not that much lower than for the velocities.

5.3.3. Synthetic inversions

We next examine the results from the one- and two-step inversions for synthetic data without 3D density variations. In both the one-step and two-step inversions, the input S-wave and P-wave velocity models are nearly perfectly recovered, so we are not going to show them here. Both the one-step and two-step recovered density models contain non-zero 3D and hence have a ghost pattern, since the input density model had no 3D variations (Fig. 5.8). At first glance, the amplitudes of the ghost pattern are much smaller than the amplitudes of the real data density models (Fig. 5.8c,d for comparison), which is confirmed by looking at RMS amplitudes of all four density models (Fig. 5.9a). The difference in RMS amplitude between the ghosts and the observed density is biggest at the top and bottom of the mantle, making these depth ranges least affected by the ghost pattern. Furthermore, the ghost pattern does not contain a dense sliver with the same lateral extent as observed in the real data inversion, making the partly dense base of the LLSVPs a more robust observation. In the mid-mantle, the two-step observed density moves closer to the ghost pattern, making this region more prone to be contaminated by the ghost pattern.

The ghost pattern for both inversions has cross-correlation coefficients between 0.4-0.8, with the one-step ghost and real density models having the highest cross-correlation throughout the mantle (Fig. 5.9b). As the observed real data density are well-correlated to S- and P-wave velocity anomalies in the lower mantle, the ghost density is also well-correlated to 3D v_s and v_p in both inversion methods (Fig. 5.9c). However, cross-correlation between the ghost pattern and 3D v_s and v_p drops in the mid- and upper mantle, even becoming quite negative for the one-step inversion. Therefore it is not immediately obvious whether the ghost pattern in density is due to leakage of v_s and/or v_p structures. In any case, the ghost patterns are generally small compared to density derived from observed data, and will thus not pose a problem for interpreting our density models.

5.3.4. Effect of a density starting model

We explore the influence of a density starting model by starting our real data inversions from a density model correlated to the S-wave velocity model, by factor 0.3, and a density model anti-correlated by factor -0.3. The resulting density models in the one-step inversion look very similar (Fig. 5.10b,d), so the effect of the starting model seems negligible. Furthermore, both of the density models resulting from non-zero starting models look very similar to the density model started from PREM (Fig. 5.10e), and have the same average spectral misfit of 0.47. The dense western base of the LLSVPs is present in both cases, but its lateral extent varies. The dense base of the LLSVP expands across the CMB in the anti-correlated starting model case, compared to the density model started from PREM. In the correlated case, the dense LLSVP base becomes slightly less widespread.

The two-step inversion shows more dependence on the density starting model.

The density model started from positive correlation with $\delta \ln v_s$ stays close to its starting model in the upper two slices at 100 and 400 km depth (Fig. 5.11b) and is

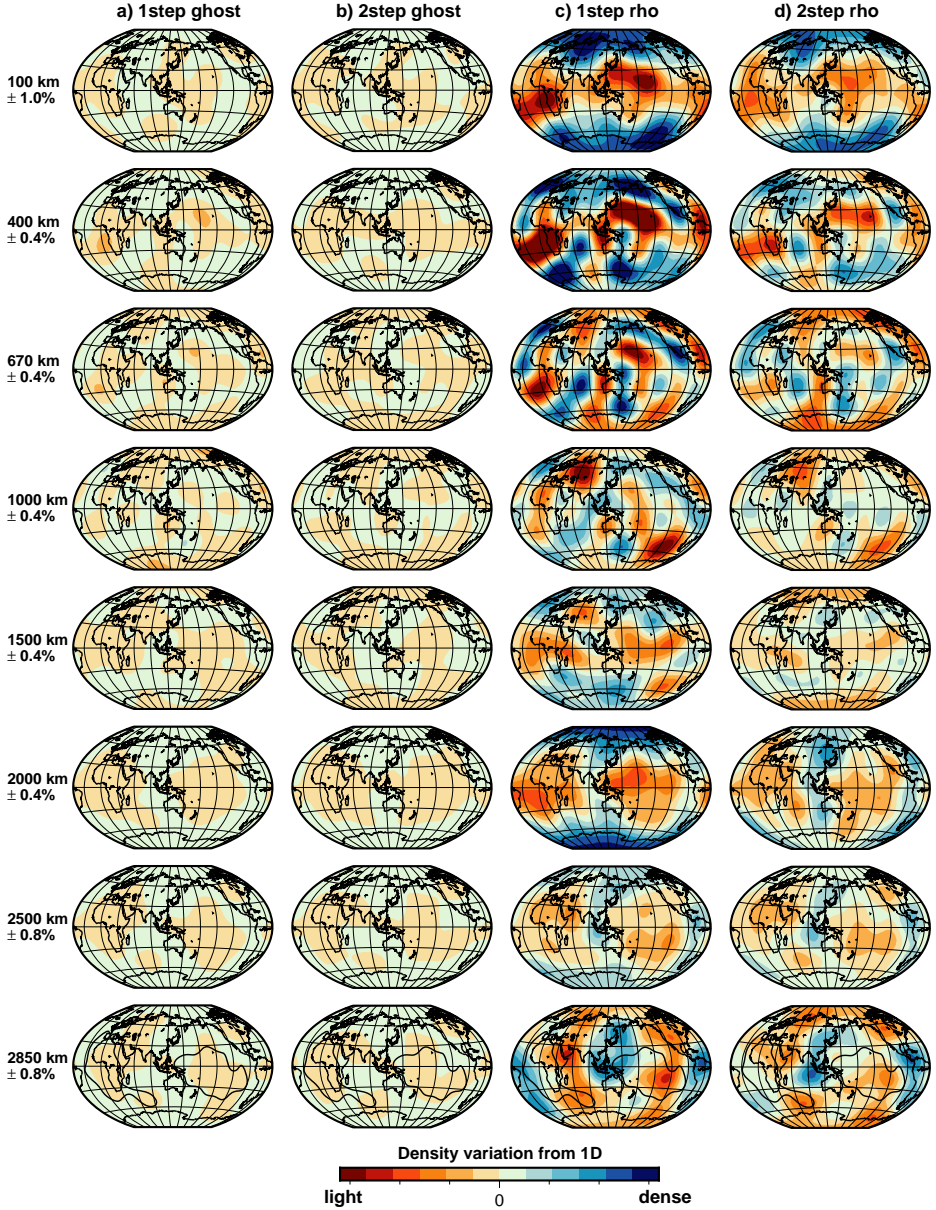


Figure 5.8: Depth slices through the ghost density recovered models from the a) one-step and b) two-step synthetic inversion, compared to the real data c) one-step and d) two-step inversions for density.

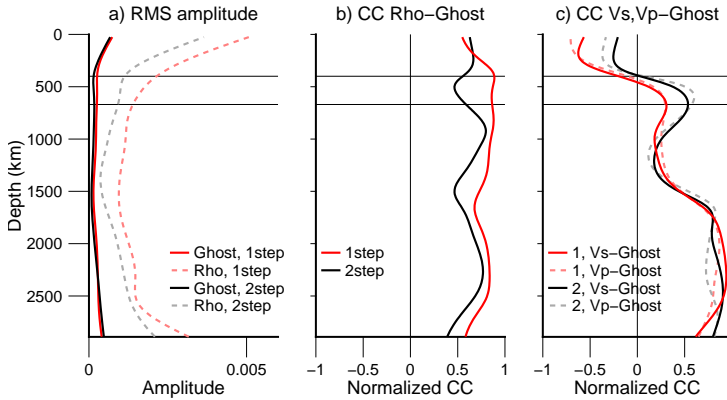


Figure 5.9: a) RMS amplitudes of ghost density for the one- (red) and two-step (black) synthetic inversions compared to the RMS amplitudes of density of the one- (red dashed) and two-step (grey dashed) real data inversions; b) cross-correlation between ghost density and observed density for the one- (red) and two-step (black) inversions; c) cross-correlation between observed $\delta \ln v_s$, $\delta \ln v_p$ models and the ghost density (1=one-step inversion, 2=two-step inversion).

thereby not well-correlated to the density model started from anti-correlation (Fig. 5.11d) or from PREM (Fig. 5.11e). The density model started from anti-correlation is not able to deviate from its starting position in most of the lower mantle, failing to produce the light LLSVPs (Fig. 5.11d). It does slightly better in the lowermost mantle, where we see a more extreme version of the same thing happening as in the one-step inversion: The lateral extent of the dense base strongly depends on the starting model. For a correlated starting model, with entirely light LLSVPs, the LLSVPs do not get a dense base anymore. Conversely, for an anti-correlated starting model, with entirely dense LLSVPs, the LLSVPs stay mostly dense. In terms of average spectral misfit, density started from a positive correlation has the same misfit as density started from PREM, and density started from a negative correlation has a slightly higher misfit (0.50 compared to 0.49). The presence of a dense base within part of the LLSVPs is therefore more disputed in the two-step inversion than in the one-step inversion.

The RMS amplitudes of density models derived from all three starting models do not show outliers (Fig. 5.12a). An interesting observation is that all the one-step density models have a larger amplitude near the CMB than their two-step counterparts. The ability of density models to deviate from their starting model is quantified by the cross-correlation curves between the starting model and end result (Fig. 5.12b,c). The cross-correlation curves of the one-step inversion (in red) are almost mirror images of each other, showing that when one density model deviates a lot from its starting model, the other agrees more with its starting model. We recognize the solid red curve in Fig. 5.12b (cross-correlation between starting model $0.3\delta \ln v_s$ and the resulting density model) as the cross-correlation between the density and v_s model in our PREM inversion (Fig. 5.7b) shifted approximately 0.2 to the right. Both one-step density models started from non-zero density have cross-

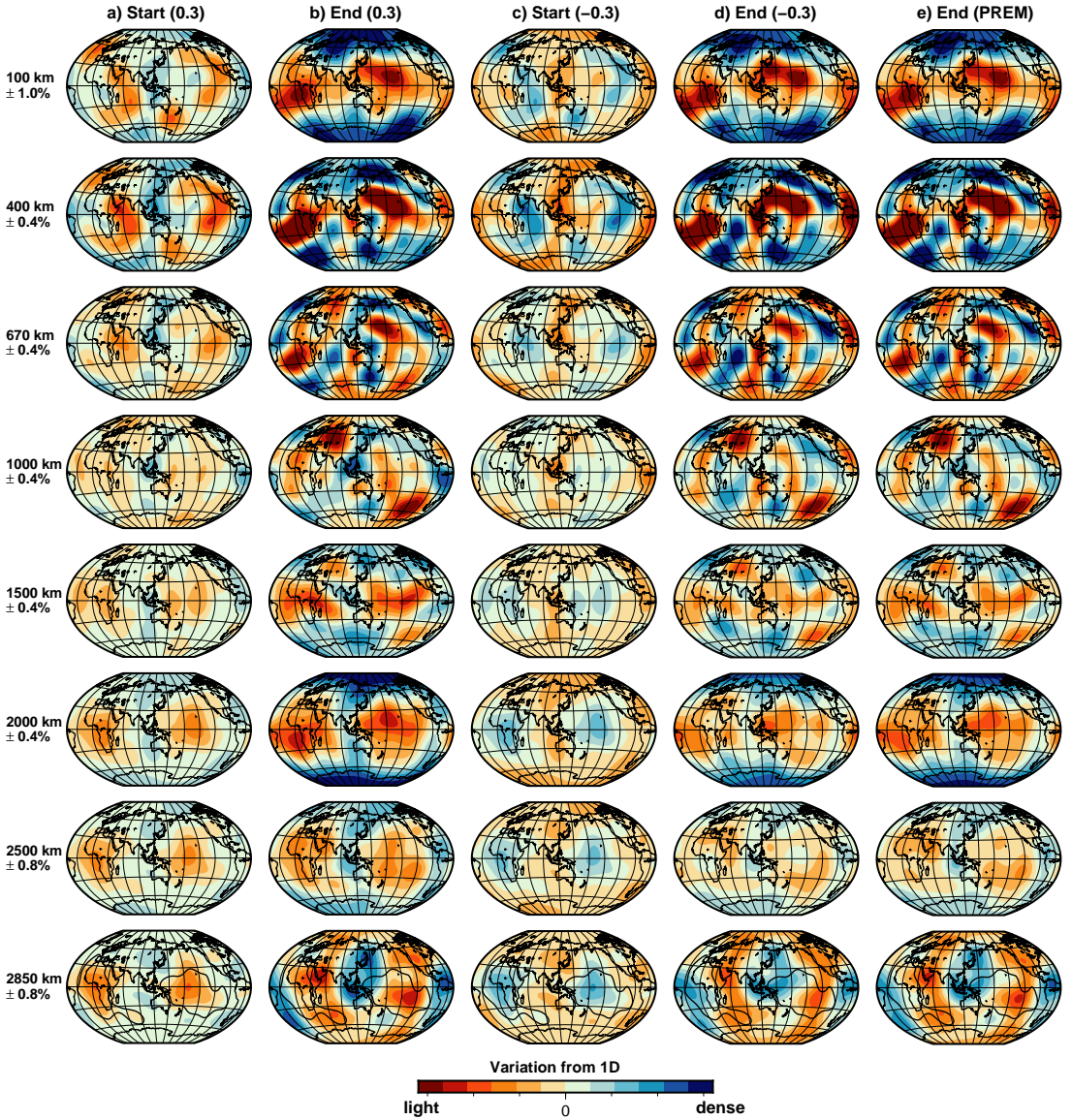


Figure 5.10: Density models for different starting models in the one-step inversion. a) Starting model scaled to $\delta \ln v_s$ by factor 0.3, b) resulting density model. c) Starting model scaled to $\delta \ln v_s$ by factor -0.3, d) resulting density model. The resulting density models can be compared to e) the observed density started from PREM.

correlation coefficients close to 1.0 with the density model started from PREM, with the positively cross-correlated starting model performing marginally better (Fig. 5.12c).

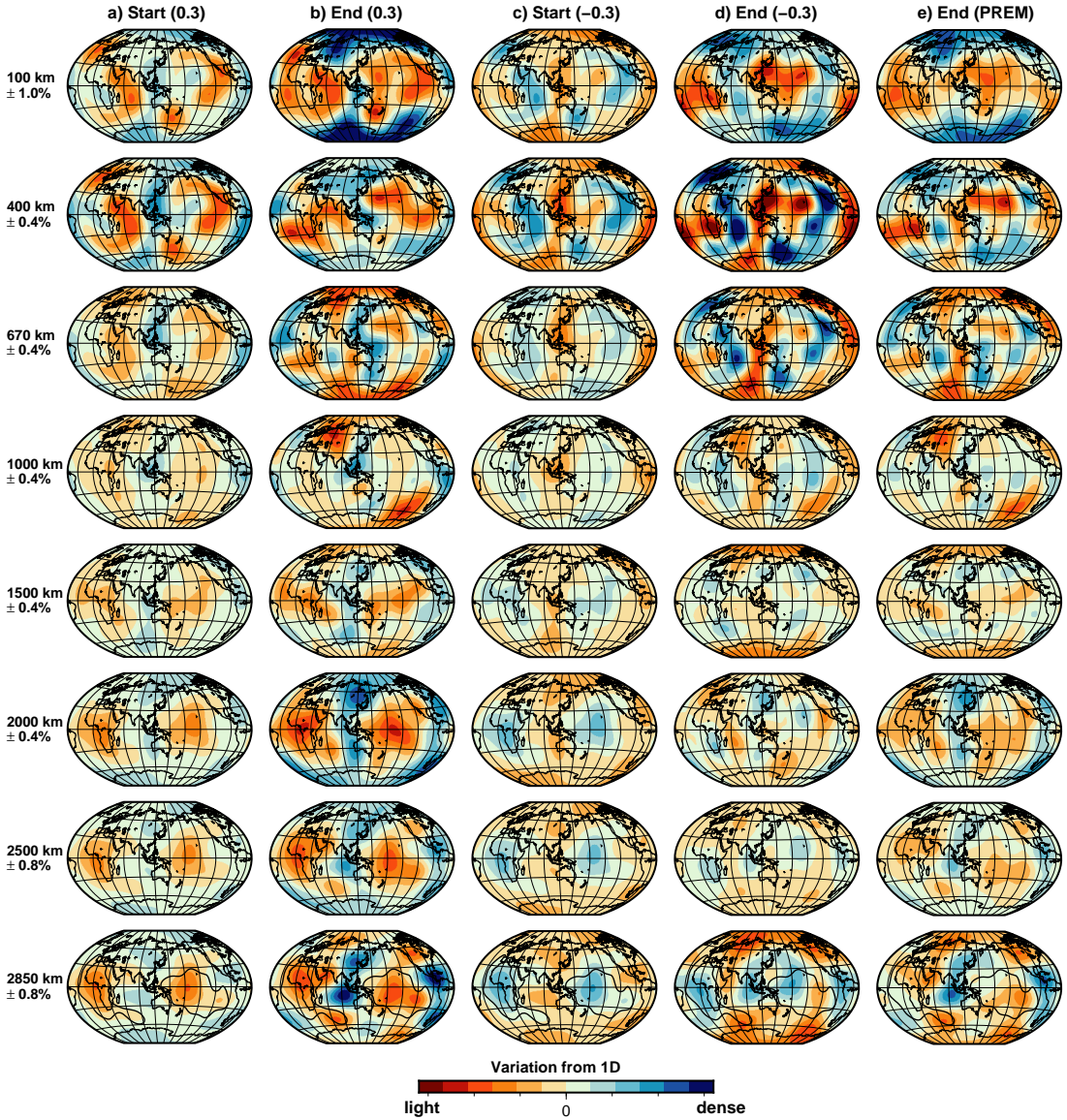


Figure 5.11: Density models for different starting models in the two-step inversion. a) Starting model scaled to $\delta \ln v_s$ by factor 0.3, b) resulting density model. c) Starting model scaled to $\delta \ln v_s$ by factor -0.3, d) resulting density model. The resulting density models can be compared to e) the observed density started from PREM.

The two two-step density models started from a non-zero density are more positively correlated to their starting model than their one-step counterparts (compare the black/grey lines in Fig. 5.12b to the red lines). We observe a similar shape

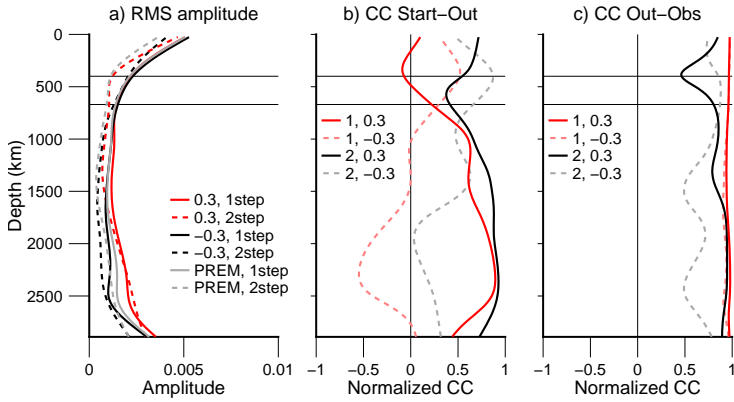


Figure 5.12: a) RMS amplitudes of the density models started from correlation ($0.3\delta\ln v_s$), anti-correlation ($-0.3\delta\ln v_s$) and PREM, for the one- and two-step inversions; b) cross-correlations between the density starting model (scaled to $\delta\ln v_s$ by 0.3 and -0.3) and resulting model for the one- and two-step inversion; c) cross-correlations between the density output model for (anti-)correlated starting model and the density observed when starting from PREM.

in the solid black curve in Fig. 5.12b (cross-correlation between starting model $0.3\delta\ln v_s$ and the resulting density model) as the cross-correlation between density and v_s in the inversion started from PREM (Fig. 5.7c), but it is shifted roughly 0.7 to the right, especially in the upper mantle. This is another indication that the density model started from positive correlation to $\delta\ln v_s$ is not able to move to the density model started from PREM in the upper mantle, also shown by the poor cross-correlation between these two density models (Fig. 5.12c). The density models started from negative correlation to $\delta\ln v_s$ are not able to match the density model started from PREM in the lower mantle (Fig. 5.12c).

5.4. Discussion and Conclusion

The poor correlation between density and velocities in the upper mantle indicates the presence of chemical heterogeneity. In the case of cratonic roots we find positive velocity anomalies accompanied by near-zero to negative density anomalies. Negative buoyancy due to low temperatures is compensated by compositional heterogeneity resulting in net positive or neutral buoyancy (e.g. Jordan, 1978). Although we should be cautious when trying to interpret small-scale structures in a model that lacks odd degrees, the Congo craton could be an example of such a cratonic root. Chemical heterogeneity in the rest of the upper mantle could be caused by crustal materials being entrained in the upper mantle due to subduction or delamination of the lower continental crust (Anderson, 2006). Subducted MORB (Mid-Ocean Ridge Basalt) could be a potential candidate for the high velocity, high density structures in the upper mantle, and probably in the top of the lower mantle (Wang et al., 2020).

As our density models do not suffer from ghost density, except potentially in

the mid-mantle, we believe that our lower mantle density observations are robust. According to Kuo & Romanowicz (2002), density could only be retrieved with their relatively small normal mode data set when its amplitude exceeded 50% of the S-wave model. In our case, the density models exceed that amount in most of the mantle, which is another indicator of the robustness of our observed dense basal sliver and poor density-velocity correlation in the upper mantle.

In contrast to the findings of Akbarashrafi (2020), the one-step inversion has an almost negligible dependence on the density starting model, both the correlated and anti-correlated density-to- v_s starting models resulted in nearly identical density models. The two-step inversion showed more dependence on the starting model; it especially affects the presence and details of the partly dense base of LLSVPs. These observations suggest that differences between previous two-step density models, which were sometimes started from a 3D density model (e.g. Ishii & Tromp, 1999), could partly be explained by the two-step inversion being less robust and more susceptible to the chosen starting model.

Recently, van Tent et al. (2020) employed a Hamiltonian Monte Carlo method to assess the uncertainties related to density in a two-step inversion using the same normal mode data set as we use here. They found the uncertainties to be less than 30% throughout the mantle and proceeded to declare their density model as robust. We have not discovered a way to quantify uncertainties for the one-step inversion, but seeing as the one-step density model has lower spectral misfits and performed better in the starting model test, it will probably not have larger uncertainties than the two-step inversion.

A possible explanation for the high density, low velocity basal part underneath part of the LLSVPs is iron enrichment (Trampert et al., 2004) due to iron penetration from the outer core to the lowermost solid mantle (e.g. Kanda & Stevenson, 2006) or through iron partitioning in partial melt (Nomura et al., 2011). Another potential explanation concerns recycling of MORB over millions of years, creating warm low velocity blobs with a dense base of basaltic material, under the condition of sufficiently dense MORB (e.g. Jones et al., 2020). However, Deschamps et al. (2012) argue that this MORB would have to heat up to unrealistically high temperatures to reach the observed low velocity signal. Finally, the dense sliver could be of primordial composition, reflecting its origin as remnant of an ancient magma ocean (e.g. Labrosse et al., 2007).

Potential candidates for the high density, high velocity circum-Pacific ring are post-perovskite (as S-wave velocity and density both increase (e.g. Oganov & Ono, 2004)) or subducted basaltic material (e.g. Brandenburg & Van Keken, 2007), although viscous forces might be too strong for the subducted material to penetrate all the way down to the CMB (Wang et al., 2020).

A partly dense base of the LLSVPs is a way to reconcile previously conflicting density constraints from the Earth's tides (Lau et al., 2017) and CMB Stoneley modes (Koelemeijer et al., 2017). The sensitivity of the Earth's body tides increases with depth and reaches a maximum at the CMB and they prefer dense LLSVPs. Stoneley modes, on the other hand, peak in density sensitivity further above the CMB, and prefer light LLSVPs. As Koelemeijer et al. (2017) already stated, the

Stoneley modes cannot rule out a dense 100 km thick layer just above the CMB, which was later confirmed in a synthetic study by Robson et al. (2021). Even though we are not using the Earth's body tides, some of the Earth's gravest normal modes have sensitivity to density all the way to the CMB, explaining why we are able to make robust observations of a dense sliver just above the CMB.

Our discontinuity topography amplitudes (0.8-1.6 km) are lower than previously determined for the CMB (Fig. 5.2), and even more significantly lower for the '400' and '670' topography, which is in the range of 10-30 km in reflected body wave studies (e.g. Houser et al., 2008a; Guo & Zhou, 2020). We picked topography models with the same damping as the elastic models, but we could have chosen lower damping for topography in order to get amplitudes that match better with previous estimates. It would not alter the patterns. The weak anti-correlation of the '400' to the '670' could point to a contribution of thermal variations between slabs (thick MTZ) and plumes (thin MTZ). Our CMB topography is largely elevated underneath the light part of the LLSVPs and vice versa, which seems to be due to some kind of isostatic compensation. We repeat here that we do not know how possible trade-offs between density and discontinuity topography could affect our results, and we should be cautious in interpreting them.

In summary, we have made robust observations of large-scale density structure in the mantle using an extensive normal mode data set and one- and two-step inversions. The one-step inversion performs better in terms of misfit and dependence on a density starting model. From the negative and neutral cross-correlation between velocity and density anomalies in the upper mantle and MTZ, we infer this region of the mantle to be thermochemical in nature. The upper part of the LLSVPs is both slow and light, and might reflect a more thermal signature, but at the core-mantle boundary we find a sliver of excess density in both inversion methods that corresponds to slow velocity anomalies, indicating a thermochemical origin. Therefore LLSVPs are partly dense, partly light structures, which reconciles previous conflicting inferences of their buoyancy.

5.5. Outlook

We have some suggestions for future work on density, and discuss a few here. Ishii & Tromp (2004) included inner core sensitive modes in their joint inversion for mantle density and inner core anisotropy, which helped to constrain the amplitude of the density anomalies in the lower mantle. We did not include inner core sensitive modes here, but it is an interesting avenue to pursue with our expanded normal mode data set.

The free-air gravity anomaly is uniquely sensitive to density and discontinuity topography. Including this data type will provide more independent constraints on these two parameters, as for example Ishii & Tromp (1999) and Ishii & Tromp (2001) have done already.

Throughout this thesis, we have limited our inversions to even-degree structure, since our current normal mode data set does not have sufficient odd-degree sensitivity, as we explored in Chapter 3. By not inverting for odd degrees, we dismiss the possibility of the two LLSVPs being different in shape, strength and thermo-

chemical nature. Recent geochemical evidence suggests that the two LLSVPs have had a different evolutionary history through the supercontinent cycles of Rodinia and Pangaea (Doucet et al., 2020). We need to include odd degrees in the future to investigate if this LLSVP hypothesis is reflected in their seismic signatures. Instead of, or complementary to, including odd degrees, we can increase the maximum spherical harmonic degree of the models. We have already performed one inversion for maximum degree 12 (Fig. C1 for one-step and Fig. C2 for two-step). The dense western base is still present as part of the LLSVPs, although now the top of this sliver is fluctuating up and down.

We may also explore different parameter combinations to invert for, apart from 3D v_s , v_p , ρ , such as 3D v_s , v_ϕ (bulk sound velocity), ρ , or 3D μ (shear modulus), κ (bulk modulus), ρ . The latter is especially interesting, since these parameters directly relate to mineral physical experimental data, and the density kernels become less oscillatory around zero. Ishii & Tromp (2001) have tried this for their normal mode data set and found the cross-correlations between the three density models to be quite similar. We have already performed an initial inversion for 3D μ , κ and ρ , using 7 B-splines and up to degree 6, and do not agree with that statement. While the shear modulus anomalies agree well with S-wave velocity anomalies, and the 3D bulk modulus has some features in common with bulk sound structures from Chapter 4, the density model disagrees with our previously obtained density models, especially in the lower mantle (Fig. C3 for one-step and Fig. C4 for two-step). The LLSVPs are entirely dense in this parameterization. We do not yet know why, and therefore moved this result to the section discussing future work.

C1. Appendix C

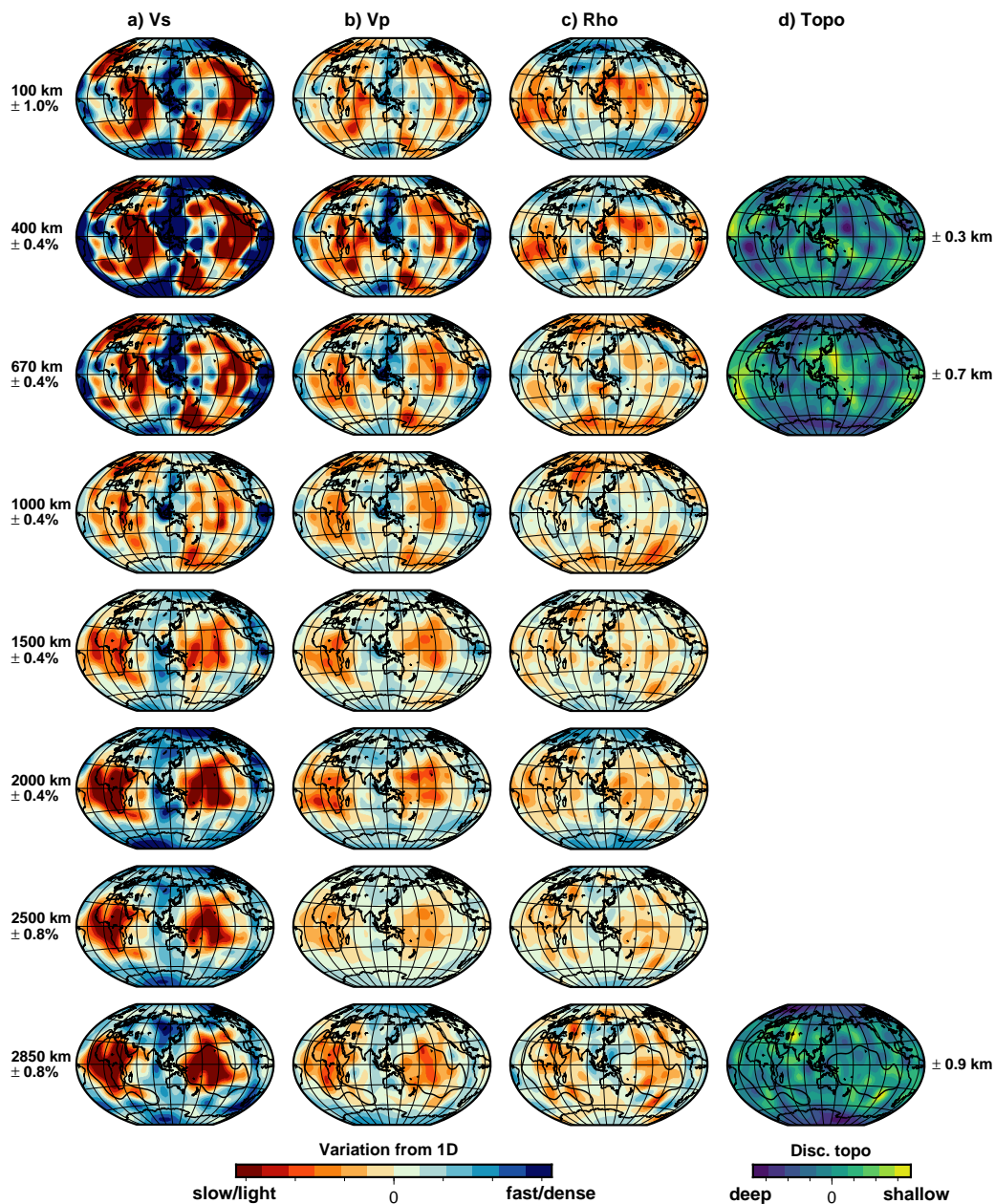


Figure C1: Depth slices through one-step models of anomalies up to degree 12 in a) shear-wave velocity v_s , b) compressional-wave velocity v_p , and c) density ρ , with d) discontinuity topography for the 400, 670 and CMB.

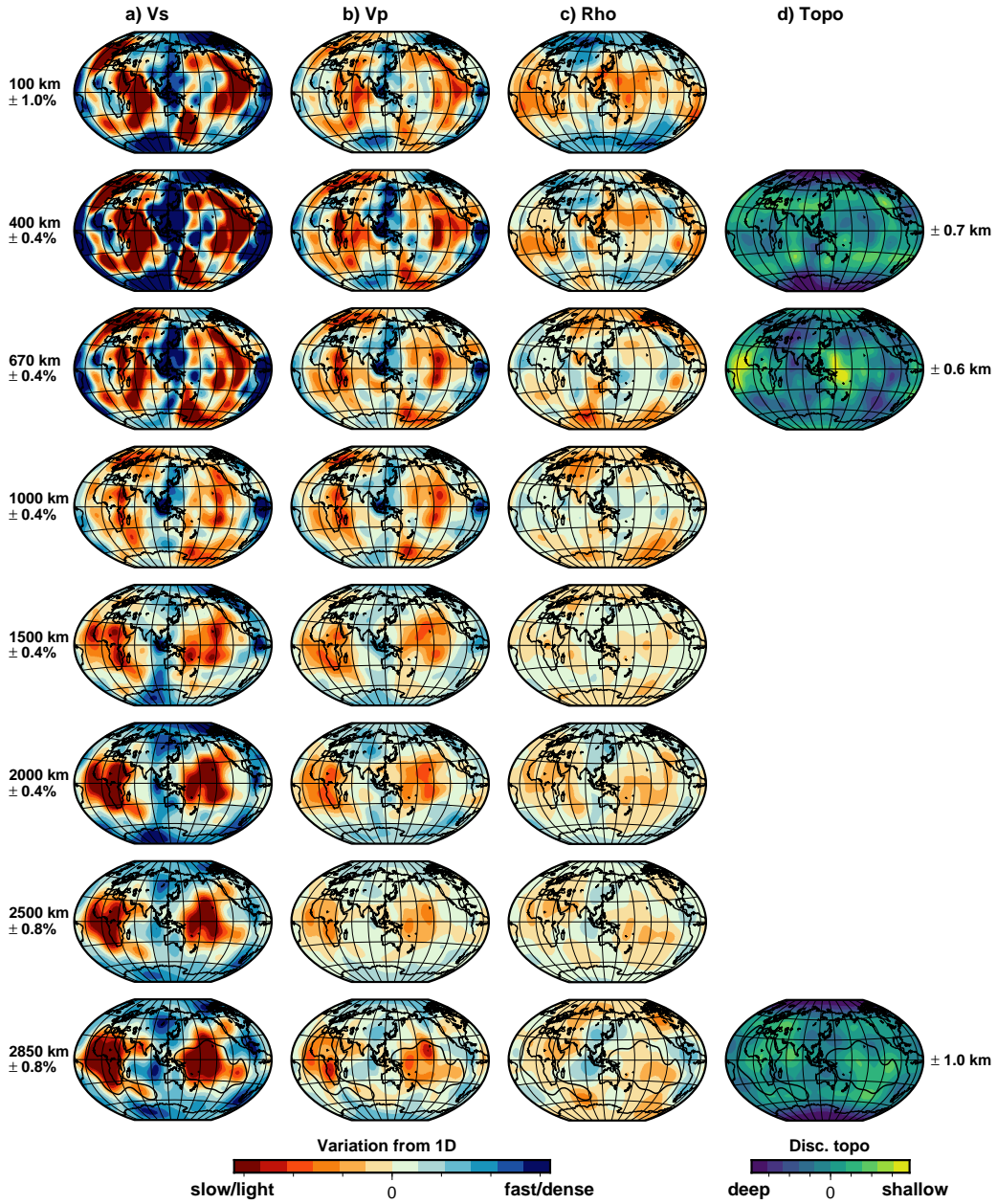


Figure C2: Depth slices through two-step models of anomalies up to degree 12 in a) shear-wave velocity v_s , b) compressional-wave velocity v_p , and c) density ρ , with d) discontinuity topography for the 400, 670 and CMB.

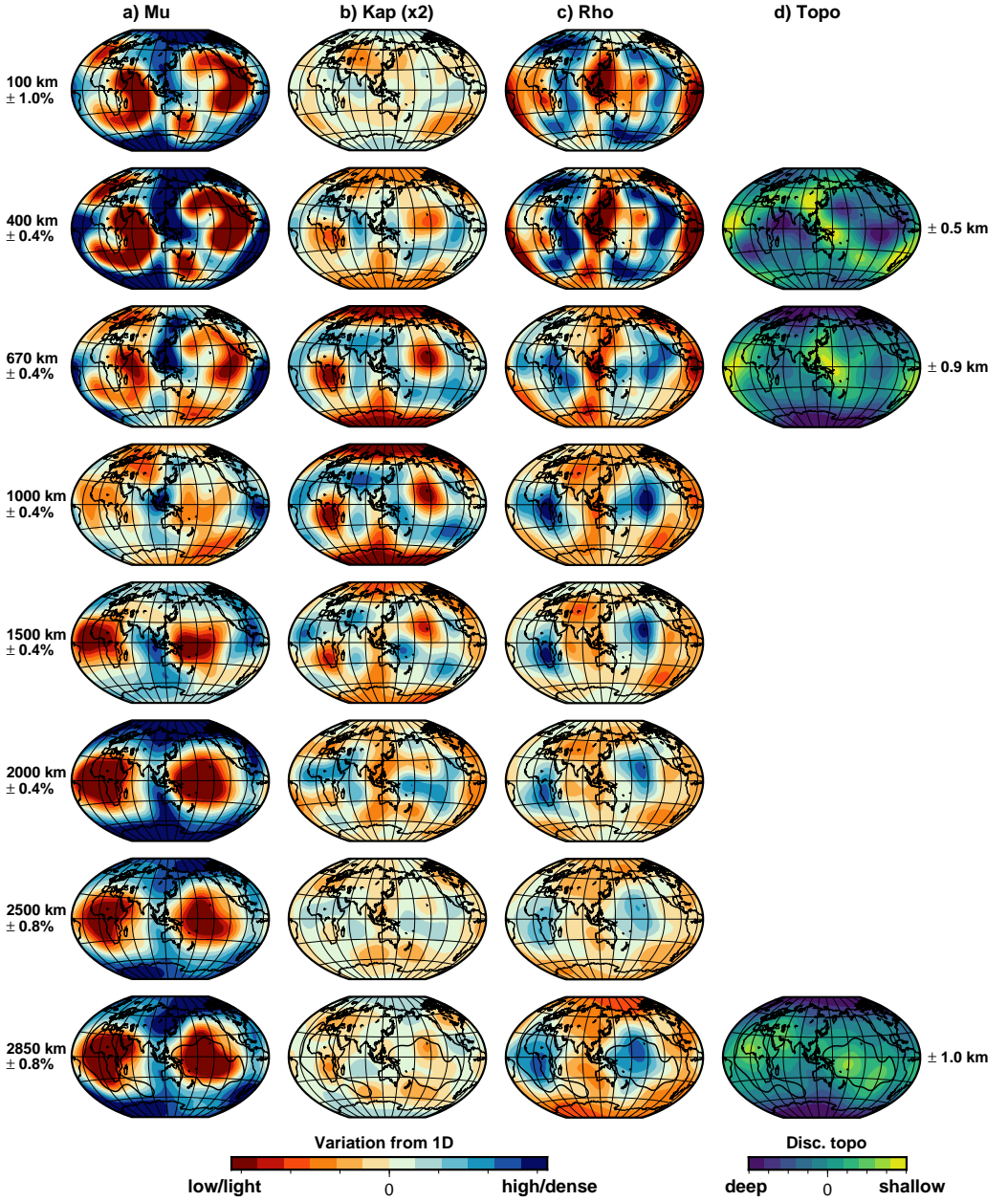


Figure C3: Depth slices through one-step models of a) shear modulus μ , b) bulk modulus κ (times two for visualization purposes), and c) density ρ , with d) discontinuity topography for the 400, 670 and CMB.

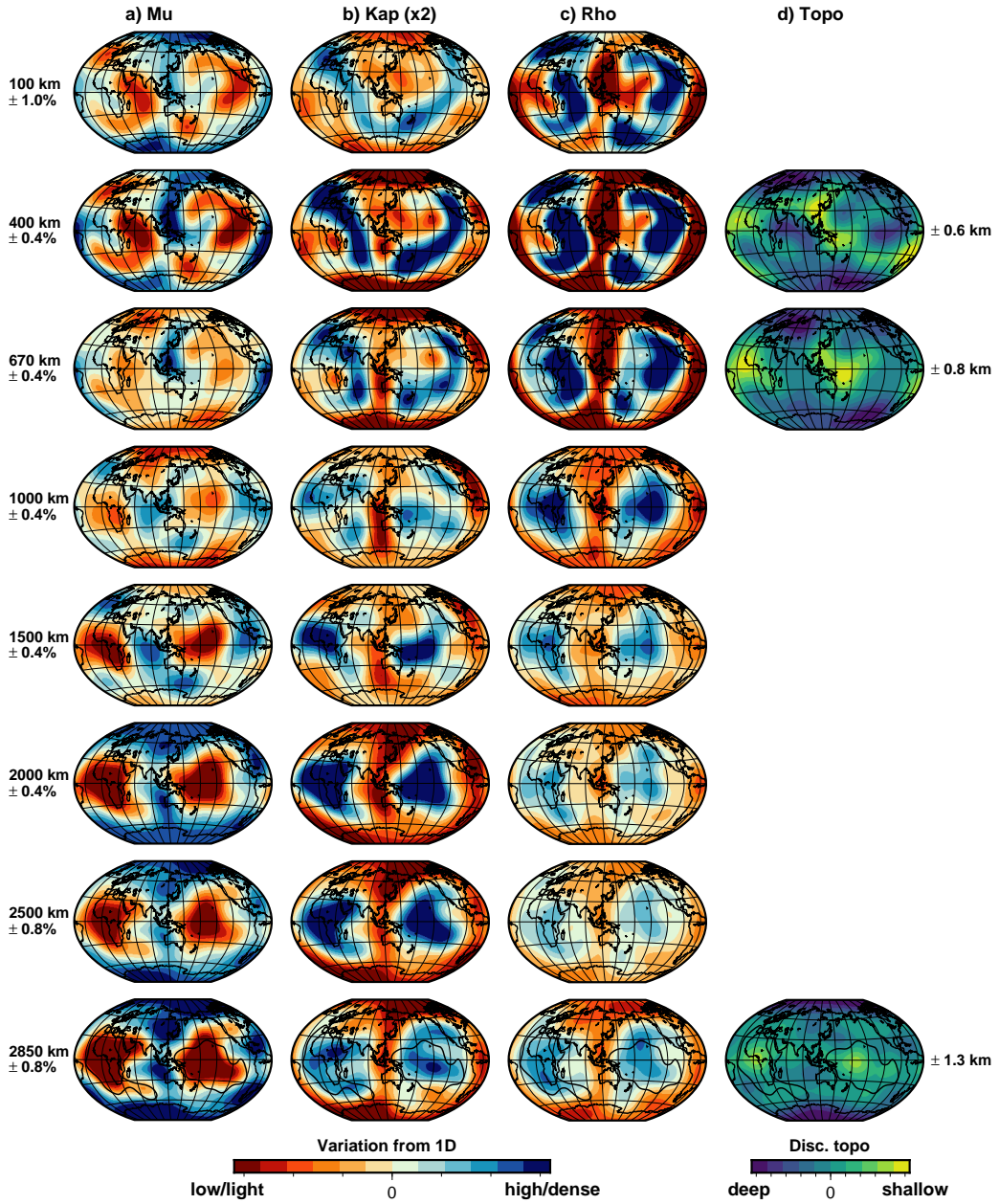


Figure C4: Depth slices through two-step models of a) shear modulus μ , b) bulk modulus κ (times two for visualization purposes), and c) density ρ , with d) discontinuity topography for the 400, 670 and CMB.

6

Towards a one-step inversion for 3D shear attenuation in the mantle

Seismic attenuation, or loss of seismic energy, is a key parameter for mapping variations in temperature, partial melt, composition, and potentially water content, thereby providing important information about the thermal or thermochemical nature of Large Low Shear-wave Velocity Provinces (LLSVPs). Efforts in imaging attenuation anomalies have mainly concentrated on the upper mantle, which all show highly attenuating mid-oceanic spreading ridges. We will employ the one-step normal mode inversion to make a global model of 3D shear attenuation for the first time. Small-scale scattering and focussing, which are difficult to separate from intrinsic attenuation for high-frequency body waves, become less important for low-frequency modes. Furthermore, by cross-coupling modes and jointly inverting for elastic and anelastic structure, scattering and focussing are implicitly included. Since this is the first effort of applying one-step direct spectrum inversion to attenuation, we first perform synthetic inversions to find the optimum way of jointly inverting for v_s and q_μ structure. Our preferred method of first inverting for v_s alone, and using the resulting v_s model as starting point for a joint v_s and q_μ inversion, is then applied to the real data, using various normal mode subsets. We compare our one-step 3D attenuation model to the two-step model by Talavera-Soza et al. (2021b). Some of the high attenuation regions between the one- and two-step models overlap, but others do not, and these differences grow larger for an increasing number of modes included in the one-step inversion. Dependence on the attenuation starting model is high. Discrepancies between the one-step and two-step attenuation models could be explained by the former being more affected by leakage of elastic structures. Future efforts of mapping attenuation with the one-step inversion should include more detailed elastic structure, to avoid this leakage.

6.1. Introduction

The Earth’s mantle is a dissipating medium, causing seismic travelling waves (or standing waves) to transform their energy into heat and decay in amplitude over time due to anelastic processes. Focussing and scattering of seismic energy, which are elastic processes, also affect the measured amplitudes, but are not dissipating energy. In studying attenuation in the Earth’s interior, it is important to separate the intrinsic attenuation (i.e. the anelastic loss of energy) from the apparent attenuation (including focussing and scattering).

Attenuation is often described by “quality factor” Q , of which the inverse $q = Q^{-1}$ is “attenuation” that describes the energy loss per oscillation. The latter can be defined by

$$Q^{-1} = \Delta E / 2\pi E_{max} \quad (6.1)$$

where ΔE is the amount of energy dissipated per cycle and E_{max} is the peak energy contained in the same volume in a cycle (e.g. Knopoff, 1964). Attenuation may occur in bulk and shear strain, described by Q_κ and Q_μ respectively. As most attenuation is concentrated in shear, Q_κ is often assumed to be infinite or very high, implying near-zero bulk attenuation.

Attenuation causes physical dispersion of seismic wave velocities. Dispersion effects due to attenuation need to be taken into account when interpreting seismic velocity models derived from long- or short-period waves (Karato, 1993). Q itself is mildly frequency dependent, and can be approximated by a power law of the form $q \propto \omega^{-\alpha}$. The value of α has been constrained between 0.2 and 0.4 by laboratory measurements (see review by Romanowicz & Mitchell (2015)), although this was later challenged by Lau & Faul (2019) who found normal modes to reside on a plateau of frequency-dependence. These conclusions have evolved from the idea of an “absorption band” (Liu et al., 1976; Anderson & Given, 1982), where a superposition of various relaxation mechanisms creates a range in the seismic frequency spectrum with nearly constant Q , and strong frequency-dependence at the edges of this range. We assume that Q_μ in the mantle falls within the absorption band (a statement that was indirectly proven by Dannberg et al. (2017)) for normal mode frequencies, meaning that the dependence of Q_μ on frequency is small.

Combined with 3D velocity structure, lateral variations in intrinsic seismic attenuation provide constraints on temperature anomalies, differences in grain size and the presence of (partial) melt and water in the mantle. Seismic attenuation strongly depends on temperature (e.g. Anderson & Given, 1982), increasing attenuation with increasing temperature. Anelastic effects are therefore important in determining temperature sensitivities (Karato, 1993; Jackson et al., 2002; Matas & Bukowinski, 2007), although they might be of the order of uncertainties in the elastic temperature derivatives (Trampert et al., 2001). Thus, an increase in temperature would lead to low velocity in combination with strong attenuation. Conversely, low-velocity regions accompanied by low attenuation (i.e. not much energy loss) could point towards some degree of compositional heterogeneity.

The relation between grain size on the one hand and seismic velocities and attenuation on the other hand is also well established. Grain size strongly affects these seismic variables: at a fixed temperature, smaller grains increase attenuation and

decrease velocities, and vice versa (e.g. Jackson et al., 2002; Faul & Jackson, 2005; Dannberg et al., 2017).

Partial melt decreases S-wave velocity, and increases attenuation, although the extent of this increase is debated (e.g. Chantel et al., 2016; Debayle et al., 2020). In addition to mid-ocean ridges and subduction zones, partial melt could be present at the base of the mantle in Ultra Low Velocity Zones (ULVZs) to explain the significant drop in v_s compared to v_p (see review by Garnero & McNamara (2008)). These small-scale structures, of tens of kilometres across, likely reside below the detection limit of normal modes, that sample large-scale structures, or a smoothed average of smaller scale structures.

The effect of water, which is structurally bound under mantle conditions and not in the form of a free fluid, on attenuation is least well-known. The role of water is probably limited to the upper mantle, as experiments and theoretical calculations have shown that perovskite does not incorporate significant amounts of water under lower mantle conditions (Panero et al., 2015). However, recent experiments on upper-mantle olivine have shown that velocity and attenuation appear to be insensitive to elevation in water content (Cline II et al., 2018), so structurally bound water cannot explain low velocity or high attenuation structures. Instead, they propose high oxygen fugacity in subduction zones and other oxidized regions as explanation for observations of high attenuation in the upper mantle.

6.1.1. 1D and 3D models of shear attenuation

The 1D profiles of normal-mode derived shear attenuation (Fig. 6.1) all contain a layer of high attenuation (i.e. low Q_μ) in the upper mantle, specifically the low-velocity zone underneath the lithosphere. Low attenuation (i.e. high Q_μ) is found in the lithosphere, and in the lower mantle, where Q_μ is generally increasing with depth, with some 1D profiles showing exceptions for the lowermost mantle where Q_μ decreases. All models also share the feature of infinite attenuation ($Q_\mu = 0$) in the fluid outer core (not shown in Fig. 6.1, as it stops at the CMB), due to the shear modulus dropping to zero there. These 1D attenuation models based on normal modes show good agreement among themselves. However, the range for body-wave models would lie between $Q_\mu = 270 - 620$ in the lowermost mantle (e.g. Lawrence & Wyssession, 2006a; Hwang & Ritsema, 2011), which agrees less well with the 1D attenuation profiles shown in Fig. 6.1, possibly illustrating the frequency dependence of attenuation.

This frequency dependence is why we will compare our 3D normal mode attenuation models to global models derived from either normal modes or surface waves, as body wave studies yield different attenuation models due to their higher frequencies. Efforts to map attenuation variations in the mantle have mainly been concentrated on the upper mantle. Global upper mantle 3D attenuation models (Fig. 6.2b-d) display a strong correlation with tectonic features in the uppermost few hundred kilometers and are commonly anti-correlated to shear-wave velocity anomalies (Fig. 6.2a). Low velocities correspond to high attenuation below mid-ocean ridges, and high velocities correspond to low attenuation below continental shields. This observation agrees with an upper mantle where heterogeneities are

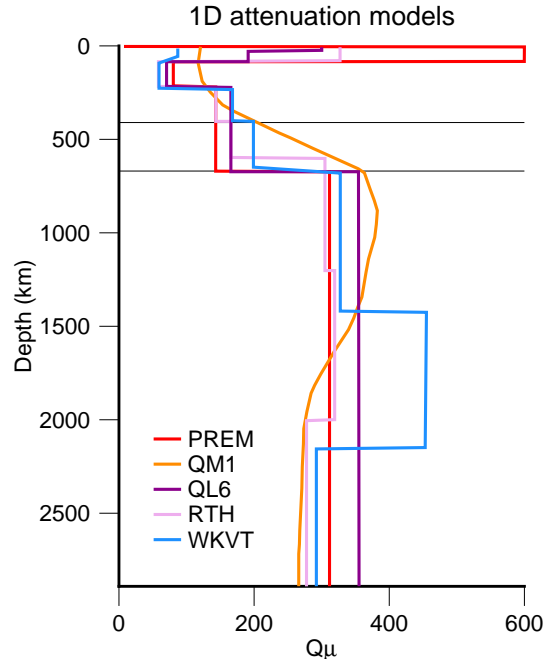


Figure 6.1: Normal-mode derived 1D shear attenuation profiles in the mantle, from: PREM: Dziewonski & Anderson (1981), QM1: Widmer et al. (1991), QL6: Durek & Ekström (1996), RTH: Resovsky et al. (2005), WKVT: de Wit et al. (2014). The 400- and 670-discontinuities are also shown.

mainly caused by temperature differences, with oxygen fugacity possibly playing a role. Deeper into the upper mantle, the correlation between tectonics and q_μ becomes less clear. Although the attenuation models are correlated to tectonics, cross-correlation coefficients between upper mantle attenuation models generally do not exceed 0.5 (Adenis et al., 2017).

The only few studies that have imaged lower mantle 3D shear attenuation were body wave studies. In a global study, Lawrence & Wyssession (2006b) identified a region at the top of the lower mantle beneath eastern Asia with high attenuation, explained by increased water content transported there by subducting Pacific lithosphere. They also observed a low attenuation, high velocity ring around the Pacific in the lower mantle, and highly attenuating, slow LLSVPs within. This observation was matched by Hwang & Ritsema (2011), who separated their teleseismic body wave data set into a Pacific (sampling the Pacific LLSVP) and circum-Pacific subset, and found higher attenuation for the LLSVP than for its surroundings. In a regional study sampling the African LLSVP using the PcS phase, Liu & Grand (2018) inferred that this LLSVP was more attenuating than the surrounding mantle. Thus high attenuation is now linked to both LLSVPs. In another regional study, Zhang et al. (2019) found a significantly larger Q_μ in the lower mantle beneath North-east China (i.e. low attenuation) by comparing observed amplitude ratios between core-reflected phases to synthetic amplitude ratios, which agrees with Lawrence & Wyssession (2006b).

It is important to note that small-scale scatterers become increasingly important

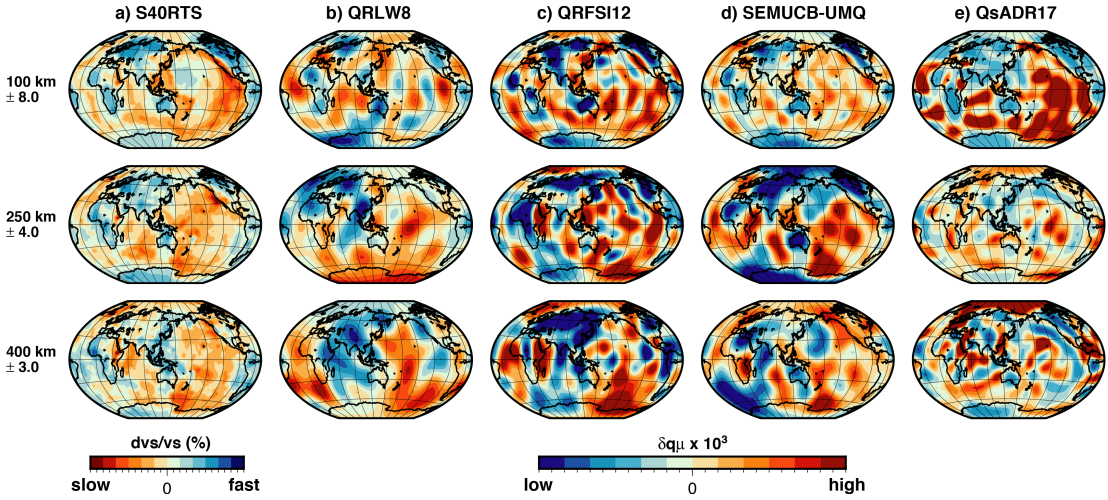


Figure 6.2: Upper mantle a) S-wave velocity model S40RTS (Ritsema et al., 2011), compared to four shear attenuation models b) QRLW8 (Gung & Romanowicz, 2004), c) QRFSI12 (Dalton et al., 2008), d) SEMUCB-UMQ (Karaoğlu & Romanowicz, 2018), e) QsADR17 (Adenis et al., 2017).

in high-frequency body wave studies. However, scattering and focussing were not taken into account in any of these studies directly, which may have resulted in scattering or focussing being falsely interpreted as intrinsic attenuation.

An important factor in any attenuation study is quantifying the effect of source parameters such as earthquake magnitude and radiation pattern. Errors in the moment tensor solutions published in the Global Centroid Moment Tensor database (www.globalcmt.org) could be more than 10% due to unmodeled 3D mantle heterogeneity (Hjörleifsdóttir & Ekström, 2010; Karaoğlu & Romanowicz, 2018). Talavera-Soza (2021a) studied the effects of unaccounted magnitude variations in the scalar moment M_0 on recovered anelastic splitting functions in synthetic tests, and found small but systematic biases in these splitting functions. A thorough investigation of source parameters on 3D attenuation structure in the one-step inversion is very much required, but beyond the scope of this chapter.

In this chapter, we will perform the one-step direct spectrum inversion for 3D global mantle shear attenuation. There are two main advantages to using normal modes for studying attenuation: i) scatterers are probably small compared to normal-mode wavelengths, and ii) focussing and defocussing is included in the theory of cross-coupling between modes. As far as we are aware, a one-step inversion of normal mode spectra for 3D attenuation has not been done before. Therefore we first need to decide between four ways of directly inverting synthetic spectra to find the preferred method of inverting the real data. We will then compare our results to the two-step splitting function model for anelastic structure of the mantle by Talavera-Soza et al. (2021b) and to other observations of 3D mantle attenuation.

6.2. Data and methods

The basic normal mode inversion workflow does not drastically change when adding attenuation. We introduce shear attenuation to the inversions by adding the anelastic splitting matrix \mathbf{A} as imaginary part to the elastic splitting matrix \mathbf{E} to obtain the total splitting matrix: $\mathbf{H} = \mathbf{E} + i\mathbf{A}$. We compute the partial derivatives for the anelastic part separately from the elastic part, and either concatenate them, or keep them separate, depending on the inversion method.

Table 6.1: Mode groups used in this study. Two-step modes represent the 14 modes/mode groups used in the two-step inversion of Talavera-Soza et al. (2021b). The $n = 0 - 4$ modes are all modes up to and including overtone number 4. The modes in italics are the higher order fundamental modes mentioned in the text.

Two-step modes	n=0-4 modes	
${}_0S_5$	${}_0S_2$	${}_1S_2 - {}_0S_4 - {}_0T_3$
${}_0S_6$	${}_0S_3 - {}_2S_1$	${}_1S_4$
${}_0S_7$	${}_0S_4 - {}_1S_2$	${}_1S_5 - {}_2S_4$
${}_1S_4$	${}_0S_5$	${}_1S_6 - {}_2S_5$
${}_1S_7$	${}_0S_6$	${}_1S_7$
${}_1S_8$	${}_0S_7$	${}_1S_8$
${}_1S_9$	${}_0S_8 - {}_4S_1 - {}_0T_9$	${}_1S_9$
${}_1S_{10}$	${}_0S_9 - {}_0T_{10}$	${}_1S_{10}$
${}_2S_4 - {}_1S_5$	${}_0S_{11} - {}_2S_7 - {}_0T_{12}$	${}_1S_{11} - {}_0S_{15}$
${}_2S_5 - {}_1S_6$	${}_0S_{13} - {}_0T_{14}$	${}_1S_{12} - {}_0S_{17}$
${}_2S_6$	${}_0S_{14} - {}_2S_9 - {}_0T_{15}$	${}_2S_1 - {}_0S_3 - {}_0T_2$
${}_2S_{12}$	${}_0S_{15}$	${}_2S_6$
${}_2S_{13}$	${}_0S_{16}$	${}_2S_8 - {}_4S_3$
${}_3S_9$	${}_0S_{17} - {}_2S_{11}$	${}_2S_{10} - {}_4S_5$
	${}_0S_{19} - {}_1S_{13}$	${}_2S_{12}$
	${}_0S_{21} - {}_1S_{14}$	${}_2S_{13}$
	${}_0S_{22} - {}_2S_{14}$	${}_2S_{17} - {}_7S_5$
	${}_0S_{23} - {}_1S_{15}$	${}_2S_{25} - {}_3S_{25}$
	${}_0S_{24} - {}_2S_{15}$	${}_3S_6$
	${}_0S_{25} - {}_1S_{16}$	${}_3S_7 - {}_5S_5$
	${}_0S_{26} - {}_2S_{16}$	${}_3S_9$
	${}_0S_{27}$	${}_4S_2 - {}_0S_{10} - {}_0T_{11}$
	${}_0S_{28}$	${}_4S_4 - {}_1T_8$
	${}_0S_{29}$	
	${}_0S_{30}$	

Since we are performing the one-step direct spectrum inversion for attenuation for the first time, we need to test multiple ways of inverting the spectra to find out which one works best. We will perform four synthetic tests:

- i) inverting for v_s and q_μ anomalies simultaneously with the same norm damping,
- ii) or with ten to a hundred times more norm damping for attenuation;

- iii) alternating between iterations that update the v_s model and those that update the q_μ model;
- iv) first inverting for v_s structure, keeping q_μ fixed, followed by inverting for v_s and q_μ simultaneously.

We expect attenuation to be less well constrained by the data than S-wave velocity, so either alternating between the two parameters (iii) or first inverting for v_s only and then for both parameters (iv) would be the preferred methods. Based on the full-waveform inversion study by Karaoğlu & Romanowicz (2018), the alternating iterations method (iii) could be the best way. On the other hand, option (iv) would be the preferred choice based on splitting function inversions, in which the elastic splitting function coefficients c_{st} are measured first, of which the result is used as starting point for an inversion for the elastic and anelastic coefficients ($c_{st} + d_{st}$) simultaneously (Mäkinen & Deuss, 2013; Talavera-Soza, 2021a).

In the synthetic tests to find the preferred inversion method, we decided to invert normal modes with overtone numbers $n = 0 - 4$ (excluding higher order fundamentals; Table 6.1), with ever increasing model complexity, i.e. inverting for higher spherical harmonic degrees and more radial parameters. Input 3D attenuation models are scaled to simplified existing 3D S-wave velocity models by scaling factor R_q , which is defined by

$$\delta q_\mu = R_q \frac{\delta v_s}{v_s} \quad (6.2)$$

After confirming our preferred inversion method, we will apply it to real data, starting with the modes selected for the anelastic splitting functions of Talavera-Soza et al. (2021b) (Table 6.1), and then increasing the subset of modes. As we suspect the attenuation signal in normal mode spectra to be of similar amplitude as density, or even smaller, the radial parameterization chosen for the first real data inversions consists of three evenly spaced B-splines (Fig. 6.3). This parameterization will most likely avoid overparameterization, but will clearly not give us detailed depth resolution, and could cause aliasing. Therefore, this depth parameterization is merely a starting point, and we will test other parameterizations in the future.

S-wave velocity is parameterized as variations with respect to 1D PREM v_s (Dziewonski & Anderson, 1981): $\delta v_s/v_s$ or $\delta \ln v_s$. Due to the large ranges in 1D attenuation with depth (Fig. 6.1), 3D variations in attenuation are commonly expressed in terms of δq_μ , so irrespective of a 1D reference model or globally averaged value. By plotting the attenuation models in this way, changes in amplitude with depth are more apparent (Dalton et al., 2008).

In most synthetic test and in all real data inversions, density and v_p structure are positively correlated to v_s anomalies with factors 0.3 and 0.5, respectively. We have already seen in previous chapters that this is an oversimplification, so we intend to relax these constraints in the future. We are not performing crustal corrections for attenuation, since there is no reliable 3D crustal attenuation model available. This choice will likely not alter our conclusions, since the impact of crustal attenuation is probably minimal (Dalton et al., 2008; Karaoğlu & Romanowicz, 2018).

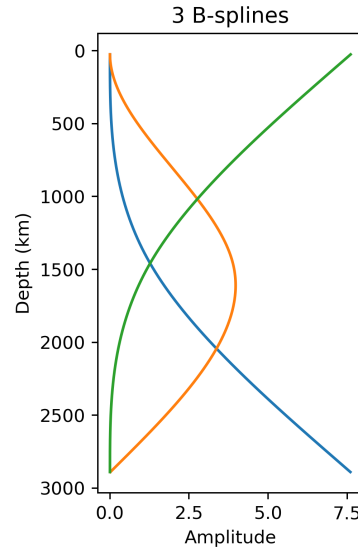


Figure 6.3: Radial parameterization of 3 B-splines, where each spline is represented by a different colour.

6

We do not properly account for the anelastic effects of the Earth's ellipticity yet. This should not pose a problem for the synthetic inversions, as ellipticity is not included in the anelastic part of the splitting matrix that is used for computing synthetic spectra, nor in the partial derivatives part. Therefore the absence of ellipticity corrections is self-consistent in synthetic tests. For real data, however, the lack of ellipticity corrections could cause strange patterns in the anelastic zonal coefficients m_{20} , although the effect of ellipticity in the anelastic splitting matrix is probably small.

6.3. Synthetic 3D $v_s + q_\mu$ inversions

We perform various inversions of synthetic spectra to find the preferred method out of the list of four from the previous section. Starting with the most simple synthetic test, where the input 3D S-wave velocity and shear attenuation models consist of one layer covering the whole mantle, we find that the first two inversion methods (options i and ii) recover v_s anomalies quite well, but poorly recover q_μ structure (Fig. 6.4b,c). The latter two inversion methods (options iii and iv) do recover the input shear attenuation model very well (Fig. 6.4d,e). We therefore discard the first two options in the list of possible inversion methods, and continue our synthetic tests with increasingly complicated input models with the latter two methods.

The input model now consists of two layers, in the ranges of 24-670 km and 670-2891 km depth. S-wave velocity anomalies are anti-correlated to 3D attenuation in the upper layer, according to $\delta q_\mu = 0.3\delta \ln v_s$, and correlated in the bottom layer, according to $\delta q_\mu = -0.3\delta \ln v_s$. To avoid confusion, the colour scale for attenuation is flipped with respect to that of velocity, since high attenuation could be related to high temperatures (hot means red). Therefore, correlation means low velocities (red)

corresponding to weak attenuation (blue), so the colours in v_s and q_μ are opposite. Anti-correlation means low velocities (red) corresponding to high attenuation (red), so the colours in v_s and q_μ match.

Option iv), i.e. first inverting for v_s , then for v_s and q_μ jointly (Fig. 6.5c), performs better in recovering the input attenuation model than option iii), i.e. alternating between inversions for v_s and q_μ (Fig. 6.5b). Furthermore, the success of option iii) is more dependent on norm damping than option iv) and therefore less robust. We also see that the intermediate v_s model for method iv), so the starting v_s model for the joint $v_s + q_\mu$ inversion, improves significantly after this joint inversion. The method of alternating iterations is the preferred inversion method for a full waveform inversion for 3D S-wave velocity and shear attenuation (Karaoğlu & Romanowicz, 2018), but it appears to be less effective for our one-step direct spectrum inversion.

The spectral misfits per mode (Fig. 6.6) improve by including q_μ in the misfit calculation, with respect to v_s only (compare black triangles to black squares). We can furthermore distinguish between modes that are sensitive to upper and lower

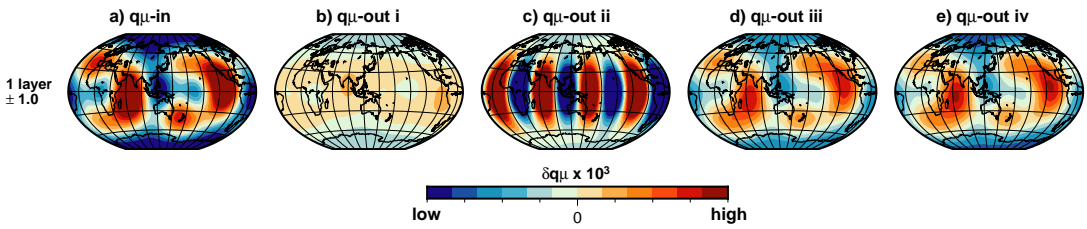


Figure 6.4: Synthetic tests for one layer, with a) input q_μ model, and the four output models for b) jointly inverting for v_s and q_μ with the same damping, c) and ten times more damping for q_μ , d) alternating between inversions for v_s and q_μ , e) first inverting for v_s , then for v_s and q_μ jointly.

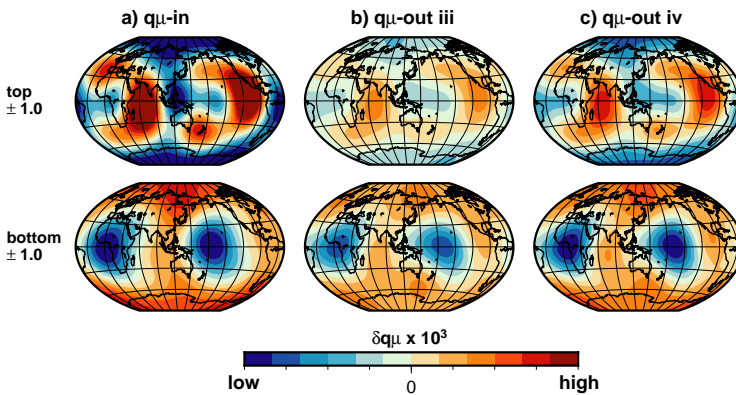


Figure 6.5: Synthetic tests for two layers (24-670 and 670-2891 km), with a) input q_μ model, and the two output models for b) alternating between inversions for v_s and q_μ , and c) first inverting for v_s , then for v_s and q_μ jointly.

mantle attenuation. Modes that are sensitive to upper mantle attenuation show the greatest improvement in misfit when only upper mantle 3D attenuation is added to the velocity model (red stars), which are ${}_0S_{19}-{}_1S_{13}$, ${}_2S_{12}$, ${}_2S_{13}$, ${}_4S_3-{}_2S_8$, ${}_4S_5-{}_2S_{10}$. Most of the other modes show a larger sensitivity to the lower mantle, by having a lower misfit for the 3D v_s plus lower mantle q_μ model (grey stars). This distinction between upper- and lower mantle attenuation modes agrees with the picture we get from their sensitivity kernels for shear modulus μ , strengthening our confidence that we are fitting shear attenuation structure.

We continue our synthetic tests for v_s and q_μ with option iv) first inverting for v_s structure, keeping q_μ fixed, followed by inverting for v_s and q_μ simultaneously, which is similar to the splitting function approach of first inverting for the elastic splitting coefficients, and then for the elastic and anelastic coefficients jointly (Mäkinen & Deuss, 2013; Talavera-Soza, 2021a). The input models of 3D v_s and q_μ are parameterized with 3 B-splines along the radius and up to spherical harmonic degree 4 laterally. They are the result of a two-step splitting function inversion by Talavera-Soza et al. (2021b). We recover the input models (Fig. 6.7a,d) almost perfectly using method iv) (Fig. 6.7c,e). The fit of the S-wave velocity model improves when we start to include shear attenuation in the inversion, mainly by better matching the amplitudes (compare intermediate model Fig. 6.7b and end result Fig. 6.7c to the input model Fig. 6.7a).

6

6.4. Real data inversions

After establishing that the best way of inverting for v_s and q_μ anomalies is by method iv), i.e. first inverting for v_s and then jointly for v_s and q_μ , we apply this method to real data in an inversion using the same model parameterization (3 B-splines, up to spherical harmonic degree 4) as the last synthetic test. We compare our

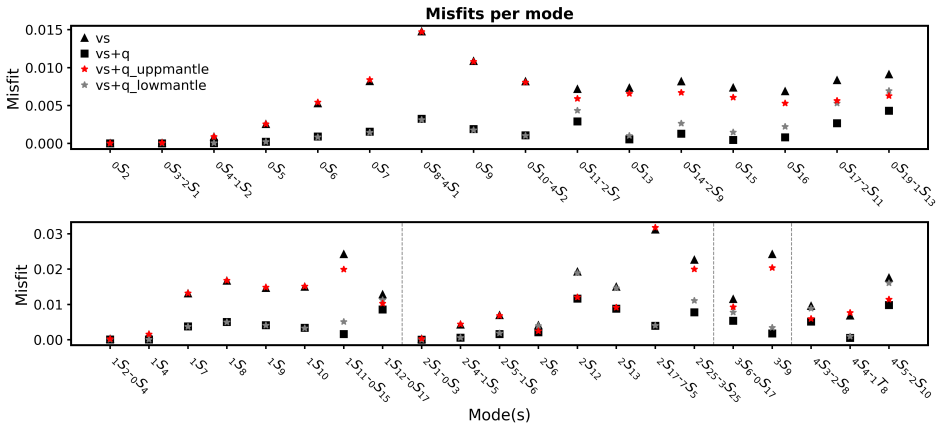


Figure 6.6: Misfit per mode or group of modes, for synthetic inversion iv) with two layers. Showing misfits for the v_s model only (black triangles), the combined $v_s + q_\mu$ model (black squares), $v_s +$ upper layer q_μ only (red stars), and $v_s +$ lower layer q_μ only (grey stars).

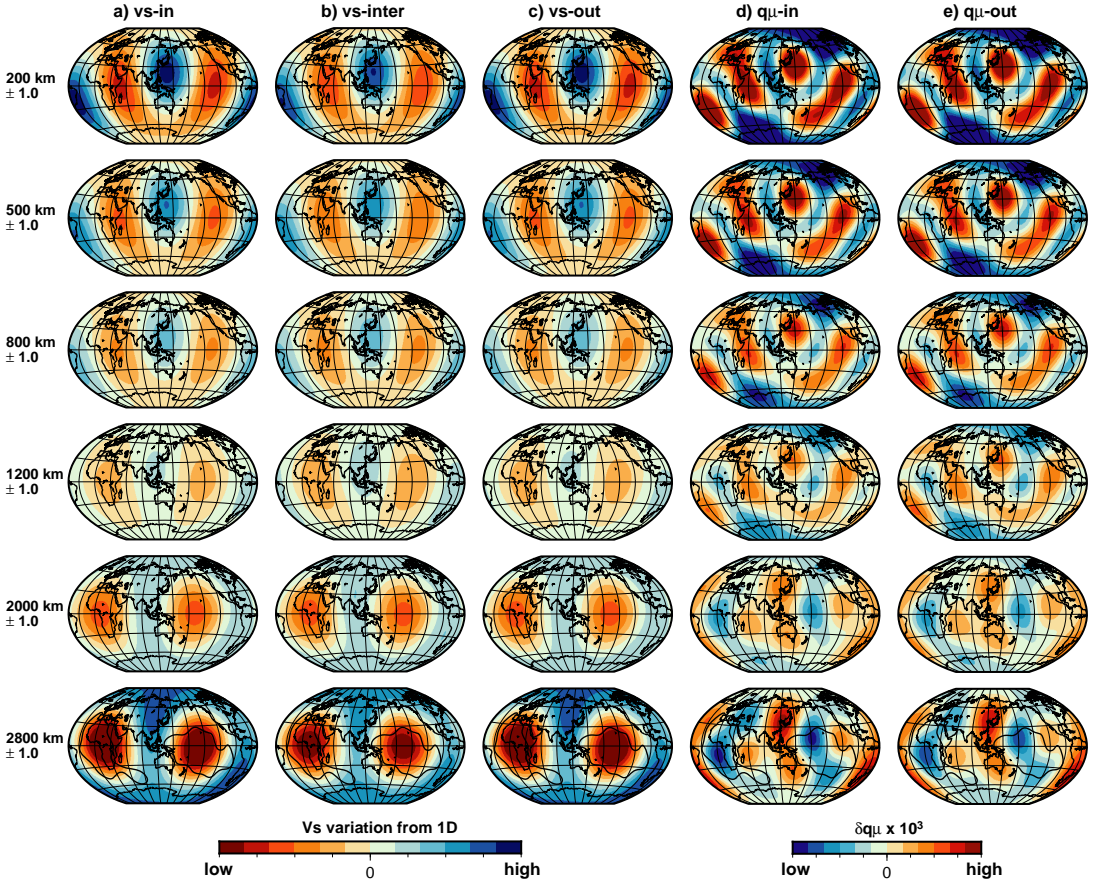


Figure 6.7: Synthetic tests for 3 B-splines up to degree 4, with a) input v_s model, b) v_s after only inverting for v_s , c) final v_s model after joint inversion, d) input q_μ model, and e) final q_μ model.

results from the one-step direct spectrum inversion to attenuation models inferred from the two-step inversion of anelastic splitting functions (Talavera-Soza et al., 2021b). For a fair comparison, we employ the same modes as in the two-step splitting function inversion of Talavera-Soza et al. (2021b) for our one-step inversion. The v_s model resulting from the one-step inversion (Fig. 6.8c) corresponds well with large-scale structures of previously obtained v_s models. The two-step v_s model does not resemble previously obtained v_s models as well, which shows that the two-step inversion is more affected by the limited number of splitting functions, at least for the elastic part.

Turning our attention to the attenuation models, we observe different structures at all depths between the two-step (Fig. 6.8d) and one-step models (Fig. 6.8e). Although most of the high attenuation (red) regions in the upper mantle overlap, they are not connected in the same way. The checkerboard-like pattern in the one-

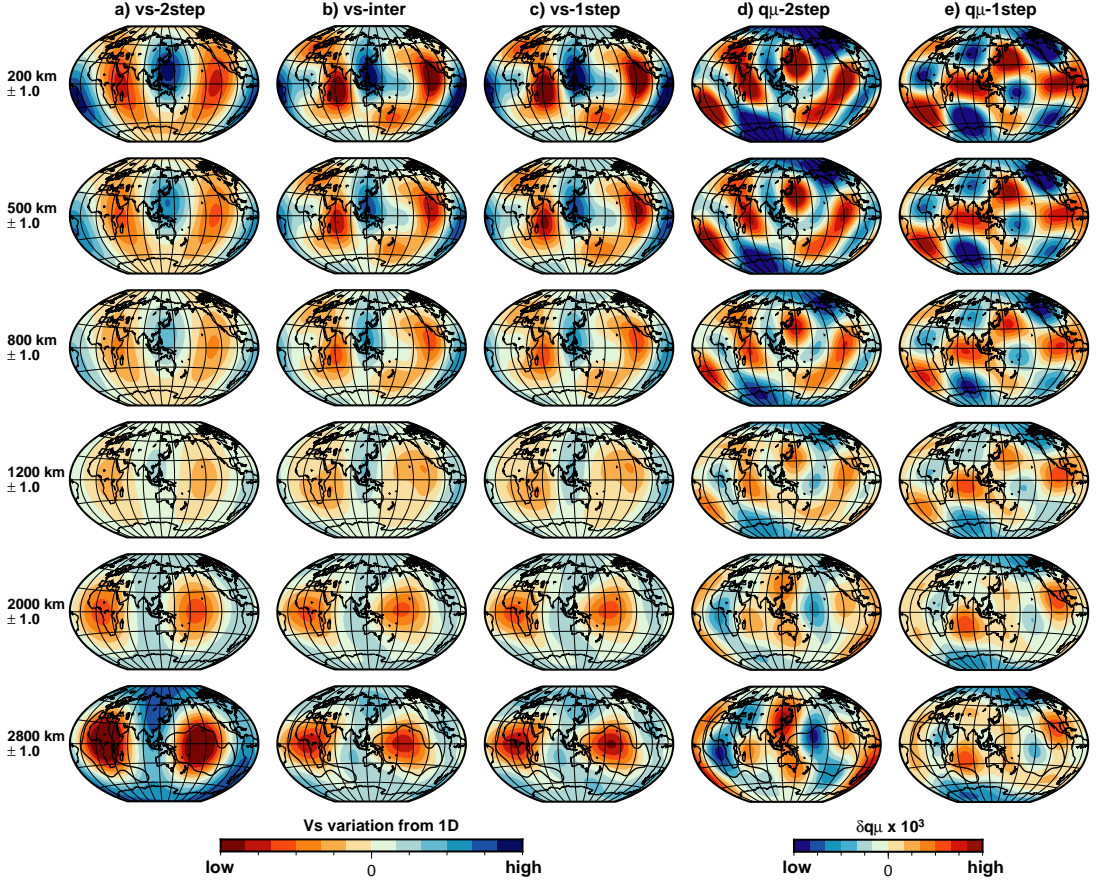


Figure 6.8: Real data inversion for 3 B-splines up to degree 4, with a) two-step v_s model for reference, b) v_s after only inverting for v_s , c) final one-step v_s model after joint inversion, d) two-step q_μ model for reference, and e) one-step q_μ model.

step model is not caused by abnormally high values of model coefficients $\text{Re}(m_{42})$ and $\text{Im}(m_{42})$. We will assess the robustness of this pattern by including more upper mantle sensitive modes, as there are only two upper mantle modes included in the current inversion (${}_2S_{12}$ and ${}_2S_{13}$).

Lower mantle attenuation also varies in pattern between the one- and two-step inversion, although attenuation inside the center of the LLSVPs is low (blue) in both models (Fig. 6.8d,e). The one-step attenuation model shows more of a highly attenuating ring around these low attenuation cores, but the surrounding regions in the two-step model are also more attenuating.

The average spectral misfit for the two-step v_s and q_μ models (Fig. 6.8a,d) is 0.48 for the two-step modes only. In comparison, the average spectral misfit for the one-step v_s and q_μ models (Fig. 6.8c,e) for the same subset of modes is 0.39.A

major part of this misfit difference can be contributed to the better fitting one-step v_s model, since the spectral misfit for the one-step v_s model by itself is 0.40, and for the two-step v_s model by itself is 0.47. The spectral misfit only changes by a small amount due to the inclusion of 3D attenuation, and even increases a bit for the two-step models.

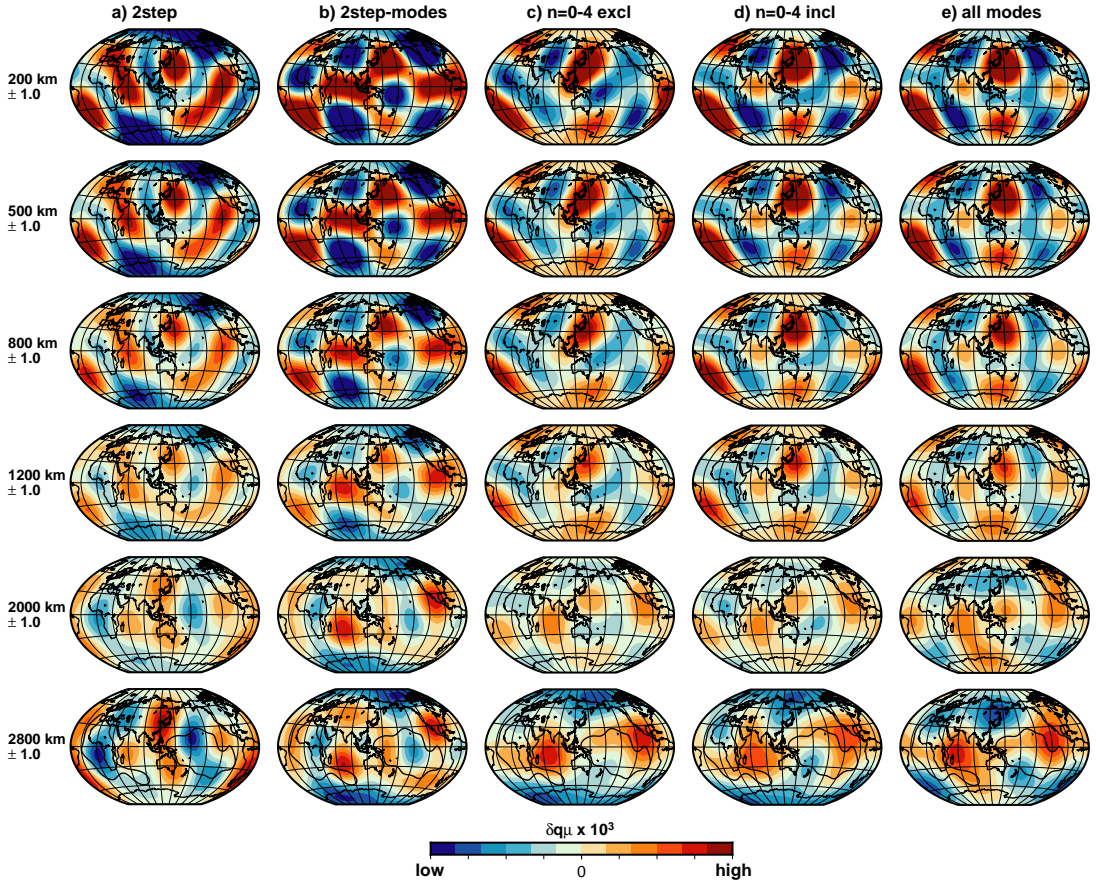


Figure 6.9: Attenuation models for real data one-step inversions (3 B-splines up to degree 4) for various subsets of normal mode data. a) Two-step q_μ model is plotted for reference. One-step q_μ models in order of increasing number of modes: b) only including the two-step modes, c) including all modes with overtone number 0-4, excluding higher order fundamentals, and d) including higher order fundamentals, and finally e) including all modes.

Several additional inversions are performed for the same model parameterization and for an increasing number of modes. The starting point is the same number of modes from the two-step splitting function inversion of Talavera-Soza et al. (2021b), for which we already described the models (Fig. 6.8; Fig. 6.9b). We then add all other modes from our normal mode data set with overtone numbers n between 0

and 4, first excluding the higher order fundamentals (Fig. 6.9c), and consequently including higher order fundamental modes with upper mantle sensitivity (Fig. 6.9d). We finally include all modes in the extended normal mode data set which was first introduced and used in Chapter 4 (Fig. 6.9e). The average spectral misfit increases with the number of modes (Fig. D1), possibly implying that some of the added modes are not contributing constructively towards an attenuation model.

Including more upper mantle sensitive modes makes the highly attenuating regions more isolated and alters their position. Ultimately only two high attenuation blobs remain in the same position with respect to the two-step model: one in the South-Atlantic Ocean and one east of China. Attenuation patterns in the lower mantle also change significantly when progressively including more modes in the one-step inversion. Whereas the cores of the LLSVPs were characterized by low attenuation for the two-step modes only (Fig. 6.9b), this low attenuation region shifts more towards the south in case of the Pacific LLSVP, and north for the African LLSVP when adding more modes. The highly attenuating ring has changed into two connected major regions of high attenuation.

Overall, adding more modes to the one-step inversion creates greater dissimilarities between the one-step model on the one hand, and two-step model created with a small subset of modes on the other hand.

The models of Fig. 6.9 were compared to each other based on the same number of effective eigenvalues. However, this picture changes when we compare them based on their optimum model, i.e. at the kink in the L-curve of each inversion (models: Fig. 6.10, L-curves: Fig. D1). The model for the two-step modes only does not change, since it was already at the kink. The other three models drastically change, having much lower numbers of effective eigenvalues and smaller model sizes than before. This observation implies that the three models depicted earlier (Fig. 6.9c,d,e), with comparable numbers of effective eigenvalues, consist of a significant portion of filled model null space. Much of the patterns remain the same in these models picked at the kink, albeit with smaller amplitudes.

In addition to the two-step model, we compare the two-step modes one-step attenuation model to upper mantle models QRLW8 (Gung & Romanowicz, 2004) and QRFSI12 (Dalton et al., 2008), showing only degrees 2 and 4 to match the degrees in our model (Fig. 6.11). The comparison shows that we are limited by our coarse radial parameterization of 3 B-splines, as the one-step and two-step attenuation models barely change across the upper mantle, whereas QRLW8 (7 cubic B-splines in depth range 80-670 km) and QRFSI12 (8 splines in depth range 24.4-650 km) do. The checkerboard pattern in the one-step upper mantle model looks very similar to QRFSI12 at 250 km depth, and also shares some large-scale features with QRLW8 at 100 km depth.

6.4.1. Starting model

We change the attenuation starting model from 1D PREM to the 3D two-step starting model, to see whether or not the one-step inversion prefers to move away from the two-step 3D attenuation model. For one test, we use the smallest subset of modes: two-step modes only. For the other test, we use the other extreme of the

number of modes used: all modes in our data base.

The resulting models we show here (Fig. 6.12b,d) are picked at the kink in the L-curve, and compared to the models resulting from the inversion started from PREM (Fig. 6.12c,e), also picked at the kink in the L-curve. The inversion moves further away from the two-step starting model towards the attenuation model started from PREM for the smallest subset of modes than for the largest set of modes. The average spectral misfit drops from 0.40 for the two-step starting model to 0.39 for the end result, which is the same as the misfit for the model started from PREM.

Let us discuss the inversion for the two-step modes first. The upper- and mid-

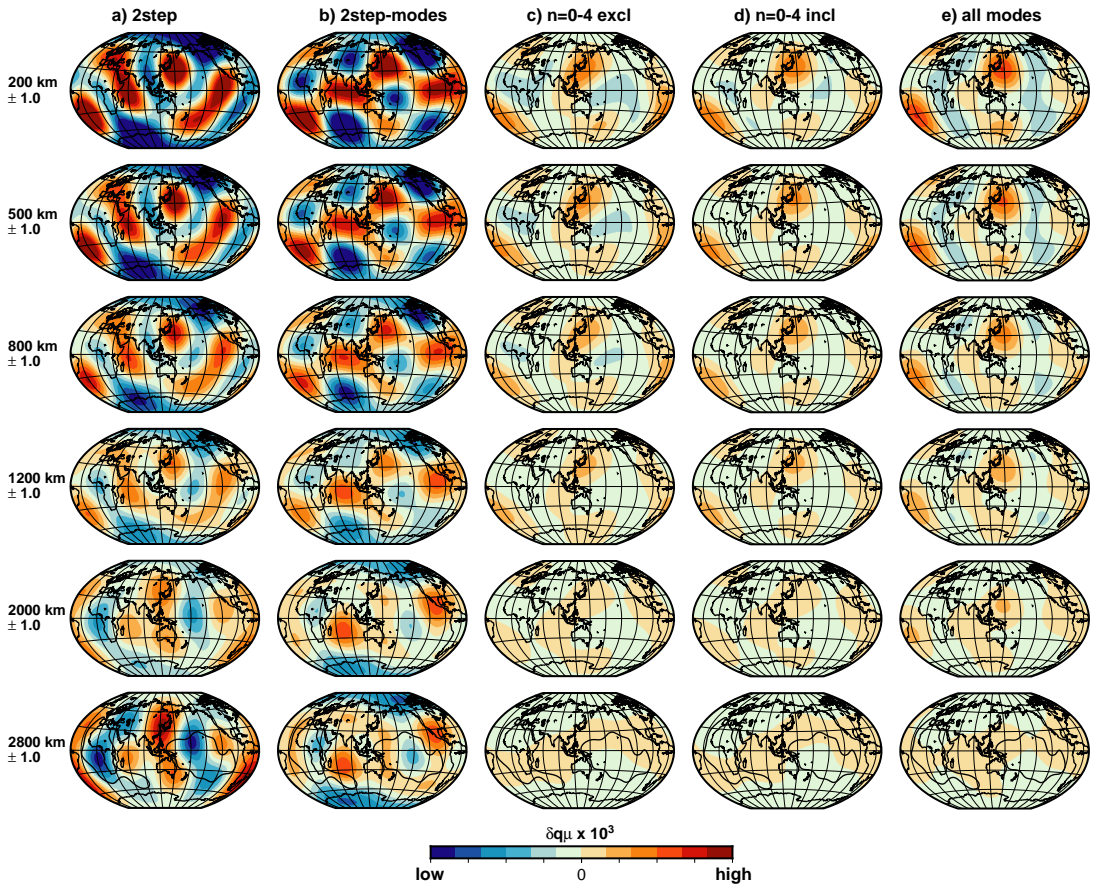


Figure 6.10: Attenuation models at the “kink” of the L-curves for real data one-step inversions (3 B-splines up to degree 4) for various subsets of normal mode data. a) Two-step v_s model is plotted for reference. One-step q_μ models in order of increasing number of modes: b) only including the two-step modes, c) including all modes with overtone number 0-4, excluding higher order fundamentals, and d) including higher order fundamentals, and finally e) including all modes.

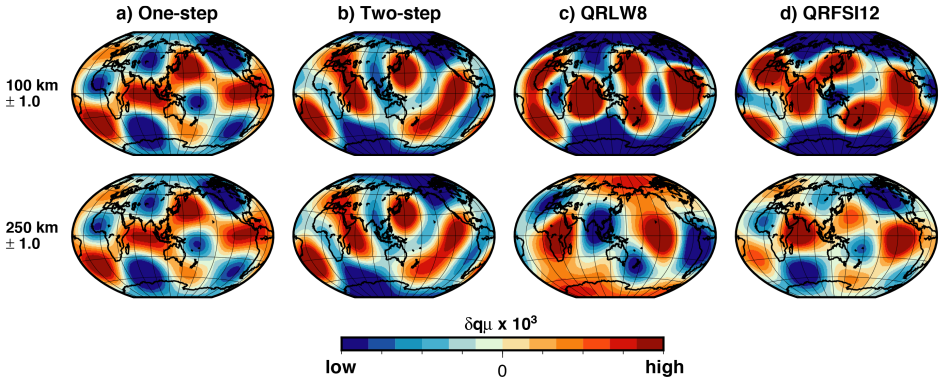


Figure 6.11: Attenuation models from the a) one-step inversion with the two-step modes, b) two-step inversion, compared to two existing upper mantle q_μ models c) QRLW8 (Gung & Romanowicz, 2004) and d) QRFSI12 (Dalton et al., 2008), only showing degrees 2 and 4.

mantle show the characteristic checkerboard pattern both when started from the two-step model (Fig. 6.12b) and when started from PREM (Fig. 6.12c). The high attenuation regions in the lower mantle east of Africa and around Mexico become stronger with respect to the starting model, which are regions of especially high attenuation in the q_μ model started from PREM.

The inversion using all normal modes is not able to move away from its starting position as easily, which makes the resulting model very dependent on the starting model. Strangely, the average spectral misfit does drop from 0.65 for the two-step starting model to 0.61 for the end result, which is comparable to the misfit of q_μ started from PREM. Apparently, very different q_μ models can yield very similar misfits if we take all modes into account. In terms of q_μ structure, we do see some hints of attenuation heterogeneities inferred from starting model PREM incorporated into the model started from the two-step q_μ model, such as the very low attenuation zones south of the Pacific and north of the African LLSVP in the deepest model slice. For lower norm damping, i.e. beyond the kink in the L-curve where the model size increases but the misfit barely decreases, the inversion started from the two-step model would produce a model very similar to that resulting from starting model PREM, with larger amplitudes.

Cross-correlation between the q_μ model started from PREM and the q_μ model started from the two-step model improves with respect to correlation between the former and the two-step starting model (Fig. 6.13). This confirms what we see in the depth slices: the model started from the two-step model moves closer to the model started from PREM, especially in the mid-mantle for the two-step modes only. Correlation between both the two-step starting model and its resulting model to the model initiated from PREM remains low in the lower mantle, so dependence on the starting model is most severe here.

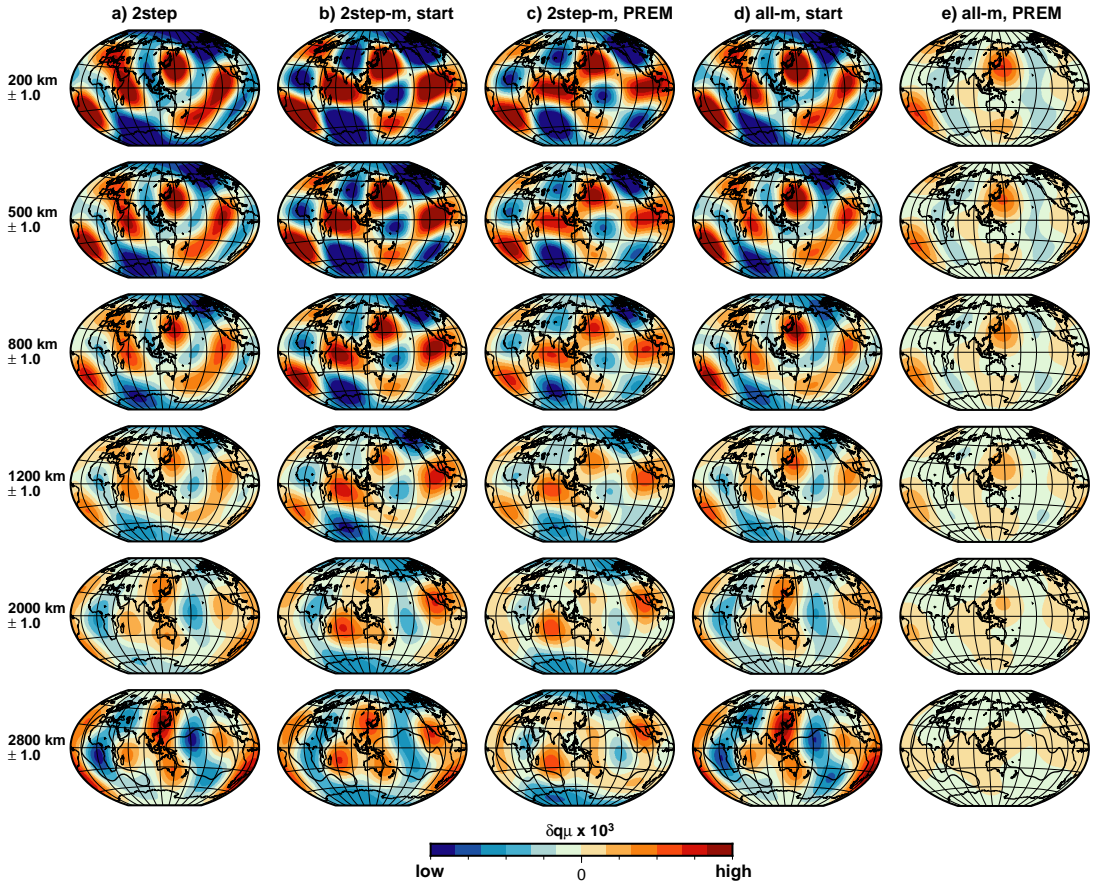
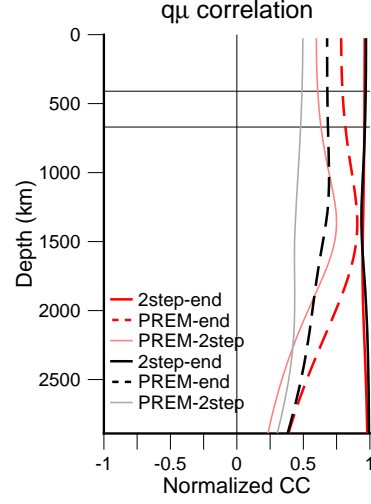


Figure 6.12: a) Starting q_μ model, b) resulting model for two-step modes subset, compared to c) the attenuation model started from PREM. Inversion results for all modes, with d) using the two-step model as starting model, and e) using PREM as starting point.

6.5. Synthetic inversions simulating real data

We now simulate a real data inversion by having more complicated input models for the synthetic data than what we invert for, contrary to the first synthetic tests at the beginning of this chapter. The final synthetic spectral data set is computed for the 3D one-step v_s , v_p and density models from Chapter 5, parameterized with 7 B-splines in the radial direction and up to degree 6 spherical harmonics laterally. The input 3D attenuation model is still the two-step model. We then either invert for v_s (v_p and density scaled to v_s with factors 0.5 and 0.3) and q_μ structure, or for v_s , v_p , density and q_μ structure. As in the recently established preferred inversion method, we invert for the elastic parameters first, and then for elastic and anelastic structures jointly. The output models are parameterized up to degree 4, and with 3 B-splines radially. We use two subsets from the normal mode data set to perform

Figure 6.13: Cross-correlation with depth between the two-step starting model and the result (red curve for two-step modes, black curve for all modes), between the resulting q_μ model started from PREM and started from the two-step model (red dashed curve for two-step modes and black dashed curve for all modes), and between the resulting q_μ model started from PREM and the two-step model (lightred curve for two-step modes and grey for all modes).



this synthetic inversion: i) the modes used by Talavera-Soza et al. (2021b) for the two-step attenuation model, and ii) the modes from Fig. 6.6 with overtone numbers $n = 0 - 4$, excluding the higher order fundamentals.

At first glance, the recovered attenuation models (Fig. 6.14b-e) do not resemble the input model (Fig. 6.14a) as well as in the previous synthetic test where the input model parameterization was the same as the output model parameterization. The effects of how many modes are included and whether or not v_p and density structure are independently inverted for are not strong. We see the same upper mantle patterns in 3D attenuation emerging from all four output models, in which the highly attenuating regions are more isolated. Recovered lower mantle patterns are slightly shifted with respect to the input models, although the low LLSVP attenuation in the input model is a shared feature among all output models.

We look at the cross-correlation with depth for the input and output models for more details on how much the heterogeneity patterns differ. From the cross-correlation between the input model on one hand and the four output models on the other hand (Fig. 6.15), we see that the upper mantle output models all have the same degree of correlation to the input model. Overall, the synthetic inversions that use the smaller two-step subset of modes recover the input model better (black curves in Fig. 6.15). Inverting for v_p and ρ heterogeneity separately from v_s (dashed curves) improves the correlation to the input model in the mid-mantle, but reduces it in the lowermost mantle.

In the previous synthetic test, we did not invert for all the input elastic structure, which has a parameterization of 7 B-splines radially and spherical harmonics up to degree 6. Not accounting for higher order elastic structure could lead to leakage in anelastic structure. Therefore, in a final synthetic test, we invert for attenuation in the same way as before, but increase either the number of B-splines, or the maximum spherical harmonic degree, or both, for the v_s part of the inversion. We use the smallest normal mode subset (two-step modes) and scale v_p and ρ anomalies

to v_s anomalies, since the previous test showed that inverting for v_s , v_p and ρ independently did not have a large impact, except in the mid-mantle.

Increasing the number of B-splines from 3 to 7 for the elastic part does not significantly affect the output attenuation model (compare Fig. 6.14b to Fig. 6.16b). Increasing the maximum spherical harmonic degree from 4 to 6 does affect the output attenuation model, towards a more positive correlation to the input model (Fig. 6.17). However, high and low attenuation regions in the lower mantle are shifted with respect to the input model (Fig. 6.16c), causing the low correlation in the lower mantle between input and output model (Fig. 6.17). When we invert the elastic part for both 7 B-splines and maximum degree 6, we finally obtain an output attenuation model that resembles the input attenuation model the most out

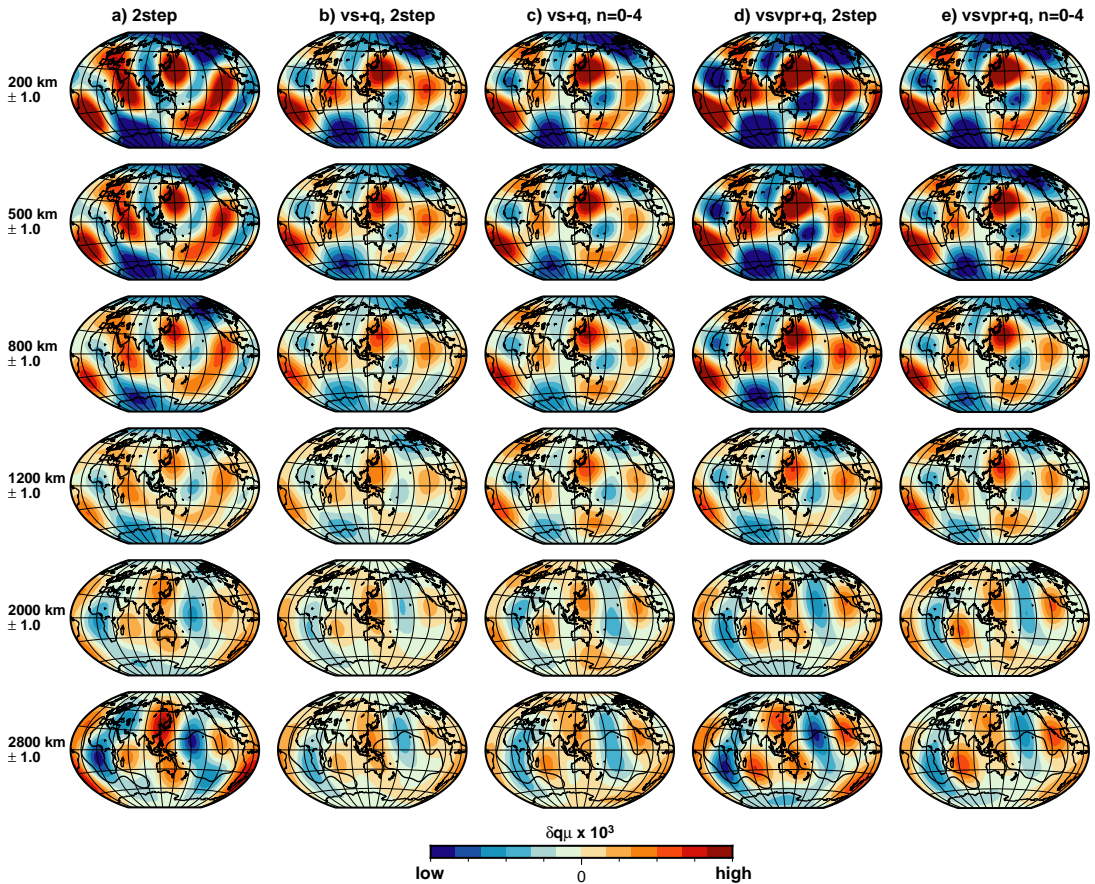


Figure 6.14: Synthetic tests for 7 B-splines up to degree 6 as elastic input models, and a) the 3 B-splines, degree 4 two-step input q_μ model. Recovered attenuation models for one-step v_s and q_μ inversion b) for two-step modes, and c) for overtone numbers 0-4. Recovered attenuation models for one-step v_s , v_p , ρ , and q_μ inversion d) for two-step modes, and e) for overtone numbers 0-4.

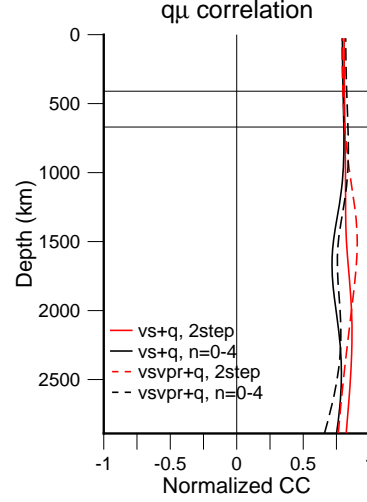


Figure 6.15: Cross-correlation with depth between the two-step input attenuation model and the four output models from Fig. 6.14b-e.

of all synthetic tests in this section, albeit with lower amplitudes. The correlation coefficient of the recovered model with the input model exceeds 0.9 in the lower mantle, and even 0.95 in the upper mantle (Fig. 6.17).

6

6.6. Discussion and conclusion

Synthetic spectra constructed for 3D input v_s and q_μ models only are well recovered, even for an increasingly complicated radial parameterization of one layer up to 3 B-splines. The best inversion method for these synthetic data is first inverting for 3D v_s structure only, keeping 1D q_μ fixed, and then allowing both 3D v_s and 3D q_μ to vary, starting from the previously obtained v_s model.

We are not able to recover q_μ anomalies as well when the synthetic spectra are computed for independent input v_s , v_p , ρ and q_μ models and we invert for elastic structures that are less detailed than the input model structures. Surprisingly, the smallest subset of modes, i.e. the two-step modes only, yields the output q_μ models that are most positively correlated to the input. Potentially because the small subset contains modes that are most sensitive to 3D variations in shear attenuation.

We see the same checkerboard-like structure in upper mantle q_μ in the above-mentioned synthetic tests as in real data inversions. It is not until we invert for all the complexities in the elastic input models, especially in the v_s model, that we get rid of this checkerboard pattern and are able to recover the input model attenuation structure accurately. This should then also be applied to the real data inversions, where elastic structure was kept very simple for now, to minimize leakage of elastic into anelastic structure. It could explain the discrepancies between the attenuation models derived from splitting functions (Talavera-Soza et al., 2021b) and from the spectra directly. Leakage might be less of a problem in a two-step splitting function inversion, since elastic and anelastic structures are conveniently separated into c_{st} and d_{st} coefficients.

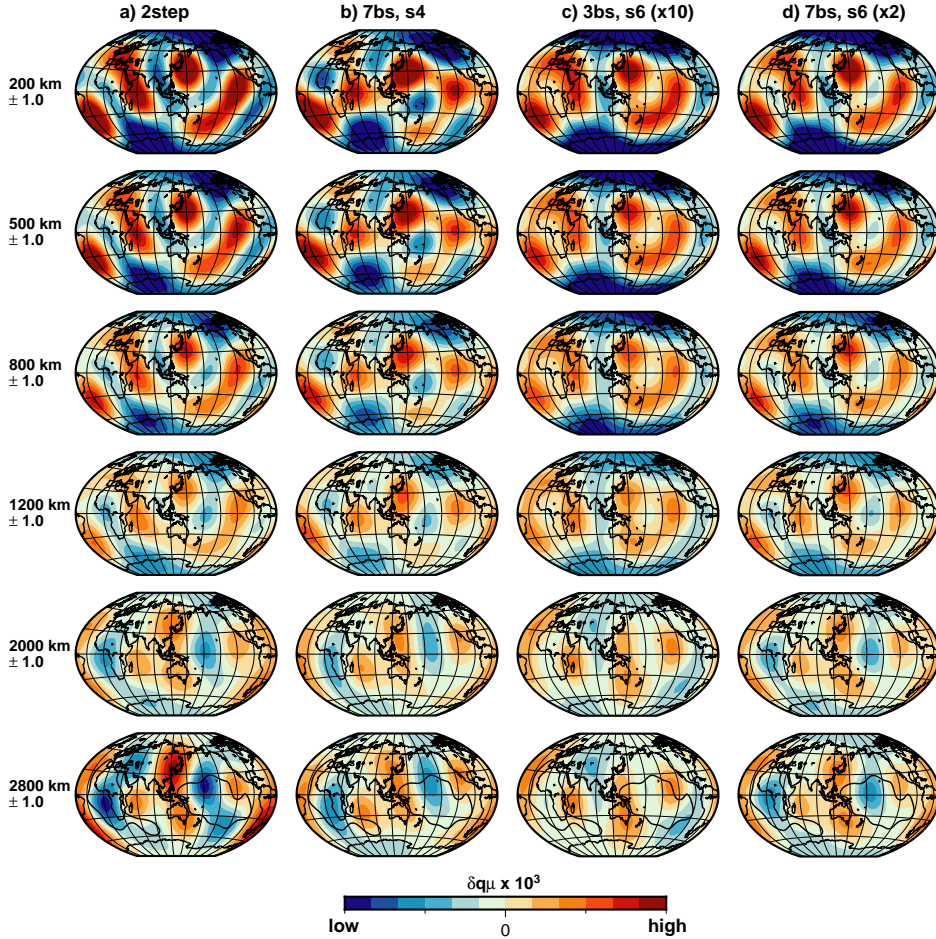
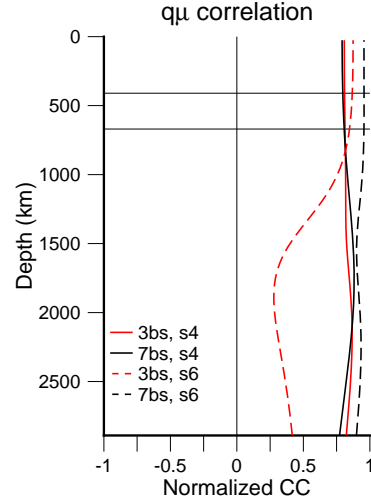


Figure 6.16: Synthetic tests for 7 B-splines up to degree 6 as elastic input models, and various output parameterizations for the elastic part. a) 3 B-splines, degree 4 two-step input q_μ model. Recovered attenuation models for one-step v_s and q_μ inversion for two-step modes, for parameterization for the elastic part b) of 7 B-splines, up to degree 4, c) of 3 B-splines, up to degree 6, d) of 7 B-splines, up to degree 6.

The real data inversions have shown that we have to be careful about mode selection in the inversion part where elastic and anelastic structures are jointly inverted for. By selecting too many modes to constrain attenuation structure, we run the risk of fitting normal mode spectra of modes that do not carry much information on mantle shear attenuation, thereby filling the model null space. This problem affects the two-step subset of modes the least, out of all the subsets we investigated.

As this is a preliminary study into the feasibility of applying the direct spectrum inversion to attenuation, without a thorough investigation into source effects, we cannot draw any definite conclusions yet on the attenuation structure of the

Figure 6.17: Cross-correlation with depth between the two-step input attenuation model and the three output models from Fig. 6.16b-d. Cross-correlation between the two-step input model and the recovered attenuation model for 3 B-splines, max. degree 4 is shown for reference (solid red).



mantle. However, the centers of LLSVPs remain low attenuation zones for the real data inversion of the two-step modes, which is a promising result for the robustness of this observation. Low attenuation in LLSVPs may be explained by larger grain size (low attenuation) dominating over higher temperature (high attenuation) effects (Dannberg et al., 2017). In turn, the high attenuation regions around the LLSVPs could be due to post-perovskite, which has been shown to be possibly highly attenuating (Goryaeva et al., 2016) and potentially fine-grained (Yoshino & Yamazaki, 2007). Post-perovskite is also preferentially linked to colder regions such as a slab graveyard surrounding LLSVPs. If normal modes prefer low attenuation in LLSVPs, we have to find a way to reconcile these normal mode observations of low attenuation with body wave observations of highly attenuating LLSVPs.

D1. Appendix D

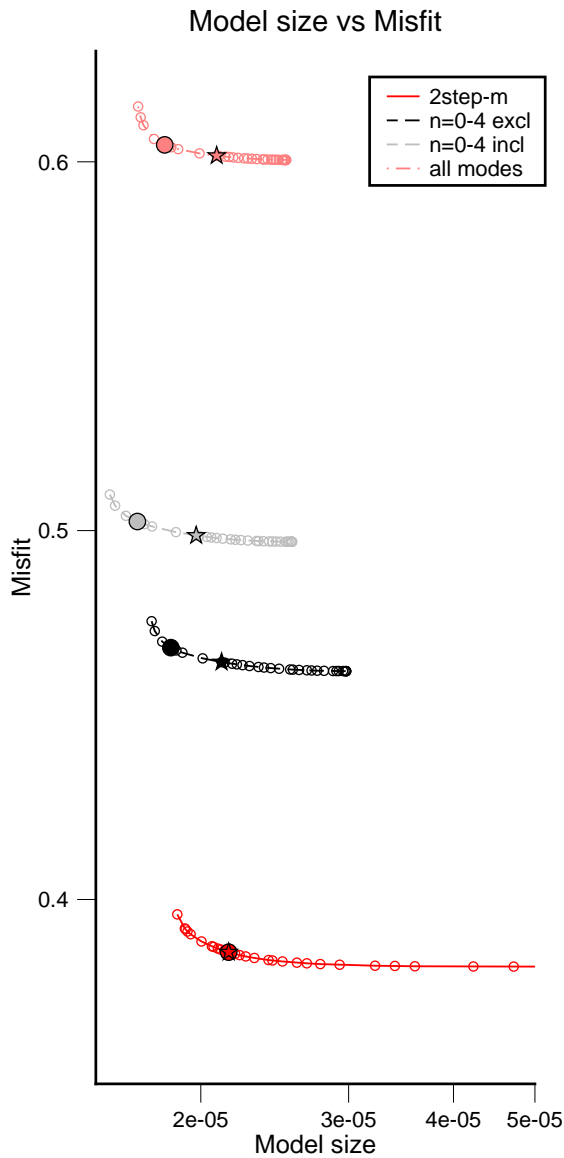


Figure D1: Misfit versus model size L-curves for real data $v_s + q_\mu$ inversions, first iteration, for different numbers of modes: only including the two-step modes (red), including all modes with overtone number 0-4, excluding higher order fundamentals (black), and including higher order fundamentals (grey), and including all modes (lightred). Big filled-in circles represent models chosen at the “kink” and stars represent models chosen for comparable numbers of eigenvalues.

7

Synthesis

7.1. General findings

The aim of this thesis was to provide novel constraints on the thermochemical nature of the lower mantle, and the LLSVPs specifically. In order to do so, we have performed, in chronological order, the one-step direct spectrum inversion and two-step splitting function inversion for i) v_s only, ii) v_s and v_p jointly, iii) v_s , v_p , density and topography on the 400- 670- and CMB-discontinuities jointly, and finally iv) the one-step inversion for v_s and q_μ jointly. With each additional parameter, the difference between the one-step and two-step models increases, as normal mode sensitivity decreases for v_p compared to v_s , and decreases even more for density and attenuation. Both inversion methods are always started from the same initial spectral data set, so we conclude that the inversion method generally matters more for the resulting models when normal mode sensitivity decreases for a certain parameter.

In Chapter 3 we find that the average spectral misfit is lower for the one-step v_s inversion than for the two-step v_s inversion. In later chapters we see that the average spectral misfits for the one-step inversion are lower for every combination of mantle parameters we invert for. This is to be expected, as the second step of the two-step inversion tries to fit the intermediate splitting functions, originally derived from the spectra, whereas the one-step inversion fits the spectra directly.

The effect of the chosen inversion method on thermochemical interpretations is already significant when inverting for v_s and v_p structure (Chapter 4), on top of the effect of how the ratio $R_{S/P}$ between v_s and v_p anomalies is computed. The 1D representative R-RMS, obtained by dividing the RMS amplitudes of the v_s and v_p models, exceeds $R_{S/P}$ predicted for a thermally dominated mantle in the lower mantle, agreeing with previously inferred chemical heterogeneity. R-RMS subsequently strongly decreases towards the CMB, which also agrees with previous studies. R-median, on the other hand, is always lower than $R_{S/P}$ predicted for a thermally dominated mantle, except for the two-step models just above the CMB. 1D $R_{S/P}$ are therefore less robust and heavily debated, and we prefer to look at the distributions of v_s , v_p anomalies and $R_{S/P}$. Both the one-step and two-step models show a

large spread in v_s anomalies in the lower mantle, coinciding with the depth range of high R-RMS values. On top of that, we infer a dominant role of chemical heterogeneity for the depth range 1100-1400 km from the one-step inversion, based on the wide spread of $R_{S/P}$ and a de-correlation between v_s and v_p structure, whereas we infer chemical heterogeneity around 200-670 km depth in the two-step inversion, based on the wide spread of v_s anomalies and $R_{S/P}$.

The inversion method also affects S- Φ correlation derived from our joint 7 B-splines $v_s + v_\phi$ real data inversions (Chapter 4). We must be cautious when interpreting upper and lowermost mantle bulk sound velocity anomalies because of their high starting model dependency and large ghost patterns, especially in the two-step inversion. This is also where the one-step and two-step model deviate the most from each other. Patterns in 3D v_ϕ agree well in the rest of the mantle. The one-step correlation never becomes negative, whereas the two-step correlation does move towards anti-correlation in the lower mantle, albeit still close to de-correlation. We obtain more negative S- Φ correlation in the lower mantle when extracting $\delta \ln v_\phi$ from 7 B-splines v_s and v_p models, and even more negative for 21 splines v_s and v_p models computed in this chapter.

We make robust normal mode observations of mantle density structures in Chapter 5, of comparable amplitude to v_p anomalies, which are not suffering from strong ghost patterns observed previously. The one-step density inversion is less affected by the starting model, although both the one- and two-step inversions show the same large-scale features independent of the starting model. De-correlation of v_s and density anomalies in the upper mantle leads to another hint towards chemical heterogeneity, since a purely thermally dominated mantle would result in positive correlation. Correlation between 3D v_s and density increases towards the lower mantle, and decreases again towards the CMB, reflecting a possible thermal dominance in the mid-lower mantle, and chemical heterogeneity at the base of the mantle. The most striking feature at the base of the mantle is a dense sliver underlying part of the otherwise low density LLSVPs. Such a dense base could reconcile previously conflicting observations of lower mantle LLSVP density.

Finally, in Chapter 6, we obtain promising results for imaging 3D variations in shear attenuation in the mantle, especially in the relatively unknown lower mantle, with the one-step inversion for the first time. Synthetic tests recovering input v_s and q_μ structure lead to a preferred way of inverting for elastic (v_s) structure first, keeping q_μ fixed, and using the resulting model as starting point for a joint inversion of elastic and anelastic structure ($v_s + q_\mu$). Applying this method to real data is challenging, probably because of the small spectral signal of attenuation. Selecting modes with sufficient sensitivity to shear attenuation is important, as adding more and more modes with only limited sensitivity does not guarantee a better attenuation model. It also appears to be crucial to resolve fine-scale elastic structure to avoid leakage of such unresolved structure into attenuation. Our one-step attenuation model shares some similarities with the two-step model by Talavera-Soza et al. (2021b), using the same normal mode data set, but differs in the position of high- and low-attenuation regions.

7.1.1. On the nature of LLSVPs

We have provided novel observations of the large-scale structure of LLSVPs. To summarize our findings, we show cross-sections through our preferred v_s and v_p models from Chapter 4 (Figs. 7.1a-d and 7.2a-d) with higher radial (21 splines) and lateral resolution (up to degree 12) than in the combined v_s , v_p , ρ and discontinuity topography from Chapter 5 (7 B-splines, up to degree 6). Our preferred density models do originate from this latter inversion (Figs. 7.1e,f and 7.2e,f). The attenuation models shown in this summary (Figs. 7.1g,h and 7.2g,h) are derived from the smallest subset of modes used in Chapter 6, so for the same modes as in the splitting function inversion of Talavera-Soza et al. (2021b). These models have the lowest resolution, both radially and laterally, which will very likely improve in the continuation of the research presented here. We also show depth slices at 2800 km through these four models (Fig. 7.3).

The LLSVPs (or LLVPs) are expressed differently in models of v_s and v_p , with a more concentrated low-velocity base in v_s and more diffuse low velocity anomalies in v_p , especially in the two-step v_p model. As noted before, low velocity material is horizontally deflected at various depths in the mantle, suggesting ponding of plume material potentially due to viscosity contrasts. We are not able to image individual plume conduits with normal modes, so instead we might be looking at the smeared version of several adjacent plumes.

LLSVPs are mostly slow and lighter-than-average structures, reflecting a dominant role of temperature, except for part of their base. There we find a slow yet dense basal sliver, which has to be compositionally distinct. Potential candidates for this layer are (i) enrichment in iron, either through penetration from outer core material into the solid mantle or through iron partitioning in partial melt, (ii) recycling of MORB over millions of years creating warm low velocity blobs with a dense base of basaltic material, if MORB is sufficiently dense, or (iii) a layer of preserved dense primordial material, i.e. remnants of an ancient magma ocean.

Although shifted in position, the bulk of LLSVPs is characterized by low attenuation in both the one-step and two-step models. Low attenuation in LLSVPs can be explained by larger grain size dominating over higher temperature effects. However, with the current resolution, we cannot rule out smaller volumes of high attenuation below the detection limit. The high attenuation regions around the LLSVPs could be due to highly attenuating fine grain-sized post-perovskite. Post-perovskite is preferentially linked to colder regions such as a slab graveyard surrounding LLSVPs, fitting this hypothesis.

7.2. Suggestions for future work

A number of interesting future research directions arise from the results presented in this thesis. Here we present some ideas that would contribute to valuable insights into the nature of the Earth's deep interior, but have not been carried out in this thesis due to time limitations.

- We have only shown preliminary results for the one-step attenuation inversion due to time constraints. Synthetic inversions demonstrate that our real data

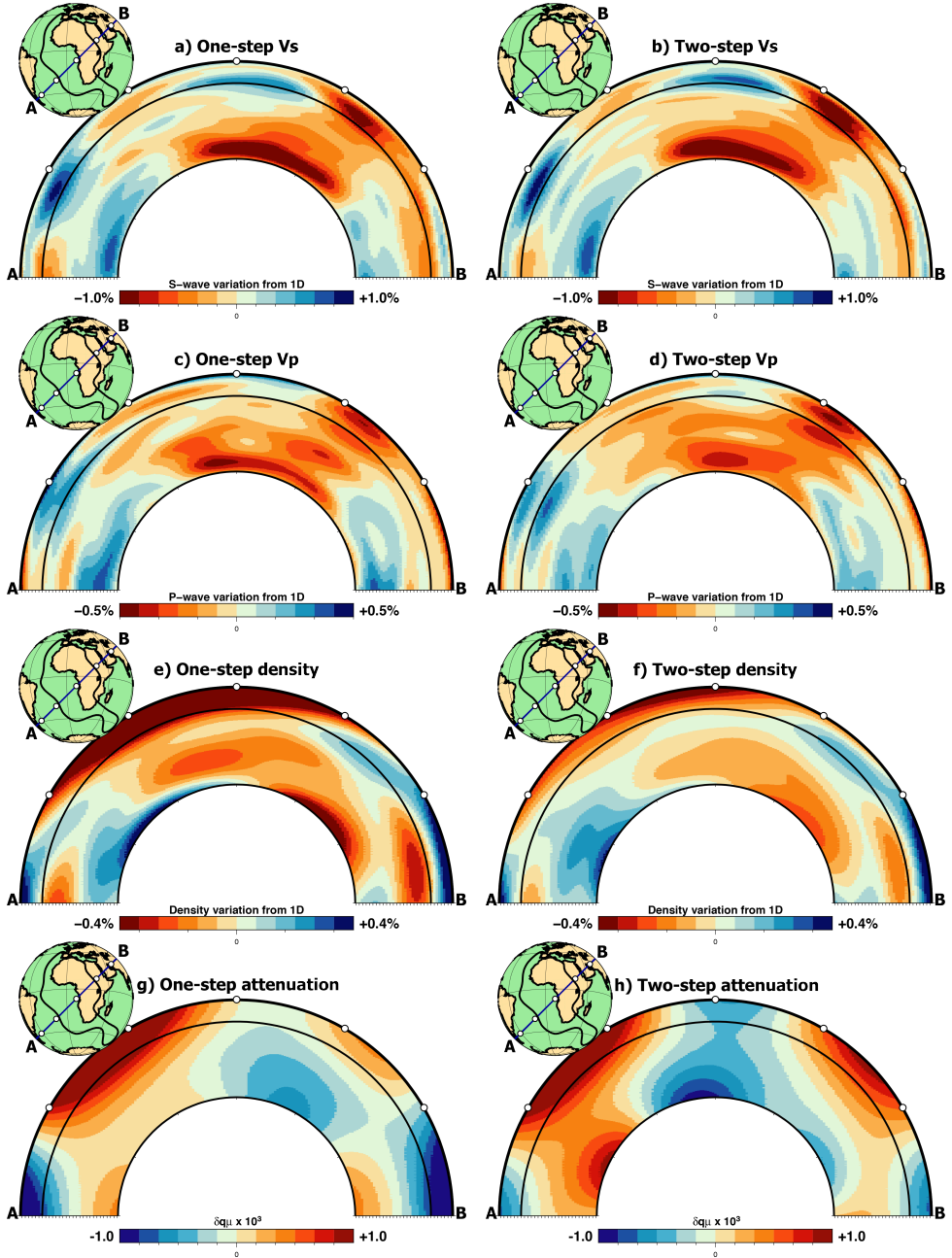


Figure 7.1: Summary of cross-sections through the African LLSVP in preferred one-step (left column) and two-step (right column) models, with a) one-step v_s model, b) two-step v_s model, c) one-step v_p model, d) two-step v_p model from Chapter 4; e) one-step and f) two-step density models from Chapter 5; g) one-step and h) two-step shear attenuation Talavera-Soza et al. (2021b) models from Chapter 6. Cross-sections through the Pacific LLSVP look the same, due to inclusion of even degrees only. The 670-discontinuity is shown by a black line.

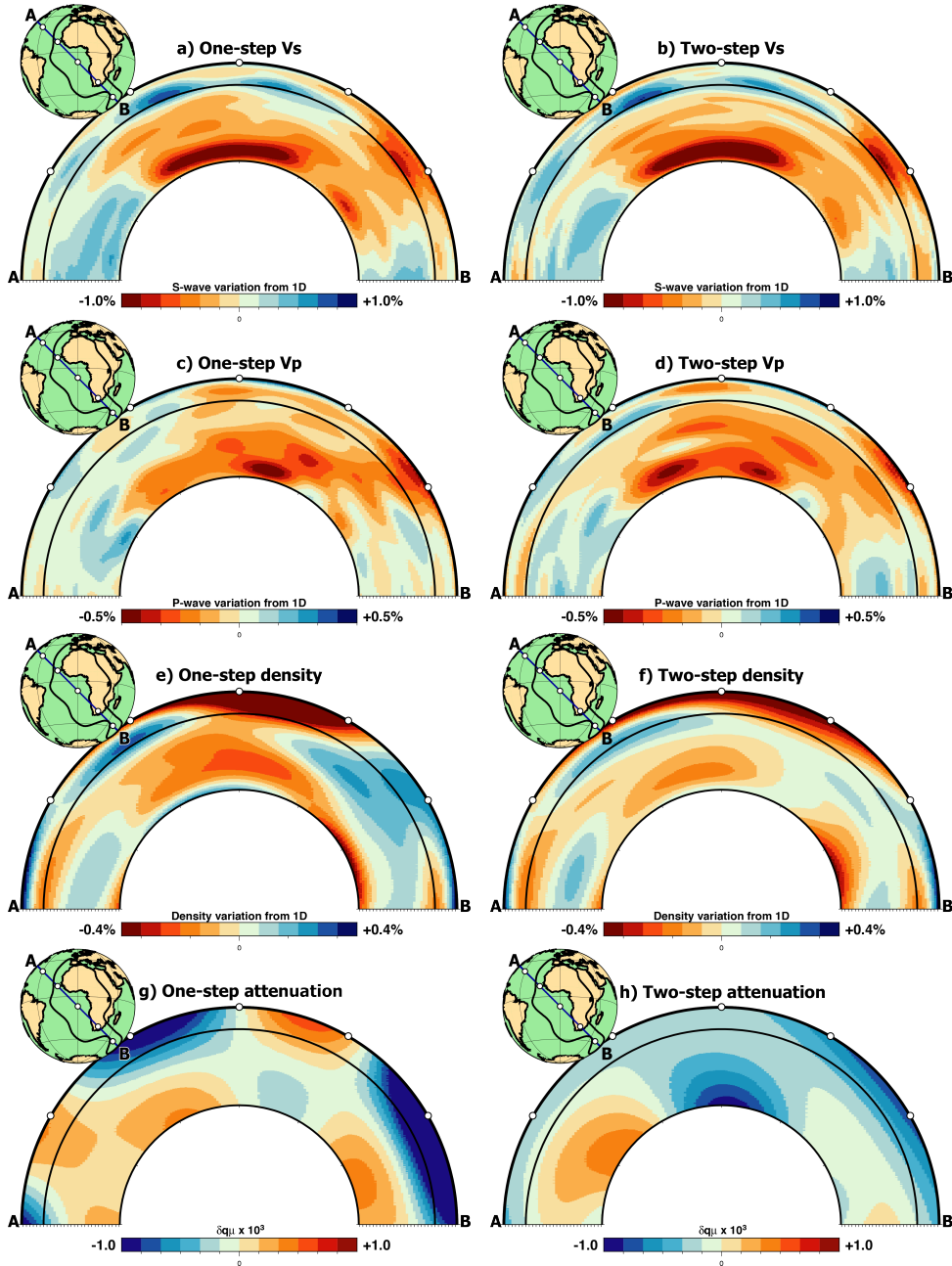


Figure 7.2: Same as in Fig. 7.1, but for a different cross-section.

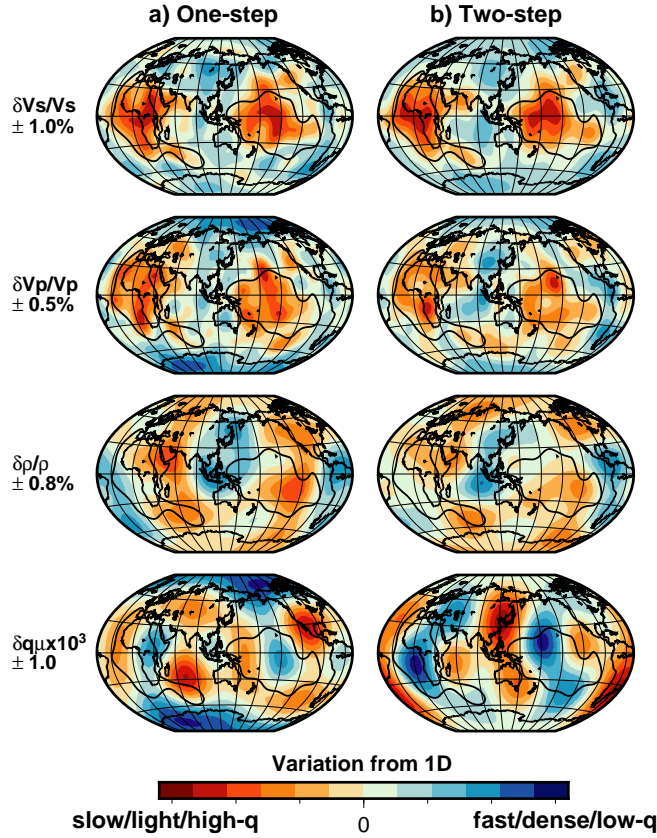


Figure 7.3: Depth slices at 2800 km through a) the preferred four one-step models for v_s , v_p , ρ and q_μ heterogeneity, and b) the four two-step models for the same variables.

one-step attenuation models could be improved by inverting for more complex elastic structures, to reduce any leakage from elastic to anelastic structures. Other future endeavours related to attenuation include an assessment of source uncertainties, and the inclusion of proper ellipticity corrections.

- One of the most obvious next steps is to increase the extent of group coupling. The current normal mode data set is limited to self- and group coupling in the one-step direct spectrum inversion, with a maximum of three modes cross-coupled per mode group. This limited amount of cross-coupling was dictated by working with an un-parallelized legacy code. Full-coupling in a certain frequency band is the most accurate method for computing synthetic spectra, but requires a lot of computational power and fundamental changes to the entire code. We therefore first need to parallelize certain pieces of the code (e.g. computation of partial derivatives) to be able to handle a gradual increase in cross-coupling smoothly.

- ▷ Part of the reason for expanding the cross-coupling between modes is introducing more odd-degree sensitivity. We have seen in Chapter 3 that our current normal mode data set contains significantly more mode pairs that couple for even-degree than odd-degree structure. LLSVPs are dominated by degree 2 structure, but do not necessarily share the same thermochemical signature and origin (Doucet et al., 2020). Constraints on odd-degree heterogeneity in LLSVPs primarily come from body waves in joint inversions for normal modes, surface waves and body waves (e.g. Ritsema et al., 2011; Koelemeijer et al., 2016), but it will be insightful to add large-scale normal mode observations by extending cross-coupling for odd degrees.
- We have largely neglected one of the two main types of normal modes in this thesis: toroidal modes. Recent advances in toroidal mode splitting function measurements on the horizontal components of seismograms (Schneider & Deuss, 2021) spark new research ideas, as toroidal modes provide more information on horizontally polarized structures. These measurements can be easily added to our spheroidal vertical component data set, both in terms of spectral segments for the one-step inversion, and in terms of splitting functions for the two-step inversion.
 - ▷ Adding observations from toroidal modes and spheroidal-toroidal cross-coupling constrains anisotropy in the mantle, which is an indicator of mantle flow patterns. Anisotropy in the deep Earth has primarily been mapped using body waves, such as S-wave splitting (e.g. Vinnik et al., 1989; Reiss et al., 2019). When inverting for anisotropy, it might be important to include attenuation as well, to account for dispersion effects (Karaoğlu & Romanowicz, 2018). The first steps of including mantle anisotropy involve solving for the most simple forms of anisotropy: radial and azimuthal anisotropy.
- The novel normal mode observations of lower mantle density presented in Chapter 5 can be used as a basis for geodynamic modelling, to find a geodynamically viable origin for the partly dense base of LLSVPs. The geodynamic density model has to be subjected to a tomographic filter before being compared to our normal mode density model, as the latter model has limited resolution with maximum spherical harmonic degree 6 or 12. As well as fitting our density observations, this geodynamic model should also comply with our 3D v_s and v_p models. The modelled geochemical assemblages and temperatures have to be translated to seismic velocities, for example through lookup tables generated for a thermodynamic mineralogical model of specific mantle composition (Stixrude & Lithgow-Bertelloni, 2011).
- We have looked at anomalies of isotropic S-wave and P-wave velocity and density in a joint inversion, and v_s and shear attenuation in another joint inversion. In an ultimate inversion we would invert for all of these parameters at once, including anisotropy, to minimize any trade-offs.
 - ▷ The inner core is a region of strong anisotropy, partially constrained by

normal mode studies (e.g. Durek & Romanowicz, 1999; Beghein & Trampert, 2003). The scope of this thesis excluded the inner core, and hence the inner core sensitive modes have been excluded from our inversions to avoid inner core heterogeneity falsely mapped as mantle anomalies. In future studies, inner core sensitive modes may be included, to solve for a combined model of simple inner core anisotropy and mantle structure, similar to Ishii & Tromp (2004). The addition of inner core modes in their study did not alter the density patterns, but did help to constrain density amplitudes. Interaction or cross-coupling between inner core and mantle modes potentially provides new insights on mantle anomalies.

Acknowledgements

My time here in Utrecht is finally drawing to a close; after a BSc, MSc and PhD degree I quietly seem to have become “deel van het meubilair” (which translates to “part of the furniture”). It feels strange to leave all the familiar faces and places, but I am ready to embrace a new environment!

First and foremost, I would like to thank my promotor Arwen Deuss for her guidance throughout the past 4.5 years. I am grateful to have gotten the opportunity to continue seismology research after my master’s thesis project, and to venture into the interesting world of normal modes. I have learnt a great deal from you academically, and I appreciate your ongoing support and concern for the wellbeing of your students, which was especially valuable during the pandemic.

I would also like to thank committee members Sanne Cottaar, Gabi Laske, Jeroen Ritsema, Barbara Romanowicz and Jeannot Trampert for taking the time to read my thesis and providing useful and insightful comments and suggestions. Special thanks to Sanne for welcoming me into the Cambridge group, and for giving me the opportunity to revisit body waves.

This PhD experience has been extraordinary thanks to Su and Simon, aka #cbreakoffe, aka the 2.40 gang. Thank you very much for taking the time from your busy lives to be my paronyms! From our first conference together (the unforgettable GRC near Boston) until the last (virtual) coffee chats, it has been a fantastic ride filled with beer-drinking at FEST/poster sessions/random places in Utrecht, arm-waving in the office to get each other’s attention, scaring people away in a bar in Vancouver with our rendition of Bohemian Rhapsody (with Alberto and Rûna of course), beaver and squirrel adventures, and the first year Earth Sciences party that never happened. It is the end of an era, as Simon said, and it’s very sad we will no longer share an office, or even live in the same country, but I’m sure we will visit each other (and do more road triiips!).

Many thanks to Elmer and Hanneke for guiding me through the first steps in conducting research as a bachelor’s student and writing a paper on it. Thank you to Hanneke for chatting about cycling holidays and always giving great advice, and to Ivan for introducing me to reverse time migration during my master’s thesis. Thanks to current and past seismology staff members Jeannot, Laura, Theo, Arie, Henk, Rhys, Kabir, Yanadet and Haydar, for the good times and scientific input, and to honorary member Paula, for answering my silly questions.

I also remember the good old times in Van Unnik with former office mates Wen and Haorui fondly. Wen, thank you for inviting us into your home for Chinese new year and getting to know your lovely little family, and for forwarding job offers I had not seen yet. Haorui, you always manage to put a smile onto everybody’s faces with your out-of-the-blue comments and stories (and delicious food!). I would like to thank all of the current and past seismos Ashim, Rûna, Henry, David, Leon,

Janneke, Thomas, Eldert, Rens, Loes, Annemijn, Sahar, Nienke, Maria, Evangelos, Suzanne, and honorary members of the seismo family Alberto, Antoine, Tracy, Cindy, Qianqian, Linyu, Dilaila, Ronja, for the amazing memories these past few years.

They say that exercise is good for the mind, which was definitely true during various lockdowns, so a special mention for the groups from cycling (Simon, Ashim, Boris), climbing (Jetske, Simon, Dilaila), football (Alberto, David, Leon, Haorui, Ashim, Rûna, Andreas, and students), spinning (Jetske, Boris, Niels), and the most consistent factor in my life: the Olympos running group, led by the wonderful José.

And now a few words in Dutch: mijn studie jaren waren niks zonder aardwetenschappen/aardwetenschattjes Bente, Iris, Laura, Imke, Sara, Guus, Roald, Carlijne en Yvette. We hebben met z'n allen fantastische veldwerken, stedentripjes, Sinterkersten-nieuwvieringen, en natuurlijk de (semi-)wekelijkse kookavondjes in en om Utrecht meegemaakt. Alhoewel de frequentie dat we elkaar zien uiteraard wat naar beneden is bijgeschroefd, blijft het altijd fijn om nieuwe herinneringen met elkaar te maken! Ik had ook het geluk om in een heel gezellig studentenhuys in Zeist terecht te komen, met Jetske, Julian, Niels, Franka en nog veel meer leuke mensen. Daar heb ik ook geleerd om nooit meer al mijn muren rood en oranje te verven...

De jaren vóór de universiteit heb ik gedeeld met het clubje van Old School: Anouk, Hannah, Lisa, Esther, Rebecca, Tessa en Febe. Ik vind het tof dat we tien jaar na de middelbare nog steeds contact hebben! Wat zijn we groot geworden hè, met huwelijken, huizen kopen en volwassen banen... Bedankt Meneer van den Bor, voor de geweldige aardrijkskundelessen en het delen van uw fascinatie voor stenen. Hopelijk hebben ze daarboven heerlijke omfietswijken, proost!

Als laatste wil ik natuurlijk stilstaan bij m'n kleine maar fijne familie. Nadia, je verdient al het geluk in de wereld, en wat is het fijn dat je Abderrahim weer hebt gevonden. Ik ben verder vereerd om in de voetsporen te treden van de originele doctoren Jagt: ome John en tante Elena. Pap en mam, veel dank voor jullie steun (op allerlei manieren) en interesse in wat ik heb gedaan in de afgelopen jaren. Dit proefschrift is voor jullie! Mir, ik kijk op tegen je doorzettingsvermogen, waardoor je het tot een studie rechten hebt geschopt! Jij en Lars zijn toppers, en het is altijd gezellig met jullie. Ook bedankt aan mijn schoonfamilie voor, zoals mijn moeder het beschreef, "een warm bad" waarin ik terecht ben gekomen. Is het raar om de hondjes te bedanken? Ik doe het gewoon: Pip en Ody, bedankt voor al jullie opgewektheid! En ik vergeef jullie voor het opeten en uitkotsen van mijn oordopjes toen jullie kwamen logeren.

Lieve Boris, we hebben elkaar door het begin van de pandemie gesleept met fietstochtjes, theesessies op de bank, Pandemic spelen en hardlooprondjes. Sorry voor de sneertjes die je te verduren kreeg in stressvolle periodes, maar gelukkig kreeg ik er uiteindelijk ook een paar terug ;) We gaan spannende nieuwe tijden tegemoet, maar ik heb er alle vertrouwen in en vooral ook zin in om die met jou te beleven!

Bibliography

- Adenis, A., Debayle, E., & Ricard, Y., 2017. Attenuation tomography of the upper mantle, *Geophysical Research Letters*, **44**(15), 7715–7724.
- Akbarashrafi, F., 2020. *Resolvability of the 3D density structure of the Earth's mantle using normal mode theory*, Ph.D. thesis, University Utrecht.
- Akbarashrafi, F., Al-Attar, D., Deuss, A., Trampert, J., & Valentine, A., 2018. Exact free oscillation spectra, splitting functions and the resolvability of Earth's density structure, *Geophysical Journal International*, **213**(1), 58–76.
- Al-Attar, D., Woodhouse, J. H., & Deuss, A., 2012. Calculation of normal mode spectra in laterally heterogeneous Earth models using an iterative direct solution method, *Geophysical Journal International*, **189**(2), 1038–1046.
- Anderson, D. L., 2006. Speculations on the nature and cause of mantle heterogeneity, *Tectonophysics*, **416**(1-4), 7–22.
- Anderson, D. L. & Given, J. W., 1982. Absorption band Q model for the Earth, *Journal of Geophysical Research: Solid Earth*, **87**(B5), 3893–3904.
- Antolik, M., Gu, Y. J., Ekström, G., & Dziewonski, A. M., 2003. J362D28: a new joint model of compressional and shear velocity in the Earth's mantle, *Geophysical Journal International*, **153**(2), 443–466.
- Austermann, J., Kaye, B. T., Mitrova, J. X., & Huybers, P., 2014. A statistical analysis of the correlation between large igneous provinces and lower mantle seismic structure, *Geophysical Journal International*, **197**(1), 1–9.
- Badro, J., Fiquet, G., Guyot, F., Rueff, J.-P., Struzhkin, V. V., Vanko, G., & Monaco, G., 2003. Iron partitioning in Earth's mantle: toward a deep lower mantle discontinuity, *Science*.
- Ballmer, M. D., Schmerr, N. C., Nakagawa, T., & Ritsema, J., 2015. Compositional mantle layering revealed by slab stagnation at ~ 1000-km depth, *Science advances*, **1**(11), e1500815.
- Ballmer, M. D., Schumacher, L., Lekic, V., Thomas, C., & Ito, G., 2016. Compositional layering within the large low shear-wave velocity provinces in the lower mantle, *Geochemistry, Geophysics, Geosystems*, **17**(12), 5056–5077.
- Ballmer, M. D., Houser, C., Hernlund, J. W., Wentzcovitch, R. M., & Hirose, K., 2017. Persistence of strong silica-enriched domains in the Earth's lower mantle, *Nature Geoscience*, **10**(3), 236–240.
- Becker, T. W. & Boschi, L., 2002. A comparison of tomographic and geodynamic mantle models, *Geochemistry, Geophysics, Geosystems*, **3**(1).

- Beghein, C. & Trampert, J., 2003. Robust normal mode constraints on inner-core anisotropy from model space search, *Science*, **299**(5606), 552–555.
- Biondi, B. & Almomin, A., 2014. Simultaneous inversion of full data bandwidth by tomographic full-waveform inversion, *Geophysics*, **79**(3), WA129–WA140.
- Biot, M. A., 1965. *Mechanics of incremental deformations*, John Wiley & Sons, Inc.
- Bower, D. J., Gurnis, M., & Seton, M., 2013. Lower mantle structure from paleogeographically constrained dynamic Earth models, *Geochemistry, Geophysics, Geosystems*, **14**(1), 44–63.
- Brandenburg, J. & Van Keken, P., 2007. Deep storage of oceanic crust in a vigorously convecting mantle, *Journal of Geophysical Research: Solid Earth*, **112**(B6).
- Brodholt, J. P., Helffrich, G., & Trampert, J., 2007. Chemical versus thermal heterogeneity in the lower mantle: The most likely role of anelasticity, *Earth and Planetary Science Letters*, **262**(3–4), 429–437.
- Bullen, K., 1949. Compressibility-pressure hypothesis and the Earth’s interior, *Geophysical Journal International*, **5**, 335–368.
- Burke, K., 2011. Plate tectonics, the Wilson Cycle, and mantle plumes: geodynamics from the top, *Annual Review of Earth and Planetary Sciences*, **39**, 1–29.
- Burke, K., Steinberger, B., Torsvik, T. H., & Smethurst, M. A., 2008. Plume generation zones at the margins of large low shear velocity provinces on the core–mantle boundary, *Earth and Planetary Science Letters*, **265**(1–2), 49–60.
- Chaloner, J. W., Thomas, C., & Rietbrock, A., 2009. P-and S-wave reflectors in D” beneath southeast Asia, *Geophysical Journal International*, **179**(2), 1080–1092.
- Chandler, B. C., Chen, L.-W., Li, M., Romanowicz, B., & Wenk, H.-R., 2021. Seismic anisotropy, dominant slip systems and phase transitions in the lowermost mantle, *Geophysical Journal International*, **227**(3), 1665–1681.
- Chantel, J., Manthilake, G., Andrault, D., Novella, D., Yu, T., & Wang, Y., 2016. Experimental evidence supports mantle partial melting in the asthenosphere, *Science advances*, **2**(5), e1600246.
- Christensen, U. R. & Hofmann, A. W., 1994. Segregation of subducted oceanic crust in the convecting mantle, *Journal of Geophysical Research: Solid Earth*, **99**(B10), 19867–19884.
- Cline II, C., Faul, U., David, E., Berry, A., & Jackson, I., 2018. Redox-influenced seismic properties of upper-mantle olivine, *Nature*, **555**(7696), 355–358.
- Cobden, L. & Thomas, C., 2013. The origin of D” reflections: A systematic study of seismic array data sets, *Geophysical Journal International*, **194**(2), 1091–1118.
- Cobden, L., Mosca, I., Trampert, J., & Ritsema, J., 2012. On the likelihood of post-perovskite near the core–mantle boundary: A statistical interpretation of seismic observations, *Physics of the Earth and Planetary Interiors*, **210**, 21–35.
- Cobden, L., Thomas, C., & Trampert, J., 2015. Seismic Detection of Post-perovskite Inside the Earth, in *The Earth’s Heterogeneous Mantle*, eds Khan, A. & De-

- schamps, F., Springer.
- Cottaar, S. & Lekic, V., 2016. Morphology of seismically slow lower-mantle structures, *Geophysical Supplements to the Monthly Notices of the Royal Astronomical Society*, **207**(2), 1122–1136.
- Cottaar, S. & Romanowicz, B., 2012. An unusually large ULVZ at the base of the mantle near Hawaii, *Earth and Planetary Science Letters*, **355**, 213–222.
- Courtillot, V., Davaille, A., Besse, J., & Stock, J., 2003. Three distinct types of hotspots in the Earth’s mantle, *Earth and Planetary Science Letters*, **205**(3–4), 295–308.
- Creasy, N., Pisconti, A., Long, M. D., Thomas, C., & Wookey, J., 2019. Constraining lowermost mantle anisotropy with body waves: A synthetic modelling study, *Geophysical Journal International*, **217**(2), 766–783.
- Dahlen, F. & Tromp, J., 1998. *Theoretical global seismology*, Princeton University Press.
- Dalton, C. A., Ekström, G., & Dziewoński, A. M., 2008. The global attenuation structure of the upper mantle, *Journal of Geophysical Research: Solid Earth*, **113**(B9).
- Dannberg, J., Eilon, Z., Faul, U., Gassmöller, R., Moulik, P., & Myhill, R., 2017. The importance of grain size to mantle dynamics and seismological observations, *Geochemistry, Geophysics, Geosystems*, **18**(8), 3034–3061.
- Davaille, A., 1999. Simultaneous generation of hotspots and superswells by convection in a heterogeneous planetary mantle, *Nature*, **402**(6763), 756–760.
- Davaille, A. & Romanowicz, B., 2020. Deflating the LLSVPs: bundles of mantle thermochemical plumes rather than thick stagnant “piles”, *Tectonics*, **39**(10), e2020TC006265.
- Davies, D. R., Goes, S., Davies, J. H., Schuberth, B., Bunge, H.-P., & Ritsema, J., 2012. Reconciling dynamic and seismic models of Earth’s lower mantle: The dominant role of thermal heterogeneity, *Earth and Planetary Science Letters*, **353**, 253–269.
- Davies, G. F. & Gurnis, M., 1986. Interaction of mantle dregs with convection: Lateral heterogeneity at the core-mantle boundary, *Geophysical Research Letters*, **13**(13), 1517–1520.
- de Wit, R., Käuffl, P., Valentine, A., & Trampert, J., 2014. Bayesian inversion of free oscillations for Earth’s radial (an)elastic structure, *Physics of the Earth and Planetary Interiors*, **237**, 1–17.
- Debaille, E., Bodin, T., Durand, S., & Ricard, Y., 2020. Seismic evidence for partial melt below tectonic plates, *Nature*, **586**(7830), 555–559.
- Della Mora, S., Boschi, L., Tackley, P., Nakagawa, T., & Giardini, D., 2011. Low seismic resolution cannot explain S/P decorrelation in the lower mantle, *Geophysical Research Letters*, **38**(12).

- Deschamps, F. & Trampert, J., 2003. Mantle tomography and its relation to temperature and composition, *Physics of the Earth and Planetary Interiors*, **140**(4), 277–291.
- Deschamps, F., Cobden, L., & Tackley, P. J., 2012. The primitive nature of large low shear-wave velocity provinces, *Earth and Planetary Science Letters*, **349**, 198–208.
- Deuss, A. & Woodhouse, J. H., 2001. Theoretical free-oscillation spectra: the importance of wide band coupling, *Geophysical Journal International*, **146**(3), 833–842.
- Deuss, A., Irving, J. C., & Woodhouse, J. H., 2010. Regional variation of inner core anisotropy from seismic normal mode observations, *Science*, **328**(5981), 1018–1020.
- Deuss, A., Ritsema, J., & van Heijst, H., 2013. A new catalogue of normal-mode splitting function measurements up to 10 mHz, *Geophysical Journal International*, **193**(2), 920–937.
- Doucet, L. S., Li, Z.-X., El Dien, H. G., Pourteau, A., Murphy, J. B., Collins, W. J., Mattioli, N., Olierook, H. K., Spencer, C. J., & Mitchell, R. N., 2020. Distinct formation history for deep-mantle domains reflected in geochemical differences, *Nature Geoscience*, **13**(7), 511–515.
- Durand, S., Debayle, E., Ricard, Y., & Lambotte, S., 2016. Seismic evidence for a change in the large-scale tomographic pattern across the D'' layer, *Geophysical Research Letters*, **43**(15), 7928–7936.
- Durek, J. J. & Ekström, G., 1996. A radial model of anelasticity consistent with long-period surface-wave attenuation, *Bulletin of the Seismological Society of America*, **86**(1A), 144–158.
- Durek, J. J. & Romanowicz, B., 1999. Inner core anisotropy inferred by direct inversion of normal mode spectra, *Geophysical Journal International*, **139**(3), 599–622.
- Dziewonski, A. M. & Anderson, D. L., 1981. Preliminary reference Earth model, *Physics of the Earth and Planetary Interiors*, **25**(4), 297–356.
- Dziewonski, A. M., Hager, B. H., & O'Connell, R. J., 1977. Large-scale heterogeneities in the lower mantle, *Journal of Geophysical Research*, **82**(2), 239–255.
- Dziewonski, A. M., Lekic, V., & Romanowicz, B. A., 2010. Mantle anchor structure: an argument for bottom up tectonics, *Earth and Planetary Science Letters*, **299**(1–2), 69–79.
- Edmonds, A., 1960. *Angular Momentum in Quantum Mechanics*, Princeton University Press.
- Ekström, G., Nettles, M., & Dziewoński, A., 2012. The global cmt project 2004–2010: Centroid-moment tensors for 13,017 earthquakes, *Physics of the Earth and Planetary Interiors*, **200**, 1–9.
- Faul, U. H. & Jackson, I., 2005. The seismological signature of temperature and grain size variations in the upper mantle, *Earth and Planetary Science Letters*, **234**(1–2), 119–134.

- Fichtner, A., Zunino, A., & Gebraad, L., 2019. Hamiltonian Monte Carlo solution of tomographic inverse problems, *Geophysical Journal International*, **216**(2), 1344–1363.
- Forte, A. M. & Mitrovica, J. X., 2001. Deep-mantle high-viscosity flow and thermochemical structure inferred from seismic and geodynamic data, *Nature*, **410**(6832), 1049–1056.
- French, S. W. & Romanowicz, B., 2015. Broad plumes rooted at the base of the Earth's mantle beneath major hotspots, *Nature*, **525**(7567), 95–99.
- Fukao, Y. & Obayashi, M., 2013. Subducted slabs stagnant above, penetrating through, and trapped below the 660 km discontinuity, *Journal of Geophysical Research: Solid Earth*, **118**(11), 5920–5938.
- Garnero, E. J. & Helmberger, D. V., 1996. Seismic detection of a thin laterally varying boundary layer at the base of the mantle beneath the central-Pacific, *Geophysical Research Letters*, **23**(9), 977–980.
- Garnero, E. J. & McNamara, A. K., 2008. Structure and dynamics of Earth's lower mantle, *science*, **320**(5876), 626–628.
- Garnero, E. J., Revenaugh, J., Williams, Q., Lay, T., & Kellogg, L. H., 1998. Ultralow velocity zone at the core-mantle boundary, *The core-mantle boundary region*, **28**, 319–334.
- Garnero, E. J., McNamara, A. K., & Shim, S.-H., 2016. Continent-sized anomalous zones with low seismic velocity at the base of Earth's mantle, *Nature Geoscience*, **9**(7), 481–489.
- Giardini, D., Li, X.-D., & Woodhouse, J. H., 1987. Three-dimensional structure of the Earth from splitting in free-oscillation spectra, *Nature*, **325**(6103), 405–411.
- Gleeson, M., Soderman, C., Matthews, S., Cottaar, S., & Gibson, S., 2021. Geochemical Constraints on the Structure of the Earth's Deep Mantle and the Origin of the LLSVPs, *Geochemistry, Geophysics, Geosystems*, **22**(9), e2021GC009932.
- Goryaeva, A. M., Carrez, P., & Cordier, P., 2016. Low viscosity and high attenuation in MgSiO₃ post-perovskite inferred from atomic-scale calculations, *Scientific reports*, **6**(1), 1–10.
- Gu, Y. J., Dziewonski, A. M., Su, W., & Ekström, G., 2001. Models of the mantle shear velocity and discontinuities in the pattern of lateral heterogeneities, *Journal of Geophysical Research: Solid Earth*, **106**(B6), 11169–11199.
- Gülcher, A. J. P., Ballmer, M. D., & Tackley, P. J., 2021. Coupled dynamics and evolution of primordial and recycled heterogeneity in Earth's lower mantle, *Solid Earth*, **12**(9), 2087–2107.
- Gung, Y. & Romanowicz, B., 2004. Q tomography of the upper mantle using three-component long-period waveforms, *Geophysical Journal International*, **157**(2), 813–830.
- Guo, Z. & Zhou, Y., 2020. Finite-frequency imaging of the global 410-and 660-km discontinuities using SS precursors, *Geophysical Journal International*, **220**(3),

- 1978–1994.
- Hager, B. H., Clayton, R. W., Richards, M. A., Comer, R. P., & Dziewonski, A. M., 1985. Lower mantle heterogeneity, dynamic topography and the geoid, *Nature*, **313**(6003), 541–545.
- He, X. & Tromp, J., 1996. Normal-mode constraints on the structure of the Earth, *Journal of Geophysical Research: Solid Earth*, **101**(B9), 20053–20082.
- He, Y. & Wen, L., 2009. Structural features and shear-velocity structure of the “Pacific Anomaly”, *Journal of Geophysical Research: Solid Earth*, **114**(B2).
- He, Y., Wen, L., & Zheng, T., 2006. Geographic boundary and shear wave velocity structure of the “Pacific anomaly” near the core–mantle boundary beneath western Pacific, *Earth and Planetary Science Letters*, **244**(1–2), 302–314.
- Hirose, K., 2002. Phase transitions in pyrolitic mantle around 670-km depth: Implications for upwelling of plumes from the lower mantle, *Journal of Geophysical Research: Solid Earth*, **107**(B4), ECV–3.
- Hirose, K., Takafuji, N., Sata, N., & Ohishi, Y., 2005. Phase transition and density of subducted MORB crust in the lower mantle, *Earth and Planetary Science Letters*, **237**(1–2), 239–251.
- Hjörleifsdóttir, V. & Ekström, G., 2010. Effects of three-dimensional Earth structure on CMT earthquake parameters, *Physics of the Earth and Planetary Interiors*, **179**(3–4), 178–190.
- Hosseini, K., Sigloch, K., Tsekhmistrenko, M., Zaheri, A., Nissen-Meyer, T., & Igel, H., 2019. Global mantle structure from multifrequency tomography using P, PP and P-diffracted waves, *Geophysical Journal International*, **220**(1), 96–141.
- Houser, C., Masters, G., Flanagan, M., & Shearer, P., 2008a. Determination and analysis of long-wavelength transition zone structure using SS precursors, *Geophysical Journal International*, **174**(1), 178–194.
- Houser, C., Masters, G., Shearer, P., & Laske, G., 2008b. Shear and compressional velocity models of the mantle from cluster analysis of long-period waveforms, *Geophysical Journal International*, **174**(1), 195–212.
- Hutko, A. R., Lay, T., & Revenaugh, J., 2009. Localized double-array stacking analysis of PcP: D” and ULVZ structure beneath the Cocos plate, Mexico, central Pacific, and north Pacific, *Physics of the Earth and Planetary Interiors*, **173**(1–2), 60–74.
- Hwang, Y. K. & Ritsema, J., 2011. Radial $Q\mu$ structure of the lower mantle from teleseismic body-wave spectra, *Earth and Planetary Science Letters*, **303**(3–4), 369–375.
- Ishii, M. & Tromp, J., 1999. Normal-mode and free-air gravity constraints on lateral variations in velocity and density of Earth’s mantle, *Science*, **285**(5431), 1231–1236.
- Ishii, M. & Tromp, J., 2001. Even-degree lateral variations in the earth’s mantle constrained by free oscillations and the free-air gravity anomaly, *Geophysical*

- Journal International*, **145**(1), 77–96.
- Ishii, M. & Tromp, J., 2004. Constraining large-scale mantle heterogeneity using mantle and inner-core sensitive normal modes, *Physics of the Earth and Planetary Interiors*, **146**(1–2), 113–124.
- Jackson, I., Fitz Gerald, J. D., Faul, U. H., & Tan, B. H., 2002. Grain-size-sensitive seismic wave attenuation in polycrystalline olivine, *Journal of Geophysical Research: Solid Earth*, **107**(B12), ECV–5.
- Jenkins, J., Deuss, A., & Cottaar, S., 2017. Converted phases from sharp 1000 km depth mid-mantle heterogeneity beneath Western Europe, *Earth and Planetary Science Letters*, **459**, 196–207.
- Jones, T. D., Maguire, R. R., van Keken, P. E., Ritsema, J., & Koelemeijer, P., 2020. Subducted oceanic crust as the origin of seismically slow lower-mantle structures, *Progress in Earth and Planetary Science*, **7**(1), 1–16.
- Jordan, T. H., 1978. Composition and development of the continental tectosphere, *Nature*, **274**(5671), 544–548.
- Julian, B. R., Foulger, G. R., Hatfield, O., Jackson, S. E., Simpson, E., Einbeck, J., & Moore, A., 2015. Hotspots in hindsight, in *The Interdisciplinary Earth: A Volume in Honor of Don L. Anderson*, vol. 1, pp. 105–121, eds Foulger, G. R., Lustrino, M., & King, S. D., The Geological Society of America.
- Kanda, R. V. & Stevenson, D. J., 2006. Suction mechanism for iron entrainment into the lower mantle, *Geophysical Research Letters*, **33**(2).
- Karaoğlu, H. & Romanowicz, B., 2018. Inferring global upper-mantle shear attenuation structure by waveform tomography using the spectral element method, *Geophysical Journal International*, **213**(3), 1536–1558.
- Karato, S.-I., 1993. Importance of anelasticity in the interpretation of seismic tomography, *Geophysical Research Letters*, **20**(15), 1623–1626.
- Karato, S.-I. & Karki, B. B., 2001. Origin of lateral variation of seismic wave velocities and density in the deep mantle, *Journal of Geophysical Research: Solid Earth*, **106**(B10), 21771–21783.
- Kellogg, L. H., Hager, B. H., & Van der Hilst, R. D., 1999. Compositional stratification in the deep mantle, *Science*, **283**(5409), 1881–1884.
- Kendall, J.-M. & Silver, P., 1998. Investigating causes of D'' anisotropy, *The core-mantle boundary region*, **28**, 97–118.
- Kennett, B., Widiyantoro, S., & Van Der Hilst, R., 1998. Joint seismic tomography for bulk sound and shear wave speed in the earth's mantle, *Journal of Geophysical Research: Solid Earth*, **103**(B6), 12469–12493.
- Kennett, B. L., Engdahl, E., & Buland, R., 1995. Constraints on seismic velocities in the Earth from traveltimes, *Geophysical Journal International*, **122**(1), 108–124.
- Knopoff, L., 1964. Q, *Reviews of Geophysics*, **2**(4), 625–660.
- Koelemeijer, P., 2021. Toward Consistent Seismological Models of the Core–Mantle

- Boundary Landscape, *Mantle Convection and Surface Expressions*, pp. 229–255.
- Koelemeijer, P., Deuss, A., & Ritsema, J., 2013. Observations of core-mantle boundary Stoneley modes, *Geophysical Research Letters*, **40**(11), 2557–2561.
- Koelemeijer, P., Ritsema, J., Deuss, A., & Van Heijst, H.-J., 2016. SP12RTS: a degree-12 model of shear- and compressional-wave velocity for Earth’s mantle, *Geophysical Journal International*, **204**(2), 1024–1039.
- Koelemeijer, P., Deuss, A., & Ritsema, J., 2017. Density structure of Earth’s lowermost mantle from Stoneley mode splitting observations, *Nature communications*, **8**, 15241.
- Koelemeijer, P., Schuberth, B. S., Davies, D. R., Deuss, A., & Ritsema, J., 2018. Constraints on the presence of post-perovskite in Earth’s lowermost mantle from tomographic-geodynamic model comparisons, *Earth and Planetary Science Letters*, **494**, 226–238.
- Koelemeijer, P. J., 2014. *Normal mode studies of long wavelength structures in Earth’s lowermost mantle*, Ph.D. thesis, University of Cambridge.
- Kreielkamp, P., Stein, C., & Hansen, U., 2022. LLSVPs of primordial origin: Implications for the evolution of plate tectonics, *Earth and Planetary Science Letters*, **579**, 117357.
- Kuo, C. & Romanowicz, B., 2002. On the resolution of density anomalies in the Earth’s mantle using spectral fitting of normal-mode data, *Geophysical Journal International*, **150**(1), 162–179.
- Kustowski, B., Ekström, G., & Dziewoński, A., 2008. Anisotropic shear-wave velocity structure of the Earth’s mantle: A global model, *Journal of Geophysical Research: Solid Earth*, **113**(B6).
- Kuwayama, Y., Hirose, K., Cobden, L., Kusakabe, M., Tateno, S., & Ohishi, Y., 2021. Post-Perovskite Phase Transition in the Pyrolitic Lowermost Mantle: Implications for Ubiquitous Occurrence of Post-Perovskite Above CMB, *Geophysical Research Letters*, p. e2021GL096219.
- Labrosse, S., Hernlund, J., & Coltice, N., 2007. A crystallizing dense magma ocean at the base of the Earth’s mantle, *Nature*, **450**(7171), 866–869.
- Laske, G. & Widmer-Schmidrig, R., 2007. Theory and observations: Normal mode and surface wave observations, in *Seismology and Structure of the Earth: Treatise on Geophysics*, vol. 1, pp. 117–168, ed. Schubert, G., Elsevier.
- Lau, H. C. & Faul, U. H., 2019. Anelasticity from seismic to tidal timescales: Theory and observations, *Earth and Planetary Science Letters*, **508**, 18–29.
- Lau, H. C., Mitrovica, J. X., Davis, J. L., Tromp, J., Yang, H.-Y., & Al-Attar, D., 2017. Tidal tomography constrains Earth’s deep-mantle buoyancy, *Nature*, **551**(7680), 321–326.
- Lau, H. C., Robson, A., Koelemeijer, P., & Romanowicz, B. A., 2020. How much and where? Exploring Excess Density within the LLSVPs by reconciling Stoneley Mode and Earth Tide Observations., in *AGU Fall Meeting Abstracts*, vol. 2020,

pp. DI009–03.

- Lawrence, J. F. & Wyssession, M. E., 2006a. QLM9: A new radial quality factor ($Q\mu$) model for the lower mantle, *Earth and Planetary Science Letters*, **241**(3–4), 962–971.
- Lawrence, J. F. & Wyssession, M. E., 2006b. Seismic evidence for subduction-transported water in the lower mantle, *Geophysical Monograph-American Geophysical Union*, **168**, 251.
- Lay, T. & Helmberger, D. V., 1983. A lower mantle S-wave triplication and the shear velocity structure of D”, *Geophysical Journal International*, **75**(3), 799–837.
- Lei, W., Ruan, Y., Bozdağ, E., Peter, D., Lefebvre, M., Komatitsch, D., Tromp, J., Hill, J., Podhorszki, N., & Pugmire, D., 2020. Global adjoint tomography—model GLAD-M25, *Geophysical Journal International*, **223**(1), 1–21.
- Lekic, V., Cottaar, S., Dziewonski, A., & Romanowicz, B., 2012. Cluster analysis of global lower mantle tomography: A new class of structure and implications for chemical heterogeneity, *Earth and Planetary Science Letters*, **357**, 68–77.
- Li, X.-D. & Romanowicz, B., 1996. Global mantle shear velocity model developed using nonlinear asymptotic coupling theory, *Journal of Geophysical Research: Solid Earth*, **101**(B10), 22245–22272.
- Li, X.-D., Giardini, D., & Woodhouse, J. H., 1991. Large-scale three-dimensional even-degree structure of the Earth from splitting of long-period normal modes, *Journal of Geophysical Research: Solid Earth*, **96**(B1), 551–577.
- Li, Y., Deschamps, F., & Tackley, P. J., 2014. The stability and structure of primordial reservoirs in the lower mantle: insights from models of thermochemical convection in three-dimensional spherical geometry, *Geophysical Journal International*, **199**(2), 914–930.
- Liu, C. & Grand, S. P., 2018. Seismic attenuation in the African LLSVP estimated from PcS phases, *Earth and Planetary Science Letters*, **489**, 8–16.
- Liu, H.-P., Anderson, D. L., & Kanamori, H., 1976. Velocity dispersion due to anelasticity; implications for seismology and mantle composition, *Geophysical Journal International*, **47**(1), 41–58.
- Lu, C., Forte, A. M., Simmons, N. A., Grand, S. P., Kajan, M. N., Lai, H., & Garnero, E. J., 2020. The sensitivity of joint inversions of seismic and geodynamic data to mantle viscosity, *Geochemistry, Geophysics, Geosystems*, **21**(4), e2019GC008648.
- Mäkinen, A. M. & Deuss, A., 2013. Normal mode splitting function measurements of anelasticity and attenuation in the Earth’s inner core, *Geophysical Journal International*, **194**(1), 401–416.
- Mao, W. L., Mao, H.-k., Sturhahn, W., Zhao, J., Prakapenka, V. B., Meng, Y., Shu, J., Fei, Y., & Hemley, R. J., 2006. Iron-rich post-perovskite and the origin of ultralow-velocity zones, *Science*, **312**(5773), 564–565.
- Marquardt, H. & Miyagi, L., 2015. Slab stagnation in the shallow lower mantle

- linked to an increase in mantle viscosity, *Nature Geoscience*, **8**(4), 311–314.
- Masters, G., Laske, G., Bolton, H., & Dziewonski, A., 2000a. The relative behavior of shear velocity, bulk sound speed, and compressional velocity in the mantle: Implications for chemical and thermal structure, *Earth's deep interior: Mineral physics and tomography from the atomic to the global scale*, **117**, 63–87.
- Masters, G., Laske, G., & Gilbert, F., 2000b. Matrix autoregressive analysis of free-oscillation coupling and splitting, *Geophysical Journal International*, **143**(2), 478–489.
- Masters, T. & Widmer, R., 1995. Free oscillations: frequencies and attenuations, *Global Earth Physics: a handbook of physical constants*, **1**, 104.
- Matas, J. & Bukowski, M. S., 2007. On the anelastic contribution to the temperature dependence of lower mantle seismic velocities, *Earth and Planetary Science Letters*, **259**(1-2), 51–65.
- McNamara, A. K., 2019. A review of large low shear velocity provinces and ultra low velocity zones, *Tectonophysics*, **760**, 199–220.
- McNamara, A. K., Van Keken, P. E., & Karato, S.-I., 2002. Development of anisotropic structure in the Earth's lower mantle by solid-state convection, *Nature*, **416**(6878), 310–314.
- Mégnin, C. & Romanowicz, B., 1995. Estimation of inner core mode splitting functions combining a genetic algorithm with a direct iterative inversion scheme, *EOS, Trans. Am. geophys. Un.*, **76**, 355.
- Mégnin, C. & Romanowicz, B., 2000. The three-dimensional shear velocity structure of the mantle from the inversion of body, surface and higher-mode waveforms, *Geophysical Journal International*, **143**(3), 709–728.
- Meschede, M. & Romanowicz, B., 2015. Lateral heterogeneity scales in regional and global upper mantle shear velocity models, *Geophysical Journal International*, **200**(2), 1078–1095.
- Mooney, W. D., Laske, G., & Masters, T. G., 1998. CRUST 5.1: A global crustal model at 5×5 , *Journal of Geophysical Research: Solid Earth*, **103**(B1), 727–747.
- Mosca, I., Cobden, L., Deuss, A., Ritsema, J., & Trampert, J., 2012. Seismic and mineralogical structures of the lower mantle from probabilistic tomography, *Journal of Geophysical Research: Solid Earth*, **117**(B6).
- Moulik, P. & Ekström, G., 2016. The relationships between large-scale variations in shear velocity, density, and compressional velocity in the Earth's mantle, *Journal of Geophysical Research: Solid Earth*, **121**(4), 2737–2771.
- Murakami, M., Hirose, K., Kawamura, K., Sata, N., & Ohishi, Y., 2004. Post-perovskite phase transition in MgSiO_3 , *Science*, **304**(5672), 855–858.
- Ni, S., Tan, E., Gurnis, M., & Helmberger, D., 2002. Sharp sides to the African superplume, *science*, **296**(5574), 1850–1852.
- Nomura, R., Ozawa, H., Tateno, S., Hirose, K., Hernlund, J., Muto, S., Ishii, H., &

- Hiraoka, N., 2011. Spin crossover and iron-rich silicate melt in the Earth's deep mantle, *Nature*, **473**(7346), 199–202.
- Oganov, A. R. & Ono, S., 2004. Theoretical and experimental evidence for a post-perovskite phase of MgSiO₃ in Earth's D" layer, *Nature*, **430**(6998), 445–448.
- Pachhai, S., Tkalčić, H., & Masters, G., 2016. Estimation of splitting functions from Earth's normal mode spectra using the neighbourhood algorithm, *Geophysical Journal International*, **204**(1), 111–126.
- Panero, W. R., Pigott, J. S., Reaman, D. M., Kabbes, J. E., & Liu, Z., 2015. Dry (Mg, Fe) SiO₃ perovskite in the Earth's lower mantle, *Journal of Geophysical Research: Solid Earth*, **120**(2), 894–908.
- Pisconti, A., Thomas, C., & Wookey, J., 2019. Discriminating between causes of D" anisotropy using reflections and splitting measurements for a single path, *Journal of Geophysical Research: Solid Earth*, **124**(5), 4811–4830.
- Pratt, R. G., Shin, C., & Hick, G., 1998. Gauss–Newton and full Newton methods in frequency–space seismic waveform inversion, *Geophysical journal international*, **133**(2), 341–362.
- Reiss, M., Long, M., & Creasy, N., 2019. Lowermost mantle anisotropy beneath Africa from differential SKS-SKKS shear-wave splitting, *Journal of Geophysical Research: Solid Earth*, **124**(8), 8540–8564.
- Resovsky, J. & Ritzwoller, M., 1998. New and refined constraints on three-dimensional Earth structure from normal modes below 3 mHz, *Journal of Geophysical Research: Solid Earth*, **103**(B1), 783–810.
- Resovsky, J. & Ritzwoller, M., 1999. A degree 8 mantle shear velocity model from normal mode observations below 3 mHz, *Journal of Geophysical Research: Solid Earth*, **104**(B1), 993–1014.
- Resovsky, J. & Trampert, J., 2003. Using probabilistic seismic tomography to test mantle velocity–density relationships, *Earth and Planetary Science Letters*, **215**(1–2), 121–134.
- Resovsky, J., Trampert, J., & Van der Hilst, R., 2005. Error bars for the global seismic Q profile, *Earth and Planetary Science Letters*, **230**(3–4), 413–423.
- Resovsky, J. S. & Ritzwoller, M. H., 1999b. Regularization uncertainty in density models estimated from normal mode data, *Geophysical research letters*, **26**(15), 2319–2322.
- Rickers, F., Fichtner, A., & Trampert, J., 2013. The Iceland–Jan Mayen plume system and its impact on mantle dynamics in the North Atlantic region: evidence from full-waveform inversion, *Earth and Planetary Science Letters*, **367**, 39–51.
- Ringwood, A. E., 1991. Phase transformations and their bearing on the constitution and dynamics of the mantle, *Geochimica et Cosmochimica Acta*, **55**(8), 2083–2110.
- Ritsema, J. & Lekić, V., 2020. Heterogeneity of seismic wave velocity in Earth's mantle, *Annual Review of Earth and Planetary Sciences*, **48**, 377–401.

- Ritsema, J. & van Heijst, H.-J., 2002. Constraints on the correlation of P-and S-wave velocity heterogeneity in the mantle from P, PP, PPP and PKP ab traveltimes, *Geophysical Journal International*, **149**(2), 482–489.
- Ritsema, J., van Heijst, H. J., & Woodhouse, J. H., 1999. Complex shear wave velocity structure imaged beneath Africa and Iceland, *Science*, **286**(5446), 1925–1928.
- Ritsema, J., Deuss, A., Van Heijst, H. J., & Woodhouse, J. H., 2011. S40RTS: a degree-40 shear-velocity model for the mantle from new Rayleigh wave dispersion, teleseismic traveltime and normal-mode splitting function measurements, *Geophysical Journal International*, **184**(3), 1223–1236.
- Robertson, G. & Woodhouse, J., 1996. Ratio of relative S to P velocity heterogeneity in the lower mantle, *Journal of Geophysical Research: Solid Earth*, **101**(B9), 20041–20052.
- Robson, A., Lau, H. C., Koelemeijer, P., & Romanowicz, B., 2021. An analysis of core–mantle boundary Stoneley mode sensitivity and sources of uncertainty, *Geophysical Journal International*, **228**(3), 1962–1974.
- Romanowicz, B., 2001. Can we resolve 3D density heterogeneity in the lower mantle?, *Geophysical Research Letters*, **28**(6), 1107–1110.
- Romanowicz, B. & Mitchell, B., 2015. 1.25—Deep earth structure: Q of the Earth from crust to core, *Treatise on geophysics*, **1**, 789–827.
- Romanowicz, B. & Wenk, H.-R., 2017. Anisotropy in the deep Earth, *Physics of the Earth and Planetary Interiors*, **269**, 58–90.
- Rost, S., Garnero, E. J., Williams, Q., & Manga, M., 2005. Seismological constraints on a possible plume root at the core–mantle boundary, *Nature*, **435**(7042), 666–669.
- Rudolph, M., Moulik, P., & Lekić, V., 2020. Bayesian Inference of Mantle Viscosity From Whole-Mantle Density Models, *Geochemistry, Geophysics, Geosystems*, **21**(11), e2020GC009335.
- Rudolph, M. L., Lekić, V., & Lithgow-Bertelloni, C., 2015. Viscosity jump in Earth’s mid-mantle, *Science*, **350**(6266), 1349–1352.
- Saltzer, R. v., Van der Hilst, R., & Karason, H., 2001. Comparing P and S wave heterogeneity in the mantle, *Geophysical research letters*, **28**(7), 1335–1338.
- Scherbaum, F., Krüger, F., & Weber, M., 1997. Double beam imaging: mapping lower mantle heterogeneities using combinations of source and receiver arrays, *Journal of Geophysical Research: Solid Earth*, **102**(B1), 507–522.
- Schneider, S. & Deuss, A., 2021. A new catalogue of toroidal-mode overtone splitting function measurements, *Geophysical Journal International*, **225**(1), 329–341.
- Schneider, S. & Deuss, A., 2021b. Large-scale radial mantle anisotropy constrained by combining toroidal and spheroidal modes, in *AGU Fall Meeting 2021*, AGU.
- Schubert, G., Masters, G., Olson, P., & Tackley, P., 2004. Superplumes or plume

- clusters?, *Physics of the Earth and Planetary Interiors*, **146**(1-2), 147–162.
- Schuberth, B. S., Bunge, H.-P., & Ritsema, J., 2009. Tomographic filtering of high-resolution mantle circulation models: Can seismic heterogeneity be explained by temperature alone?, *Geochemistry, Geophysics, Geosystems*, **10**(5).
- Shephard, G. E., Matthews, K. J., Hosseini, K., & Domeier, M., 2017. On the consistency of seismically imaged lower mantle slabs, *Scientific reports*, **7**(1), 1–17.
- Simmons, N. A., Forte, A. M., & Grand, S. P., 2009. Joint seismic, geodynamic and mineral physical constraints on three-dimensional mantle heterogeneity: Implications for the relative importance of thermal versus compositional heterogeneity, *Geophysical Journal International*, **177**(3), 1284–1304.
- Simmons, N. A., Forte, A. M., Boschi, L., & Grand, S. P., 2010. GyPSuM: A joint tomographic model of mantle density and seismic wave speeds, *Journal of Geophysical Research: Solid Earth*, **115**(B12).
- Stixrude, L. & Lithgow-Bertelloni, C., 2011. Thermodynamics of mantle minerals-II. Phase equilibria, *Geophysical Journal International*, **184**(3), 1180–1213.
- Stockmann, F., Cobden, L., Deschamps, F., Fichtner, A., & Thomas, C., 2019. Investigating the seismic structure and visibility of dynamic plume models with seismic array methods, *Geophysical Journal International*, **219**(Supplement_1), S167–S194.
- Su, W.-J. & Dziewonski, A. M., 1997. Simultaneous inversion for 3-D variations in shear and bulk velocity in the mantle, *Physics of the Earth and Planetary Interiors*, **100**(1-4), 135–156.
- Tackley, P. J., 2012. Dynamics and evolution of the deep mantle resulting from thermal, chemical, phase and melting effects, *Earth-Science Reviews*, **110**(1-4), 1–25.
- Tackley, P. J. et al., 1998. Three-dimensional simulations of mantle convection with a thermo-chemical basal boundary layer: D"?, *The Core-Mantle Boundary Region, Geodyn. Ser.*, **28**, 231–253.
- Talavera-Soza, S., Cobden, L. J., Faul, U., & Deuss, A. F., 2021b. Global 3D Model of Mantle Attenuation using Normal Modes, in *AGU Fall Meeting Abstracts*, vol. 2021.
- Talavera-Soza, S. A., 2021a. *Observing seismic attenuation in the Earth's mantle and inner core using normal modes*, Ph.D. thesis, Utrecht University.
- Tan, E. & Gurnis, M., 2005. Metastable superplumes and mantle compressibility, *Geophysical Research Letters*, **32**(20).
- Tanaka, S., Suetsugu, D., Shiobara, H., Sugioka, H., Kanazawa, T., Fukao, Y., Barruol, G., & Reymond, D., 2009. On the vertical extent of the large low shear velocity province beneath the South Pacific Superswell, *Geophysical Research Letters*, **36**(7).
- Tarantola, A., 2005. *Inverse problem theory and methods for model parameter esti-*

- mation, vol. 89, SIAM.
- Tarantola, A. & Valette, B., 1982. Generalized nonlinear inverse problems solved using the least squares criterion, *Reviews of Geophysics*, **20**(2), 219–232.
- Tesoniero, A., Cammarano, F., & Boschi, L., 2016. S- to- P heterogeneity ratio in the lower mantle and thermo-chemical implications, *Geochemistry, Geophysics, Geosystems*, **17**(7), 2522–2538.
- Thomas, C., Wookey, J., Brodholt, J., & Fieseler, T., 2011. Anisotropy as cause for polarity reversals of D" reflections, *Earth and Planetary Science Letters*, **307**(3-4), 369–376.
- Thomas, C., Cobden, L., & Jonkers, A. R., 2022. D" reflection polarities inform lowermost mantle mineralogy, *Earth and Space Science Open Archive*, p. 28.
- Thorne, M. S., Garnero, E. J., & Grand, S. P., 2004. Geographic correlation between hot spots and deep mantle lateral shear-wave velocity gradients, *Physics of the Earth and Planetary Interiors*, **146**(1-2), 47–63.
- Torsvik, T. H., Smethurst, M. A., Burke, K., & Steinberger, B., 2006. Large igneous provinces generated from the margins of the large low-velocity provinces in the deep mantle, *Geophysical Journal International*, **167**(3), 1447–1460.
- Torsvik, T. H., Burke, K., Steinberger, B., Webb, S. J., & Ashwal, L. D., 2010. Diamonds sampled by plumes from the core–mantle boundary, *Nature*, **466**(7304), 352–355.
- Torsvik, T. H., van der Voo, R., Doubrovine, P. V., Burke, K., Steinberger, B., Ashwal, L. D., Trønnes, R. G., Webb, S. J., & Bull, A. L., 2014. Deep mantle structure as a reference frame for movements in and on the Earth, *Proceedings of the National Academy of Sciences*, **111**(24), 8735–8740.
- Trampert, J. & Van Der Hilst, R. D., 2005. Towards a quantitative interpretation of global seismic tomography, *Geophysical Monograph Series*, **160**, 47–62.
- Trampert, J., Vacher, P., & Vlaar, N., 2001. Sensitivities of seismic velocities to temperature, pressure and composition in the lower mantle, *Physics of the Earth and Planetary Interiors*, **124**(3-4), 255–267.
- Trampert, J., Deschamps, F., Resovsky, J., & Yuen, D., 2004. Probabilistic tomography maps chemical heterogeneities throughout the lower mantle, *Science*, **306**(5697), 853–856.
- Tsuchiya, T. & Tsuchiya, J., 2006b. Effect of impurity on the elasticity of perovskite and postperovskite: Velocity contrast across the postperovskite transition in (Mg, Fe, Al)(Si, Al) O₃, *Geophysical Research Letters*, **33**(12).
- Tsuchiya, T., Tsuchiya, J., Umemoto, K., & Wentzcovitch, R. M., 2004. Phase transition in MgSiO₃ perovskite in the earth's lower mantle, *Earth and Planetary Science Letters*, **224**(3-4), 241–248.
- Tsuchiya, T., Wentzcovitch, R. M., Da Silva, C. R., & De Gironcoli, S., 2006. Spin transition in magnesio-wüstite in Earth's lower mantle, *Physical Review Letters*, **96**(19), 198501.

- van Tent, R., Deuss, A. F., Fichtner, A., Gebraad, L., & Trampert, J., 2020. An Analysis of Normal-Mode Based 3-D Mantle Density Models using Hamiltonian Monte Carlo Methods, in *AGU Fall Meeting Abstracts*, vol. 2020, pp. DI005–0003.
- van Tent, R., Cobden, L. J., Deschamps, F., Fichtner, A., Gebraad, L., Schneider, S., Trampert, J., & Deuss, A. F., 2021. Reconciling 3-D Mantle Density Models using Recent Normal-Mode Measurements and Thermochemical Convection Modelling, in *AGU Fall Meeting 2021*, AGU.
- Vinnik, L. P., Farra, V., & Romanowicz, B., 1989. Azimuthal anisotropy in the Earth from observations of SKS at Geoscope and NARS broadband stations, *Bulletin of the Seismological Society of America*, **79**(5), 1542–1558.
- Virieux, J. & Operto, S., 2009. An overview of full-waveform inversion in exploration geophysics, *Geophysics*, **74**(6), WCC1–WCC26.
- Wang, W., Xu, Y., Sun, D., Ni, S., Wentzcovitch, R., & Wu, Z., 2020. Velocity and density characteristics of subducted oceanic crust and the origin of lower-mantle heterogeneities, *Nature communications*, **11**(1), 1–8.
- Wang, Y. & Wen, L., 2004. Mapping the geometry and geographic distribution of a very low velocity province at the base of the Earth’s mantle, *Journal of Geophysical Research: Solid Earth*, **109**(B10).
- Waszek, L., Schmerr, N. C., & Ballmer, M. D., 2018. Global observations of reflectors in the mid-mantle with implications for mantle structure and dynamics, *Nature communications*, **9**(1), 1–13.
- Wenk, H.-R., Cottaar, S., Tomé, C. N., McNamara, A., & Romanowicz, B., 2011. Deformation in the lowermost mantle: From polycrystal plasticity to seismic anisotropy, *Earth and Planetary Science Letters*, **306**(1-2), 33–45.
- White, W. M., 2015. Probing the Earth’s deep interior through geochemistry, *Geochemical Perspectives*, **4**(2).
- Widmer, R., Masters, G., & Gilbert, F., 1991. Spherically symmetric attenuation within the Earth from normal mode data, *Geophysical journal international*, **104**(3), 541–553.
- Williams, Q. & Garnero, E. J., 1996. Seismic evidence for partial melt at the base of Earth’s mantle, *Science*, **273**(5281), 1528–1530.
- Woodhouse, J., 1980. The coupling and attenuation of nearly resonant multiplets in the Earth’s free oscillation spectrum, *Geophysical Journal International*, **61**(2), 261–283.
- Woodhouse, J. & Dahlen, F., 1978. The effect of a general aspherical perturbation on the free oscillations of the Earth, *Geophysical Journal International*, **53**(2), 335–354.
- Woodhouse, J. & Deuss, A., 2007. Theory and observations–Earth’s free oscillations, in *Seismology and Structure of the Earth: Treatise on Geophysics*, vol. 1, pp. 79–116, ed. Schubert, G., Elsevier.
- Woodhouse, J. & Girnius, T., 1982. Surface waves and free oscillations in a region-

- alized earth model, *Geophysical Journal International*, **68**(3), 653–673.
- Woodhouse, J. H. & Dziewonski, A. M., 1984. Mapping the upper mantle: Three-dimensional modeling of Earth structure by inversion of seismic waveforms, *Journal of Geophysical Research: Solid Earth*, **89**(B7), 5953–5986.
- Yang, H.-Y. & Tromp, J., 2015. Synthetic free-oscillation spectra: an appraisal of various mode-coupling methods, *Geophysical Journal International*, **203**(2), 1179–1192.
- Yoshino, T. & Yamazaki, D., 2007. Grain growth kinetics of CaIrO₃ perovskite and post-perovskite, with implications for rheology of D'' layer, *Earth and Planetary Science Letters*, **255**(3-4), 485–493.
- Yu, S. & Garnero, E. J., 2018. Ultralow velocity zone locations: A global assessment, *Geochemistry, Geophysics, Geosystems*, **19**(2), 396–414.
- Yuan, K. & Romanowicz, B., 2017. Seismic evidence for partial melting at the root of major hot spot plumes, *Science*, **357**(6349), 393–397.
- Zhang, B., Ni, S., & Chen, Y., 2019. Seismic attenuation in the lower mantle beneath Northeast China constrained from short-period reflected core phases at short epicentral distances, *Earth and Planetary Physics*, **3**(6), 537–546.

Curriculum Vitæ

E.A.A.M. (Lisanne) Jagt

10-06-1994 Born in Amersfoort, the Netherlands.

Education

2017-2022 **Ph.D. in Seismology**,
Utrecht University, the Netherlands

2015-2017 **M.Sc. Earth Structure and Dynamics** (cum laude),
Utrecht University, the Netherlands

2012-2015 **B.Sc. Earth Sciences** (cum laude),
Utrecht University, the Netherlands

Working experience

2022- **Postdoc in Deep Earth Seismology**,
Cambridge University, Cambridge, United Kingdom

2022 **Postdoc in Seismology**,
Utrecht University, Utrecht, the Netherlands

2016-2017 **Student assistant data management**,
ORFEUS Data Centre, De Bilt, the Netherlands

2015-2017 **Teaching assistant**,
Utrecht University, Utrecht, the Netherlands

List of Publications

Schneider, S., Talavera-Soza, S., Jagt, L., & Deuss, A. (2022). FrosPy: A Modular Python Toolbox for Normal Mode Seismology. *Seismological Research Letters*, **93**(2A), 967-974.

Jagt, L., & Deuss, A. (2021). Comparing one-step full-spectrum inversion with two-step splitting function inversion in normal mode tomography. *Geophysical Journal International*, **227**(1), 559-575.

Jagt, L., Ruigrok, E., & Paulssen, H. (2017). Relocation of clustered earthquakes in the Groningen gas field. *Netherlands Journal of Geosciences*, **96**(5), s163-s173.